Elucidating interplay, stability and charge transfer dynamics at lead halide perovskite nanocrystal / 2D transition metal dichalcogenide interface for solar cell applications

Azmat Ali

To cite this version:

Azmat Ali. Elucidating interplay, stability and charge transfer dynamics at lead halide perovskite nanocrystal / 2D transition metal dichalcogenide interface for solar cell applications. Condensed Matter [cond-mat]. Sorbonne Université, 2023. English. NNT : 2023SORUS375 . tel-04361436

HAL Id: tel-04361436
https://theses.hal.science/tel-04361436

Submitted on 22 Dec 2023

Sorbonne Université

Ecole doctorale 397 Physique et Chimie des Matériaux

UMR 7588 CNRS-INSP / Physico-chimie et dynamique des surfaces

Elucidating interplay, stability and charge transfer dynamics at lead halide perovskite nanocrystal / 2D transition metal dichalcogenide interface for solar cell applications

Conducted at the **Paris Institute of Nanosciences (INSP)**

Presented by **AZMAT ALI**

To obtain the degree of **doctorate of philosophy** in *Physics and Chemistry of Materials* from Sorbonne Université

Defended on : 14/11/2023

Before the jury composed of:

Président of the jury (Philip Schulz)	Directeur de recherche	IPVF	Examinateur
Arnaud Etcheberry	Directeur de recherche émérite,	ILV	Rapporteur
Selina Olthof	Professeure associée	IPC-UOC	Rapporteure
Nadine Witkowski	Professeure		Directrice de thèse
Fredrik O. L. Johanssson	Docteur	Uppsala Université	Invité

*“Dedicated to my parents, specially to my father (**Ali Khan**)”*

Acknowledgements

Today, November 14, 2023, marks the culmination of an incredibly successful three-year journey at INSP, Sorbonne Université, Paris, France. The transformative transition from Azmat Ali to Dr. Azmat Ali has been a roller coaster of exhilarating highs and challenging lows.

Hailing from the remote region of Abbottabad, Pakistan, the path to earning a Ph.D. from the esteemed Sorbonne Université was undeniably challenging. The demanding nature of the work, especially during Synchrotron runs, magnified these challenges. Yet, the opportunity to fulfill a long-standing dream from high school – to work at a synchrotron – made this Ph.D. journey feel like a dream come true.

The last few months of this academic pursuit were crazy. Working round the clock, navigating through the complexities of research and the final thesis, it often felt like a surreal and demanding race against time. Yet, in the end, the culmination of these efforts brought forth not just the prestigious title but also the highest qualification attainable in one's academic journey.

Getting a PhD is always the teamwork and a process which involves many people. I would like to thank all those who helped me to achieve this milestone. Firstly, I would like to thank to Prof Selina Olthof, Dr. Arnaud Etcheberry, and Dr. Philip Schulz for accepting the invitation to be part of my thesis committee, positively evaluating the thesis, and engaging in stimulating scientific discussions following my defense presentation. Secondly, I would like to express my deepest gratitude to my supervisor, Prof Nadine Witkowski, for accepting me as her another international PhD student, notably being the first non-European and Pakistani in this role, and her invaluable guidance all these three years. I still remember meeting her on Friday, just before another lockdown in France due to Covid-19 pandemics, and signing the contract so that I will be in stable financial position and paying my first-year fees although which I paid back later to her. Also, I would like to thank her for believing and confidence that she had shown one me that I will make it through this roller-coaster journey. In particular, her speech at the end really touched my heart specially, for acknowledging and appreciating my hard-work of these years, the challenges that we had while working with the spray and spectrometer for XPS. I am immensely thankful for her friendly yet highly professional and intelligent guidance.

The next person to whom I owe a lot is Dr. Fredrik O.L. Johansson, one of the most brilliant, smartest, and kindest people that I have ever met. I am short on words to say thanks to him. Thank you, Fredrik, for teaching me how the synchrotron works and all the intricate phenomena involved in photoelectron spectroscopy (also known as XPS). I would like to extend my thanks for teaching me everything from data treatment to data analyzing and writing the papers. Your company while working at the synchrotron was truly enjoyable, and your professionalism attitude left a lasting impression on me. Lastly, I am immensely grateful for your patience in answering all my questions and many of the stupid ones as well.

I would also like to thank Hervé Cruguel for all his help during beamtime and suggesting me to start thesis writing as early as possible which undoubtedly helped me at the end. Another incredible and kind person to whom I should say thank is Sébastien Royer, for all his help while working in the laboratory, in particular when I was working with vacuum spray. Furthermore, I like to thank Dylan Amelot for his help for teaching me how vacuum spray works. Besides, I thank to Emmanuel Lhuillier for providing the perovskite nanocrystals. Also, I would like to thank all the members of the Physuf team and the INSP, in particular Maximiliano Marangolo, Director of the INSP and Geoffroy Prévot, Team Leader. I also think of Sylvie, Cécile at the secretariat who helped me many times, or Corinne and François at the IT department, Emrick for our RBS measurement sessions, Yunlin for XRD measurements, and Erwan for providing Au substrate. I also like to thank Mariam Ahmad from University of Southern Denmark for providing MoO_x substrates. Also, I would like to thank Abhay Shukla and IMAT for my PhD funding.

It would be unfair if I did not thank the beamline scientists at the TEMPO beamline, Mathieu Silly and Lenart Dudy at Soleil Synchrotron, and at the PM4 beamline at BESSY II Synchrotron, Ruslan Ovsyannikov, and Erika Giangrisostomi. I am particularly grateful to Erika Giangrisostomi for the lengthy calls discussing the factors that need to be considered when quantifying the peak intensities of core-levels of a material.

Lastly, this significant achievement is not mine alone to celebrate. I would also like to thank all the friends at INSP, specially mention to Luis Lechaptois, for all the coffee breaks and lunch that we had at the university's canteen. Guillaume for helping to deal with French administration stuff and playing a role of translator for me when I had to write to prefecture for visa extension. Zakarya for helping me in writing French summary of my thesis. Also, my friends outside INSP, Imran khan receiving me from the airport, Saim, Khadim, Wahid, Sami, Ihsan, Gufrhan, Faraz and Wasif for all the weekends gathering that we had.

Finally, I extend my heartfelt dedication to my family, parents, brothers and sister. I like to mention my eldest brother Ali Raza, who encouraged me for further education when I wanted to drop out after my high school. A profound acknowledgment of my father's unwavering support that acted as a steady anchor throughout the twists and turns of my educational career. In fact, my father wanted one of us (siblings) to become a medical doctor but all of us like engineering. Therefore, my motivation for this PhD is actually to fulfill his wish, albeit not in the form of medical doctor but at least as a PhD doctor. It feels like a dream come true to fulfill his wish. Besides, his encouragement and belief in my abilities have been instrumental in reaching this pinnacle of academic success. Finally, the end of thesis also marks the end of three incredible years at Jussieu, in the city of love (Paris), of which I will keep unforgettable memories that I will cherish forever.

Thank You all.

With love,

Dr. Azmat Ali

Table of Contents

Abstract

Lead halide perovskites are considered strong contenders for the next generation of photovoltaics, nonetheless the intrinsic instability of halide perovskite remains a bottleneck for the commercialization of this technology. The striking properties of halide perovskites, fully inorganic $CsPbBr_3$, used in this thesis, when combined with the exceptional properties of nanocrystals (NCs), can result in a material that possesses the attributes of both. Yet, the fundamental properties of perovskite NCs are strongly modified at the interface with charge transport layers and exposure to light. In this thesis, using photoelectron spectroscopy (PES), the dynamical processes that occur at the surface and in the interfaces of $CsPbBr_3$ NCs on metal, semiconductor and oxides, when exposed to infrared (IR) and ultraviolet (UV) light are investigated. The decomposition of perovskite on all the substrates under UV illumination gives a common degradation product of metallic lead (Pb^0) and bromide gas ($Br_2(g)$). However, for the $CsPbBr_3$ NCs on gold (Au), both UV light and intense x-rays irradiation not only leads to the anticipated degradation product, Pb^0 and $Br_2(g)$, but also gives rise to a new chemical specie, which is associated with the underpotential deposition of lead (Pb_{UPD}) on the Au surface. Furthermore, UPD of Pb is shown to occur only when the perovskite structure breaks and a direct contact of perovskite and Au is made. Moreover, UV light degradation to the perovskite NCs with regard to metallic lead formation occurs to a lesser extent on ITO and MoO_x than on MoS_2 and Au, revealing that substrates with wider bandgaps prevent the decomposition of the perovskite. Similarly, different effects of NCs to IR light is observed on Au, and MoS_2 and MoO_x. IR illumination affects the perovskite NCs on Au in the same way as the UV light and intense x-rays do, but no bromide gas is formed. IR illumination of the $CsPbBr_3$ NCs on MoS_2 and MoO_x results in intraband surface photovoltage. This photovoltage stems from the deep defects-states located in the middle of the bandgap. However, no decomposition of the perovskite is observed. The findings of this thesis emphasize the substrate dependent properties of the perovskite and their influence when exposed to IR and UV light.

Résumé

Les pérovskites d'halogénure de plomb sont considérées comme des candidats sérieux pour la prochaine génération de photovoltaïques, mais l'instabilité intrinsèque des pérovskites d'halogénures reste un obstacle à la commercialisation de cette technologie. Les propriétés remarquables des pérovskites d'halogénure, $CsPbBr_3$ entièrement inorganique, utilisées dans cette thèse, lorsqu'elles sont combinées aux propriétés exceptionnelles des nanocristaux (NC), peuvent donner lieu à un matériau qui possède les attributs des deux. Cependant, les propriétés fondamentales des NCs de pérovskite sont fortement modifiées à l'interface avec les couches de transport de charge et par l'exposition à la lumière. Cette thèse étudie, à l'aide de la spectroscopie de photoélectrons (PES), les processus dynamiques qui se produisent à la surface et dans les interfaces des NCs $CsPbBr_3$ sur les métaux, les semi-conducteurs et les oxydes, lorsqu'ils sont exposés à la lumière infrarouge (IR) et à la lumière ultraviolette (UV). La décomposition de la pérovskite sur tous les substrats sous illumination UV donne un produit de dégradation commun de plomb métallique (Pb^0) et de bromure gazeux ($Br_2(g)$). Cependant, pour les NCs $CsPbBr_3$ sur l'or (Au), l'irradiation par la lumière UV et les rayons X intenses conduit non seulement au produit de dégradation anticipé, Pb^0 et $Br_2(g)$, mais donne également lieu à une nouvelle espèce chimique, qui est associée au dépôt sous-potentiel de plomb (Pb_{UPD}) sur la surface de l'Au. En outre, il est démontré que l'UPD de Pb ne se produit que lorsque la structure pérovskite se brise et qu'un contact direct entre la pérovskite et l'Au est établi. De plus, la dégradation des NC de pérovskite par la lumière UV en ce qui concerne la formation de plomb métallique se produit dans une moindre mesure sur ITO et MoO_x que sur MoS_2 et Au, ce qui révèle que les substrats avec des bandes interdites plus larges empêchent la décomposition de la pérovskite. De même, on observe des effets différents des NCs à la lumière IR sur Au, MoS_2 et MoO_x. L'illumination IR affecte les NCs de pérovskite sur Au de la même manière que la lumière UV et les rayons X intenses, mais aucun gaz de bromure n'est formé. L'illumination IR des NCs $CsPbBr_3$ sur MoS_2 et MoO_x entraîne un phénomène photoélectrique de surface intra-bande. Cette tension provient des défauts profonds situés au milieu de la bande interdite. Cependant, aucune décomposition de la pérovskite n'est observée. Les résultats de cette thèse mettent en évidence les propriétés de la pérovskite qui dépendent du substrat et leur influence lorsqu'elle est exposée à la lumière IR et UV.

Introduction

Climate change has devastating consequences worldwide. The main culprits of climate change are emission of greenhouse gases, which predominantly include carbon dioxide (CO_2), among others.[1] The vast majority of CO_2 emission comes from combustion of the fossil fuel such as coal, petroleum and natural gas, which are the primary sources of energy production. This over 50% increase in emission of CO_2 compared to preindustrial revolution resulted in 1 °C rise in the temperature and this rise in temperature will continue if release of CO_2 is not slowdown.[2] This necessitates the requirement for alternatives energy-producing sources, such as renewable energy sources, that can reduce the production of CO_2. However, in 2021, only 16% of the world's energy production comes from low-carbon emission sources such as, 7% from hydropower, 4% from nuclear (non-renewable) and 5% combined from solar, wind and geothermal among others.[3] Among renewable energy sources, solar is one of the cleanest, cost-effective and abundant sources of energy available to produce power worldwide. The potential of solar energy is unparalleled, as each hour of sunshine delivers 430 quintillion (10^{18}) joules of energy compared to the annual global needs of around 410 quintillion joules.[4] However, only 4.5% of total global electricity generation are produced from solar, which means the potential of solar is not fully harnessed yet in spite of concerted efforts devoted to it.[5] Currently, the most effective and well-known way of producing electricity from the sun is by the exploitation of photovoltaic effects.

The current global photovoltaic (PV) market is dominated by mono and poly-crystalline silicon solar cells. However, despite silicon being abundant, the cost of purifying and crystallizing silicon to manufacture solar cells compromises their cost-effectiveness. The current competitor to silicon solar cells are thin-film solar cells, based on copper indium gallium selenide (CIGS) and cadmium telluride (CdTe). However, unlike silicon, thin-film solar cells are made from rare materials, gallium and tellurium, and their manufacturing complexities and high costs limit their large-scale production and deployment.[6]

Solar cells based on emerging PV technologies, such as lead halide perovskite, do not require costly manufacturing processes, and the materials used for their fabrication are not scarce either. Yet, they have the potential to compete against currently commercialized photovoltaics. As in just over a decade, a certified efficiency of more than 25% recorded in the laboratory-based lead halide perovskite solar cells, opening the perspective for the large-scale modules to compete with silicon-based PV technology.[7] Using perovskite nanocrystals (PNCs) and by exploiting their ability of multiple exciton generation can increase the efficiency of halide perovskite based solar cells even further. PNCs demonstrated a remarkable photoluminescence (PL) efficiency of 90%,[8] demonstrating that PNCs can be used as photoactive layer in solar cells. Despite that, the long-term stability (about 20 years) hinders the commercialization of lead halide perovskite solar cells.

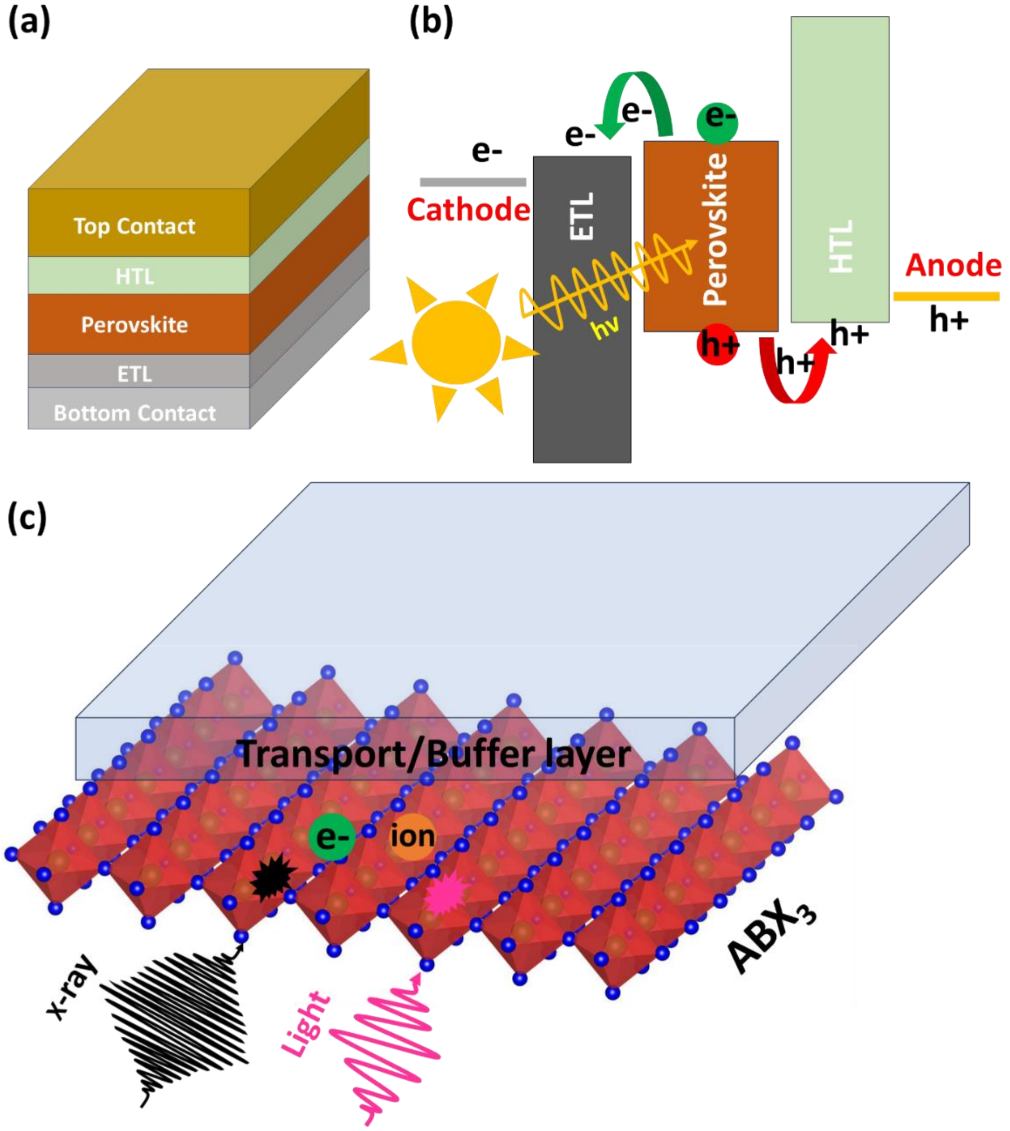

Figure. (a) schematic illustration of layer stacking in a solar cell device, (b) energy level diagram of the device shown in (a), and (c) light and ionizing radiation can lead to the generation electrical and ionic conductivity in lead halide perovskite.[9]

A solar cell device consists of multiple stacked layers, as shown in Figure above. These layers are used for the separation and extraction of the charge generated upon the absorption of a photon. Both the efficiency and device stability are strongly dependent upon the interaction between the different interfaces (the region where two materials make contact). These interfacial regions are very thin, in the range of tens of nanometers, and their chemical and electronic structure defines the device functioning. In lead halide perovskite, properties of the interface are identified to have a control over not only the device functionality but also its stability.[10,11]

In this context, it is essential to explore the surface and interface properties of lead halide perovskite nanocrystals (PNCs). The composition of the perovskite explored in this thesis is $CsPbBr_3$ all inorganic PNCs that are expected to be more robust towards radiation than the hybrid Formamidinium (FA) or methylammonium (MA) compositions. Thus, the electronic structure, energy band alignment and charge transport in $CsPbBr_3$ PNCs are crucial to investigate for their successful implementation in device. It is important to determine whether only shallow or both shallow and deep defect states exist and what are the origins of these defect states in $CsPbBr_3$ PNCs. Also, it is of utmost importance to understand whether these intrinsic properties of $CsPbBr_3$ PNCs are preserved at the interface, and more specifically, how the interactions at the interface between $CsPbBr_3$ PNCs and different charge transport layers play role in preserving the integrity of the interface. Besides that, knowledge of charge transfer dynamics at the interface can lead to development of a system which is most promising for fabricating efficient devices. Lastly, and perhaps more significantly, the long-term stability of $CsPbBr_3$ PNCs under external stresses such as x-rays and sunlight needs investigation to find whether instability of perovskite is intrinsic and/or it is dictated by the interaction happening at interface with other charge transport materials. This questioning is the main topic of the manuscript and will help in deciphering the fundamental mechanisms that influence the stability under theses stressors.

In this spirit, photoelectron spectroscopy (PES), a technique of choice for this study, is a surface sensitive technique used to characterize the $CsPbBr_3$ PNCs surface and its interfaces with other charge transport layers. PES allows to study the electrical and chemical changes of $CsPbBr_3$ PNCs on gold (Au) under radiation (infrared (IR), ultraviolet (UV) and x-rays), and on molybdenum disulfide (MoS_2), molybdenum oxide (MoO_x) and indium-doped tin oxide (ITO) under IR and UV illumination.

Starting from **Chapter 1,** the basic concepts related to the energy level alignment and interfacial electronic structure of materials are discussed. In **Chapter 2**, the concept of PES used to characterize the materials and other experimental techniques used in this thesis are presented. In **Chapter 3**, the behavior of $CsPbBr_3$ PNCs at the interface with Au under IR, UV and x-rays is investigated. The aim is to find how stable $CsPbBr_3$ PNCs are on Au under IR, UV and x-rays and to determine if the response of NCs is same under each type of radiation. Moreover, whether direct contact of perovskite and Au under radiation can lead to an interfacial chemical reaction, identify the nature and origin of such a reaction, and propose measures to prevent it. Furthermore, whether or not IR, UV and x-rays decompose the PNCs, and to what extent such degradation of the PNCs varies with radiation type.

In **Chapter 4**, the stability and response of the interface of $CsPbBr_3$ perovskite nanocrystals (PNCs) on MoS_2, MoO_x and ITO, upon IR and/or UV illumination, are discussed. The aims and objectives are to provide valuable insights of the $CsPbBr_3$ PNCs behavior, composition, and electronic structure at the interface with MoS_2 and MoO_x under IR and UV light. Also, to investigate whether the interface of PNCs with MoS_2 and MoO_x is stable under IR and UV light and with ITO under UV light or interfacial chemical reactions can happen at these interfaces. One of the main goals of this thesis is to determine whether MoS_2 can be an effective buffer layer to avoid possible chemical interaction that can happens under the UV light at the interface between $CsPbBr_3$ PNCs and MoO_x, and at the interface of PNCs with Au and ITO electrodes. The investigation of degradation processes of $CsPbBr_3$ PNCs under UV illumination and whether decomposition of PNCs is substrate dependent, i.e., do the substrate upon which NCs deposited affects the degradation of perovskite, are also a focus of this thesis. Besides that, the objective is also to explore the ways to prevent the decomposition of $CsPbBr_3$ PNCs.

However, before getting into details of the $CsPbBr_3$ PNCs interaction at different interfaces under the IR and UV light, the fundamental concept that governs and plays the role in electronic structure, band alignment and chemical interaction at the interfaces of the materials will be discussed in the chapter that follows.

References

1. Ma, Q., and R. H. Tipping. "The distribution of density matrices over potential-energy surfaces: Application to the calculation of the far-wing line shapes for CO 2." The Journal of chemical physics 108.9 (1998): 3386-3399.
2. Hausfather, Zeke. "Analysis: When might the world exceed 1.5 °C and 2°C of global warming?" Carbon Brief 4 (2020).
3. Looney, Bernard. "Statistical review of world energy, 2020|." Bp 69 (2020): 66.
4. Lee, Carlos. "Photonics: The key to a more sustainable world." Electro Optics 316 (2021): 26-27.
5. https://www.iea.org/energy-system/renewables/solar-pv.
6. Lee, Taesoo D., and Abasifreke U. Ebong. "A review of thin film solar cell technologies and challenges." Renewable and Sustainable Energy Reviews 70 (2017): 1286-1297.
7. Kim, Jin Young, et al. "High-efficiency perovskite solar cells." Chemical reviews 120.15 (2020): 7867-7918.
8. Protesescu, Loredana, et al. "Nanocrystals of cesium lead halide perovskites (CsPbX3, X= Cl, Br, and I): novel optoelectronic materials showing bright emission with wide color gamut." Nano letters 15.6 (2015): 3692-3696.
9. Tress, Wolfgang. "Metal Halide Perovskites as Mixed Electronic–Ionic Conductors: Challenges and Opportunities□ From Hysteresis to Memristivity." The journal of physical chemistry letters 8.13 (2017): 3106-3114.
10. Schulz, Philip, David Cahen, and Antoine Kahn. "Halide perovskites: is it all about the interfaces?" Chemical reviews 119.5 (2019): 3349-3417.
11. Kim, Gee Yeong, et al. "Large tunable photoeffect on ion conduction in halide perovskites and implications for photodecomposition." Nature materials 17.5 (2018): 445-449.

CHAPTER 1: Energy Level Alignment and Interfacial Electronic Structure

With the rapid advancement of thin-film photovoltaics technology, it is critical to determine the energetic of photoactive layers and their related charge transport layers, i.e., the energy positions of electronic bands and their alignment with adjacent layers.[1] Since the perfection and periodicity of crystalline lattices are essential to understand the fundamentals of semiconductor physics, these properties are severely disrupted at the junctions and interfaces between absorber and various charge transport layers for the extraction and transportation of charge carriers.[2] As surface and interface engineering is utilized to optimize these interfaces, it is important to, not only to study the energy level alignment at various interfaces but also to comprehend the mechanisms that influence these interface energetics.

The energy levels, presented in Figure 1.1, comprise the work function (WF), vacuum level (E_{vac}), Fermi level (E_F), energy bandgap (E_g), ionization potential energy (IE), electron affinity (EA), conduction band maximum (E_{CBM}) and valence band minimum (E_{VBM}) for inorganic materials or lowest occupied molecular orbital (LUMO) and highest molecular orbital (HOMO) in case of organic materials, they regulate the device's behavior i.e., charge carrier generation and transportation.

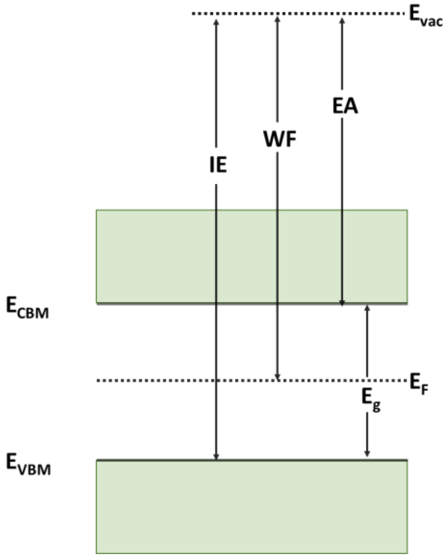

Figure 1.1. A semiconductor's energy level diagram with flat bands, E_{CBM} (conduction band minimum) or LUMO (lowest occupied molecular orbital), E_{VBM} (valence band minimum) or HOMO (highest occupied molecular orbital), IE (ionization potential), WF (work function), EA (electron affinity), E_g (bandgap), and E_{vac} (Vacuum level) are defined in Ref (4).

All these properties are inherent to a material, regardless of whether it is a metal, semiconductor, insulator, organic, inorganic, or hybrid.[3] Nevertheless, significant differences in energy levels between samples of the same material are observed due to a variety of internal and external factors, including the material's purity (doped or undoped), structure (crystallographic orientation), morphology (surface roughness), processing condition (wet or dry), and surface composition (clean or contaminated) etc.[4] For instance, the work function of polycrystalline gold (Au) increased from 4.5-4.7 eV to 5.0-5.1 eV when Au is atomically cleaned in ultra-high vacuum.[5] Moreover, energy levels can be strongly modified in the interface region, that can strongly influence the device performance.[6] Each of these parameters will be discussed independently before delving into how they affect carrier extraction and transportation at various interfaces, such as the metal/semiconductor and/or semiconductor/semiconductor interfaces.

1.1 Factors Shaping Interfacial Electronic Structure

1.1.1 Work function

Naturally, electrons are bound to the solid in the periodic potential represented by the crystallographic structure of a material. These electrons are prevented from escaping into the vacuum at the surface by a potential barrier that terminates at E_{vac}. Hence, E_{vac} is defined as the energy of electron at rest just outside of the solid but still affected by potential of the solid.[7,8] This E_{vac} is referred as E_{vac} at surface and denoted by $E_{vac}(s)$. On the other hand, the energy of an isolated electron at rest at infinite distance from the surface is called $E_{vac}(\infty)$. This $E_{vac}(\infty)$ is invariant and can be viewed as a level at fixed energy from Fermi level (E_F). However, since E_{vac} varies even for same materials for different crystallographic surface, therefore experimentally determined E_{vac} is always considered as a $E_{vac}(s)$ but not the $E_{vac}(\infty)$. This $E_{vac}(s)$ is central to the definition of the properties that follow. For example, the work function, which is defined as the minimum energy required to promote an electron from the Fermi level to $E_{vac}(s)$. Thus, the work function of a material is a property of its surface and depends strongly on $E_{vac}(s)$. The dependency of WF on the surface (for example in the case of tungsten single crystal) effectively demonstrates the reliance of WF on $E_{vac}(s)$. Tungsten exhibits varying WF values of 4.63, 5.25 and 4.47 eV for the (100), (110) and (111) surfaces respectively, demonstrating that this dependence of WF is exclusively due to energy difference of an electron just outside solid, i,e., $E_{vac}(s)$ as the E_F inside the solid is common level.[9] This surface dependence of the WF could be attributed to the different electron tailing at different surfaces; thus, WF is regarded as a feature of a material's surface but not the bulk.[10,11] More importantly, the work function is measured as the combination of two components, the dominant one (i.e., bulk components) crossponds to the chemical potential that derives from the electronic density and density of states, and the less dominant one (i.e., surface component) crossponds to surface dipole component, which originates from the redistribution of charges at the surface of solids. This second component is an inherent feature of the surface of a solid and it is fundamental part of both work function and E_{vac}(s), which keeps the significance only at the surface. Hence, work function of a material depends upon the to the both chemical potential and surface dipole of a material.[4] For the metals, since E_{VBM} and E_{CBM} overlap, ionization potential energy (IE) and electron affinity (EA), which will be defined in next section, are identical to WF. However, WF in semiconductors has a value that falls between IE and EA. Hence, WF in semiconductors as described above depends upon the position of E_{vac} and on E_F, which in turn impacted by the density of states, temperature, carrier density and doping concentration of a material.[5] And electron chemical potential, which depends upon the chemical identity, impurity presence, and stoichiometry of a semiconductor material.[3]

1.1.2 Ionization potential energy (IE) and electron affinity (EA)

The energy difference between E_{vac}(s) and top of the E_{VBM} or minimum energy required to move an electron from top of E_{VBM} to E_{vac}(s) is called IE and it is considered a positive quantity. Inversely, the energy gained by dropping an electron from E_{vac} to the lowest of E_{CBM}, is the EA of a materials and also considered a positive quantity.[5] Important to note here that similar to the work function stated above, IE and EA defined here have significance only at the surface. Inorganic semiconductor of interest have EAs and IEs in the range of 2-4 eV and 4.5-6.5 eV.[12] Ideally, IE and EA of semiconductor should match with the electrodes WF (metals) contacts on either side to minimize the energy losses; however, this is not always the case and often a charge transport layer (electrons charge transport layer and hole transport layer) has been inserted to match the EA and IE of semiconductor respectively to WF of metals on either side.

1.1.3 Energy bandgap (E_g)

Finally, the energy bandgap (E_g) or the transport gap, is the difference in energy between E_{CBM} and E_{VBM}. This E_g defines all carrier injection and extraction barriers at metal/semiconductor and semiconductor/semiconductor heterojunctions which are utmost important in device architecture. The transport gap is different from the optical bandgap. The transport gap is the energy difference between the top of valence band and bottom of the conduction band, which essentially means electron and holes are separated whereas, optical bandgap of a material correspond to the energy difference between the top of valence band and bottom of the conduction band of an electrostatically bound (electron-hole) pair. This difference comes from the fact that in the case of optical bandgap, energy needed to separate this (electron-hole pair) is not considered. Therefore, rigorously speaking, the difference between transport gap and optical gap is the measure of electron-hole pair binding energy (E_B). For the inorganic semiconductors, the difference between transport gap and optical bandgap is modest (few meV) due to low exciton binding energy of electron-hole pair; however, this difference is larger in organic semiconductors (from 0.3 to 1.5 eV) due to high exciton binding energy of electron-hole pair.[13]

The photoemission (PES) is the most efficient and quantitative way of measuring WF, IE, and E_g not only of neat materials but also at the different interfaces. EA/E_{CBM} can be obtained by either inverse photo emission (IPES) or two photon-photoemission (2PPE).[8] It can also be obtained from the optical bandgap for the inorganic semiconductors since difference between transport gap and optical bandgap is not that large as described above due to low exciton binding energy with which electron-hole pair is bound. By measuring all these energy levels, a complete energy landscape can be drawn of different photoactive layers with different charge transport layers (CTLs).

1.2 Energy Level Alignment at the Interface

An interface is formed when two materials make contact or one material is deposited on top of another. The position and shape of energy levels at the interface dictate the device properties. To find the energy band positions and alignments, investigation of different interfaces such as, metal/semiconductor interface, or semiconductor/semiconductor interface is of great importance. Upon the contact of two materials, changes occur right at the interface of two materials during the contact, either the shifting of vacuum level by “interfacial dipole” or the aligning of the Fermi level by “band bending”. [3] Additionally, both interfacial dipole and band bending can also be involved in this energy level alignment at the interface. Moreover, multiple phenomena might be implicated during this energy level alignment that dictates interfacial energetics, which will be discussed in depth for each of the interfaces in the following.

1.2.1 Metal/semiconductor Interface

The interface between metal and semiconductors, commonly known as Schottky-Mott interface, is found everywhere in contemporary electronics. Often metal is used as a contact for P-N junction in semiconductors; other times, metal-semiconductors performs essential electronics functions. Usually, for the device to work efficiently, an ohmic contact is desired at metal-semiconductor interface; however, this is often not the case and a barrier is formed at this interface which is called Schottky barrier. The Schottky-Mott model predicts this barrier height based on the work function of the metal relative to the electron affinity (for n-type) or ionization potential energy (p-type) of semiconductor as shown in the following equations.

$$\phi_e = WF_m - EA \qquad (1.1)$$

$$\phi_h = IE - WF_m \qquad (1.2)$$

Generally, the WFs of metal and semiconductor differ, and Fermi level (E_F) is not in electrical equilibrium (where E_F of both materials should be at the same energy).

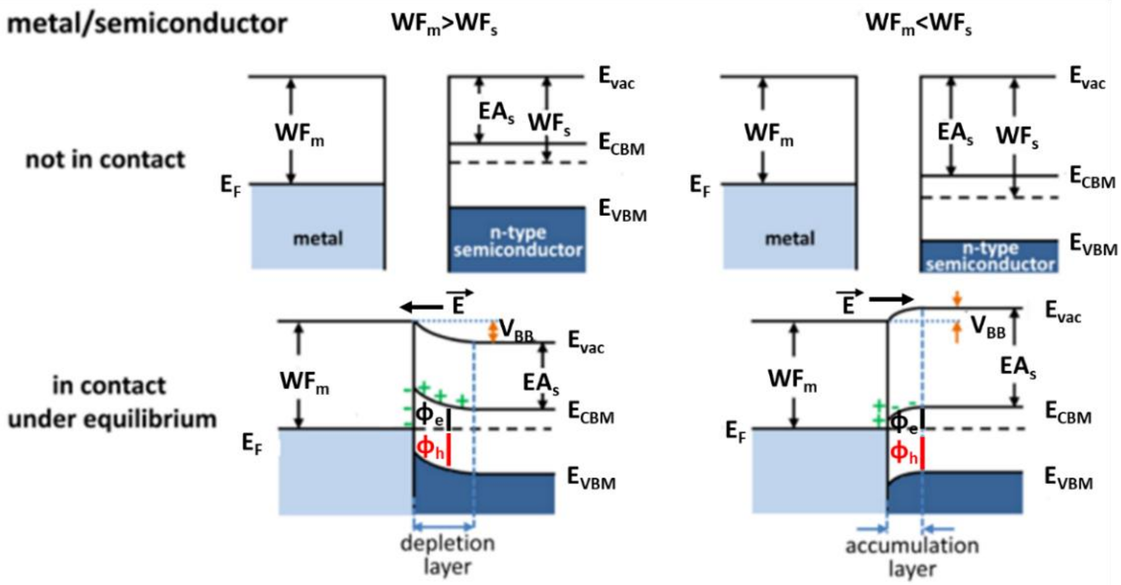

Figure 1.2. Metal and n-type semiconductor energy band diagrams adopted from Ref.[16]

When metal and semiconductor contact develops redistribution of the charge occurs if the number of mobile carriers in the semiconductor layer is large enough, and bring the Fermi level (E_F) at equilibrium by bending the bands.[14] This band bending (V_{BB}) is the process by which all electronic levels in a material curve up or down at the interface relative to bulk due to electrostatic field, which is created when aligning the E_F levels.[15] Figure 1.2 is an example of an ideal energy level diagram (band diagram at zero temperature with no impurities or imperfections in both metal and semiconductor) of a metal with an n-type semiconductor before and after contact based on Schottky-Mott rule.

Left hand side of Figure 1.2 shows the scenario, when the WF of metal (WF_m) is greater than that of semiconductor (WF_s), resulting in transfer of electrons from the semiconductor to the metal, lowering the semiconductor E_F and raising the metal E_F. In equilibrium, the WF difference disappears at the interface and the E_F align across the interface. The movement of the charge carrier from semiconductor to metal causes negative and positive charging of the metal and semiconductor, respectively, resulting in the formation of an electric field ($\vec{E}$) from semiconductor to metal. Because the amount of accessible free carriers in semiconductor is not enough, established ($\vec{E}$) cannot be efficiently screened (unlike in metal, where ($\vec{E}$) = 0 in bulk). This results in the establishment of a depletion zone along the interface, which hinders further carrier movement, and therefore the band of semiconductor surface bends upwards at the interface owing to charge accumulation and built-in ($\vec{E}$) between semiconductor and metal.[14,16]

Similarly, the right-hand side of Figure 1.2 depicts the situation where electrons move from metal to semiconductor, resulting in positive and negative charge of metal and semiconductor, respectively, generating an accumulation layer. As a result, the direction of ($\vec{E}$) is from metal to semiconductor, driving electrons towards the metal. Because the electron's potential energy is smaller at the contact, V_{BB} is downward towards the metal surface.[4,14,16]

(a) Fermi level pinning

Although the Schottky-Mott model correctly predicted the existence of band bending as illustrated in the preceding example, it was found experimentally that it incorrectly describe the height of the Schottky barrier, i.e., carrier injection barriers are no longer dependent on the work function of metal (WF_m).[17,18] This absence of strong dependence of carrier injection barrier on metal work function given advent to an intriguing phenomenon known as “Fermi level pinning” due to existence of energetically unfavorable states. In 1947, John Bardeen reported that the phenomenon of Fermi level pinning naturally arises if charged states exist in semiconductors right at the interface, with energies within the semiconductor’s bandgap. These states might be present either on the surface semiconductor-vacuum surface (surface states) or appears due to metal-semiconductor chemical bonding (metal-induced gap states). The surface states in the case of intrinsic semiconductor (where, the VBM is entirely filled, but the CBM is completely empty) do not induce any band bending due to no transfer of charge between the bulk and the surface as shown in Figure 1.3 (a). However, when a semiconductor is doped, the Fermi level of the bulk is moved with respect to the undoped semiconductor due to transfer of charge between gap states and semiconductor. It is shifted up for p-doped semiconductors (closer to the conduction band) and down for n-doped semiconductors (closer to the valence band). In disequilibrium, the Fermi energy is lower or higher than that of surface states for p- and n- doping respectively. Electrons flow from the bulk to the surface or vice versa due to the energy difference aligns the Fermi level at equilibrium. As a result, for n-doped semiconductors, the energy bands bend upward, whereas for p-doped semiconductors, they bend downward as shown in Figure 1.3 (b) and (c) respectively.[19,20]

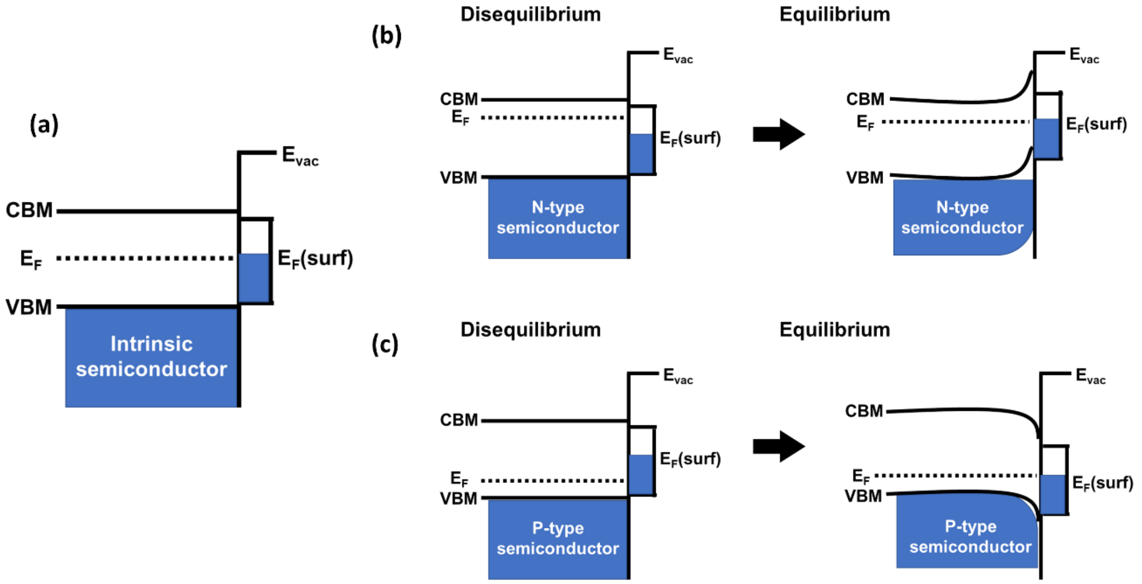

Figure 1.3. shows an energy band diagram of a doped semiconductor with surface states caused band bending adopted from Ref.[19]

These surface states induced bending of Fermi level is highly undesirable since it limits a significant degree of doping flexibility in semiconductors. This is because in this case, the Fermi energy of semiconductor is dictated by surface states instead of dopant concentration. This given rise to a phenomenon called Fermi level pinning as the semiconductor's bands would necessarily align relative to gap states which are in turn pinned the Fermi level (due to their high density), all without influence from metal. Similarly, for the case of metal-induced gap states charge transfer takes place between metal and gap states without any effect of semiconductor, which essentially means the semiconductor is shielded from the metal's features.

(b) Interfacial dipole (Δ)

As described above gap states are present that causes the deviation of metal-semiconductor interface from Schottky-Mott rule. However, in addition to gap states, interfacial dipole can also lead to the variation in barrier height. During the contact of metal and semiconductor new localized interface states in the interface region formed that are dependent on the interface atomic structure. Since these new interface states have very different charge distribution from the charge distribution of two starting surfaces (metal and semiconductor), the net change in potential energy occurs as a result of charge rearrangement at the interface, forming the basis for a dipole, which is responsible for shift of vacuum level. The origin of this dipole has a variety of causes such as charge transfer across the interface, redistribution of electronic clouds, interfacial chemical reaction, and other types of electronic state redistribution.[3,21,22] Hence, the equations for injection barrier modified by interfacial dipole (Δ) are as follows.

$$\phi_h = IE - WF_m - \Delta \tag{1.3}$$

$$\phi_e = WF_m - EA + \Delta \tag{1.4}$$

As stated, this interfacial dipole originated as a result of charge transfer between metal and semiconductor. Although the direction of charge transfer is usually self-evident, the exact quantity of charge transferred cannot be established unequivocally. This is because there is no precise method to determine where the metal begins and the semiconductor ends at an Metal/Semiconductor contact. Nonetheless, conventionally, interfacial dipole is considered positive when charge transfer from metal to semiconductor and negative when it is transfer from semiconductor to metal.[23] For instance, when a semiconductor (strong acceptor like TCNQ) is deposited on a low WF metal (Al) in Figure 1.4 (a1) charge transfers from semiconductor to metal, and when a semiconductor (strong donor like NPD) is deposited on high WF metal (Au) in Figure

1.4 (a2) charge transfer from metal to semiconductor, this charge carrier transfer between metal and semiconductor, causing separation of the positive and negative charges (cation and anion formation), consequently, gives rise to a interfacial dipole.[22,23]

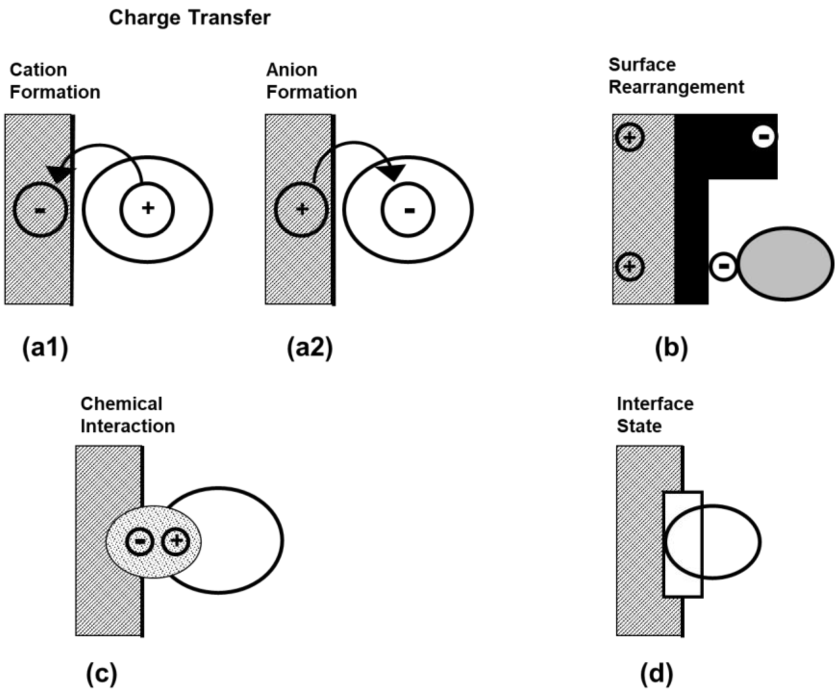

Figure 1.4: Possible causes creating an interfacial dipole and causing a vacuum level change adopted from Ref.[3]

This same mechanism is described also for semiconductors with strong acceptors and donors, e.g., PTCDA/Alq_3.[26] The second cause of dipole formation is attributed to the electron cloud rearrangement at the metal surface. Usually, the vacuum level shift is ascribed to the transfer of charge between metal and semiconductors. However, for the case of Xenon (Xe) insulator, where no charge transfer is probable, vacuum level shift has been observed. Therefore, this vacuum level shift or change in metal work function is attributable to electron cloud rearrangement at the metal surface as shown in Figure 1.4 (b).[27] As it is widely known that in the case of a metal, electronic cloud tails towards vacuum, this electronic can be pushed back by the repulsion of an adsorbate electron cloud.[28] As a result, vacuum side charges positively in comparison to the bare surface resulting in an interfacial dipole.

Another probable origin of an interfacial dipole is chemical interaction between metal and semiconductor as shown in Figure 1.4 (c). These chemical interactions lead to creation of new chemical bonds or the rearrangement of existing ones, causing the vacuum level to move up or down hence creation of interfacial dipole. It is worth to mention here that polarity shown in Figure 1.4 (c) could be opposite depending on the interaction since the direction of dipole depends upon the direction of transfer of charge, which could be from metal to semiconductor or semiconductor to metal as described for Figure 1.4 (a1,a2).[29]

Last but not the least, as described before gap states exist which have various intrinsic and extrinsic origins, for example, metal-induced gap states formed by the penetration of metal wavefunctions into semiconductor can also cause the vacuum level shift and thereby to the formation of an interfacial dipole, as shown in Figure 1.4 (d).[30-33] To summarize, all the above phenomena shown in Figure 1.4 cause the formation of interfacial dipole at metal/semiconductor interface which in turn leads to variations in barrier heights.

(c) Band bending

Finally, in addition to interfacial dipole shown in Figure 1.5 (a), for an interface of metal with thick semiconductor, band bending (where the Fermi levels of metal and semiconductors are aligned) also occurs at the interface as a result of charge carrier relaxation within the semiconductor as shown in Figure 1.5 (b). For instance, when the work function of metal is larger than that of the semiconductor, some electrons move from semiconductor to metal work function because metal is more comfortable for electrons, leading to positive and negative charging of semiconductors and metal respectively.

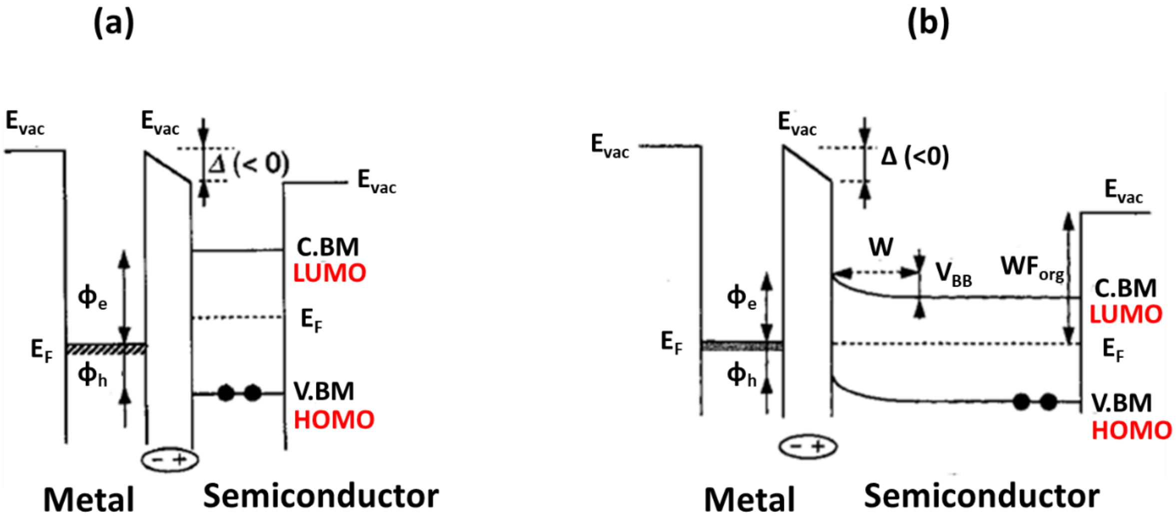

Figure 1.5. Energy band diagram of metal and semiconductor. (a) with a shift vacuum level (E_{vac}) due to dipole formation, and (b) interfacial energy diagram with band bending where the energy levels are bent by the charge redistributions in the semiconductor to achieve electrical equilibrium with the alignment of Fermi levels of metal and semiconductor adopted from Ref.[3]

This charging makes the metal less comfortable for electrons, and there might also be the redistributions of mobile charge carriers in the semiconductor layer. This charge flow and distribution continues until the Fermi levels are aligned between the metal and the bulk of the semiconductor. Such a redistribution of charge at the interface is dictated by the Poisson equation, which describes the relationship between the distribution of charges and electrostatic potential. Consequently, a diffusion layer (W) with band bending forms to align the Fermi energies of the two materials, with a built-in potential (V_{bi}) in semiconductor.[35] The thickness of such a diffusion layer depends upon the built-in potential (V_{bi}), dielectric constant of semiconductor, and the spatial distribution of the available donor or acceptor levels. For example, for the interface of silicon (Si) with metal, the estimated thickness of diffusion layer was 10 µm, with a given dopant concentration of 1016 /cm^3, ε=12, and V_{bi} = 0.5 eV.[35] But, more importantly, the band bending is only conceivable when there are a sufficient number of mobile charge carriers accessible, which may be achieved by using a thicker semiconductor or a material with a good semiconducting property.[3,4] A thin or poor semiconducting characteristics' materials usually show flat band situation with only interfacial dipole as shown in Figure 1.5 (a). To summarize, the energy level alignment at the interface as a result of interfacial dipole dictates the charge carriers injection and extraction while the band bending in thicker region governs the separation of charge carriers.

1.2.2 Semiconductor/semiconductor Interface

In contrast to the metal/semiconductor interface discussed above, which can be unpredictable due to the strong interaction between the two materials, the semiconductor/semiconductor interface is more predictable. This predictability arises because fewer intrinsic charge carriers are available within the semiconductor material and their low mobility, resulting in significantly reduced interaction between the two semiconductors. Nonetheless, it is critical to understand the semiconductor/semiconductor interface and the underlying mechanisms that control it, as modern electrical and optoelectronic devices consist of multiple layers of one or more semiconductors.

Semiconductors have two types of junctions which includes homojunction and heterojunction. A homojunction is formed by different doping in the same semiconductor, whereas a heterojunction is formed between two different semiconductors.

(a) Homojunction

As stated above when two identical semiconductor layers with different doping come into contact, it is referred to as a homojunction. For example, in a semiconductor like silicon, an n-type (donor-doped) and p-type (acceptor doped) form the homojunction, which is known as P-N junction. A P-N junction is one of the most successfully proven strategies to prevent the recombination of thermally excited charge carriers in the semiconductors. At the P-N junction, electrons from n-type (majority carriers are electrons) diffuse into p-type (majority carriers are holes) and holes from p-type diffuse into n-type. These electrons and holes recombine at the interface, and this region is depleted of any mobile charge carrier; hence, it is referred to as the depletion region. However, immobilized ionized donors and acceptors left behind in this area generate an electric field as shown in Figure 1.6 (a), which act as a barrier for the further diffusion of carriers, leading to the formation of a potential difference across the junction, known as the built-in potential (potential built due to potential energy difference between the Fermi levels of the two semiconductors).[36] At equilibrium the Fermi level must be aligned across the P-N junction, which is achieved by the existence of the built-in potential in the depletion region. This potential swing the energy levels, resulting in the bending of the bands at the junction, as shown in Figure 1.6 (b). To conclude, the created electric field at the p-n junction as a result of immobilized ionized donor and acceptor at the junction aids in the spatial separation of charge carriers. Hence, the P-N junction is regarded as the core of photovoltaics since it promotes spatial separation of charges.[37]

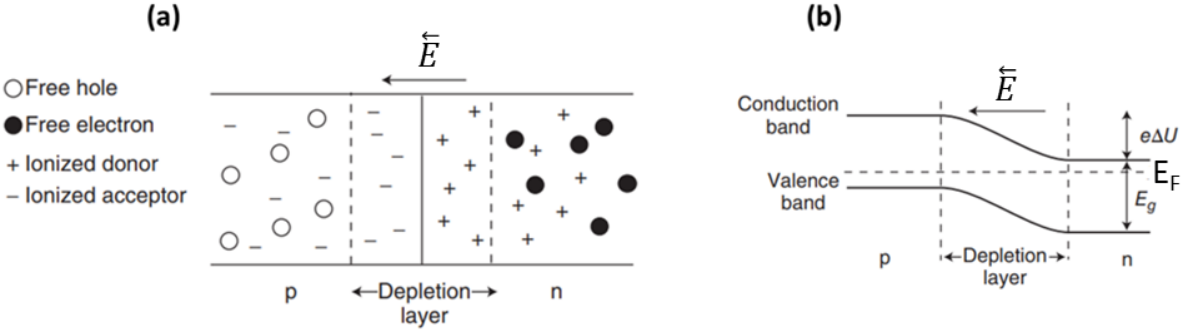

Figure 1.6. P-n junction (a) formation of depletion layer (b)Energy level diagram with constant chemical potential.[36]

(b) Heterojunction

The second type of semiconductor junction which is known as heterojunction formed when

when two different semiconductors materials come into contact. To ensure that charge carriers generated through absorption are efficiently collected by the corresponding electrodes in real devices, a semiconductor active layer is typically placed between different charge transport layers, such as an electrons transport layer (with a hole blocking layer) and a holes transport layer (with an electron blocking layer). Consequently, the heterojunction interface also plays a critical role in facilitating charge transfer and optimizing device performance. The energy band alignment at the interface is a key factor that influences the behavior of the semiconductor junction, and there are three types of energy band alignment exist in heterojunctions: (1) straddling gap, (2) staggered gap, and (3) broken gap, as illustrated in Figure 1.7.[38]

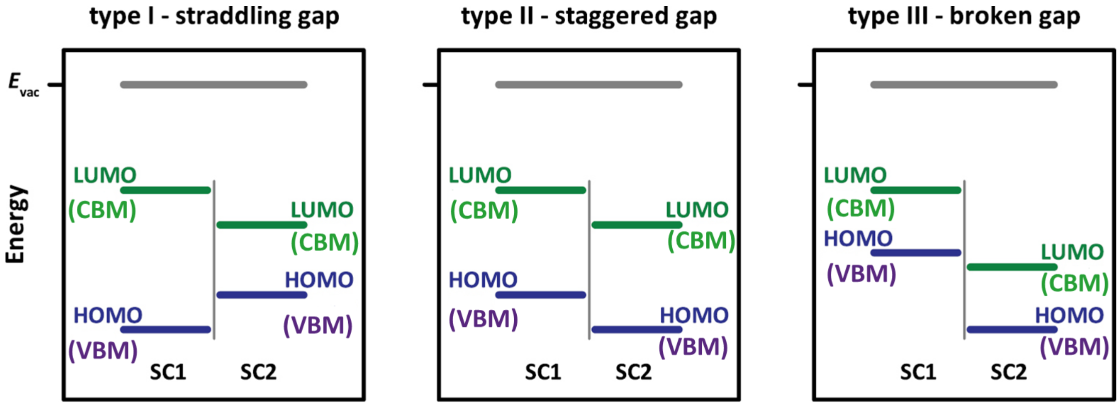

Figure 1.7. Schematic drawing of three different band alignment in semiconductor heterojunctions: straddling, staggered, and broken gap, adopted from Ref.[36]

Type I (Straddling gap) The type of heterojunction in which bandgap of one semiconductor is entirely contained in the other semiconductor bandgap, i,e., E_{CBM} (SC2) > E_{CBM} (SC1) and E_{VBM}(SC2) < E_{VBM}(SC1). The discontinuity of bands is such that both types of carriers, electrons and holes, need energy (ΔE_{CBM} and ΔE_{VBM}, respectively) to change from the materials with the smaller bandgap to the one with the larger gap, while the carriers from other side losses this energy when they cross the junction. Type I heterojunction is quite common, and it is the found in light-emitting diodes (LEDs), where electrons and holes move in such a way that they recombine and emit the light.

Type II (Staggered gap) In Staggered gap configuration bandgaps of both semiconductor overlaps but ΔE_{CBM} or ΔE_{VBM} changes sign, i,e., if one carrier gains energy (if electrons move from SC1 to SC2), the other one needs energy (the holes) to move from SC1 to SC2 . Staggered gap type II configuration prevails in photovoltaics, where the separation of electrons and holes occurs following the formation of a bonded hole-pair, also known as an exciton, at the interface between the donor and acceptor layers (in the case of organic photovoltaics).

Type III (broken gap) In the broken gap structure the bandgaps of two semiconductors do not overlap at all. The carriers transfer mechanism works similar to “type II” but more pronounced. Broken gap configurations is desired when one type of carrier needs to be transported while completely blocking the other type of carriers in the same direction. The broken gap structure, for example, is typical in InAs/GaSb heterojunctions.

(c) Band alignment

The band alignment in semiconductor heterojunction interfaces follows the Anderson rule, which defines the interface electronic structure based on vacuum alignment, and calculates the electron injection barrier (or hole injection barrier) as the difference between the electron affinities (or ionization potential energies) of the two semiconductors.[39] However, the Andersons’s rule fails to accurately predict the true band offset primarily due to an assumption that materials behave, as they are separated by large vacuum distance, while in reality there is no vacuum at these heterojunctions since solids occupy the space. Hence use of electron affinities (ionization potential energies) lead to incorrect result.[40] Furthermore, the proposed Anderson rule works on the same principle as Schottky-Mott rule in metal/semiconductor interface without considering any disruption of the potential at the junction that give rise to an interfacial dipole and/or chemical bonding effects as they were considered for the Schottky-Mott interface, and explained in metal semiconductor interface section. There have been numerous efforts aimed at understanding semiconductor heterojunction since it does not follow simple band alignment and in particular, surface and the interfacial states present on semiconductors plays significant rule on band alignment. Typically, the periodicity of crystal terminates or disrupts at the surface, resulting in a defective surface. Due to chemical nature of this surface, certain atoms resting on it do not have sufficient number of nearby atoms with which to form bonds, leading to a large number of incomplete bonds, invariably known as dangling bonds.[40] These dangling bonds, being by nature reactive, can be compensated by different processes, in particular through a relaxation and/or reconstruction of the surface, i.e., a rearrangement of the surface atoms and/or a modification of the configuration of the chemical bonds between atoms, or can be saturated by the adsorption of atoms on the surface, such as impurities. These processes correspond to a change in structure and therefore give rise to the appearance of new energy levels specific to the surface, which are generally found in the semiconductor gap. These new energy levels in a material create the band bending which is known as surface state induced band bending. To summarize, surface and interfacial states, either inherent to a semiconductor or formed during the formation of interface between two semiconductors induce the phenomenon of interfacial dipole and/or band bending, which play a critical role in the alignment of bands in semiconductors in the similar way that they do in the formation of metal and semiconductor interfaces, and thus should be considered. Moreover, whether the phenomena of interfacial dipole, band bending, or both can affect band alignment at the semiconductor/semiconductor interface will be discussed in greater detail in the section “Energy level alignment in perovskite”.

1.2.3 Semiconductor/metal oxide Interface

Despite considerable improvements in charge transport and collection at the electrodes as a result of collaborative efforts, non-radiative recombination occurs due to energy level mismatch between charge transport layers and electrodes. Therefore, metal oxides have been used as a buffer layer between metal and semiconductor (charge transport layers) to provide not only a better energy level alignment but also charge selective layer/blocking layer to improve charge collecting efficiency. Metal oxides are considered as promising materials owing to their high transparency due to wide bandgap, wide range of work function (extreme low of 3.5 eV for defective ZrO_2 to the extreme high of 7.0 eV for stoichiometric V_2O_5), easy processability (both vacuum and solution processing), and excellent electron mobility.[41] During device functioning, charge carriers pass through (different materials used to make the device) many interfaces along the way. These interfaces frequently have an energy barrier that prevents charge carriers from passing through, causing the device to perform poorly. Therefore, it is critical to investigate the underlying physics and intriguing phenomenon of performance increase by oxide layer insertion at the interface of semiconductor and metal oxides.[41]

A completely stoichiometric semiconducting oxide's Fermi level would theoretically be midway between valence band maxima (VBM) and conduction band minima (CBM) . However, owing to imperfections inherent to metal oxide during its deposition, a perfectly stoichiometric semiconducting oxide (without any defects) does not exist in reality. The most frequent defects are oxygen vacancies and metal vacancies, although additional defects such as, metal or oxygen interstitial, an oxygen ion on metal, and a metal ion on oxygen also exist.[42] All of these defects cause the creation of new occupied or unoccupied states close to the conduction and valence band edges. Consequently, metal oxide can be either n-type or p-type semiconductor. In general, oxygen deficiency (or metal cation) ended up causing an oxide to behave n-type, whereas metal deficiency (or excess oxygen) makes an oxide behave as p-type. For instance, oxygen vacancies present in MoO_3 make it to behave as n-type semiconductor while Cu vacancies presents in Cu_2O make it to behave as a p-type semiconductor.[42]

While the work function (WF) of metal oxide is crucial in determining energy level alignment, it may vary by up to 1 eV depending on the material. For example, WF of MoO_3 varies from 5.3 to 6.9 eV.[43] For metal oxide, WF is defined as the sum of electron chemical potential and surface dipole as stated in definition of work function. Surface roughness, crystal face, radiation exposure, and adsorbate coverage all have an effect on the surface dipole component, whereas chemical identity, impurity presence, and stoichiometry all have an influence on the electron chemical potential.[42,43] Furthermore, because metal oxide has a continuous range of stoichiometries due to the various types of defects outlined above, such as oxygen vacancies, oxygen interstitial defects, cation vacancies, and cation interstitial defects, WF can be adjusted by changing the concentration of defects. For example, removing oxygen tends to decrease WF (due to decrease in electronegativity of lower oxidation state cation and increase in valence donor states), while adding oxygen tends to increase WF.[44,45]

Also, interfacial chemical reaction is expected depending upon the type of oxide and substrate upon which it is deposited. For example, it has been found that when MoO_x is deposited on cobalt (Co); an interfacial chemical reaction leads to the formation of Co-O with the reduction of Mo^{+6} oxidation state to Mo^{+4} and Mo^{+3} states. This chemical reaction also induces a large interfacial dipole that significantly increases the work function of cobalt substrate, while the formation of gap states facilitated the hole injection and transportation.[46]

Metal oxides, even though possess defects that make them either n-type or p-type as discussed above, can be coupled together to make a better energy alignment at the electrode. For example, the case presented in the following in which the interfacial energetics of bi-layer hole extraction contact consisting of solution-processed nickel oxide ($sNiO_x$) and vacuum deposited molybdenum trioxide (MoO_3) is determined by XPS and UPS.

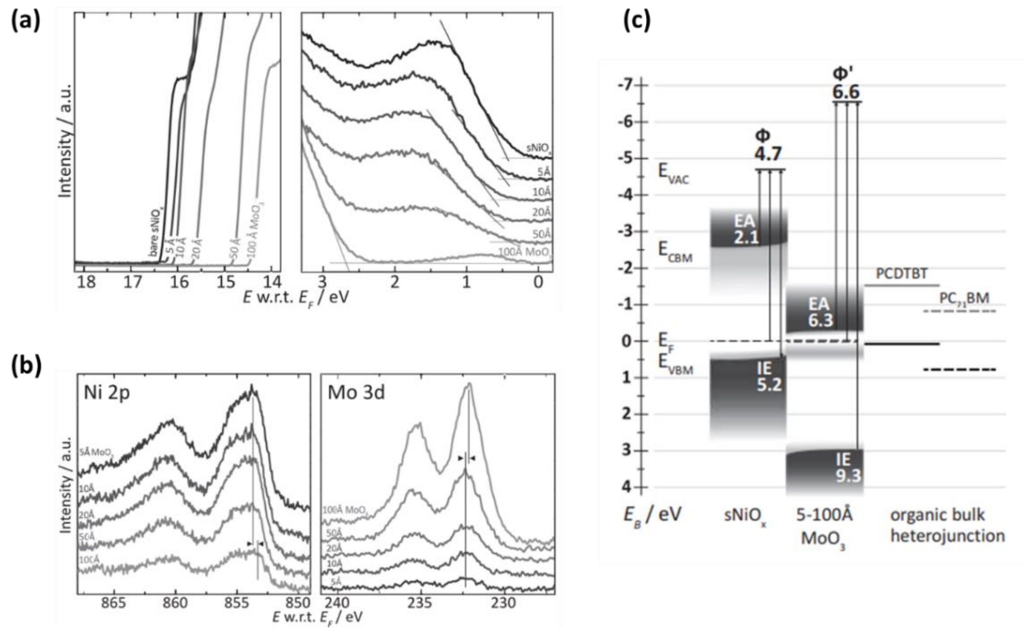

Figure 1.8. (a)UPS spectra of bare sNiO$_x$ and sNiO$_x$ with incrementally deposited MoO$_3$ on top, (b) Ni 2p and Mo3d core level of sNiO$_x$ and MoO$_3$ deposited on top, and (c) energy level diagram of sNiO$_x$/MoO$_3$ interface.[47]

The cutoff photoemission spectra of sNiO$_x$ with sequentially deposited MoO$_3$ (5 to 100 Å) on top is shown in Figure 1.8 (a). The bare sNiO$_x$ Possesses WF of 4.7 eV and VBM is at 0.5 eV (as shown in Figure 1.8 (b)) with bandgap of 3.2 eV, implying that it has p-type properties. A substantial change in photoemission cutoff with incremental MoO$_3$ deposition suggests a rise in vacuum level and hence an increase in WF, which is ascribed to charge transfer from sNiO$_x$ to MoO$_3$ with the creation of an interfacial dipole. The WF of MoO$_3$ calculated at 6.6 eV and VBM found at 2.7 eV below E$_F$ using bandgap of 3.0 eV at 100 Å thickness, which revealed that it exhibits n-type semiconducting properties.

XPS is used to observe the changes in core levels (CLs) as shown in Figure 1.8 (b). The Ni 2p CL shifted towards lower binding energy of 0.2-0.3 eV with increasing thickness of MoO$_3$, suggesting upwards band bending. On the other side of interface, Mo3d peak shifted with the same amount and in same direction, indicating downward band bending. By combing both XPS and UPS spectra an energy level diagram was constructed and shown in Figure 1.8 (c).

Hence, it can be concluded that, this broken-gap configured bilayer (high work function n-type MoO$_3$ doped by oxygen vacancies and NiO$_x$ p-type with nickel vacancies) despite having defects is capable of being both effective hole extraction and electron blocking. The high built-in field of MoO$_3$, attributed to its high WF, allows for efficient hole extraction, while the electron blocking ability of NiO_x, attributed to its low EA, reduces recombination.[47] This implies that nonetheless metal oxides possess different defects depending on the type of oxides, they can be attractive as buffer layers to transport the charge carriers towards the electrodes efficiently.

To summarize, energy level alignment of metal oxides with other materials is strongly influenced by several factors including, the type of oxide, its stoichiometry, defects it possesses, and the substrate upon which it is deposited (because of interfacial chemical reaction it can have with substrate specially in case of metals).

1.3 Energy Level Alignment in Halide Perovskite

Halide perovskites are a type of semiconductor known for their rich electronic phenomenon such as surface states and dopants induced band bending that strongly affect their electrostatic landscape. Halide perovskites have the perovskite crystal structure of ABX_3, where A-site is occupied by monovalent cations such as methylammonium (MA^+), Formamidinium (FA^+), and (Cs^+), B-site is occupied by divalent cation, either Pb^{+2} or Sn^{+2}, and X-site is occupied by monovalent halide anions, such as Br^-, Cl^-, I^-. The word “perovskite” from here on will be used throughout this chapter which refers to halide perovskite unless stated otherwise. Since perovskite being highly defective, even the same perovskite like $MAPbI_3$ shows different properties depending upon the preparation methods and conditions. Different properties (type of semiconductor, n-type or p-type) of perovskite, has different energy level alignment at various interfaces between perovskite and charge transport layers.[48] It has been reported that point defects like lead (Pb) and iodide (I) vacancies have been identified near to either VB or CB. Consequently, based on the nature of the defects, perovskite adopts either p-type or n-type conductivity.[49] Similarly, substrate’s property strongly affects the energy levels of subsequently deposited perovskite.[49,50] For instance, Schulz et al., shows perovskite films adopts p-type characteristics on p-type substrate (NiO_x), and n-type on n-type substrate (TiO_x) owing to the shallow defects present on the perovskite surface.[50]

In a complete solar cell device multiple layers are stacked together, which implies many interfaces are involved such as, metal/semiconductor (metal/perovskite), semiconductor/semiconductor (hole transport layer/perovskite and electron transport layer). Hence, to optimize carrier injection barriers not only each interface should be investigated independently but also the underlying phenomenon that controls such interfacial energy level alignment at these interfaces should also be documented. In the following each of these interfaces will be discussed.

1.3.1 Metal/perovskite interface

The interface of perovskite with metal contact is critical because it controls either hole extraction in the case of high WF metals like (Au) or electron extraction in the case of comparably lower WF metals like (Al). A thorough examination of the evolution of energy levels by progressively depositing Au was conducted with XPS, UPS, and IPES to better understand the electronic structure and charge carrier transfer process at the $MAPbI_3$/Au interface. The initial $MAPbI_3$ found as n-type semiconductor since the E_F was found was at 0.7 eV below CBM and 1 eV above VBM for the bandgap of 1.7 eV. Subsequent deposition of Au shifted E_F more towards VBM of perovskite, and at the very interface it is found at 1.1 above and 0.4 eV below CBM and VBM respectively; as a result, perovskite becomes p-type, as illustrated in Figure 1.9 (a).[51] This E_F shifts towards VBM of perovskite demonstrates the band bending in perovskite, and thus built-in field in $MAPbI_3$ facilitates holes extraction towards Au. Furthermore, offset between VBM of $MAPbI_3$ and Au decreased, indicating reduction in energy loss for holes transportations. It has been concluded that this favorable energy level alignment at $MAPbI_3$/Au interface, effectively used for hole collectors for perovskite devices.

Conversely, in another report in which $MAPbI_{3-x}Cl_x$ deposited successively on Au, it is found that band bending of 0.26 eV can be seen in perovskite over a distance of 16.3 nm due to electrons transfer from perovskite to Au until the equilibrium reached which stops further diffusion as depicted in Figure 1.9 (b).[52] It is concluded that, though Au/ $MAPbI_{3-x}Cl_x$ facilitates hole extraction, interfacial layers needed to inhibit electron-back diffusion and to prevent perovskite-Au interfacial reaction. Both of the cases presented above demonstrated the band bending in the perovskite, indicating the presence of built-in field that could facilitate hole extraction towards Au electrode. Moreover, it is suggested that a buffer layer should be inserted between perovskite and Au electrode that can limit the back diffusion of electrons consequently suppressing recombination. Although Cha et al.,[52] found the formation of Pb^0 which is attributed to the interfacial chemical reaction, the exact origin of which remains unknown.

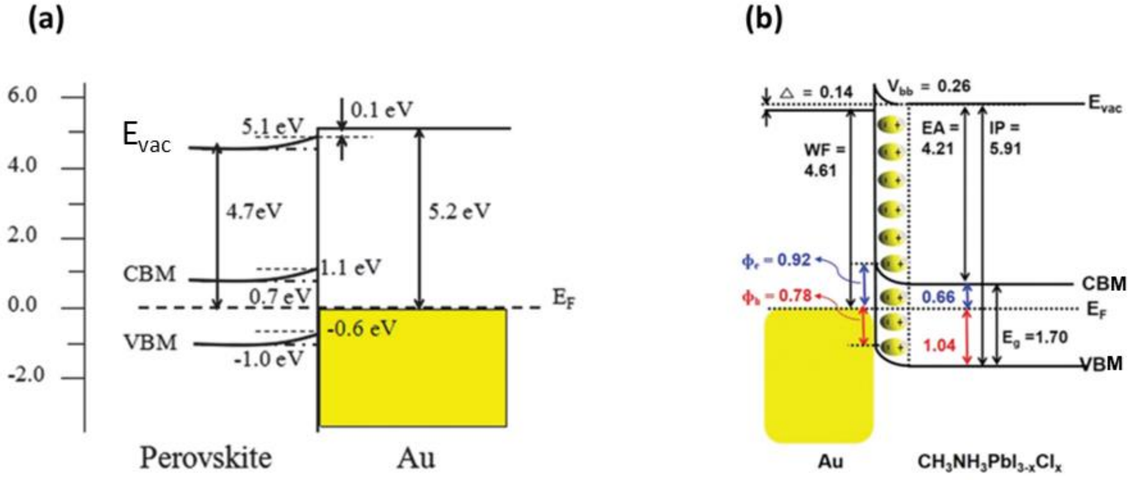

Figure 1.9. Interface of $MAPbI_3$/ Au interface (a) where Au is deposited incrementally on top of $MAPbI_3$ adopted from Ref.[51] (b) where $MAPbI_{3-x}Cl_x$ deposited incrementally on Au adopted from Ref.[52]

Therefore, it is of utmost importance to find the interfacial chemistry between interface of metal and perovskite and decipher the mechanism that might play the role in such interface interaction to not only enhance the performance but more importantly the stability of perovskite.

1.3.2 Organic semiconductor/perovskite interface

As stated above, energetics of halide perovskite are extremely sensitive to the underlying substrates and adopts the type of semiconductor, p-type on hole transport layer (HTL) and n-type on electron transport layer (ETL).[53] Perovskite is typically sandwiched between HTL and ETL to maximize carrier extraction towards the respective electrodes. As a result, finding energy level alignment at different semiconductor interfaces, such as perovskite/HTL and perovskite/ETL, is critical. Furthermore, it has been argued that carrier lifetime exceeds average diffusion time to the interface,[54] implying that bulk recombination is minimal but interface recombination contributes considerably to device losses. Though perovskite is exceptional, being defective itself causes bulk recombination as well as non-radiative recombination at interfaces due to defects on its surface preventing the Shockley-Queisser limit from being realized. Therefore, knowing the energetics of perovskite and its interfaces is essential for limiting nonradiative recombination both in bulk and at the interfaces.

For example, for the interface of perovskite/ETL, a fullerene-based ETL (PCBM) is often used on top of perovskite known also for assisting in passivating trap states in perovskite. As a result, the electronic structure at the $MAPbI_3$/PCBM interface is vital, and findings from one of the studies are displayed in Figure 1.10.[55] Here, perovskite with its $MAPbI_{3-x}Cl_x$ composition used, and its VBM is determined to be at 1.37 eV below E_F, confirming n-type character of perovskite given the optical bandgap of 1.70 eV. After 5 Å PCBM coating, the vacuum level changed to the downside by 0.3 eV, with no additional changes noticed as the thickness increased further up to 100 Å. Yet, (HOMO) of PCBM remains unchanged. Hence according to the energy level diagram constructed and shown in Figure 1.10 (c), there is no barrier exists for hole transfer since the VBM of perovskite aligns with HOMO of PCBM, whereas there exist a barrier of 0.5 eV for electron, implying that severe recombination expected at this interface. Therefore, it has been concluded that PCBM is not an ideal ETL material, and alternatives to PCBM should be investigated in order to suppress recombination and extract electrons efficiently.

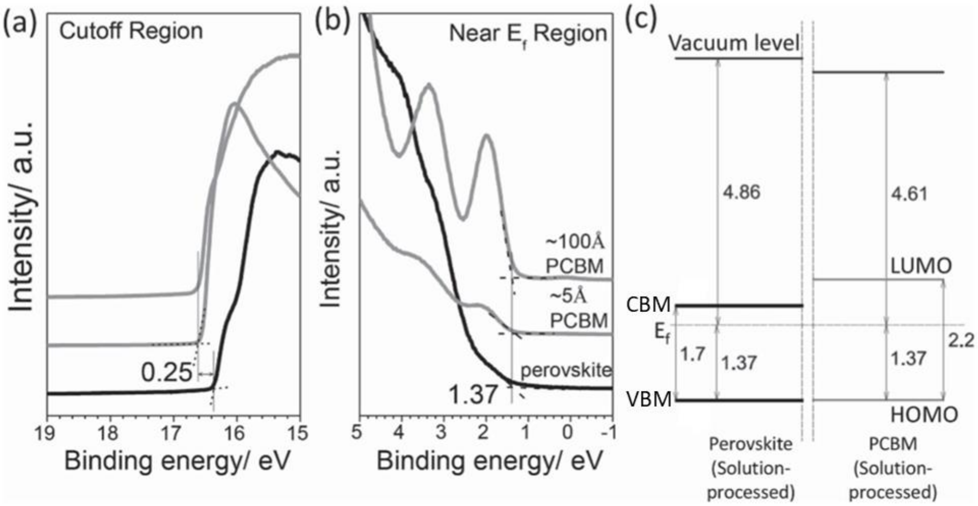

Figure 1.10. UPS spectra of a) the cutoff region and b) Valence band of an ITO/ perovskite, and with 5 and 100 Å of PCBM on top. (c) Energy level diagram of interface between perovskite/PCBM interface.[55]

Alternative to PCBM, in the same study, author employed C60 as an ETL deposited incrementally on top of $MAPbI_{3-x}Cl_x$/ITO. Similar offset between vacuum levels obtained as for the case of PCBM on top of perovskite. C60 on perovskite shifted the vacuum level downward by just 0.1 eV (left hand side of Figure 1.11 (a)) compared to 0.3 eV for PCBM; yet a shift of 0.16 eV is detected in the HOMO of C60 as thickness increases as shown in right hand side of Figure 11(a), which was also evident in core level of C 1s shown in left hand side of Figure 1.11 (b). This shift of HOMO was absent when PCBM was coated over perovskite. Hence, based on these shifts of vacuum and HOMO level across the interface a band diagram was constructed and shown on the right-hand side of Figure 1.11(b).

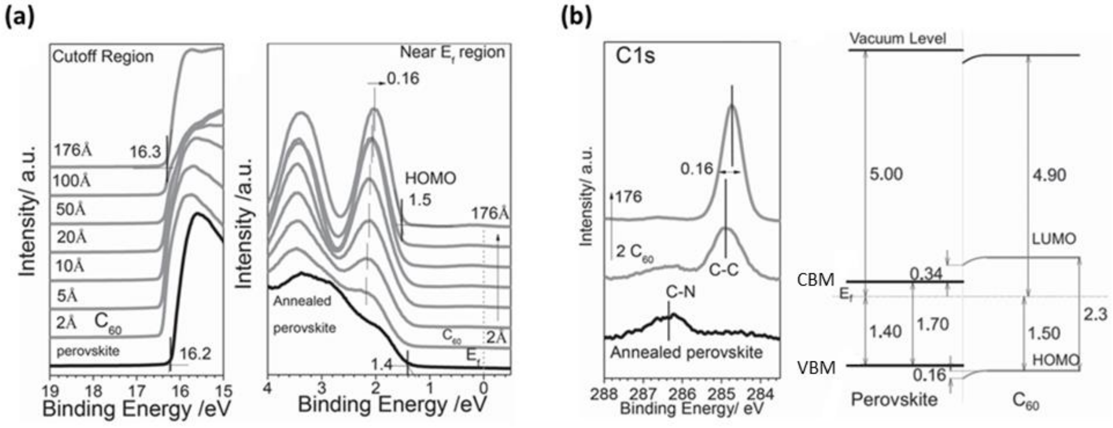

Figure 1.11. (a) UPS spectra left panel cutoff region, right panel valence band region as a function of increasing C60 deposition on perovskite/ITO substrate, (b) left panel XPS spectra of C1s core level of C60 (d) energy level diagram at perovskite/C60 interface.[55]

The observed band bending upon contact of C60 with perovskite suggests not only the charge transfer across the interface, but also makes the C60 a better candidate as an ETL than PCBM due to a low barrier for electron extraction and high barrier for hole diffusion towards C60 from perovskite.

Nonetheless, key findings of this study was that energy level alignment in both cases, whether PCBM on perovskite or C60 on perovskite, revealed type 1 (straddling junction) junctions rather than of type II junctions (staggered junction). This work refuted the widely held notion that perovskite/fullerene shares similar photogenerated mechanism as common organic solar cells with type II (staggered junction) or P-N junction, in which P-N junction provides driving force for excitons to dissociate into free carriers (electron and holes). Moreover, these findings indicate that fullerene based organic materials have the potential to passivate the trap states existing on the surface of perovskite, which aids in not only enhancing the performance of perovskite device but more importantly the stability of perovskite (trap states accelerate the instability in perovskite).

Similarly, poly(3,4-ethylenedioxythiophene) polystyrene sulfonate (PEDOT:PSS) is considered as a common candidate for hole transport layer (HTL) in perovskite solar cells. Hence interface energetics between PEDOT:PSS and perovskite have been extensively investigated and findings from one of the reports illustrated in Figure 1.12 (a), which shows the energy level diagram of $MAPbI_3$ (perovskite composition) gradually depositing perovskite (0 to 200 nm) on PEDOT:PSS.[56].

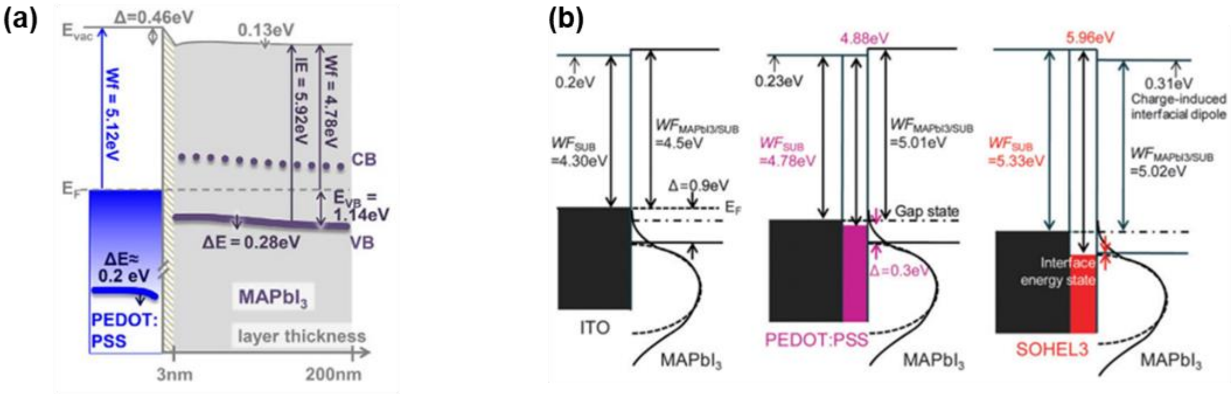

Figure 1.12. (a) Interface of PEDORT:PSS/$MAPbI_3$ interface, a passivation layer at 3nm is created as a consequence of charge transfer between $MAPBI_3$ and PEDO:PSS.[56] (b) Energy level diagrams of ITO/$MAPbI_3$, PEDOT:PSS/$MAPbI_3$ and SOHEL3 (mixture of PEDOT:PSS and PFI)/$MAPbI_3$ interfaces.[57]

An interfacial dipole is created due to charge transfer between the perovskite and PEDOT:PSS, resulting in an alteration of the vacuum level position. Additionally, band bending occurs due to charge redistribution within the perovskite. These findings indicate that although the hole injection barrier (ϕ_h) remains high, current band bending facilitates hole extraction. Furthermore, the low inherent charge carrier density leads to significant depletion regions.

Despite the fact that this work emphasizes the presence of low carrier density in perovskite, PEDOT: PSS is regarded as unsuitable hole transport layer due to its acidic nature, which can harm the underlying substrates, such as ITO, which is frequently employed as one of the electrodes in perovskite devices.

In another study, the interface of $MAPbI_3$ on different substrate such as ITO, PEDOT:PSS and SOHEL (mixture of PEDOT:PSS and perfluorinated ionomer (PFI)) has been investigated and corresponding energy level diagrams are shown in Figure 1.12 (b).[57] At the interface of ITO/$MAPbI_3$, the offset between the work function (WF) of ITO and valence band maximum (VBM) of perovskite was found 0.9 eV due to low work function of 4.30 eV of ITO substrate. This energy offset decreased to 0.4 eV due to high work function of PEDOT:PSS (4.78 eV) at the interface of PEDOT:PSS/$MAPbI_3$, thus the resulting WF of $MAPbI_3$ is 5.01 eV. However, the WF of $MAPbI_3$ does not change with further increase in the WF of substrate (SOHEL (5.33 eV)), which is attributed to the Fermi-level pinning by mid-gap states (antistites defects for example, lead occupying an iodide site yields an anti-site labeled as Pb_I) of perovskite. Hence, it is concluded that even though the presence of mid-gap states in perovskite causes E_F of SOHEL to be about 0.6-0.7 eV above valance band maximum of perovskite, the interface state of the PFI-enriched surface layer of SOHEL can be formed deeper below the Fermi level so that it matches with valence band of perovskite. Therefore, energy offset at the interface of SOHEL and perovskite was reduced significantly and charge carrier transported efficiently.

From these investigations of interface of perovskite with PEDOT:PSS it can be concluded that, SOHEL is better HTL over ubiquitously used PEDOT:PSS not only due to its better energy level alignment with perovskite but also due to enhancement of the stability of perovskite, which is main obstacles towards the commercialization of perovskite photovoltaics. This is achieved through the diffusion-blocking ability of the self-organized PFI at the surface of SOHEL, which prevents impurities from reaching perovskite from indium-doped tin oxide (ITO).

Nonetheless, SOHEL acting as an HTL improves device performance and stability, the presence of mid-gap states is highlighted, yet perovskite is known to have shallow defects. As a result, it prompts the question of whether perovskite has mid-gap states and, if so, how they affect energy level alignment at various interfaces, which includes various charge transport layers and/or buffer layers.

Similar to the interface of perovskite and HTL at the bottom, the interface of perovskite and HTL on top is another important interface that needs to be investigated, and Figure 1.13 depicts one of the studies of energy level alignment at this interface, where undoped and doped poly[bis(4-phenyl)(2,4,6- trimethylphenyl)amine] (PTAA) HTL of 15nm deposited on top of $CsPbBr_3$ thin film.[58] After undoped PTAA deposition on perovskite, a 0.1 eV shift towards lower binding energy was detected for Cs 4d and Br 3d core levels, and an even bigger of 0.2 eV shift for doped PTAA, indicating an upwards shift of E_F in the gap of $CsPbBr_3$. Similarly, the VBM of perovskite changed from 0.7 to 0.6 eV below E_F for undoped PTAA and from 0.5 eV to 0.6 eV below E_F for doped PTAA. The highest occupied molecular orbital (HOMO) of PTAA was determined at 1.1 and 0.3 eV below E_F in the undoped and doped layers, respectively. However, the buried interface of $CsPbBr_3$/PTAA was impossible to assess directly since thickness of PTAA is significantly large of 15 nm, and sufficiently thinner PTAA was impossible to produce. Hence, energy level alignment was proposed as an effect of both interfacial dipole and/or band bending. When PTAA is doped, the hole injection barrier is decreased from 0.5 to 0.2 eV, facilitating hole injection/transportation. Furthermore, doping PTAA raises the valence band of $CsPbBr_3$, boosting the built-in field and resulting in more effective charge separation and extraction. This reduced hole injection barrier attributed to the either the band bending in PTAA or dipole at the interface or the effect of both. Nonetheless, the gap states (shaded area below the LUMO level in energy level diagram) exist as evidenced by inverse photoemission spectroscopy (IPES) for both doped and undoped PTAA might have adverse effects and could result in undesirable electron recombination in complete solar cell device. Moreover, it is unclear whether band alignment at perovskite/PTAA happens via interfacial dipole or band bending formation. And existence of gap states are underlined, although the impact of gap states in band alignment is not addressed.

This work shows the effectiveness of PTAA as a material for the devices is dependent on its doping status. However, exposing the device to a high temperature of 85 °C led to permanent damage due to development of pinholes in PTAA, which resulted in dopant evaporation. Furthermore, since lithium bis(trifluoromethanesulfonyl)imide (Li-TFSI) and tributyl phosphate (tBP) are commonly used dopants for PTAA, the Lithium ion (Li^+) formation and migration also negatively affect the device. Even more importantly, under continuous light illumination at elevated temperatures, Au which is used as an electrode in a device, can migrate through PTAA into the perovskite, significantly degrading device performance.[59] The underlying mechanism and interfacial chemistry at the perovskite-PTAA and/or Au metal, are not well understood yet and require further investigation to identify alternative hole transport layers to PTAA that can result in more stable perovskite devices.

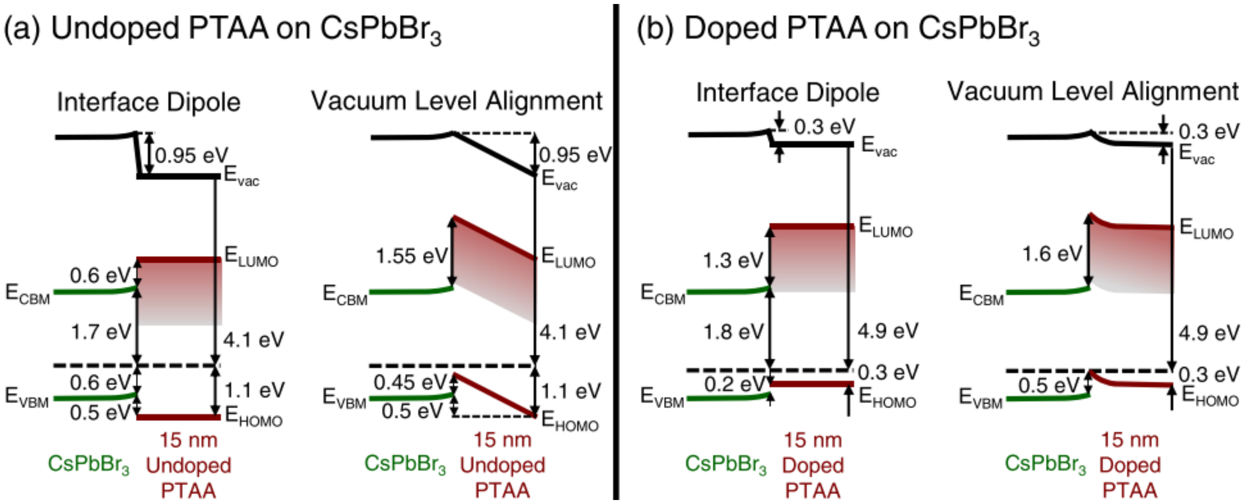

Figure 1.13. Band diagram showing probable energy level alignment at the $CsPbBr_3$ interface (a) for undoped PTAA (b) for doped PTAA. Diagram on the left assumes just interfacial dipole energy level alignment, whereas the diagram on the right considers both interfacial dipole and band bending.[58]

Another interesting and often used HTL on top of perovskite is spiro-MeOTAD (2,20,7,70-tetrakis[N,N-di(4-methoxyphenyl)amino]-9,90 -spirobifluorene). Schulz et al., investigated the interfacial energetics of incrementally deposited spiro-MeOTAD on top of perovskite with three different composition of perovskite, $MAPbI_3$, $MAPBI_{3-x}Cl_x$, and $MAPbBr_3$, using XPS, UPS and IPES, and the resulting energy level alignments are shown in Figure 1.14.[60] In all the three perovskite layers, the initial thin layer of spiro-MeOTAD exhibits no change in WF, indicating the absence of an interfacial dipole between two materials. Furthermore, the offset between VBM of perovskite and HOMO level of spiro-MeOTAD amounts to 0.4, 0,3 and 0.8 eV for $MAPbI_3$, $MAPbI_{3-x}Cl_x$, and $MAPbBr_3$ respectively, indicating that a small hole injection barrier exists from perovskite into the HTL compared to hole injection in the opposite direction. Moreover, when spiro-MeOTAD thickness increases, HOMO onset shifts toward higher binding energies (i.e., away from E_F) by amount of 100 meV for $MAPbI_{3-x}Cl_x$ and 300 meV for other two compositions of perovskite accompanied by identical shift of vacuum level, resulting in a constant ionization potential (IE) of ~5.0 eV. This shift in energy levels is the sign of small band bending in a molecule; however, no band bending is observed in the perovskite as by tracking the Pb4f core level as a function of HTL thickness. This demonstrates that the interface between perovskite and spiro-MeOTAD is completely inert and non-interacting, indicating that this small molecule HTL has the potential to be an effective HTL.

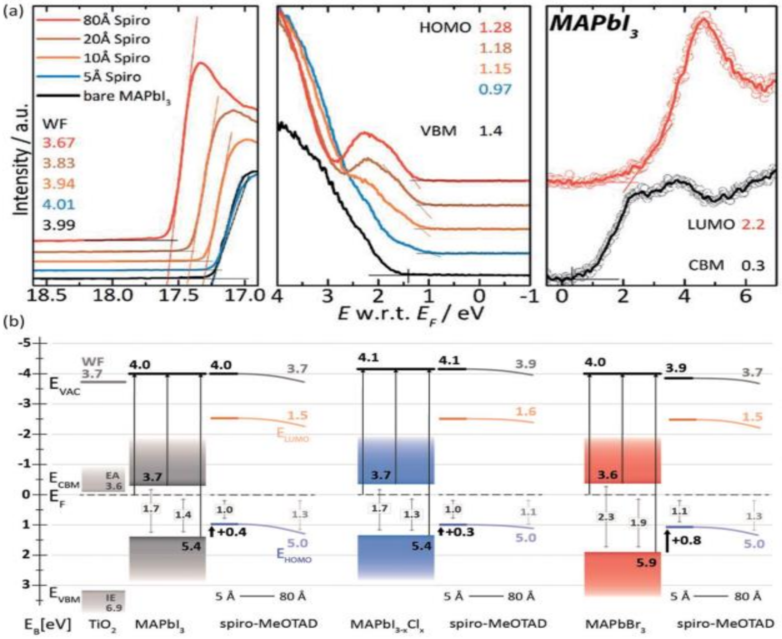

Figure 1.14. Alignment of energy levels between spiro-MeOTAD and perovskite thin films (a) UPS (left and middle figure) and IPES (right figure). (b) Energy level diagram constructed for the interface of three different perovskite layers with spiro-MeOTAD.[60]

However, high hole injection barrier and low electron injection barrier could give rise to the unwanted recombination events. Therefore, it was concluded that materials with high IEs that can match perovskite VBM while also having low electron affinity to ensure electron blocking should be investigated in order to achieve effective charge extraction and prevent undesired recombination.

Again, similar to PTAA, spiro-OMeTAD also used dopants (Li-TFSI and tBP) to increases its conductivity. Under operating conditions, it has been proposed that dopants and their byproducts can be hygroscopic, cause morphological issues, evaporate, migrate across the device, and/or engage in unwanted reactions in perovskite devices, eventually destroying the perovskite device. Moreover, spiro-OMeTAD has been found to constitute a weak barrier for ion migration from dopants, electrodes, or the perovskite itself leading to different chemical reaction and thus making the perovskite device highly unstable.[59] All of these concerns with spiro-OMeTAD show the device's instability, and additional research is needed to understand what happened at the interface when each of these mechanisms occurred.

To summarize, energy level alignment in organic semiconductor/perovskite interface occurs under vacuum level alignment or by the formation of small interfacial dipole, while Fermi level pinning can occur if the organic layer's ionization potential energy (IE) or electron affinity (EA) is larger or less than the work function (WF) of perovskite, respectively. Also, charge transfer is usually dependent on the interfacial defect states, which are most of the time inherent to perovskite and due to their benign nature does not play significant role in the energy level alignment at organic/perovskite interface. However, significant drawback of using organic transport layers is that they do not provide enough barrier for ions migration stemming from either perovskite or from electrode, resulting in interfacial chemical reaction between perovskite and metal electrode, which leads to highly unstable device under operational condition.

1.3.3 Metal oxide/perovskite interface

When it comes to metal oxide, MoO_3 is one of the first choices to be used as a hole extraction layer. Because of its Fermi level (E_F) pinning at CBM, MoO_3 is classified as an n-type semiconductor. This E_F pinning occurs due to the oxygen vacancies defects present in MoO_3. The high work function of MoO_3 pulled the highest occupied molecular orbital (HOMO) of organic materials upward towards interface, lowering the interface potential barrier and facilitating hole extraction and injection. For instance, Kroger et al., demonstrated that MoO_3 can be used to p-dope the organic semiconductor by electrons extraction from the HOMO of the organic layer and directing them towards the CBM of MoO_3 owing to the high work function and deep-lying unoccupied states, i.e. (electron affinity) of MoO_3.[61] Similar working mechanism can be envisaged for MoO_3 in case of perovskite; however, due to high reactivity of perovskite, properties at interface are strongly modified, i,e., during the evaporation of $MAPbI_3$ on MoO_3, PbI_2-rich phase formed due to decomposition of perovskite right at the interface with MoO_3.[57]

As previously mentioned, perovskite can exhibit either p-type or n-type semiconductor behavior depending on the type of substrate it is deposited on, meaning it can behave as a p-type semiconductor on a p-type substrate or as an n-type semiconductor on an n-type substrate. Schulz et al., verified this hypothesis by performing photoemission spectroscopy as shown in Figure 1.15, where perovskite valence band (VB) was found at 0.7 and 1.4 eV from E_F confirming its p-type and n-type characteristics considering optical bandgap of 1.70 eV deposited on p-type (NiO_x) and n-type (TiO_2) substrates, respectively. This adoption of p-type and n-type characteristics of perovskite according to type of substrate are attributed to the shallow trap states present in VBM and CBM of perovskite.[50] Furthermore, it is noticed that the position of E_F is retained throughout the film of perovskite (400 nm) suggesting a low density of intrinsic carrier, and thus unintentional dopants. It further suggests low density deep mid-gap states, which would have otherwise been pinned E_F and screen charge transfers to and from the high work function (NiO_x) and low work function (TiO_2) substrates. These low density of deep mid-gap states verified the previous findings of existence of energetically more favorable shallow trap states than the energetically less favorable deep mid-gap states.[57]

Nonetheless, although confirmation of slightly p-doping and n-doping of perovskite on p-type and n-type substrates respectively highlighted the unique composition of free carriers and gap states in $MAPbI_3$, no indications of interfacial chemical reaction at the interface of metal oxides and perovskite reported. This lack of observation may be due to the fact that the perovskite layer was too thick, and hence inaccessibility to the buried interface.

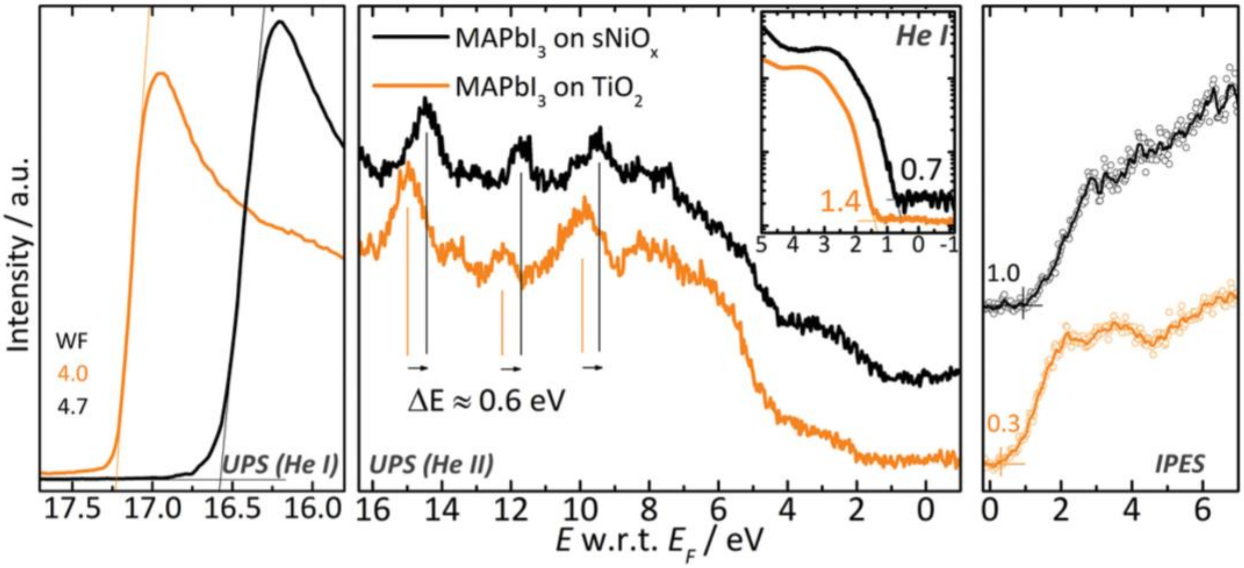

Figure 1.15. UPS and IPES spectra of MAPbI$_3$ perovskite on NiOx (black curve) and TiO2 (orange curve).[50]

To investigate interfacial energetics the right at the interface between perovskite and MoO$_3$, Wang et al., used the XPS and UPS used to study the electronic structure of $CH_3NH_3PbIBr_2$ with incremental growth of MoO$_3$ on top as shown in Figure 1.16.[62] According to the UPS data in Figure 1.16 (a), revealed the emergence of gap states for the first MoO$_3$ layer on perovskite, which were located at ~0.8 and ~1.9 eV below E$_F$. These states resulted from oxygen deficiency in MoO$_x$ and appear as Mo^{6+} and Mo^{5+} components of Mo, which would otherwise only be Mo^{6+}.

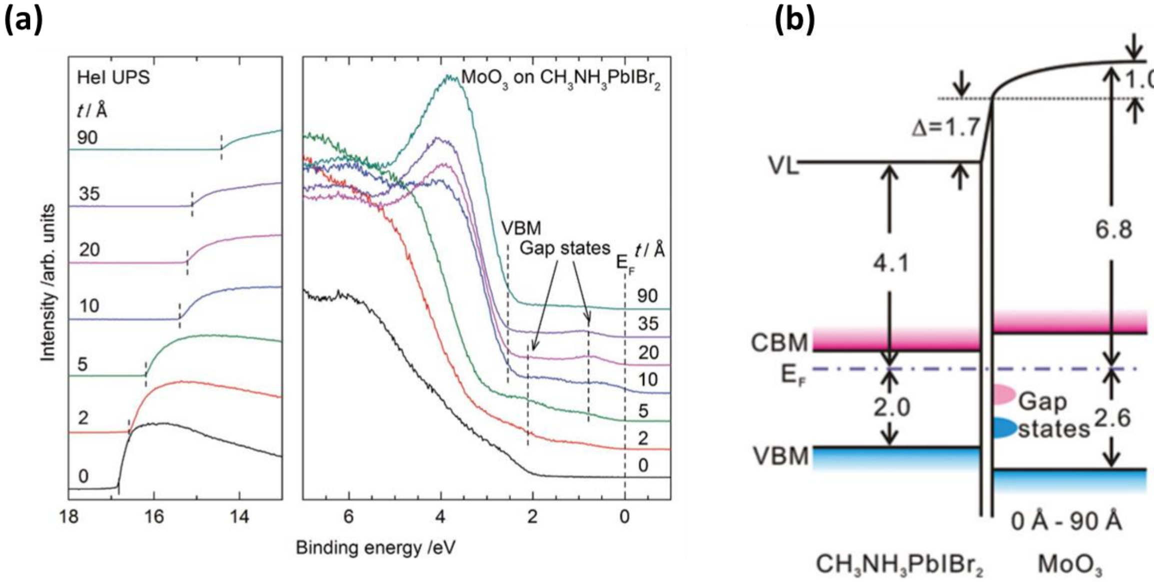

Figure 1.16. UPS spectra of $CH_3NH_3PbIBr_2$ perovskite with incremental growth of MoO$_3$ on top (b) energy level diagram of perovskite/MoO$_3$ interface.[62]

At the interface, a strong interfacial dipole is formed however no bend banding is visible because there was no obvious change observed in Pb 4f and I 3d core levels of perovskite. Furthermore, though the barrier for hole extraction from perovskite VBM to MoO_3 is not very high, there was an equal barrier for electron extraction, indicating MoO_3 might not effectively suppress recombination.

Thus, although this research demonstrated no band bending in perovskite, CLs shift found in perovskite after evaporation of MoO_3 in other reports, which is not compatible with a simple charge transfer process but complex interfacial chemistry discussed in following.

Liu et al. reported the presence of band bending at the interface between perovskite and MoO_x due to the charge transfer between the two, which contradicts the earlier findings of no band bending in perovskite after the deposition of MoO_3 on top.[63]

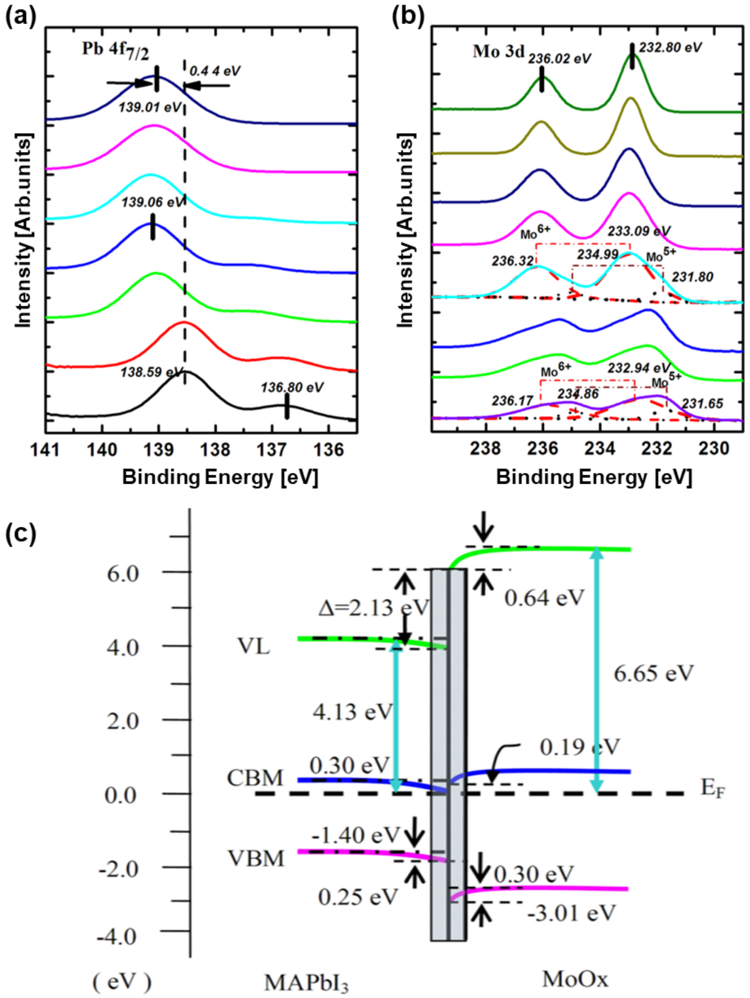

Figure 1.17. XPS spectra of (a) Pb4f ($_{7/2}$) ,(b) Mo3d core level of $MAPbI_3/MoO_x$ interface as a function of increasing MoO_x layer. (c) energy level alignment diagram at the $MAPbI_3/MoO_x$ interface.[63]

The Pb 4f core level in perovskite was founds to be shifted by 0.25 eV towards higher binding energy (Figure 1.17(a)) and concomitant shift of 0.30 eV towards lower binding energy in Mo 3d core level observed (Figure 1.17(b)) with the incremental deposition of MoO_x on $MAPbI_3$ perovskite, which are attributed to the charge transfer from $MAPbI_3$ to MoO_x. These shifts lead to the downward bending of energy levels at the perovskite side while upward bending towards MoO_x side as shown in Figure 1.17 (c).

More importantly, opposite to the previous reports, the chemical reaction occurs at the interface evidenced by decreasing intensity of Iodine (I) compared to lead (Pb) intensity. This is further corroborated by reduction of Mo^{6+} to Mo^{5+} at the interface, which is attributed to the transfer of electron from perovskite to MoO_x. Such a transfer can lead to I^- to neural I, which subsequently leaves the films in the form of I_2 through sublimation. Surprisingly, the potential barrier of 1.36 eV for hole extraction while potential barrier for electron was substantially small of 0.14 eV found which is the opposite what would be expected. Therefore, it is concluded that $MAPbI_3/MoO_x$ is not an ideal interface for hole extraction, not just because of opposite values for hole and electron extraction barrier but due to interfacial chemical reaction that occur, leading to the instability of perovskite.

Similarly, a more rigorous and in-depth analysis of interfacial chemistry of perovskite and MoO_x, discovered that band bending in the perovskite existent in both cases, either evaporation of MoO_3 directly on top of pristine $MAPbI_{3-x}Cl_x$ or even on the protected surface (thin layer of (~3 nm) spiro-OMeTAD). UPS spectra shown in Figure 1.18 (a) of incrementally grown MoO_3 on perovskite shows an interface dipole and gap states below conduction band edge (at 0.2 eV below E_F), which is attributed to the charge transfer across the interface and nonstoichiometric MoO_3. Similarly, this study also revealed a significant upward band bending (~0.5 eV) of perovskite as evidenced by shift of Pb 4f and I 3d CLs in XPS spectra.

Moreover, from Mo 3d CL of thin film of 1.5 Å (inset in the right panel of Figure 1.18 (b), a new Mo^{+4} component emerged that is assigned to MoO_2 indicating MoO_3 reduction. This reduction of MoO_3 into MoO_2 is a sign of charge transfer from oxide to perovskite and could be explained as, $Pb^{2+} \rightarrow Pb^{4+}$ oxidation and/or $2I^- \rightarrow I_2$ oxidation from $Mo^{6+} \rightarrow Mo^{4+}$ reduction. When spiro-OMeTAD is used as buffer layer between perovskite and MoO_3, it inhibits such a chemical reaction at the interface. Nonetheless, no change in band bending observed in perovskite due to high WF of MoO_3 though oxide is still being sub stoichiometric (Mo^{6+} alongside Mo^{5+} species) attributed to the charge transfer between adjacent organic and MoO_3 layers as shown in Figure 1.18 (c). However, in both cases, either MoO_3 directly on perovskite or MoO_3 on spiro-OMeTAD protected perovskite, no change in device performance was observed despite suppressing the chemical process in the latter case, which is ascribed to the low hole injection current from spiro-OMeTAD to MoO_3 owing to the non-ohmic contact at the interface, as shown in Figure 1.18 (d) [64] Nevertheless, there have been reports of ohmic contact being made between perovskite and MoO_3 by introducing a suitable organic layer.[63]

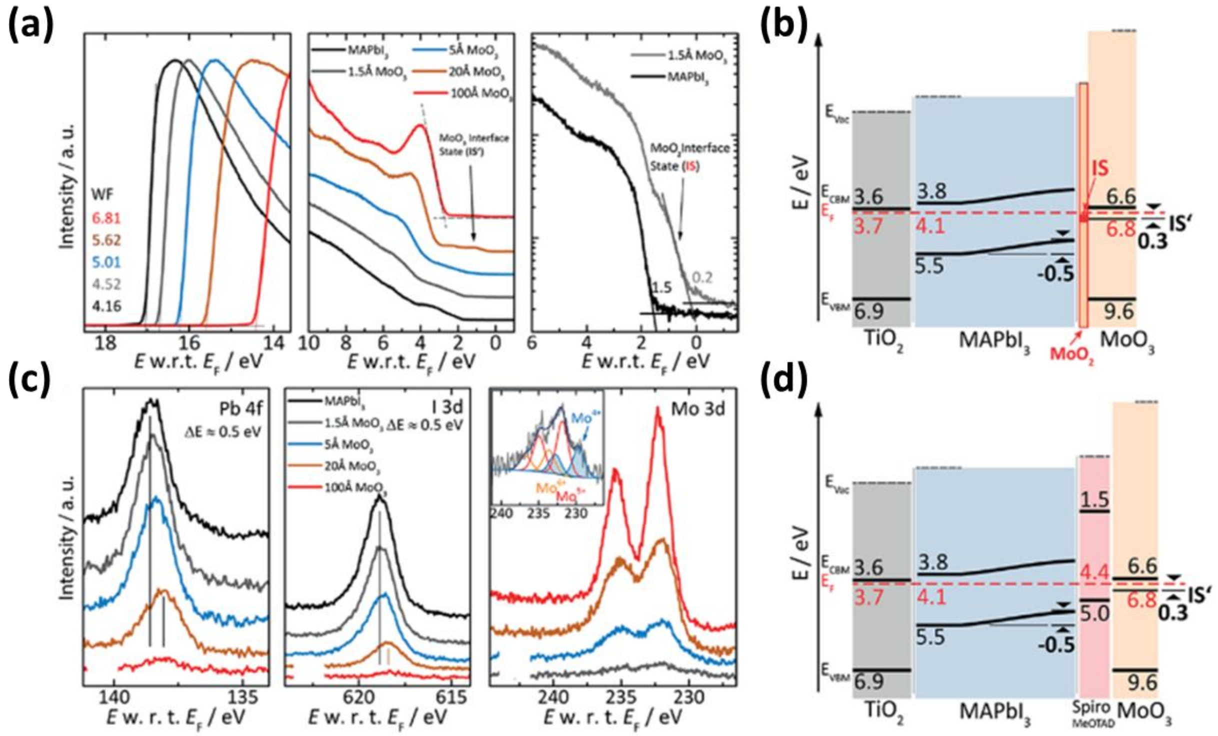

Figure 1.18. (a) UPS spectra (cutoff region, valance band region and close-up of valence band on a semilogarithmic scale (b) energy level diagram of MoO_3/$MAPbI_3$/TiO_2, (c) XPS spectra of (Pb4f, I3d and Mo3d CLs) with inset showing magnification for the 1.5Aº MoO_3, and (d) energy level diagram of MoO_3/Spiro-OMeTAD(3nm) $MAPbI_3$/TiO_2.[64]

These reports of perovskite/MoOx highlights the fact that despite the favorable energy level alignment that might facilitate the carriers extraction at the interface, the formation of defects plays the key role in terms of device performance. Nonetheless, the use of MoO_3 is significant since it performs outstandingly well in enhancing device stability by limiting moisture penetration into perovskite, which is considered bottleneck for the commercialization of perovskite.

In summary, energy level alignment and interfacial electronic structure play a crucial role in the performance of electronic devices, and understanding these concepts is essential for designing and developing more efficient devices. Like any other semiconductor material, optoelectronic properties of halide perovskite are also strongly modified at the interface with either metal electrode or charge transport layers (both organic and inorganic), and interfacial energetics at these interfaces severely impact the charge extraction efficiency which have a significant impact on device functionality. Energy level alignment at these interfaces can occur either as a result of vacuum level shift, which give rise to phenomenon of interfacial dipole, and/or Fermi level alignment (band bending). Since the surface of perovskite is terminated at AX (where A is cation and X is anion), this results in fewer coordinated partners for B-sites and X-sites, making them potential reaction sites for adjacent material. This terminated surface condition can change significantly more under high fluence of radiation exposure or electric field, leading to increased complexity in energy level alignment and interfacial chemistry with adjacent charge transport layers. Moreover, while the interface of perovskite with metal electrodes or other charge transport layers exhibits dynamical interfacial chemistry and band alignment, this interfacial energetics may become even more complicated when subjected to radiation exposure and should therefore be studied. Considering this, in this thesis I will discuss the stability and interfacial chemistry of $CsPbBr_3$ perovskite nanocrystals deposited on different substrate including gold (Au), molybdenum disulfide (MoS_2), molybdenum oxide (MoO_x) and indium tin oxide (ITO). Overall, the knowledge of energy level alignment and interfacial electronic structure has the potential for transformative advancements in electronic device design.

References

1. Du, M. H. Efficient carrier transport in halide perovskites: theoretical perspectives. J. Mater. Chem. A 2014, 2, 9091−9098.
2. Hawash, Z.; Raga, S. R.; Son, D.-Y.; Ono, L. K.; Park, N.-G.; Qi, Y. Interfacial Modification of Perovskite Solar Cells using an Ultrathin MAI Layer Leads to Enhanced Energy Level Alignment, Efficiencies, and Reproducibility. J. Phys. Chem. Lett. 2017, 8, 3947.
3. Ishii, Hisao, et al. "Energy level alignment and interfacial electronic structures at organic/metal and organic/organic interfaces." Advanced materials 11.8 (1999): 605-625.
4. Kahn, Antoine. "Fermi level, work function and vacuum level." Materials Horizons 3.1 (2016): 7-10.
5. Helander, M. G., et al. "Pitfalls in measuring work function using photoelectron spectroscopy." Applied Surface Science 256.8 (2010): 2602-2605.
6. S. M. Sze, Physics of Semiconductor Devices, 2nd ed.,Wiley, New York 1981.
7. Celii, Francis G. "DP Woodruff and TA Delchar, Modern techniques of surface science: Cambridge University Press, 1986 (ISBN 0-521-30602-7), 453 pp." (1986): 397.
8. Cahen, David, and Antoine Kahn. "Electron energetics at surfaces and interfaces: concepts and experiments." Advanced Materials 15.4 (2003): 271-277.
9. Strayer, R. W., W. Mackie, and L. W. Swanson. "Work function measurements by the field emission retarding potential method." Surface Science 34.2 (1973): 225-248.
10. Lang, N. D., and W. Kohn. "Theory of metal surfaces: charge density and surface energy." Physical Review B 1.12 (1970): 4555.
11. Lang, N. D., and W. Kohn. "Theory of metal surfaces: work function." Physical Review B 3.4 (1971): 1215.
12. Horn, Karsten. "Semiconductor interface studies using core and valence level photoemission." Applied Physics A 51.4 (1990): 289-304.
13. Bredas, Jean-Luc. "Mind the gap!" Materials Horizons 1.1 (2014): 17-19.
14. Brillson, Leonard J. An essential guide to electronic material surfaces and interfaces. John Wiley & Sons, 2016.
15. Cahen, David, and Antoine Kahn. "Electron energetics at surfaces and interfaces: concepts and experiments." Advanced Materials 15.4 (2003): 271-277.
16. Brillson, L. J. "Surfaces and interfaces of electronic materials, first edition, 2010." 93-145.
17. Hwang, Jaehyung, Alan Wan, and Antoine Kahn. "Energetics of metal–organic interfaces: New experiments and assessment of the field." Materials Science and Engineering: R: Reports 64.1-2 (2009): 1-31.
18. Olthof, Selina. "The Impact of UV Photoelectron Spectroscopy on the Field of Organic Optoelectronics—A Retrospective." Advanced Optical Materials 9.14 (2021): 2100227.
19. Jiang, Chaoran, et al. "Photoelectrochemical devices for solar water splitting–materials and challenges." Chemical Society Reviews 46.15 (2017): 4645-4660.
20. Borgwardt, Mario, et al. "Femtosecond time-resolved two-photon photoemission studies of ultrafast carrier relaxation in Cu2O photoelectrodes." Nature communications 10.1 (2019): 1-7.
21. Zojer, Egbert, Thomas C. Taucher, and Oliver T. Hofmann. "The impact of dipolar layers on the electronic properties of organic/inorganic hybrid interfaces." Advanced Materials Interfaces 6.14 (2019): 1900581.
22. Hölzel, J., F. K. Schulte, and H. Wagner. "Solid State Surface Physics." (1979).
23. Tung, Raymond T. "The physics and chemistry of the Schottky barrier height." *Applied Physics Reviews* 1.1 (2014): 011304.
24. H. Ishii, K. Sugiyama, K. Seki, Proc. SPIE Int. Symp. Organic Light-Emitting Materials and Devices, San Diego 1997, 228.

25. Ishii, Hisao, et al. "Energy-level alignment at model interfaces of organic electroluminescent devices studied by UV photoemission: Trend in the deviation from the traditional way of estimating the interfacial electronic structures." IEEE Journal of selected topics in quantum electronics 4.1 (1998): 24-33.
26. Rajagopal, A., C. I. Wu, and Antoine Kahn. "Energy level offset at organic semiconductor heterojunctions." Journal of applied physics 83.5 (1998): 2649-2655.
27. Zangwill, Andrew. Physics at surfaces. Cambridge University Press, 1988.
28. Wandelt, K., and J. E. Hulse. "Xenon adsorption on palladium. I. The homogeneous (110),(100), and (111) surfaces." The Journal of chemical physics 80.3 (1984): 1340-1352.
29. Fukagawa, Hirohiko, et al. "The Role of the Ionization Potential in Vacuum‐Level Alignment at Organic Semiconductor Interfaces." Advanced Materials 19.5 (2007): 665-668.
30. Lin, Liang, and John Robertson. "Passivation of interfacial defects at III-V oxide interfaces." Journal of Vacuum Science & Technology B, Nanotechnology and Microelectronics: Materials, Processing, Measurement, and Phenomena 30.4 (2012): 04E101.
31. Mönch, Winfried. "Metal-semiconductor contacts: electronic properties." Surface science 299 (1994): 928-944.
32. Brillson, L. J. "Metal-semiconductor interfaces." Surface science 299 (1994): 909-927.
33. Park, Soohyung, et al. "The origin of high PCE in PTB7 based photovoltaics: proper charge neutrality level and free energy of charge separation at PTB7/PC71BM interface." Scientific reports 6.1 (2016): 1-11.
34. Tengstedt, Carl, et al. "Fermi-level pinning at conjugated polymer interfaces." Applied Physics Letters 88.5 (2006): 053502.
35. Sze, S. M. "Physics of Semiconductor Devices 2nd edition A Wiley Inter-science John Wiley and Sons." New York (1981).
36. P. Hofmann, Solid State Physics: An Introduction. John Wiley & Sons, 2015.
37. Zhang, Zhen, and John T. Yates Jr. "Band bending in semiconductors: chemical and physical consequences at surfaces and interfaces." Chemical reviews 112.10 (2012): 5520-5551.
38. Opitz, Andreas. "Energy level alignment at planar organic heterojunctions: influence of contact doping and molecular orientation." Journal of Physics: Condensed Matter 29.13 (2017): 133001.
39. Schulz, Philip, David Cahen, and Antoine Kahn. "Halide perovskites: is it all about the interfaces?" *Chemical reviews* 119.5 (2019): 3349-3417.
40. Bidermane, Ieva, et al. "Experimental and theoretical study of electronic structure of lutetium bi-phthalocyanine." The Journal of Chemical Physics 138.23 (2013): 234701.
41. Greiner, Mark T., et al. "Universal energy-level alignment of molecules on metal oxides." Nature materials 11.1 (2012): 76-81.
42. Greiner, Mark T., and Zheng-Hong Lu. "Thin-film metal oxides in organic semiconductor devices: their electronic structures, work functions and interfaces." NPG Asia Materials 5.7 (2013): e55-e55.
43. Irfan, et al. "Energy level evolution of air and oxygen exposed molybdenum trioxide films." Applied Physics Letters 96.24 (2010): 116.
44. Greiner, Mark T., et al. "Transition metal oxide work functions: the influence of cation oxidation state and oxygen vacancies." Advanced Functional Materials 22.21 (2012): 4557-4568.
45. Lany, Stephan, Jorge Osorio-Guillén, and Alex Zunger. "Origins of the doping asymmetry in oxides: Hole doping in NiO versus electron doping in ZnO." Physical Review B 75.24 (2007): 241203.
46. Yuzhan, Wang, et al. "A synchrotron-based photoemission study of the MoO_3/Co interface." *Journal of Chemical Physics* 134.3 (2011).
47. Schulz, Philip, et al. "NiOX/MoO3 Bi‐layers as efficient hole extraction contacts in organic solar cells." Advanced Functional Materials 24.5 (2014): 701-706.
48. Wang, Qi, et al. "Qualifying composition dependent p and n self-doping in CH3NH3PbI3." Applied Physics Letters 105.16 (2014): 163508.

49. Yin, Wan-Jian, Tingting Shi, and Yanfa Yan. "Unusual defect physics in CH3NH3PbI3 perovskite solar cell absorber." Applied Physics Letters 104.6 (2014).
50. Schulz, Philip, et al. "Electronic level alignment in inverted organometal perovskite solar cells." Advanced Materials Interfaces 2.7 (2015): 1400532.
51. Liu, Xiaoliang, et al. "Electronic structures at the interface between Au and CH 3 NH 3 PbI 3." Physical Chemistry Chemical Physics 17.2 (2015): 896-902.
52. Cha, Myung Joo, et al. "Depth-dependent electronic band structure at the Au/CH 3 NH 3 PbI 3− x Cl x junction." Physical Chemistry Chemical Physics 21.27 (2019): 14541-14545.
53. Schulz, Philip, et al. "Charge transfer dynamics between carbon nanotubes and hybrid organic metal halide perovskite films." The Journal of Physical Chemistry Letters 7.3 (2016): 418-425.
54. Schulz, Philip. "Interface design for metal halide perovskite solar cells." *ACS Energy Letters* 3.6 (2018): 1287-1293.
55. Lo, Ming-Fai, et al. "Electronic structures and photoconversion mechanism in perovskite/fullerene heterojunctions." Advanced Functional Materials 25.8 (2015): 1213-1218.
56. Olthof, Selina, and Klaus Meerholz. "Substrate-dependent electronic structure and film formation of MAPbI3 perovskites." Scientific reports 7.1 (2017): 1-10.
57. Lim, Kyung-Geun, et al. "Universal energy level tailoring of self-organized hole extraction layers in organic solar cells and organic–inorganic hybrid perovskite solar cells." Energy & Environmental Science 9.3 (2016): 932-939.
58. Endres, James, et al. "Electronic structure of the CsPbBr3/polytriarylamine (PTAA) system." Journal of Applied Physics 121.3 (2017): 035304.
59. Rombach, Florine M., Saif A. Haque, and Thomas J. Macdonald. "Lessons learned from spiro-OMeTAD and PTAA in perovskite solar cells." Energy & Environmental Science 14.10 (2021): 5161-5190.
60. Schulz, Philip, et al. "Interface energetics in organo-metal halide perovskite-based photovoltaic cells." Energy & Environmental Science 7.4 (2014): 1377-1381.
61. Kröger, M., et al. "Role of the deep-lying electronic states of MoO3 in the enhancement of hole-injection in organic thin films." Applied physics letters 95.12 (2009): 251.
62. Wang, Qian-Kun, et al. "Energy level offsets at lead halide perovskite/organic hybrid interfaces and their impacts on charge separation." Advanced Materials Interfaces 2.3 (2015): 1400528.
63. Liu, Peng, et al. "Interfacial electronic structure at the CH3NH3PbI3/MoOx interface." Applied Physics Letters 106.19 (2015): 193903
64. Schulz, Philip, et al. "High-work-function molybdenum oxide hole extraction contacts in hybrid organic–inorganic perovskite solar cells." ACS applied materials & interfaces 8.46 (2016): 31491-31499.

CHAPTER 2: Theory and Experimental Methods

This chapter will outline the experimental methodologies and related concepts. Beginning with photoelectron spectroscopy, which will be introduced in its theoretical and technical aspects, and then the data analysis approach will be discussed. Afterwards, synchrotron radiation and experimental measurement stations will be explained. Lastly, the complementary techniques used will be introduced.

2.1 Photoelectron spectroscopy (PES)

2.1.1 Principle and use in surface and interface science

Photoelectron or photoemission spectroscopy (PES) is a method that assesses the surface chemistry, bonding structure, and composition of surfaces and/or interfaces.[1,2] PES works on the principle of photoelectric effect explained by Albert Einstein in 1905, according to which the absorption of a photon of sufficient energy by a material ejects an electron.

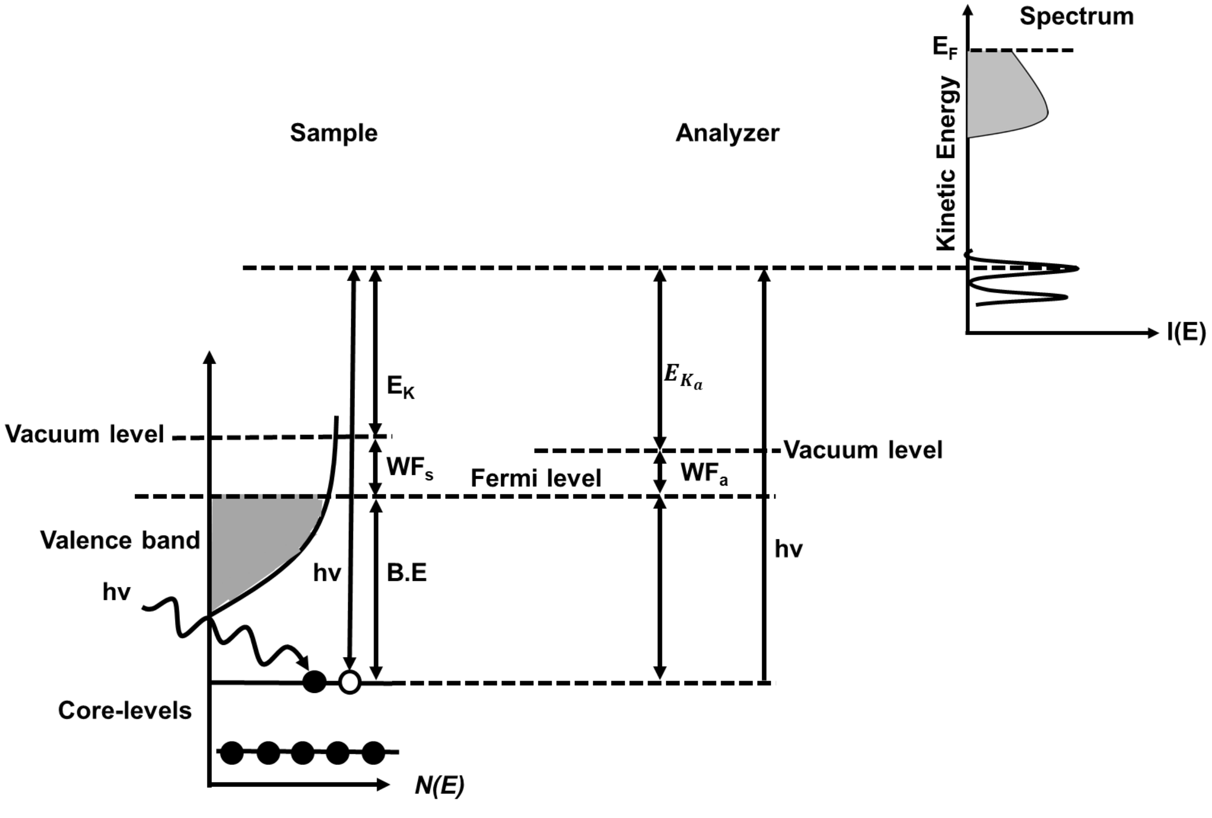

Figure 2.1. Measurement principle of photoelectron spectroscopy, left side shows electrons energy level structure of the sample, the analyzer in the middle and spectrum produced on the right adopted from Ref .[2]

When the energy of a photon hv is sufficient to eject the electron from the material, the kinetic energy of that electron (E_k) is related to the photon energy by the following relationship:

$$E_k = hv - B.E - WF_s \text{ ………………} (2.1)$$

Where B.E is the binding energy of the electron in the material referenced to the Fermi level, WF_s is the work function of the sample, which crossponds to the potential barrier between the Fermi level and vacuum level (VL). Hence B.E+WF_s is the minimum necessary photon energy to eject the electrons from the material. The remaining photon energy is used as kinetic energy for the electrons, which will be collected, gives intensity spectra as a function of kinetic energy. The measurements principle is summarized in Figure 2.1.[1] Different photon energy ranges are used to probe the different depth of the material. The obtained intensity in PES as a function of kinetic energy of photoelectrons is proportional to several factors as shown in the following equation:

$$I = Jp\sigma K\lambda \text{………………………………} (2.2)^2$$

Where J is the incident photon flux, p is the concentration of the element in probed area, σ is the effective cross-section of photoemitted electrons at a given photon energy, K is a factor that includes all instrumental and geometrical consideration of the spectrometer, and λ is the inelastic mean free path (IMFP) of electrons at corresponding kinetic energies. The effective cross-section of photoemitted electrons represents the probability per unit time and per unit area that the photon can excite an electron to a given state. The inelastic mean free path indicates the maximum depth at which an electron of a given kinetic energy can escape from the material. It thus allows an estimate of the depth at which the sample is probed.[2] The mean free path of electrons follows a universal curve, as shown in Figure 2.2, and is usually determined by electron-electron and electron-phonon collisions. At very low kinetic energies below 10 eV of electrons, electron-phonon collisions dominate and electron-electron interactions are weak, hence inelastic mean free path of electrons can be specific to a material as electron-phonons collision depends on the material's dielectric which is unique to each material. However, at kinetic energies higher than 10 eV electrons in solid can be approximately described by a free-electron gas because electron-electron interaction dominates instead of electron-phonon interaction, thus IMFP can be described as a function of electron density, which translates into the average distance between electrons (r_s) and is equivalent for all materials to a first approximation and is given by the following equation:[2]

$$\lambda^{-1} \simeq \sqrt{3}\,\frac{a_0 R}{E_{kin}} r_s^{3/2}\, ln\left[\left(\frac{4}{9\pi}\right)^{2/3} \frac{E_{kin}}{R} r_s^2\right] \ldots\ldots\ldots\ldots\ldots\ldots\ldots\ldots\ldots\ldots\ldots.(2.3)$$[2]

where a_0 = 0.529 Å is the Bohr radius, R = 13.6 eV is Rydberg constant, and E_{kin} is electron's kinetic energy. Since electron-electron interaction dominates for the region "B and C" in Figure 2.2, thus the value of IMFP varies slightly and is considered same at a given kinetic energy regardless of materials. The probing depth is predicted to be in the range of a few ångströms to a few nanometers between 20 eV and 1000 eV. Thus, photoelectron spectroscopy is an extremely efficient technique for studying surfaces and interfaces of materials. Detection of electrons with kinetic energies below 50 eV allows for probing the thickness of about 0.5 nm and hence considered highly sensitive to the surface, while kinetic energies of a few keV allow probing the buried interfaces. The theoretical aspect of photoelectron spectroscopy will be discussed next.

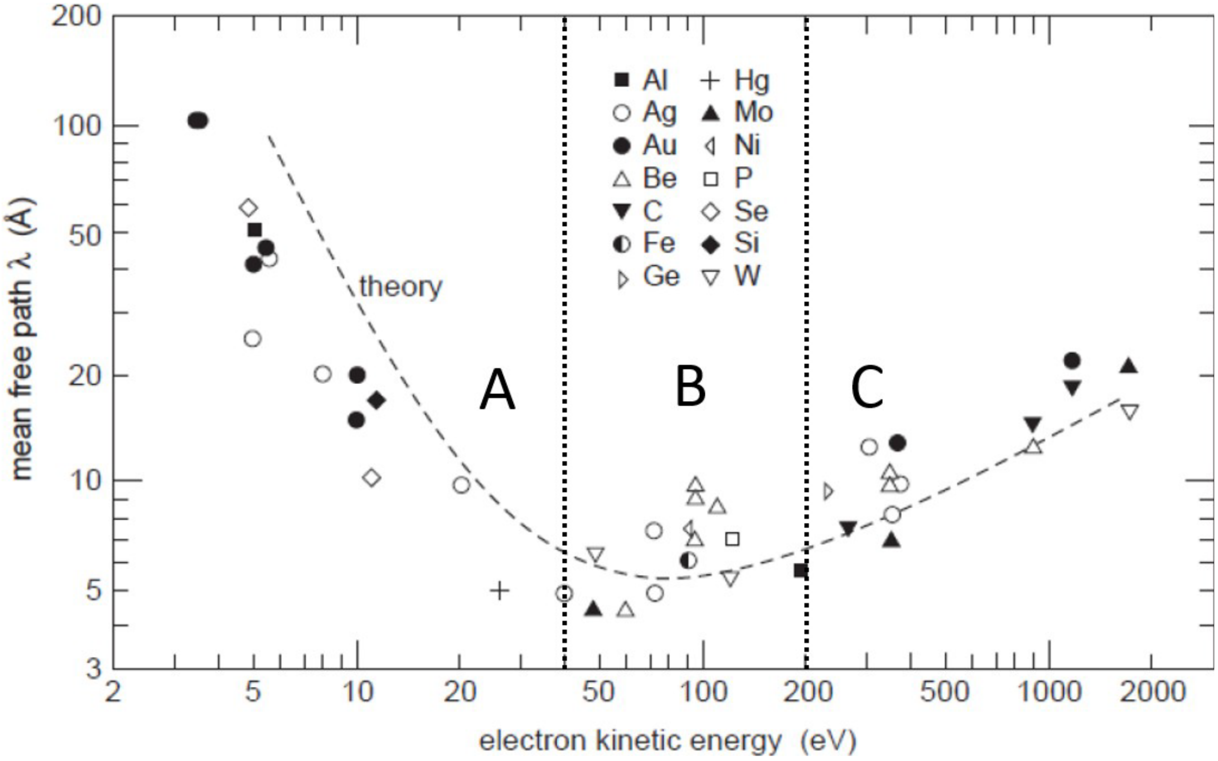

Figure 2.2. The universal curve of the inelastic mean free path of electrons in solids. Some values for different materials are shown as examples. The curve is divided into three parts which indicate the different regimes as a function of the kinetic energy of the electrons. Adapted from Ref.[3]

2.1.2 Theoretical aspect

The photocurrent measured in PES arises from the excitation of an electron in a system with N electrons being excited from an initial state i of wave function Ψ_i to a final state f of wave function Ψ_f upon by the absorption of a photon carrying the vector potential A. Figure 2.3 depicts the summary of the procedure.

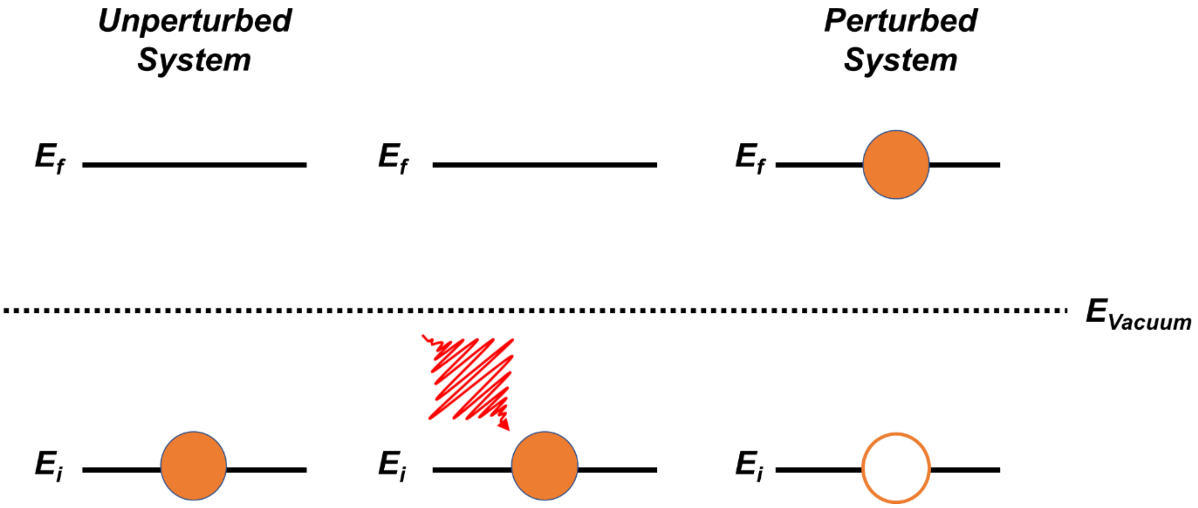

Figure 2.3. Illustration of the photoemission process in a system comprising N electrons, where the initial state on the left undergoes perturbation through the photon absorption, leading to its excitation into the final state on the right. The PES principle is centered around measuring the final state to understand the initial state. Both states are interconnected through perturbation.

The basic idea underlying photoemission is to measure the final state to understand the initial state. In this view, the transition probability (ω) per unit time from Ψ_i (initial state) to Ψ_f (final state) is related by Fermi's golden rule.[2]

$$\omega = \frac{2\pi}{\hbar}\left|\langle\psi_f|\Delta|\Psi_i\rangle\right|^2\delta\left(E_f - E_i - \hbar\nu\right)\ldots\ldots\ldots\ldots\ldots(2.4)$$

Where $\left|\langle\psi_f|\Delta|\Psi_i\rangle\right|$ represents the elements of transition matrix, and the Dirac function ensures the conservation of energy during the transition process with E_f and E_i being the energy of initial and final states, respectively, while $\hbar\nu$ representing the photon energy. The operator Δ is the electromagnetic perturbation caused by the absorption of a photon. Perturbation in the framework of dipole approximation (the simplifying assumption that the electromagnetic field is spatially constant but change temporally on the length scale of the atom due to much larger wavelength of the electromagnetic field compared to size of the atom) can be stated in the following relationship:

$$\Delta = A.p \ldots\ldots\ldots\ldots\ldots\ldots\ldots\ldots\ldots\ldots\ldots\ldots\ldots\ldots\ldots\ldots\ldots\ldots\ldots\ldots\ldots (2.5)$$

Here “A” represents the vector potential associated with electromagnetic field and “p” the electron momentum operator. Although this approach disregards the impacts of electron-electron interaction, it remains a reasonable method for materials with weak correlations (weak correlation refers to the situation where the interaction between electrons has relatively little influence on their behaviors). In this framework, it is considered that perturbation excites only one electron from “N” electrons system. Hence, considering the system under consideration has “N” electrons, the wave function of initial state can be written as the product of the orbital (ϕ_k) from which electron is excited and the wavefunction of the remaining electrons $\Psi^{k}{}_{i,R}(N-1)$:

$$\Psi_i(N) = C\phi_{i,k}\Psi^k_{i,R}(N-1) \ldots\ldots\ldots\ldots\ldots\ldots\ldots\ldots (2.6)$$

where “k” indicates that electron with quantum number k has been left out (because it was photoexcited) and “R” stands for remaining, and “C” is the operator that appropriately antisymmetrizes the wavefunction.

Similarly, the wave function of final state from which the ejected photoelectron has kinetic energy E_{kin}, can be written as:

$$\Psi_f(N) = C\phi_{f,E_{kin}}\Psi^k_{f,R}(N-1) \ldots\ldots\ldots\ldots\ldots\ldots\ldots\ldots (2.7)$$

Hence, the elements of transition matrix becomes the product of a one electron perturbation and N-1 electron as:

$$\langle\psi_f(N)|\Delta|\Psi_i(N)\rangle = \langle\phi_{f,E_{kin}}|\Delta|\phi_{i,k}\rangle\langle\Psi^k_{f,R}(N-1)|\Psi^k_{i,R}(N-1)\rangle \ldots\ldots\ldots\ldots (2.8)$$

It is assumed that (N-1) electrons remain unchanged by the perturbation (frozen orbital approximation), which implies that the ejection of photoexcited electron the remaining (N-1) electrons in the system does not experience any change in potential during the process. This approximation gives the Koopman binding energy ($E = -\varepsilon_k$), where ε_k is the energy of K orbital from which photoelectron is emitted. This approximation is sufficient to explain the main component (initial state effects) of photoemission spectra rather with limited accuracy since it does not consider the relaxation effect which occurs when an electron is ejected from an orbital, and the remaining N-1 charges attempt to reorganize themselves to minimize their energy. For example, in the case of ethyl trifluoroacetate also known as "ESCA molecule" as shown in Figure 2.4 (a), has different valence charge density on the carbon site, highest for CH_3 unit while gradually decreasing going from C−O, O−C=O to C−F_3 carbons. C 1s spectra shows four distinct peaks for C 1s of equal intensity due to difference in the chemical environment for each carbon atom and hence due to the difference in valence charge density. It costs more energy to create a core hole in the C atom in CF_3 than on that in the CH_3 unit because valence charge density is significantly reduced on C atoms in CF_3 due to fluorine's high electronegativity, resulting in poorer screening of the core hole left after photoionization. Hence, a chemical shift of 8 eV in the binding energy of C 1s atom had been noted in the presence of Fluorine ion compared to Hydrogen ion.[4]

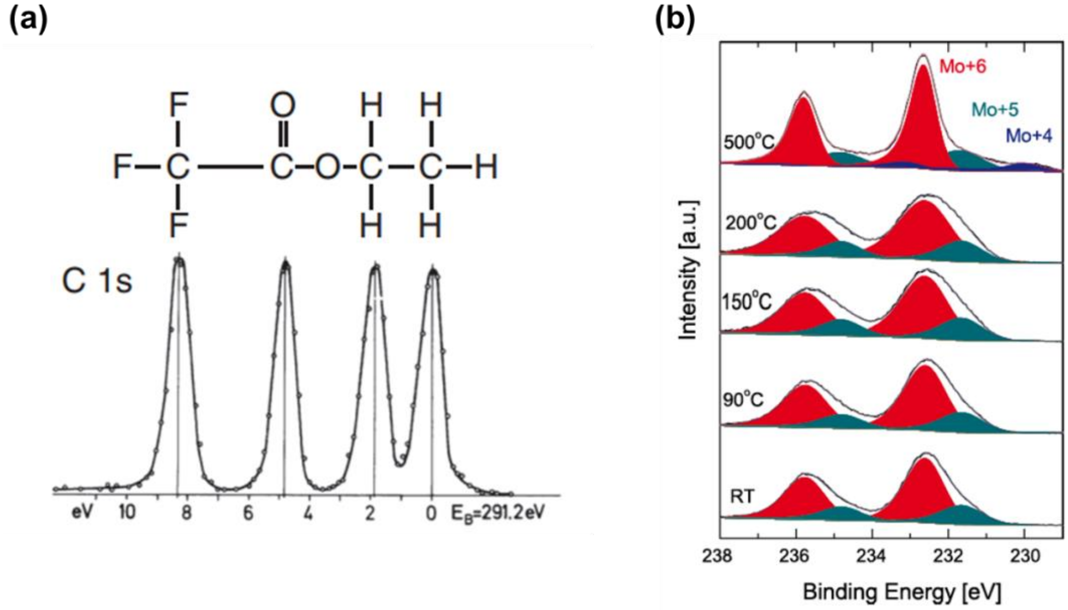

Figure 2.4. (a) Chemical structure of ethyl trifluoroacetate (top), and corresponding C 1s core-level spectrum (bottom), which shows the chemical shift induced by the difference of electronegativity that exist between different Carbon atoms in a molecule.[4] (b) Mo3d spectra of MoOx as a function of annealing temperature, where it is possible to observe shift in binding energy of Mo 3d component as function oxidation states of molybdenum.[5]

Such a chemical shift was evident only when the relaxation effects after the creation of core hole had been taken into account. This also means chemical shift is correlated with the chemical environment of the element. Similarly, the chemical shift can also be caused by different oxidation state of the atom, as demonstrated in Figure 2.4 (b), where distinct oxidation states of molybdenum can be identified in molybdenum oxide as a function of annealing temperature for molybdenum oxide.[5] Generally, it is noticed that binding energy of core levels decreases with electron density on the atom, meaning binding energy increases with oxidation state of the element as shown in Figure 2.4 (b).

Moreover, as previously stated, in addition to initial state effects, final state effects, which were ignored by Koopman's approximation, must be accounted as they are detected in PES spectra. Final state effects include spin-orbit interaction, shake-up, shake-off, and plasmons. After photoionization the unpaired electron's spin couples parallel or antiparallel to its orbital angular momentum vector, leaving the atom in two final energy states with different binding energy, which appears as peak doublet in PES spectrum.[2] A shake-up is the final state that appears when an outgoing photoelectron excites an electron from the valence band to a higher energy level. As a result, photoelectron loses its energy and give rise to a peak at higher binding energy in the spectra. If enough energy is provided this valence electron can also leave the atom, this is called shake-off and give rise to a peak at higher binding energy.[2] Another final state effect called plasmons is the collective density oscillation of electrons. When an electron moves out of the material interacting with the plasmon, it loses kinetic energy and gives rise to a peak at higher binding energy in the spectrum, also called plasmon loss feature. Therefore, the essence of the diverse information obtained from PES makes it a potent tool for elucidating the chemical and electronic characteristics of surfaces and interfaces.

2.1.3 Instrumentation

The typical instrument used in a PES experiment is shown in Figure 2.5. The illumination source consists of either an Aluminum source to produce a Alkα line having a photon energy of 1486.6 eV, alternatively Mg source can also use to make Mgkα lines having photon energy of 1253.6 eV, and a UV source producing UV light with a photon energy of 21.2 eV and 40.8 eV. Alternatively, a range of photon energies is accessible at synchrotrons to probe the desired depth of material. Usually, x-rays with low photon energies are used to probe the surface and high photo energies x-rays are used to probe the buried interfaces due to different inelastic mean free paths, as discussed before. These x-rays or UV rays are shining on the sample, causing the emission of photoelectrons that are dispersed in both angle and energy enter into the spectrometer before being collected at the detector. Different kinds of spectrometers are used, which includes hemispherical spectrometer and angle-resolved time-of-flight spectrometer, which will be discussed later in this chapter.

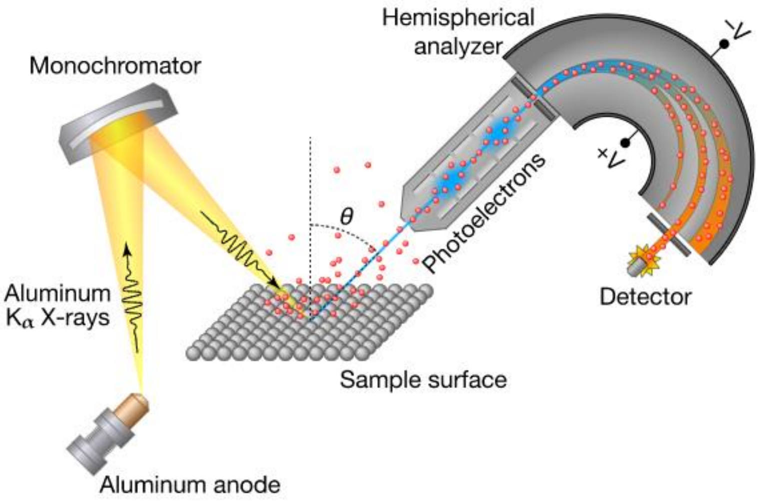

Figure 2.5. Shows the main instrument used in PES experiment. An Aluminum anode for producing Al κ∝ x-rays which are monochromatic and shine on the sample resulting in the emission of photoelectrons from sample following the principle of photoelectric effect, which are then scattered according to their kinetic energy and get collected at the detector located at the end of hemispherical spectrometer.[6]

Despite PES being hugely advantageous owing to its high surface sensitivity, it does have certain drawbacks, which are outlined below:

- Limited probing depth: probing depth is usually between 10 Å and 50 Å.
- Small probe area: between 0.2 to 1 mm^2 (sample measured under Synchrotron radiation).
- High vacuum: PES experiment is done in ultra-high vacuum of $\simeq 10^{-8}$ mbar.
- Conductive sample: PES can be performed only on conductive samples; non-conductive samples requires special treatment.

2.1.4 Data Analysis: line shape, intensity and energy

Upon the excitation of an electron, a core hole is generated. This ionized core state has a finite lifetime, meaning excited states decay through an Auger decay or fluorescence. According to Heisenberg uncertainty principle ($\Delta E \Delta t \leq \hbar/2$), a short-lived state (small Δt) will have a large uncertainty in finding the energy of that state, imposing a fundamental limit on the energy resolution that can be obtained:[7]

$$\Gamma\tau = \hbar \ldots\ldots\ldots\ldots\ldots\ldots\ldots\ldots\ldots\ldots\ldots\ldots\ldots\ldots\ldots\ldots\ldots\ldots\ldots\ldots\ldots\ldots\ldots\ldots\ldots\ldots (2.9)$$

Where Γ is the FHWM (full width at half maximum) of the core-level spectra, and τ is the core-hole lifetime, which can be represented by Lorentzian function. The core-hole lifetime is the limit of spectra resolution or in other words the width of a peak depends on the lifetime of the core hole. However, the total spectral resolution of the spectral line is much lower than the just core-hole lifetime because it contains several other contributions, such as experimental contribution (photon energy resolution and the spectrometer resolution), phonon broadening (excitation of lattice vibration), and disorder broadening (superposition of lines with different chemical shifts). All these contributions can be modelled with a Gaussian function. Hence the total line shape of the photoline is the convolution of both Lorentzian and Gaussian line profiles, which is known as the Voigt function. All these line shapes are shown in Figure 2.6 (a). In the case of metal, the photoemitted electrons can interact with electron-hole pairs formed in the metal, giving rise to asymmetric energy distribution, which appears as a tail towards lower kinetic energy in the photo line peak. This line shape is called Doniach and Sunjic line shape after its introduction in 1970 and shown in Figure 2.6 (b).[8]

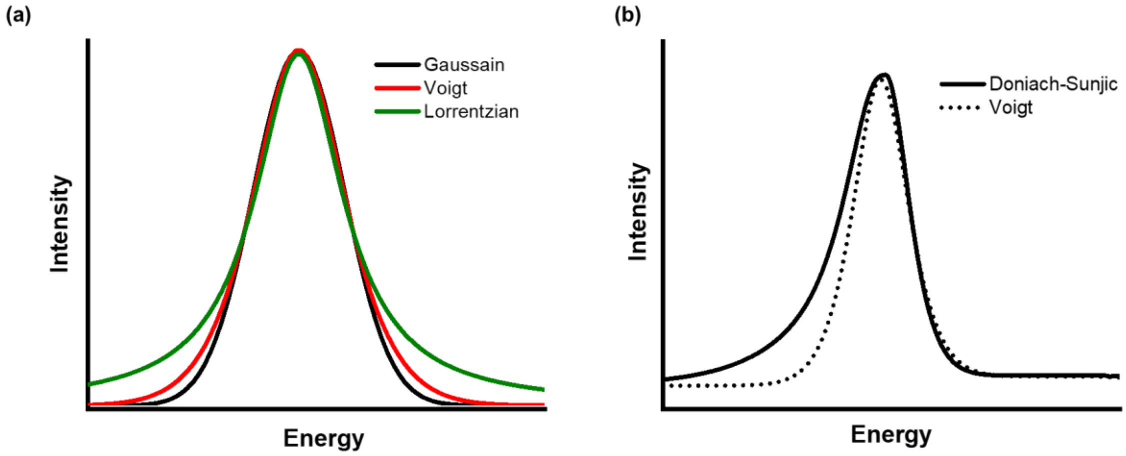

Figure 2.6. (a) Lorentzian Gaussian and Voigt line shapes with the same FWHM and (b) Voigt and asymmetric Doniach-Sunjic line shape with the same Lorentzian and Gaussian widths.

Moreover, during the photoelectron emission, there is also a possibility that these photoelectrons get scattered from the surrounding electron density, and in the case of inelastic scattering, they lose some of their energy. Hence, the electrons that lose energy in the scattering but still reach the detector contribute to the background of the peak. This background must be calculated and subtracted to fit a peak accurately. For this, Shirley suggested a background integral as:[9]

$$B_{S.i} = k_s \int_{E}^{+\infty} \Big((I(E') - B_{S,i-1}(E') \Big) dE' \ldots\ldots\ldots\ldots\ldots\ldots\ldots\ldots\ldots\ldots\ldots\ldots..\ldots(2.10)$$

Where, i is the iteration, k_s is a scattering factor giving rise to the step, the $(I(E')$ is the measured intensity at the energy E'. Shirley background shown in Figure 2.7. Additionally, many other types of background can also be used such as Tougaard background, polynomial background, Herrera-Gomez, and combination of them can also be used, for example linear-Shirley etc.

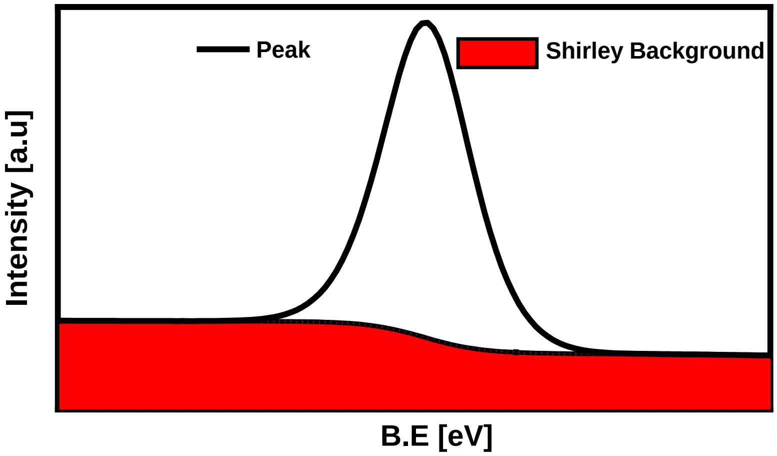

Figure 2.7. The shape of Shirley background.

2.1.5 Measurement of work function

Conceptually, a material work function (WF) can be calculated by varying the photon energy and determining the threshold photon energy (minimum energy required to emit an electron from an atom).[10] However, in photoemission (PES) measurements, only one source of photon energy is used and therefore another method is required.[11]

According to the photoelectric effect, the maximum kinetic energy of photoemitted electrons is given by:

$$E_k = hv - WF_m \ldots\ldots\ldots\ldots\ldots\ldots\ldots\ldots\ldots\ldots\ldots\ldots..\ldots(2.11)$$

Where $E_{k,max}$ is the maximum kinetic energy of electrons, hv is the photon energy, and WF_m is material's work function. This kinetic energy of photoemitted electrons from an energy-level with binding energy below Fermi-level can be written as:

$$E_k = hv - B.E - WF_m \ldots\ldots\ldots\ldots\ldots\ldots\ldots\ldots\ldots\ldots\ldots\ldots\ldots(2.12)$$

Here, $B.E$ is electron's binding energy referenced to the Fermi-level. In PES measurements, the sample makes electrical contact with the spectrometer, resulting in a contact potential differential $\Delta\phi = (WF_m - WF_s)$ due to the difference in local vacuum level between the sample and the spectrometer, where WF_s is the spectrometer's work function. By substituting the values of $\Delta\phi$ in equation (2.12)

$$E_k^{meas} = hv - B.E - WF_m + \Delta\phi = hv - B.E - WF_s \ldots\ldots\ldots\ldots\ldots\ldots\ldots(2.13)$$

From equation (2.13), it is clear that measured kinetic energy (E_K^{meas}) is independent of the sample work function but depends on the work function of spectrometer. Nevertheless, the work function of sample can be determined by correcting for the built-in potential $\Delta\phi$ (i,e., width of photoelectron spectrum).[10]

$$WF_m = hv - (E_{k,measu}^{max} - E_{k,measu}^{min}) \ldots\ldots\ldots\ldots\ldots\ldots\ldots\ldots\ldots(2.14)$$

Where $E_{k,measu}^{max}$ is the maximum kinetic energy of electrons emitted from Fermi level and detected by spectrometer, and $E_{k,measu}^{min}$ is the minimum kinetic energy of photoelectron spectrum (zero of kinetic energy scale relative to the sample) as shown in Figure 2.8.

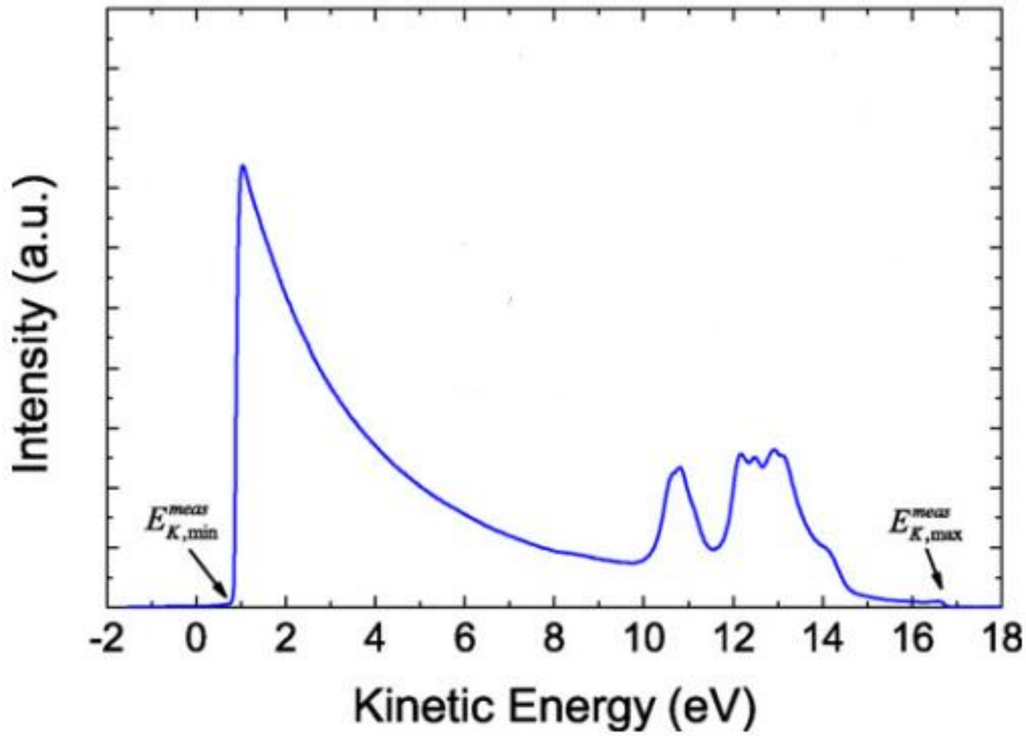

Figure 2.8. shows the intensity as a function of kinetic energy in which kinetic energy scale is corrected for the applied bias. The high intensity peak at low kinetic energy corresponds to the SEC region of the spectrum.[11]

The point of minimum kinetic energy in photoelectron spectrum $E_{k,measu}^{min}$ occurs in the region known as secondary electron cut-off (SEC) because the majority of the signal consists of low kinetic energy secondary electrons and the spectrum is abruptly "cut-off" in this region due to the local vacuum level. It means electrons with minimum kinetic energy are unable to reach the spectrometer. Hence a bias (V_{bias}) is needed to accelerate these electrons, which have zero kinetic energy, so that they can reach the detector. This applied bias is subtracted to calculate the work function by using equation 2.14.

The importance of work functions lies in the fact that it dictates the charge transport behavior in optoelectronic devices, as discussed in Chapter 1. Greiner et al.,[12] show that there is a direct relation between the cation oxidation state and work function in transition metal oxides. Reducing the oxidation state of cation in oxide leads to the decrease in work function which is attributed to the decrease in electron chemical potential upon the reduction of oxide (i,e., oxygen is removed) as depicted in Figure 2.9 (a). Furthermore, the role of oxygen vacancies in controlling the work function is highlighted in Figure 2.9 (b), and it has been described that increase in oxygen vacancies tend to decrease the work function of molybdenum oxide. To summarize, the estimate of work function of the materials is crucial as it governs the energy level alignment at the interface and defines the transport of charge carriers in the devices.

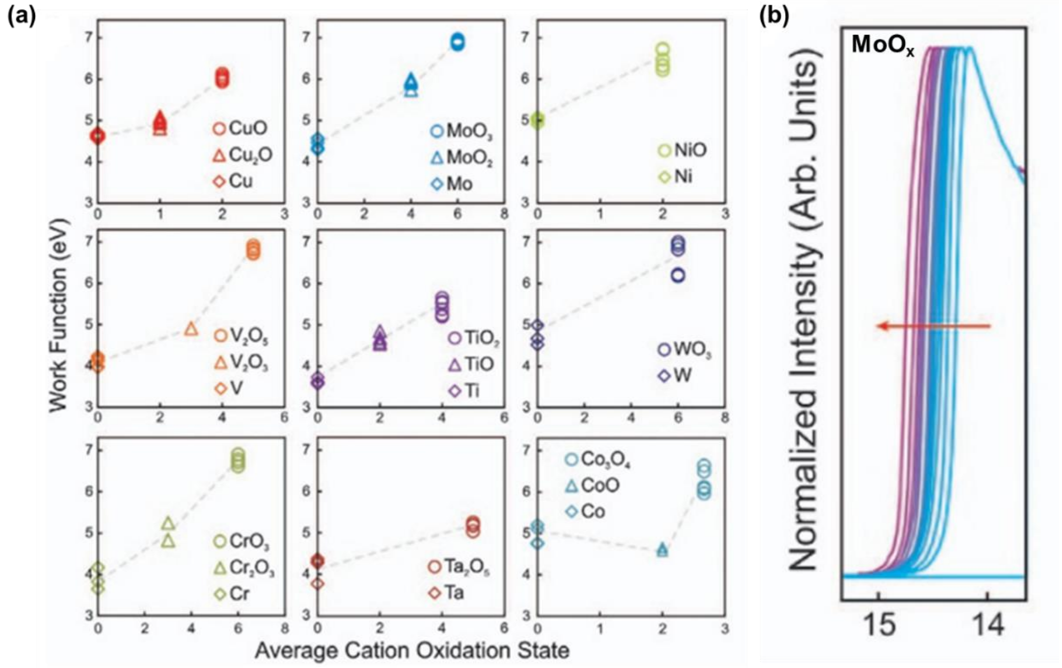

Figure 2.9. (a) plots of work function versus the average oxidation state of metal atom in transition metal oxides and metal oxides (b) secondary electron cut-off to calculate the work function of MoOx depending upon the oxygen vacancies.[12]

2.2 Experimental Setup

2.2.1 Synchrotron radiation

Different light sources are used in conducting photoemission spectroscopy (PES). Among them, synchrotron radiation is probably the more versatile due to the range of energies accessible and their high intensities with significantly greater resolution. The discovery of synchrotron radiation rests on the basic idea that when a charged particle is accelerated close to the speed of light, it emits radiation.[13] The process begins in the linear accelerator also known as (LINAC), where electrons emitted from the source (e.g., electron gun) are accelerated by using electric field and guided to the booster ring through an intense electromagnetic field. These electrons are then accelerated using radio-frequencies (RF) cavities near to the speed of light (99.99999% of light speed at 1 GeV) and transferred to transfer line from the booster ring in the form of bunches before being injected to storage rings, which are surrounded by bending magnets that keeps electrons in their defined trajectory.[14]

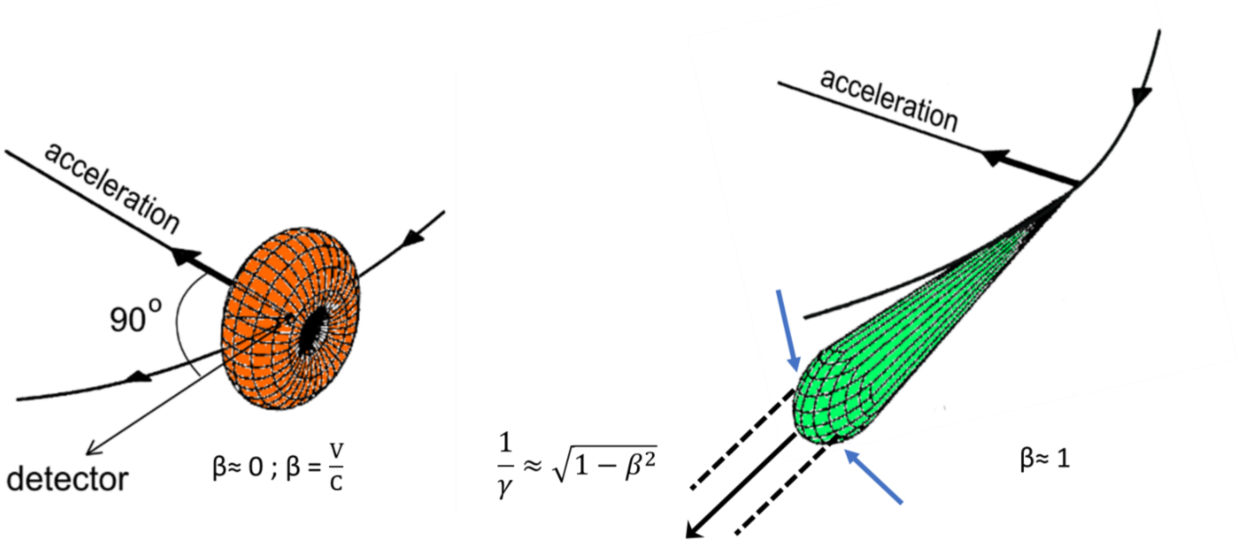

Figure 2.10. Characteristics of radiation emitted from an electron moving in a circular orbit at non-relativistic speed $\beta \approx 0$ at the (left) and at relativistic speed $\beta \approx 1$ at the right. At relativistic speed radiated energy folded in forward direction makes a narrow cone whereas at non-relativistic speed the distribution of energy is isotopic (in all direction) adopted from Ref.[14]

The bunches of electrons travelling near the speed of light in circular orbit inside the storage ring, which are kept at ultra-high vacuum (UHV) to avoid collisions between electrons and matter. When these relativistic electrons are subjected to a magnetic field generated from the bending magnet, they are accelerated and emit the radiation with energy ranging from infrared

(IR) to hard x-rays. Furthermore, since the electron velocity approaches the speed of light, the emitted radiation form a narrow emission cone as shown in Figure 2.10, the opening angle of the cone is $\theta = 1/2\gamma$ where γ is the relativistic factor $1/\sqrt{1-\beta^2}$.

This creates a brilliant and focused beam of x-rays. Insertion devices are placed into straight sections of the storage ring for generation of high brilliance (measure of photon flux and beam size; high brilliance indicates high intensity in a small area with a little divergence) radiation. A wiggler is one type of an insertion device, which consist of a few arrays of magnets that accelerate the electrons back and forth to increase the brilliance compared to bending magnet.[13,14] For even more highly brilliant radiation, undulator, an insertion device constituted by many arrays of magnets compared to few arrays in wiggler, is used. Since the electron beam passes through several periods of magnets, the total brilliance of emitted radiation is much higher than the bending magnet and wiggler. Additionally, sharp peaks in x-ray spectrum generated by undulator can be shifted by changing the separation between the magnets. The divergence and power of emitted radiation from bending magnet, wiggler and undulator are shown in Figure 2.11.

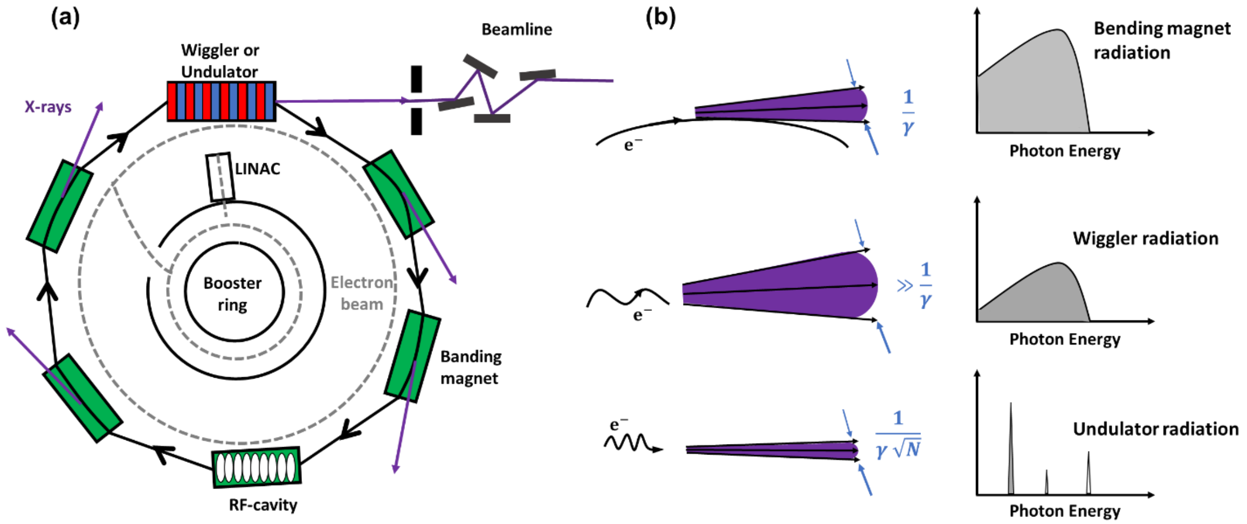

Figure 2.11. (a) Illustration of the main parts of the synchrotron, (b) Angular divergence and power structure of emitted radiation from bending magnet, wiggler and undulator.

The generated radiation passes from the storage ring to an experimental station via the beamline. The beamline is equipped with a monochromator to choose the energy of interest, and several mirrors to focus the beam on the sample. For the hard x-rays, crystals such as silicon monochromator are used while for the soft x-rays plane grating or spherical grating monochromator are used. The energy released progressively slows the electrons without being compensated for by accelerating them with a radio-frequency (RF) cavity.

The electrons in the synchrotron are grouped in the bunches and the structure of these bunches can be changed for certain purposes such as single bunch or multi-bunch pattern to perform different experiments. Single bunch mode is used in time-of-flight experiment.

The synchrotron where most of the experiments are performed is BESSY II, in Germany. The beamline used at BESSY II was Low dose/PM4, characterized by its the low flux ($1\times10^{7}-1\times10^{10}$ photons/sec). Low flux offers the opportunity to study the radiative sensitive sample, specially perovskite which otherwise degrade very quickly under x-rays. The other synchrotron where the experiment is performed is SOLEIL, in France. The beamline used to performed the experiment was TEMPO. The low dose/PM4 and TEMPO beamlines will be discussed later in this chapter.

2.2.2 The electron kinetic energy analyzer

An electron energy analyzer is used to measure the kinetic energy of photoemitted electrons from a sample. Two types that are used in our experiment will be discussed here, hemispherical electrostatic[16] and angle-resolving time-of-flight spectrometers.[17] The principle that describes them will be discussed briefly in the following.

(a) The hemispherical analyzer

The hemispherical analyzer consist of two concentric hemispherical electrodes between which an static electric field has been applied as shown in Figure 2.12 (a).[2] The photoemitted electrons from the sample pass through the lens system, which focuses these electrons on the entrance slit while conserving their angular information and applying a potential to decelerate them. The electrons that pass through the entrance slit are deflected in an electric field applied between the two hemispheres. The electrons with higher kinetic energy than the pass energy will be scattered towards the outer sphere and those with lower energies to the inner sphere. In this way, only those electrons who have a specific kinetic energy also known as pass energy (E_{pass}) are allowed to pass through by following circular orbit between the hemispheres and reach the detector, this is one way of defining the energy resolution $\Delta E/E_{pass}$.[18] A multichannel detector on the one side of the hemispherical analyzer counts the electrons that strike it and records their spatial position, which varies depending upon how close to the pass energy of electron kinetic energy is.

The resolution of spectrometer can be calculated as:

$$\Delta E = E_p \frac{S}{2R_0} \quad \text{...............................} (2.15)$$

Where S is the width of the spectrometer entrance slit and R_0 is the radius of hemisphere.

(b) The ArTOF

Another way of measuring the kinetic energy of electrons is by using a time-of-flight spectrometer and angle-resolved time-of-flight (ArTOF) is its one type as shown in Figure 2.12 (b). Instead of using orbit of an electron through an electric field to determine the kinetic energy in hemispherical analyzer, time of arrival of electron, the position of electron and length of the flight path are used to determine the kinetic energy of electron by using time-and position-sensitive detector with combination of advanced lens system in ArTOF analyzer.[19] This allows the accurate determination of the kinetic energies of electrons from a wide emission cone (±15 degree or even more), consequently, making transmission efficiency of ArTOF significantly higher of about two to three order of magnitude higher than the conventional hemisphere. The drawback is that determining kinetic energies of electrons becomes less accurate for shorter flight time (i.e., higher kinetic energies) and therefore resolution decreases for higher kinetic energies. Also, since only one electron can be in the flight in the tube, the ArTOF analyzer requires a pulse x-ray source and a known take-off time.

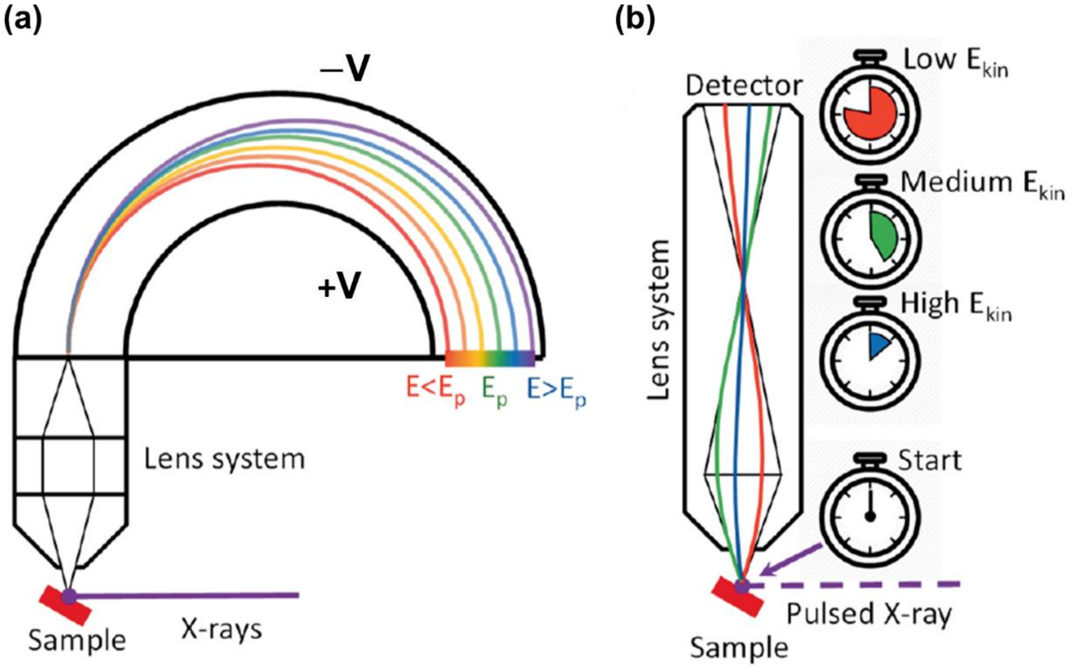

Figure 2.12. The design and function of (a) hemispherical analyzer and (b) ArTOF spectrometer adopted from Ref.[20]

2.2.3 Experimental Stations

The experiments described in this thesis were conducted at synchrotron radiation facilities and various experimental end-stations. In the following characteristics of each of the end-stations used will be discussed.

(a) Low-dose photoelectron spectroscopy at BESSY

The low-dose photoelectron spectroscopy end-station is soft x-ray bending magnets beamline located at PM4 of the synchrotron BESSY II having the unique capabilities to characterize the radiation sensitive sample. The end-station is equipped with an ArTOF electron analyzer, as described in previous section requires a pulse photon source.[19] As BESSY II normally operates in so-called hybrid mode, a pseudo single bunch (a camshafts pulse) can be isolated from the multi-bunch train by using a mechanical chopper installed at the beamline. Hence, the combination of being bending magnets beamline and using a pseudo single bunch offers the very low photon flux (1×10^9–1×10^{10} photons/sec) and making the possibility to study the samples which are sensitive to x-ray radiation, such as perovskite and organic materials. Despite the modest photon flux, measurements are nevertheless efficient due to the high transmission efficiency of the ArTOF spectrometer as discussed in previous section. Furthermore, a synchronized laser system installed at the beamline allows to study the charge transfer dynamics starting from the picoseconds scale. Alternatively, a laser with a fundamental wavelength of 1030 nm that can be used at its second harmonic 515 nm and third harmonic 343 nm to study the effects of infrared, visible, and UV illumination respectively on the materials to isolate these illumination effects from the x-ray illumination. Taking the advantage of this, in this thesis we studied the effects of infrared (1030 nm) and UV (343 nm) illumination effects on the $CsPbBr_3$ perovskite nanocrystals deposited on different substrates, which will be discussed later in the following chapters.

(b) TEMPO end-station at SOLEIL

The TEMPO (Time Resolved Experiments on Materials with Photoelectron spectroscopy) is soft x-ray beamline optimized for dynamic studies of electronic and magnetic properties of materials using photoelectron spectroscopy.[21] The nature of a material's surface and the properties at the interface can be studied precisely due to high x-ray flux coupled to high energy resolution of the electron energy analyzer and the beamline. The accessible photon energy range is between 50 eV to 1500 eV, and the beamline is equipped with a VG Scientia spectrometer with a delay line 2D detector. Also, pump probe experiments can be performed with two photons (laser + synchrotron radiation) to study the excited state in the temporal range of picoseconds to milliseconds and the phenomena of time-resolved (TR) Surface Photovoltage (SPV) can be explored in semiconductors. Laser is used to generate charge carriers and synchrotron radiation is used to probe the core levels which shifts in binding energies depending upon the type of semiconductors. A shift of core levels toward higher binding energy under the laser is the characteristics of N-type of semiconductors whereas the shift towards lower binding energy is characteristics of P-type of semiconductors, as shown in Figure 2.13.[22]

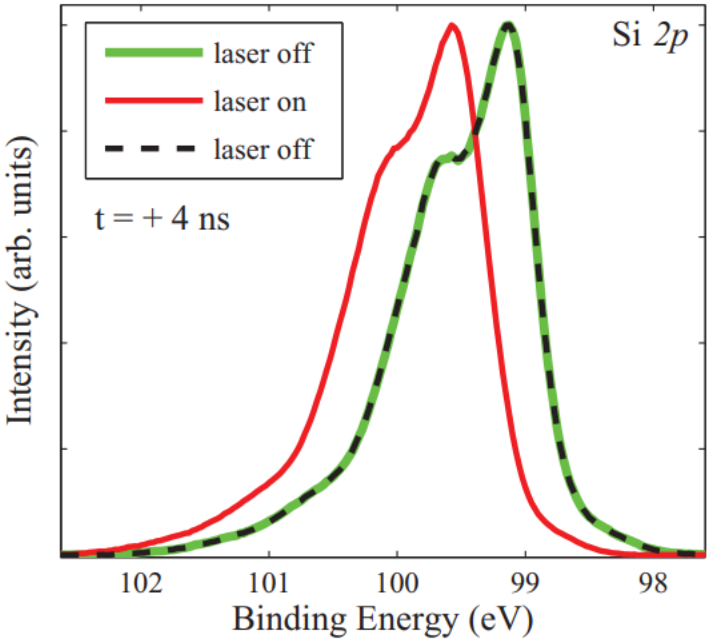

Figure 2.13. The Si 2p spectrum of the silicon measured with photon energy 140 eV at a pump-probe delay time of 4 ns. The spectrum is shifted towards higher binding energy under the laser (800 nm), suggesting silicon's N-type semiconducting properties.[22]

Moreover, following the laser, the charge recombination dynamics provide the information about the possible trap states in the materials and the diffusion of majority carriers from the bulk to surface of the material. Thus, the time-resolved SPV technique provides detailed quantitative information on the bulk properties (type of semiconductor, conductivity, lifetime, and the presence of defects) of a semiconductor material which can be used to construct the surface and interface band diagram, which can aid in understanding the properties at the surface and interface that dictates the charge transport and extraction in optoelectronic devices.[23]

However, since the x-ray flux at TEMPO beamline is very high (4×10^{13} photons/sec), to study the phenomena of time-resolved Surface Photovoltage in perovskite was inaccessible as intense x-rays instantly damaged the $CsPbBr_3$ perovskite nanocrystals (NCs), which will be explained in more details in next chapter.

2.3 Complementary techniques

The following techniques were utilized to determine if any batch-to-batch changes of synthesized CsPbBr3 perovskite nanocrystals (NCs) existed.

2.3.1 UV-vis Absorption Spectroscopy

The Ultraviolet-visible (UV-vis) absorption spectroscopy is a quantitative technique which is used to measure the concentration of absorbing specie in a material, typically, in the range of 200 nm to 800 nm. This is done by measuring the intensity of light that transmitted through a sample with respect to the incident light. When the light is shining on the sample, some of the light will be absorbed by the sample and the remaining with the lower intensity will be transmitted and measured at the detector.

The UV-vis absorption spectroscopy works on the principle of Lambert-Beer:

$$A(\lambda) = log_{10}\left(\frac{I_0}{I}\right) = \varepsilon cl \text{……………………….………(2.16)}$$

Where $A(\lambda)$ is the measured absorbance, I_0 is the intensity of incoming light at the corresponding wavelength (λ), and I is the intensity of transmitted light. ε is the molar absorption coefficient, c is the concentration of the solution while l is optical path length.

This technique measure the absorption spectra of a material both in solution and in solid form. Moreover, it can be used to measure the optical bandgap of different materials, such as NCs colloidal solution or a NCs thin film deposited on a transparent substrate. This optical bandgap can be calculated from the exciton peak in absorption spectra by using the equation:

$$E_{gap} = \frac{h\times C}{\lambda} \text{ …………………………………...……(2.17)}$$

Where E_{gap} is optical bandgap, h = Planks constant, C = speed of light and λ = cut off wavelength.

2.3.2 X-ray Diffraction

X-ray diffraction (XRD) is an analytical technique used to measure the crystal structure of material. It is different from the photoelectron spectroscopy (PES) as instead of photoelectrons measurement, it measures the diffracted x-rays by the sample. Since it measures the diffracted x-rays instead of electrons, the probing depth is in the range of micrometer making it a bulk sensitive technique. XRD works on the basis of changing the angle between the incident x-rays and sample while measuring the angle of scattered x-ray scattered by the sample. X-rays are scattered by electrons density of the atoms in a material, and these diffracted x-rays interfere destructively in most of the angles but at some angles they will interfere constructively. Constructive interference occur only when condition for the Bragg's law (equation 2.17) is satisfied, which means that path difference for x-rays, with wavelength λ, diffracted from two adjacent layers is nλ/2 where n is the order of reflection.[24] Bragg's law is given by:

$$2\mathrm{d}\ sin\theta = n\lambda \ldots\ldots\ldots\ldots\ldots\ldots\ldots\ldots\ldots\ldots (2.17)$$

Where d is the distance between crystals planes in a material, θ is the angle between incident and diffracted x-rays, and λ is the wavelength of incoming x-rays. Hence, XRD can be used to determine the interplanar distances in a material and thus its lattice parameters and from this the structure of a material.[25] In case of small crystalline particles such as NCs, this technique can also be used to determine their size using the Scherrer formula:

$$\mathrm{d} = \frac{K\lambda}{\beta cos\theta} \ldots\ldots\ldots\ldots\ldots\ldots\ldots\ldots\ldots\ldots (2.18)$$

where d is the average size of the particle size in nm, K is the Scherrer constant which depends on the crystal symmetry, λ is the incident x-ray wavelength, β is the FWHM of the XRD peak, and θ is the angle XRD peak position.

XRD is a valuable technique for measuring the bulk of a material but it poses challenges for the thin film samples due to the large mean free path in the range of micrometers of the hard x-rays used in XRD measurements. Thus, grazing incidence x-ray diffraction (GI-XRD) with a small incident angle which gives the probing depth in nanometers range, can be used to measure XRD for thin-film samples. For GI-XRD, the incidence angle remains fixed, and the exit angle is measured. The difference between diffraction geometry of XRD and grazing incidence XRD is shown in Figure 2.14 (a) and (b).

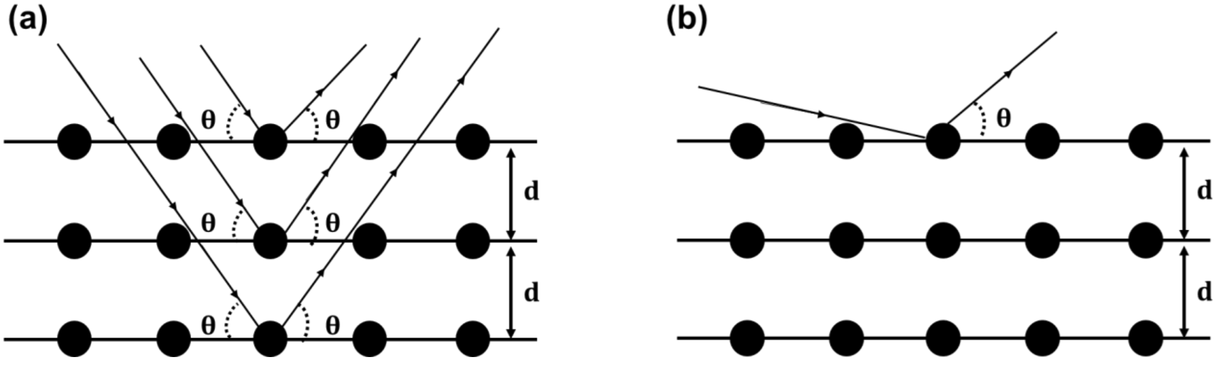

Figure 2.14. (a) The diffraction geometry in x-ray diffraction (b) the diffraction geometry for the grazing incidence x-ray diffraction.

References

1. Schulz, Philip, David Cahen, and Antoine Kahn. "Halide perovskites: is it all about the interfaces?" Chemical reviews 119.5 (2019): 3349-3417.
2. S. Hüfner, Photoelectron Spectroscopy: Principles and Applications, 3rd ed. Berlin Heidelberg: Springer-Verlag, doi2003.: 10.1007/978-3-662-09280-4.
3. Shokr, Yasser. Interaction Mechanisms and Magnetization Dynamics in Ultrathin Antiferromagnetic Films and their Correlation with Structure and Morphology. Diss. 2016.
4. Greczynski, Grzegorz, and Lars Hultman. "X-ray photoelectron spectroscopy: towards reliable binding energy referencing." Progress in Materials Science 107 (2020): 100591.
5. F. Cauduro, André L., et al. "Crystalline molybdenum oxide thin-films for application as interfacial layers in optoelectronic devices." ACS Applied Materials & Interfaces 9.8 (2017): 7717-7724.

6. https://grimmgroup.net/research/xps/background/.
7. Johansson, Fredrik. Core-hole clock spectroscopy using hard x-rays: exciting states in condensed matter. Diss. Acta Universitatis Upsaliensis, 2020.
8. Gadzuk, John William, and M. Šunjić. "Excitation energy dependence of core-level x-ray-photoemission-spectra line shapes in metals." Physical Review B 12.2 (1975): 524.
9. Végh, János. "The Shirley background revised." Journal of electron spectroscopy and related phenomena 151.3 (2006): 159-164.
10. Herring, Conyers, and M. H. Nichols. "Thermionic emission." Reviews of modern physics 21.2 (1949): 185.
11. Helander, M. G., et al. "Pitfalls in measuring work function using photoelectron spectroscopy." Applied Surface Science 256.8 (2010): 2602-2605.
12. Greiner, Mark T., et al. "Transition metal oxide work functions: the influence of cation oxidation state and oxygen vacancies." Advanced Functional Materials 22.21 (2012): 4557-4568.
13. Elder, FoRo, R. V. Langmuir, and H. C. Pollock. "Radiation from electrons accelerated in a synchrotron." Physical Review 74.1 (1948): 52.
14. Rubensson, Jan-Erik. Synchrotron Radiation: An everyday application of special relativity. Morgan & Claypool Publishers, 2016.
15. Bharti, Amardeep, and Navdeep Goyal. "Fundamental of synchrotron radiations." Synchrotron Radiation-Useful and Interesting Applications. IntechOpen, 2019.
16. Mårtensson, N., et al. "A very high-resolution electron spectrometer." Journal of Electron Spectroscopy and Related Phenomena 70.2 (1994): 117-128.
17. Öhrwall, Gunnar, et al. "A new energy and angle resolving electron spectrometer–First results." Journal of Electron Spectroscopy and Related Phenomena 183.1-3 (2011): 125-131.
18. Roy, D., and D. Tremblay. "Design of electron spectrometers." Reports on Progress in Physics 53.12 (1990): 1621.
19. Ovsyannikov, Ruslan, et al. "Principles and operation of a new type of electron spectrometer–ArTOF." Journal of Electron Spectroscopy and Related Phenomena 191 (2013): 92-103.
20. Svanström, Sebastian. The life and death of perovskites: Interfacial function and degradation of lead halide perovskites studied by photoelectron spectroscopy. Diss. Acta Universitatis Upsaliensis, 2021.
21. Bergeard, N., et al. "Time-resolved photoelectron spectroscopy using synchrotron radiation time structure." Journal of synchrotron radiation 18.2 (2011): 245-250.
22. Spencer, Ben F., et al. "Time-resolved surface photovoltage measurements at n-type photovoltaic surfaces: Si (111) and ZnO (10 1 0)." Physical Review B 88.19 (2013): 195301.
23. Livache, Clément, et al. "Charge dynamics and optolectronic properties in HgTe colloidal quantum wells." Nano Letters 17.7 (2017): 4067-4074.

24. Bragg, William Henry. "IX. Bakerian Lecture.—X-rays and crystal structure." Philosophical Transactions of the Royal Society of London. Series A, Containing Papers of a Mathematical or Physical Character 215.523-537 (1915): 253-274.
25. Ameh, E. S. "A review of basic crystallography and x-ray diffraction applications." The international journal of advanced manufacturing technology 105 (2019): 3289-3302.

CHAPTER 3: Radiation Stability of $CsPbBr_3$ Perovskite Nanocrystals at Gold Interface

This chapter introduces halide perovskite nanocrystals (HaPNCs), including their history, structure, phase and radiation stability, intriguing optoelectronic characteristics, and synthesis. In the second part of the chapter, the investigation of the stability of $CsPbBr_3$ HaPNCs at the interface with gold (Au) under, infrared (IR), ultraviolet (UV) and x-rays irradiation by photoelectron spectroscopy will be discussed. Additionally, a comparison of $CsPbBr_3$ HaPNCs stability under two types of illumination (UV and x-rays) will be discussed and a comprehensive picture of degradation mechanism will be given. Finally, these findings will be summarized with a conclusion.

3.1 Halide Perovskite Nanocrystals

Halide perovskite materials have the potential to revolutionize the field of optoelectronics, including photovoltaics, photonics, and other related technologies, due to its outstanding optical and electronic properties, making it one of the most exciting materials of the 21st century. Perovskite-based nano crystals garnered tremendous research interest due to their outstanding semiconducting properties, making them potentially useful in a wide range of applications. These nanocrystals have high photoluminescence quantum yield, tunable emission wavelength, and ease of synthesis and processing, making them ideal for different optoelectronic devices such as light-emitting diodes, solar cells, and lasers etc.[1] Moreover, halide perovskite nanocrystals (HaPNCs) have several advantages compared to their bulk counterpart, including control over the size and shape of crystals, high surface area-to-volume ratio, tunable optical properties and enhanced stability.[1,2] By changing the size of HaPNCs, wide emission colors covering ultraviolet to near-infrared have been obtained, covering many industrial needs. HaPNCs' high surface area-to-volume ratio increases the number of surface atoms that can interact with the surrounding, enhancing performance in sensing and catalysis applications.[2] The optical properties of HaPNCs are tunable by changing the chemical composition and size of crystals, allowing the opportunity to produce a broad range of colors to emit (light-emitting devices) and absorb (solar cells), making them highly desirable for these devices.[3] The attachment of ligands to HaPNCs at the surface of crystals makes them stable against harsh environmental conditions.[1] High carrier mobility, long carrier lifetimes, long diffusion length and small effective carrier masses of HaPNCs make them practical for improving charges transport properties in the devices.[4] Moreover, like bulk perovskite, nanocrystals can also be employed as an active layer in solar cells.

The synthesis of halide perovskite nanocrystals (HaPNCs) for the first time was reported in 2015,[5] and owing to their excellent structural stability at room temperature motivated their rapid integration into solar cells. Highly efficient HaPNCs quickly surpassed the efficiency of PbS-based nanocrystals. The best efficient solar cell based on HaPNCs reached 16.6% [6] and approached their counter bulk part, which has a certified efficiency of 25.5 %.[7] Undoubtedly, HaPNCs are highly advantageous due to their remarkable opto-electronic properties, as outlined above, but the most among them is the higher structural stability of nanocrystals. However, the stability of HaPNCs under light and environment remains poor.[1] Hence, the stability of HaPNCs under light needs to be investigated further, as well as their interfacial energetics with electrode and/or different charge transport layers, in order to fully optimize the HaPNCs-based devices and harness their full potential in optoelectronic applications. Hence, this chapter will begin by discussing the general characteristics of perovskite material, followed by properties related to HaPNCs, and finally, the stability of HaPNCs under radiation (IR, UV and x-ray), starting from a model system of gold (Au) substrate.

3.1.1 History and development

In the late 19th century, "H.L. Wells" conducted the initial research work on halide perovskite, while comprehensive structural characterization was done by "D. Weber D" in the 20th century.[2] In 1958, the existence of photoconductivity in $CsPbX_3$ halide perovskite was reported.[1,8] Meanwhile, the ionic conductivity in $CsPbX_3$ which is currently known as a primary reason for the instability of the halide perovskite-based devices was discovered in 1980.[9] The potential application of halide perovskite in optical and electronic devices was reported in the late 1990s and early 2000s, long before appealing broad scientific community.[10,11] However, in 2009, Kojima et al.[12] demonstrated halide perovskite as an active material in a solar cell with an efficiency of around 3 %, but the device died within minutes. It took another three years to fully grasp the potential of perovskite in the solar cell when in 2012,[13] a perovskite-based solar cells with an efficiency of 10% were reported. Since then, halide perovskite has attracted the global attention of the community, and a substantial increase in research output in terms of improving the efficiency and understanding of the basic material characteristics has been made. Recently, the halide perovskite-based solar cells with a certified efficiency of 25.5% [7] are reported which surpasses the efficiency of already commercialized silicon photovoltaics, making the perovskite a strong candidate for next-generation photovoltaics. The history of halide perovskite nanocrystals may be traced back to the development of nanocrystal forms of conventional semiconductors such as (CdSe, CdTe, PbSe, and similar).[14] The first synthesis of $CsPbX_3$ based halide perovskite nanocrystals (HaPNCs) in 2015 [5] pave the way for these nanocrystals integration in solar cells. The first successful attempt has been made of $CsPbI_3$ based HaPNCs with an efficiency of 10.80 %.[15] Till now, $Cs_{0.25}FA_{0.75}PbI_3$ and $CsPbI_3$ based HaPNCs solar cells have attained an efficiency of 17.4%,[15] which is getting close to the halide thin film perovskite based solar cells. These high efficiency of HaPNCs based solar cells are attributed to the excellent opto-electronic properties of the nanocrystals as stated above such as, high absorption coefficient, small exciton binding energy, multiple exciton generation, high photoluminescence quantum yield (PLQY) etc., which will be discussed later in more detail in the section of “optoelectronic properties” of HaPNCs.

3.1.2 Perovskite structure

Halide perovskites have the perovskite crystal structure with corresponding ABX_3 stoichiometry, where A is a monovalent cation, B is a divalent cation, and X is a monovalent halide anion. A site is occupied by either inorganic Cesium (Cs) cation, or organic Formamidinium [$HC(NH_2)_2^+$ abbreviated as (FA)] cation and Methylammonium [$CH_3NH_3^+$ abbreviated as (MA)] cation, B site is occupied by mainly by lead (Pb)$^+$ divalent cation otherwise tin (Sn)$^+$ divalent cation, and X site is occupied by halide anion such as fluoride (F)$^-$, chloride (Cl)$^-$ and bromide Br$^-$.[16]

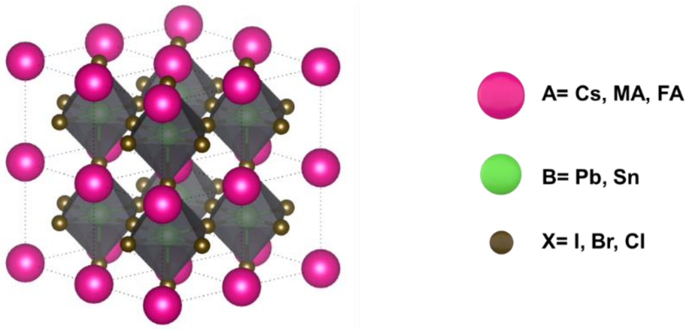

Figure 3.1. ABX_3 perovskite crystal structure.

In this structure, each B atom is surrounded by six halide atoms forming an octahedra. The corners of the these octahedra are connected to "A" atoms forming a framework as shown in Figure 3.1. The stability of this perovskite structure is determined by the choice of ions and the interaction between them. The strength of perovskite structure is predicted by an empirical index called Goldschmidt tolerance factor (t), which is based on the ionic radius of the atoms in perovskite crystal structure and is calculated using the following expression:[17]

$$t = \frac{r_A + r_X}{\sqrt{2}(r_B + r_X)}$$

Where r_A is the radius of A cation, r_B is the radius of B cation, and r_X is the radius of X anion. A "t" value between 0.8 and 1.0 is considered favorable for cubic perovskite structure, also known as the α-phase of perovskite, which has good photovoltaic properties. When "t" is large than 1.0 or smaller than 0.8, a hexagonal and orthorhombic structure respectively formed, which are non-perovskite structures and known as δ-phase.[18,19] It is important to mention here that estimating the absolute tolerance factor for hybrid (organic-inorganic) perovskite is difficult due to the non-spherical geometry of the organic cation and its continual rotation in the lattice.[20] Moreover, it is reported that perovskite materials can exist in more than one crystal structure with the same chemical composition, depending on the temperature and preparation methods used during synthesis.[21] Additionally, with changing environmental conditions, perovskite structure can go from one phase to another, for example, α-phase to δ-phase, a process known as phase transition, which will explained further below.

3.1.3 Phase transition and nanocrystals

The soft ionic nature of the bonding in lead halide perovskite compared to the highly covalent lattice of other semiconductors such as metal chalcogenides, makes them more prone to phase transition from photoactive (α-phase) to non-photoactive (δ-phase) under external stimuli such as temperature, moisture and light. For example, in the case of inorganic halide perovskite of $CsPbI_3$, which is considered intrinsically more stable due to Cs^+ being inorganic compared to its hybrids ($FAPbI_3$ and $MAPbI_3$) counterpart, is found less stable due to its relatively low tolerance factor value of $t < 0.8$.[22] As shown in Figure 3.2 that not only the formation of $CsPbI_3$ photoactive α-phase occurs at very high temperature, but more importantly, this structure is stable only at the temperature ranging from 300-360 °C. With decreasing temperature from 360 °C to room temperature photoactive (with good photovoltaic properties) α-black phase of perovskite undergoes to other phases such as β- and γ- black phases finally into the non-photoactive δ-yellow phase of CsPbI$_3$.

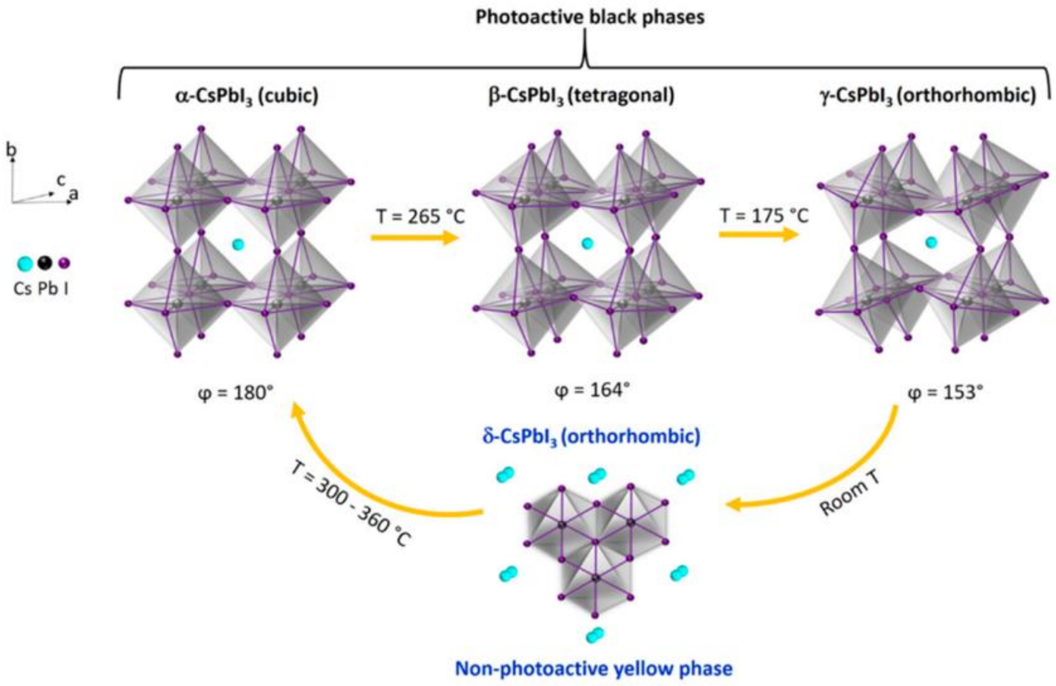

Figure 3.2. Crystalline structure and phase transition of CsPbI$_3$ from the nonperovskite (non-photoactive) δ-yellow phase to black photoactive α-phase at high temperature, and distortion into $[\mathrm{PbI}_6]^{4-}$ octahedra promote the formation of β- and γ- phase after temperature is decreased.[22]

Different strategies have been developed and proposed to mitigate this black-to-yellow phase transition of CsPbI$_3$, such as (i) changing the composition from CsPbI$_3$ to CsPbIBr$_2$ by adding Br$^-$ which reduced the phase transition temperature up to 100 °C.[23] However, alloying with Br$^-$ leads to an undesired increase in bandgap resulting in reduced near-infrared absorption. (ii) The addition of external additives also effectively stabilize the α-phase of CsPbI$_3$.[24] Yet the most efficient among all is (iii) the synthesis of low dimensional perovskite materials, like nanocrystals. The greater surface/volume ratio in halide perovskite nanocrystals (HaPNCs) was founded pertinent factor in stabilizing the α-phase of CsPbI$_3$ compared to their bulk counterpart at room temperature.[25] Swarnkar et al. shows that large surface energy contribution in CsPbI$_3$ halide perovskite nanocrystals (NCs) stabilizes the α-phase at room temperature compared to bulk CsPbI$_3$, which is unstable and exist in non-perovskite δ-yellow phase at room temperature.[26] As shown in Figure 3.3, CsPbI$_3$ NCs remain stable even after two months of storage in ambient condition and preserve the cubic structure. Although converting bulk perovskite materials into nanocrystals can increase their phase stability, it may not necessarily keep them resilient against the radiation such as UV and x-rays light. However, before investigating the radiation impacts on halide perovskite nanocrystals, the radiation tolerance of bulk perovskite will be described in the following.

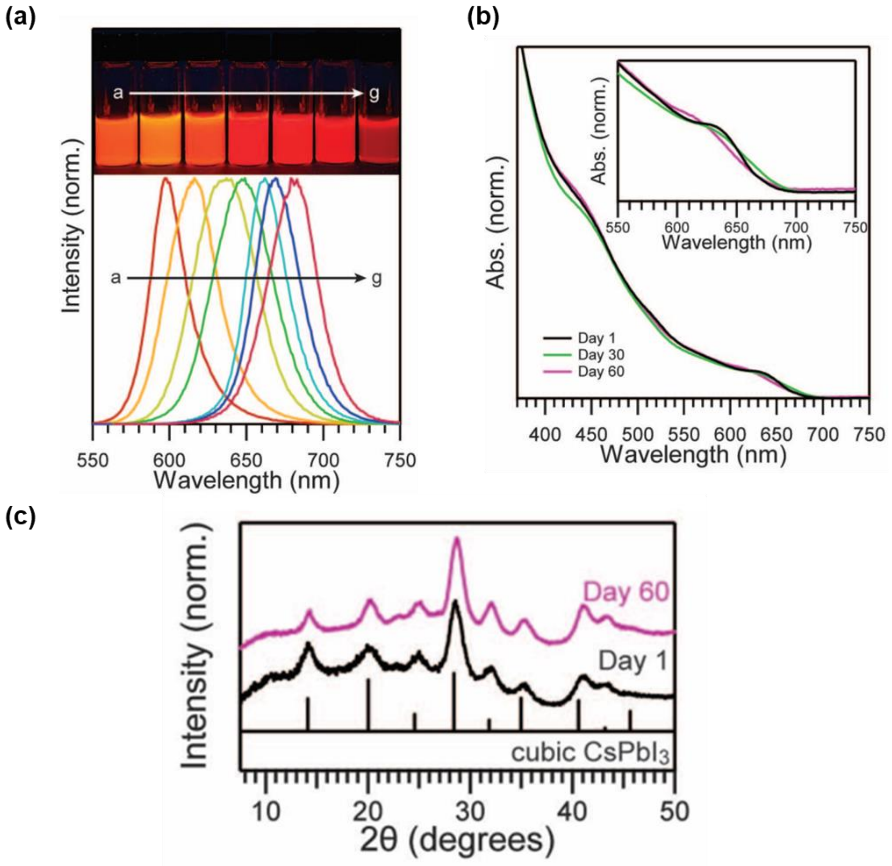

Figure 3.3 (a) shows the photoluminescence spectra of $CsPbI_3$ nanocrystals and corresponding photographs under UV illumination, while (b) absorption spectra and (c) the x-ray diffraction spectra describe the stability of these NCs over time.[26]

3.1.4 Stability under radiations

As discussed above, temperature and humidity can promote a phase shift from the photoactive perovskite phase to the non-photoactive phase; similarly, illumination to sunlight and x-ray irradiation can cause defects and structural changes in the perovskite material, which can ultimately lead to the collapse of perovskite structure and a loss of its ability to function as an efficient semiconductor. For instance, when halide perovskite $CH_3NH_3PbI_3$ is exposed to x-rays, degradation proceeds through the creation of metallic lead (Pb^0) and evaporation of organic component.[27] While in another report it has been shown that 42h of continuous exposure to x-rays causes the loss of iodine in $CH_3NH_3PbI_3$ at the same rate as that of nitrogen, consistent with the loss of MAI, suggesting a continuous decomposition of $CH_3NH_3PbI_3$ into PbI_2 without the formation of Pb^0.[28] A more comprehensive study on the degradation mechanism on both hybrid and inorganic halide perovskite under hard x-rays using photoelectron spectroscopy performed by Svanström et al.,[29] which revealed two different pathways for hybrid and inorganic halide perovskite degradation. For the hybrid halide perovskite composition $Cs_{0.17}FA_{0.83}PbI_3$, the degradation has been proposed as the radiolysis of organic cation, which leads to the formation of organic degradation product and collapse of the perovskite structure. Similar to the previous report, the appearance of PbI_2 occurs without the appearance of Pb^0. However, the inorganic halide perovskite $CsPbBr_3$ decomposition mechanism is suggested as the radiolysis of lead halide cage into halide salt, halogen gas, and metallic lead formation, which appears to be catalyzed by the appearance of defects.

Similar to x-rays, illumination to sun light can also significantly affect the perovskite and thus its interfacial energetics with adjacent layers through the formation and subsequent migration of ions and vacancies. For instance, light-soaking (continuous light illumination) can facilitate the carriers extraction through the photogenerated electric field created by mobile ions in perovskite, such as methylammonium and iodide ions and vacancies (MA^+/V_I^+, I^-/V_{MA}^-).[30] These mobile ions which are present as defects can aggregate near the selective contacts, forming a boosted P-i-N junction and facilitates carriers extraction as shown in Figure 3.4. Similarly, light soaking can improve carriers extraction at the perovskite-contact interfaces not only through ion migration, but also through lattice expansion (independent of ion migration). This lattice expansion leads to relaxation of local lattice strain, which lowers the energetic barriers at the interfaces and thus improving the device performance.[30] Despite the fact that light soaking may appear to be advantageous by providing better energy level alignment, as mentioned above, it can have detrimental impact on the stability of perovskite device, as will be discussed below.

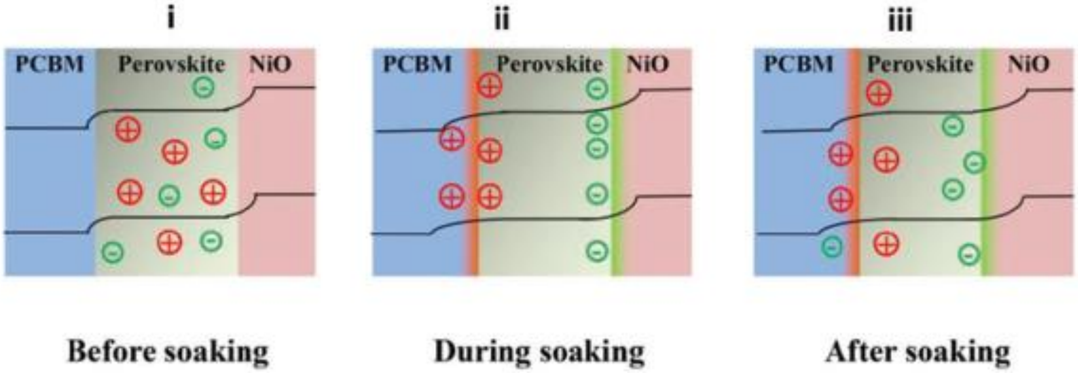

Figure 3.4. Schematic illustration of energy level alignment assisted by ions migration (i) before soaking (ii) during the soaking, and (iii) After soaking. The mobile ions are aggregates at the selective contacts due to photogenerated electric field, forming boosted P-i-n junction to facilitate the charge transfer.[30]

Zu et al. investigated the impact of white light on the electronic and chemical properties of halide perovskite ($MAPbI_{3-x}Cl_x$) thin film and its single crystal. Upon white illumination, existing band bending at the surface vanishes due to movement of carriers from bulk to surface while in dark, bend bending restored since carriers goes back to bulk from the surface, consistent with the phenomena known as surface photovoltage. However, this surface photovoltage is partially reversible and prolonged exposure to illumination completely vanishes the surface photovoltage. This has been attributed to the high concentration of donor-like surface states (metallic lead (Pb^0)) induced by illumination, that strongly pinned the Fermi level of perovskite and quenched the surface photovoltage.[31] Thus, it has been deduced that light-soaking have detrimental effect on perovskite material, which is in a stark contrast to the findings of Zhang et al.[30] who claimed improved energy level alignment upon illumination.

Furthermore, Zu et al. extended their previous work of white light illumination impact on halide perovskite surface by depositing an organic acceptor molecule on top to investigate the energy level alignment of halide perovskite with organic molecule depending upon the density of surface states. When the perovskite ($MAPb_{3-x}Cl_x$) is irradiated with white light, high density of donor-like surface sates originating from reduced lead (Pb^0) are generated, consequently this surface is referred to as having a high density of surface states (high DoSS), whereas the non-irradiated surface of perovskite is referred to as having low density of surface state as (low DoSS). When acceptor molecule (HATCN) is deposited on the surface having low density of surface states, it compensates the donors surface states by transferring electrons from these donor surface states to molecule, resulting in unpinning of Fermi level (E_F) and the initial band bending at low density of surface states get flattened. However, for the surface with high density of surface states, despite the occurrence of charge transfer from Pb^0 donor states to acceptor molecule (as evidenced by the decrease in Pb^0 amount and the emergence of an extra state in the valence band at roughly 1eV below EF in PES data), the Fermi level (E_F) remains pinned due to the high density of Pb^0 on the surface. Consequently, the initial band bending, which was disappears at low density of surface states, is still present with high density of surface states.[32] Figure 3.5 summarizes the situation of energy level alignment with organic molecule on the basis of available density of surface states present in halide perovskite.

In conclusion, both x-rays and sunlight illumination can produce the structural changes in halide perovskite, leading to modifications in its semiconducting properties. These modifications, in turn, affects the energy level alignment with adjacent transport layers depending upon the amount of the damage caused by radiation. As a result, it is critical to approach the issue with considerable care and attention while examining the effects of radiation on halide perovskite materials, given the enormous impact radiation may have.

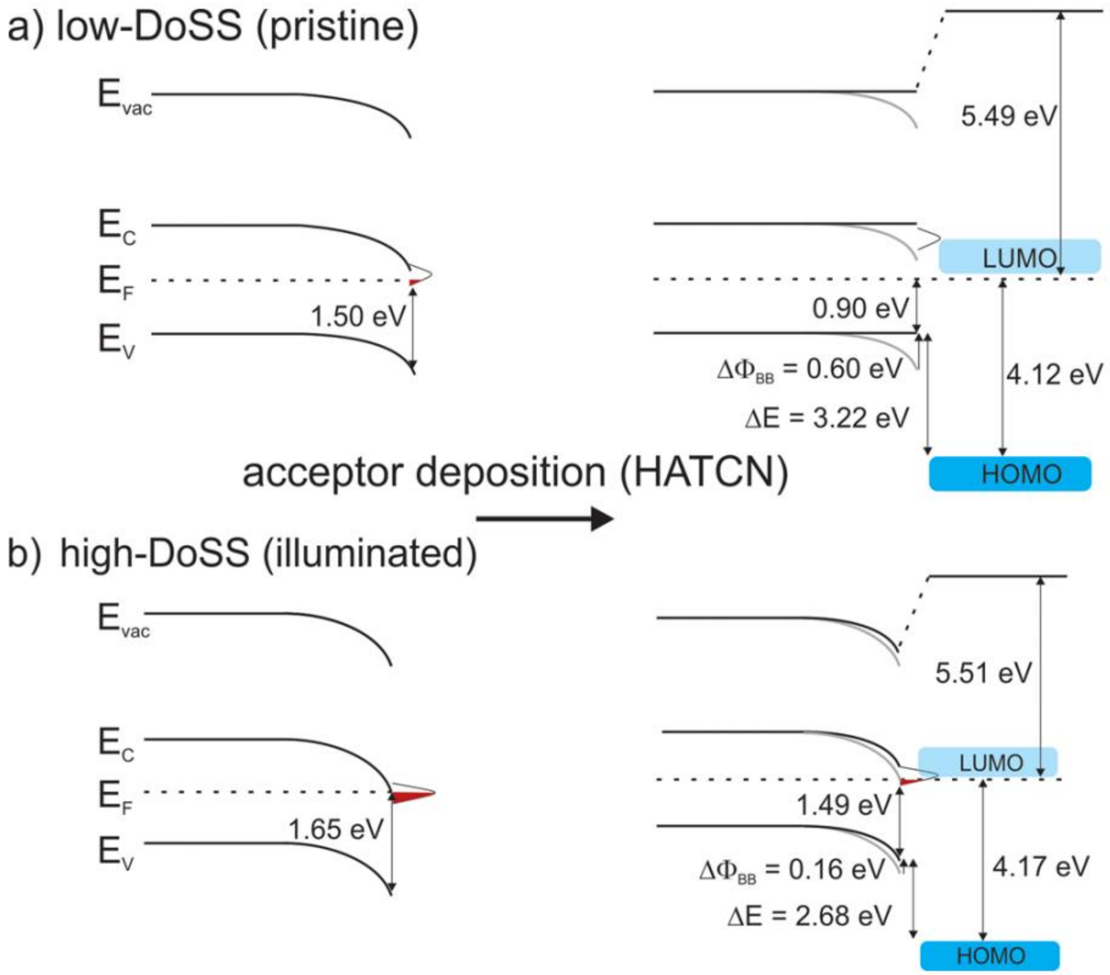

Figure 3.5. Energy level diagram constructed from XPS and UPS data of adsorption of HATCN acceptor molecule on (a) low and (b) high density of surface states (DoSS) of perovskite surfaces. Initial reduction to band bending is 0.60 and 0.16 eV for low and high DoSS respectively. Red shade indicate filled DoSS.[32]

3.1.5 Optoelectronic properties of halide perovskite nanocrystals

Halide perovskites are known for their excellent properties such as high absorption coefficient (> 10^4 cm^{-1}),[33] tunable bandgap, small exciton binding energy (10 to 150 meV),[34] excellent charge carrier mobilities (30~164 $cm^2V^{-1}s^{-1}$) long carrier diffusion length (> 1 μm),[36] and high defect tolerance. These intrinsic properties of halide perovskite can be combined with the unique properties of nanocrystals to develop semiconductors with unparalleled optoelectronic features. As shown in Figure 3.6 (b,c), the optical absorption and emission spectra of $CsPbX_3$ nanocrystals (NCs) may be tuned across the whole visible region by modifying their composition, which is equally true for the bulk, or by adjusting the size of NCs, which is one of the NCs' distinct features. Moreover, halide perovskite nanocrystals (HaPNCs) exhibits the phenomenon of quantum confinement resulting in bright and narrow photoluminescence (PL) spectra that is highly desirable for optoelectronic applications such as light emitting diodes (LEDs). Very bright emission of HaPNCs indicates that, unlike chalcogenides, surface dangling bonds present in NCs do not impart severe midgap trap states, favoring the existence of shallow trap states that do not have a significant influence on PL, thereby lending credence to the hypothesis that perovskites are highly tolerance to defects.

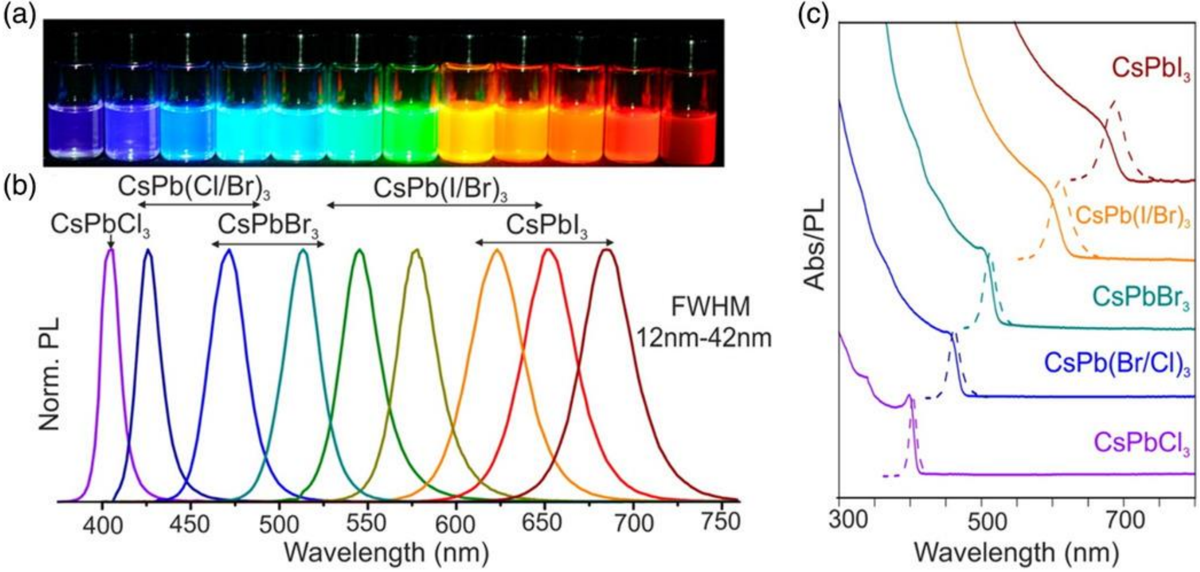

Figure 3.6. Perovskite CsPbX3 (X = Cl, Br, I) nanocrystals showing size and composition tunable bandgap energies covering the entire visible region: (a) nanocrystals solution in toluene under UV lamp, (b) PL spectra of nanocrystals, and (c) optical absorption and PL spectra.[5]

Photoluminescence efficiencies or more precisely photoluminescence quantum yield (PLQY) of HaPNCs are close to 100%[1] over the large part of visible range and with extremely narrow linewidth of 12-42 nm for $CsPbX_3$.[5] Moreover, there is limit of getting maximum efficiency from a solar cell, posed by William Shockley and Hans-Joachim Queisser calculation, known as Schockley-Queisser limit. Interestingly, HaPNCs have potential to overcome this Schockley-Queisser limit through two interconnected aspects:

1) hot carrier thermalization 2) multiple exciton generation (MEG).[37]

When a semiconductor absorbs a photon, whose energy is greater than the optical bandgap, a hot carrier is created which have excess kinetic energy above the band edges. This hot carrier relaxation occurs through scattering with carriers or phonons, resulting in carrier thermalization and subsequent carrier cooling. Theoretically, if hot carriers are utilized prior to thermalization, a PCE of up to 66% (AM 1.5 illumination, 300 K) can be attained, breaking the Schockley-Queisser limit for single junction solar cells.[38] However, this relaxation process is extremely fast in semiconductors (in the order of femtoseconds), making hot carrier harvesting difficult, but it is possible to exploit hot carrier in halide perovskite due to relatively slow relaxation process (in the order of 100 picoseconds)[39] and even slower in nanocrystals due to quantum confinement.[38]

Moreover, when the kinetic energy of hot carrier crosses certain threshold, the excess energy utilized in creating extra electron-hole (e-h) pairs instead of producing heat, given rise to a phenomena called multiple exciton generation (MEG).[40] It means multiple exciton can be generated from a single photon absorption and MEG can increase the efficiency of solar cells greater than 40%.[41] In summary, achieving carrier multiplication through MEG is considered more feasible compared to capturing hot carriers. This has resulted in reported external quantum efficiency of over 100% in lead chalcogenide, quantum dot-based solar cells.[42]

3.2 Properties of $CsPbBr_3$ Nanocrystals

The inorganic family of halide perovskites is regarded as more stable than their hybrid counterparts (which contain both organic and inorganic components). This increased stability is attributed to the absence of volatile organic content, which is the primary factor contributing to the degradation of hybrid perovskite under harsh environmental conditions such as light, heat, and moisture. Among inorganic family, $CsPbBr_3$ material, which has a bandgap of 2.30 eV is a potential candidate as a top cell in tandem configuration to harvest the unabsorbed photons in the visible region close to UV region.[43] Also, $CsPbBr_3$ single crystal have a very high charge carrier mobility of 1000 $cm^2V^{-1}s^{-1}$ with charge carrier lifetime of 2.5 μs, which is relatively higher than other members of inorganic family of halide perovskite. Significantly more important, $CsPbBr_3$ show much higher stability under the exposure of light, heat and mositure.[44] This high stability of $CsPbBr_3$ is attributed to its relatively higher defects formation energy as suggested by theoretical calculations.[45] All these inherent properties of $CsPbBr_3$ are also found in its nanocrystals form even with better stability due to attachment of ligands at the terminated surface of crystal lattice. Nonetheless, the long-term stability of these $CsPbBr_3$ nanocrystals based solar cells is yet to be investigated particularly under UV light at the electrodes and at the interfaces with other charge transport layers, in order to decipher the degradation mechanism. Considering this, in this section, the UV stability of $CsPbBr_3$ nanocrystals at its interface with gold will be discussed and its comparison with x-rays stability will be made. However, before going to the investigation of stability the synthesis of $CsPbBr_3$ nanocrystals and their optical and structural properties in the following will be discussed.

3.2.1 Synthesis of $CsPbBr_3$ nanocrystals

The $CsPbBr_3$ perovskite NCs were synthesized by E. Lhuillier at the INSP and the synthesis procedure is given in the following.

Chemicals: 1-octadecene (ODE, 90%, Aldrich), oleylamine (OLA, 80 − 90%, Acros), oleic acid (OA, 90%, Aldrich), cesium carbonate (99.9%, Aldrich), Lead bromide ($PbBr_2 \geq 98\%$ Alfa Aesar), hexane (99%, VWR) ethyl acetate (JT baker), lead acetate (Alfa Aesar, basic).

Cesium oleate: In a three necks flask, 0.8 g of $Cs_2(CO_3)$, 2.5 mL of OA and 30 mL of ODE are mixed and degassed at 80 °C for 30 min. Then the temperature drops around 100 °C and the flask is regassed for one hour. The solution is transferred to a vial and used as a stock solution.

$CsPbBr_3$ nanocrystals synthesis: In a 100 mL three-neck flask, 320 mg of $PbBr_2$ are introduced with 20 mL of ODE. The flask is degassed under vacuum for 60 min at 110 °C. Then, 1 mL of OA is introduced. Once the vacuum level has recovered, 1 mL of OLA is introduced. Quickly after that the lead salt gets fully dissolved. The flask is further degassed for another 30 min at 110 °C. The atmostphere is then switched to nitrogen and the temperature raised to 180 °C. Then, 1.6 mL of cesium oleate solution is quickly added. The reaction is conducted for 30 s before removing the heating mantle and cooling the flask with ice bath. The content of the flask is centrifugated without addition of any solvent. The formed pellet is dried and finally redispersed in fresh hexane.

3.2.2 Sample preparation

The prepared colloidal solution of $CsPbBr_3$ perovskite NCs were deposited on Au substrate (thermally deposited Au thin film on silicon substrate) with a spin speed of 2000 rpm/sec with an acceleration of 500 rpm/sec for 30 seconds (spin-coating conditions are optimized for smoother film formation) in ambient condition, resulting in a thin film of about 20 to 30 nm.

(a) Ligands exchange

To perform ligands exchange, a concentrated solution (about 100 mg/ mL) of lead acetate ($Pb(OAc_2)$) in ethyl acetate was prepared. This solution was centrifuged and only supernatant was saved. A thin film of $CsPbBr_3$ perovskite NCs was then dipped in lead acetate solution for 30 seconds and finally this this film is rinsed in pure ethyl acetate to remove unreacted ligands if remains any.

All the samples prepared in Paris at the INSP laboratory, were transported to the PM4 beamline at BESSY II synchrotron in Berlin, Germany. The following day photoelectron spectroscopy (PES) was performed on these samples.

3.2.3 Crystal structure and optical properties of $CsPbBr_3$ nanocrystals

X-ray diffraction (XRD) patterns of spin coated $CsPbBr_3$ nanocrystals (NCs) on silicon substrate are performed at the INSP and shown in Figure 3.7, which confirm the cubic α-phase perovskite structure of the NCs with lattice parameter (a = b = c = 5.83 Å), which is consistent with the literature.[46]

By using the Sherrer's equation for the diffraction peak at 30.53° associated with (200) plane of cubic α-phase structure of the $CsPbBr_3$, the average size of nanocrystals of 13 ± 3 nm has been calculated, using the formula presented in Chapter 2.

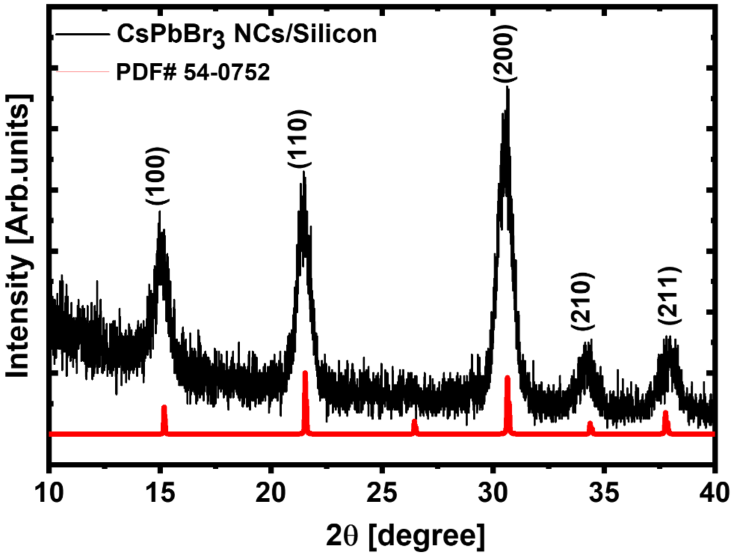

Figure 3.7. XRD pattern of the $CsPbBr_3$ nanocrystals spin-coated on silicon substrate, which are crystallized in a cubic system. The red curves is the powder diffraction file (PDF) of $CsPbBr_3$ material in cubic phase.

Using Uv-vis absorption spectroscopy, an optical bandgap of 2.30 ± 0.03 eV has been estimated from the solution absorption spectra of $CsPbBr_3$ NCs. As can be seen in Figure 3.8 absorption spectrum is barely structured suggesting the absence of quantum confinement. For the NCs to display quantum confinement, their size should be less than or equal to Bohr's radius, which is 7 nm for $CsPbBr_3$. However, the NCs have a size of 13 nm, which is twice the Bohr’s radius, resulting in the absence of quantum confinement.[5]

Thus, the $CsPbBr_3$ NCs synthesized in the present work have a cubic α-phase with an average size of approximately 13 ± 3 nm, and possess an optical bandgap of 2.30 ± 0.03 eV.

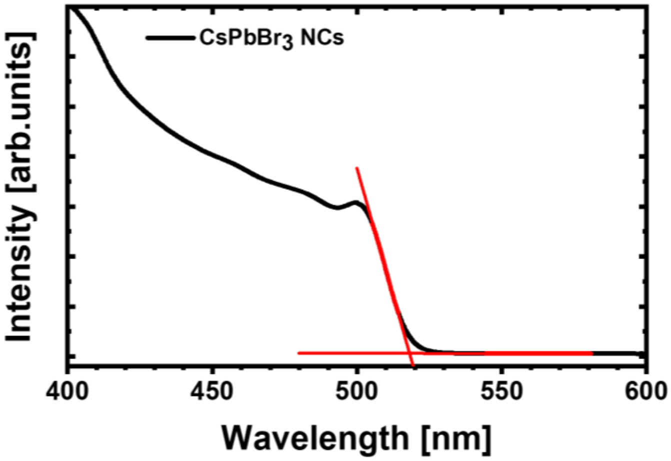

Figure 3.8. UV-vis absorption spectrum $CsPbBr_3$ nanocrystals.

3.2.4 Transport properties of $CsPbBr_3$ nanocrystals

Nanocrystals (NCs) possess a high surface-to-volume ratio inherent to nanoscale objects. This leads to an increased presence of dangling bonds, resulting in more trap states and defects. To passivate these trap states and prevent the aggregation and precipitations of the NCs, oleylamine (OLA) and oleic acid (OA) are used during the synthesis of NCs. Generally, halide perovskite nanocrystals (HaPNCs) are distributed in a disordered manner when thin film is formed, and transport of charge carriers in these NCs occurs through hopping mechanism. The charge carriers must pass through the potential barrier by tunneling between the NCs created by the ligands on the surface of NCs as shown in Figure 3.9. The potential barrier and tunneling rates are related by the following equation:[47]

$$T \propto exp\left(-2\sqrt{\frac{2m^*\Delta E}{\hbar^2}}\,\Delta x\right)$$

Where T is tunneling rates, ΔE and Δx are the height and width of tunneling barrier (defined by the surface ligands on NCs) respectively. The m^* is effective mass of an electron and $\hbar$ is the reduced Planck's constant. This equation shows that the tunneling rate decreases exponentially with increasing distance between the NCs and is partially dependent on the barrier height and carrier effective mass.

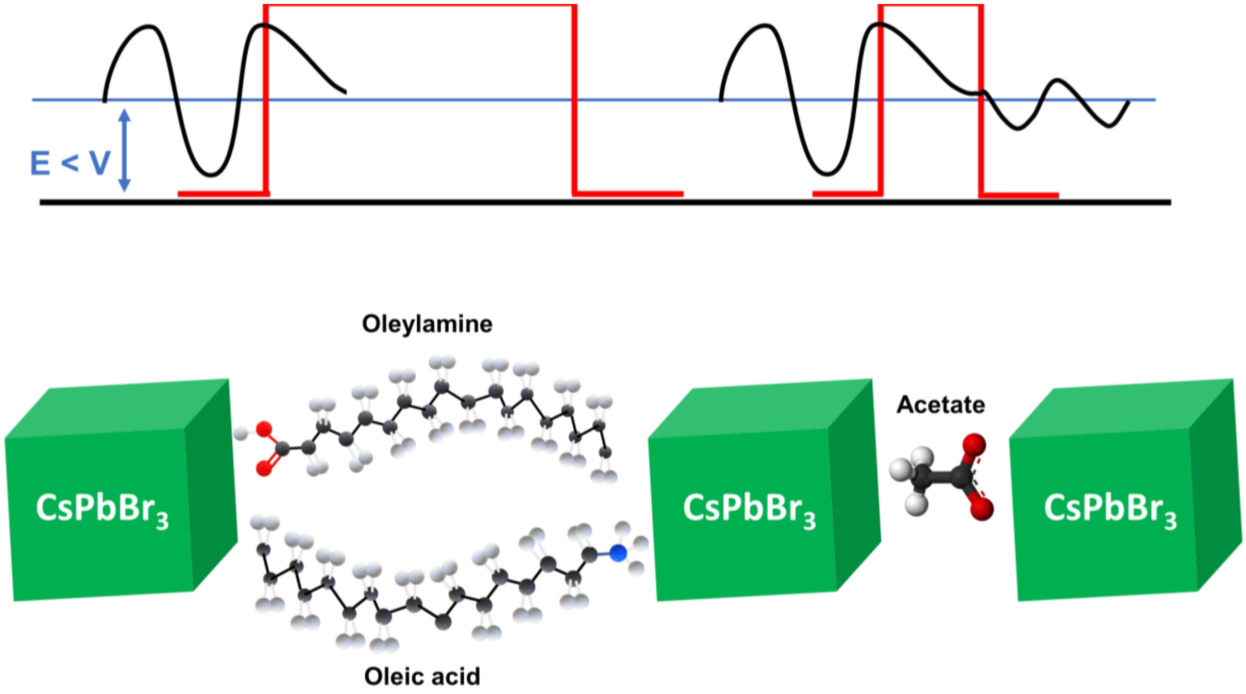

Figure 3.9. Illustration of electron tunneling barrier: for long carbon-chain ligands barrier is wide and where no tunneling is expected (left), vs narrow barrier upon the ligands exchange with acetate where tunneling occurs easily.

So, the native ligands (oleylamine and oleic acid) used during synthesis of HaPNCs have wide width due to large separation between the NCs, making tunneling transport inefficient. To address this issue, these long carbon chain ligands (~1.5 nm)[47] are exchanged with the shorter ligands, acetate (~ 0.4 nm for ethyl acetate)[47] thus reducing the width of barrier and allowing the efficient transport of charge carriers. Figure 10 summarize this process.

Moreover, tunneling rate also depends upon the order in the system which refers to how close the NCs are to one another. The closer the NCs are, the higher the coupling between them. Higher coupling between the NCs can be manifested as reduced height and width of the barrier; both of them can increase the tunneling rate and charge transport. To sum up, not only the barrier height and width but also the coupling between NCs strongly affect the transport of charge carriers and thus conductivity of NCs.[48]

The modification of surface ligands is a fast-emerging topic, and ligands exchange procedure is already developed and applied to quantum dots (CdSe, CdTe, ZnS, ZnSe, PbS etc.) with (carboxylic acids, amines etc.) ligands.[49] However, such a ligands exchange cannot be applied to halide perovskite nanocrystals (HaPNCs) due to occurrence of phase transfer of HaPNCs, which is evidenced by a color change from yellow to brown.[50] In 2016, for the first time a ligands exchange procedure is introduced for $CsPbI_3$ NCs where a saturated solution of lead acetate ($Pb(OAc)_2$) in methyl acetate (MeOAc) has been made and performed on spin-coated NCs thin films.[26] Ligands exchange not just improve the transport properties of the NCs thin-film but also enhances the stability of the NCs. This same exchange procedure applied to $FAPbI_3$ halide perovskite nanocrystals without affecting the NCs such as their size and crystal structure as shown previously.[47] More importantly, in the same study, transport measurements conducted and it has been noticed that ligands exchange from oleylamine and oleic acid to acetate increased the conductivity of $FAPbI_3$ halide perovskite nanocrystals thin-film about 100 times. This increase in conductivity was attributed to the improved conduction of charge carrier through the film due to decreased barrier width by acetate compared to oleylamine and oleic acid.[47] Considering this, we adopted the same procedure of ligands exchange from native ligands to acetate ligands after the spin-coated the $CsPbBr_3$ NCs. And all the samples on which photoemission spectroscopy was performed and will be discussed in this thesis went through the ligands exchange process as described above unless stated otherwise.

3.3 Radiation Stability of $CsPbBr_3$ Nanocrystals at Au Interface

The Stability of $CsPbBr_3$ perovskite nanocrystals under radiation such as ultraviolet (UV) and x-rays is critical. Given that 5% of the solar spectrum consists of UV radiation [51] it is imperative to study the effect of UV radiation on a device. Moreover, the highly stable perovskite devices with the stability of one-year[52] under AM 1.5 G solar illumination at a stabilized temperature of 55 °C were reported where UV rays were completely filtered, as white light-emitting diode used to measure the devices. Therefore, the stability of perovskite under UV and the underlying processes that govern it are still a subject of debate. Similarly, stability under soft x-rays is critical as well due to the small inelastic mean free path for photoelectrons, which is utilized for characterizing the surface and detecting the chemical and electronic changes at the surface of perovskite. Furthermore, in certain situations like the utilization of solar cells to generate power for spacecraft in outer space, the significance of ionizing radiation, such as x-rays, becomes exceptionally crucial as well. Additionally, due to ability of deposition of $CsPbBr_3$ on flexible substrates, it has the potential for radiation detectors, and it is regarded more competitive than currently utilized materials.[53] Overall, the stability of $CsPbBr_3$ under both UV and x-ray irradiation is critical and needs to be investigated to understand the degradation mechanism for making stable devices under these radiations.

As stated previously, gold (Au) as an electrode is an integral component of any kind of optoelectronic device owing to its chemical stability, inertness and high conductivity. Generally, the interface of Au and semiconductors is considered non-reactive as no chemical reaction is expected at the interface. However, the interface of Au with perovskite is not stable and an interfacial chemical reaction has been proposed in different studies albeit its origin remains ambigious.[54,55] Hence, the unambiguous origin of such an interfacial reaction and redox surface chemistry at the interface of perovskite with Au remain an open question, and a direct experimental assessment and conditioning of the interface is required to gain a more conclusive understanding. With regard to this, we investigated the stability of $CsPbBr_3$ nanocrystals at the Au interface under infrared (IR), ultraviolet (UV), and x-ray radiation individually and will be explained in the following.

3.3.1 Effects of infrared (IR) (1030 nm or 1.2 eV) illumination

The experiment to study the stability of $CsPbBr_3$ nanocrystals at interface with gold (Au) is performed at low x-ray flux beamline (PM4) at the synchrotron BESSY II. The low x-ray flux allows to isolate the effects of radiation (IR and UV) from x-ray induced effects. The steady state photoemission spectra of ligands exchange nanocrystals spin-coated on Au substrate were measured using an infrared (IR) femtoseconds laser installed at the beamline with the wavelength of 1030 nm or 1.2 eV, a pulse length of about 350 fs, and a repetition frequency of 207.46 kHz.

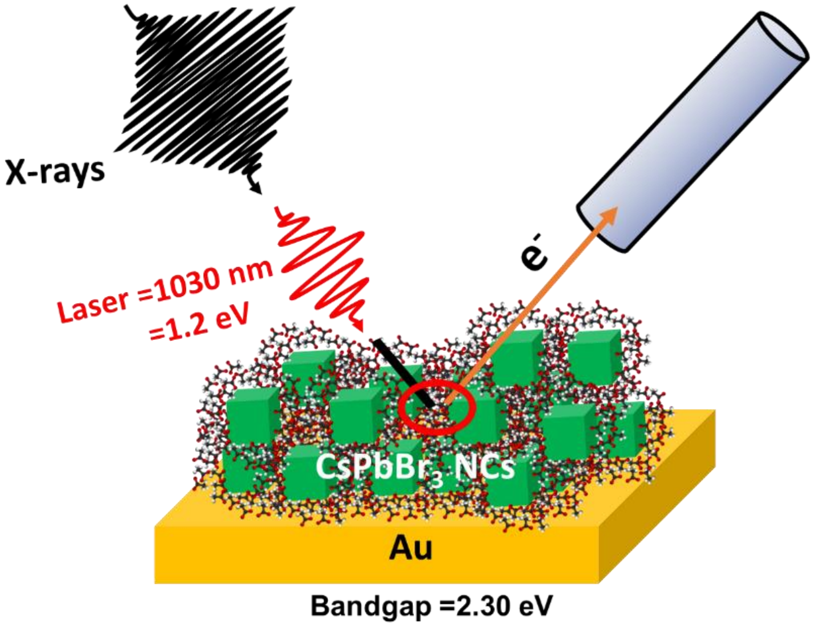

Figure 3.10. Illustration of Experimental setup.

The fluence of the laser was estimated to be about 12.5 mW/cm^2. Time evolution measurements of core level were carried out in the following sequence: Cs 4d and Br 3d and Pb 4f, 5 minutes each before the laser was switched on, Pb 4f 30 minutes during the laser, then Pb 4f, Cs 4d and Br 3d, 5 minutes each after the laser. Then, the same spot was exposed for 60 more minutes and Pb 4f core level is recorded. After switching the laser off, Pb 4f, and Cs 4d,Br 3d were recorded for 20 and 10 minutes respectively. The C 1s is not included in analysis due to its complexity of peaks fitting, which includes different carbon peaks from the (acetate) ligands and, from the adventitious carbon. Also, the analysis of valence band is not included either due to clearly visible Fermi step of the Au even when the Au is covered with $CsPbBr_3$ NCs. Experimental setup is shown in as shown in Figure 3.10.

All the measurements were taken with x-ray photon energy of 360 eV which gives the probing depth of less than 3 nm (about 2.70 nm) calculated for the kinetic energy of Pb 4f core level, which means these measurements were performed to observe the changes exclusively at the surface and not in the bulk. Nonetheless, reactions in the bulk tend to be mirrored in the surface structure if ions from the perovskite migrate and perovskite restructures itself. To extract the intensities and binding energy, the recorded core levels were fitted using Voigt functions with a background deemed appropriate, either polynomial or Shirley background using CasaXPS software. Au $4f_{7/2}$ at 84.00 eV used for binding energy calibration. Furthermore, it is important to mention here that, despite the limited probing depth at 360 eV, the interface at the corner and edges of $CsPbBr_3$ NCs with Au is still accessible but not the buried interface. This also means the majority of the PES signals are coming from the surface of the NCs.

In Figure 3.11 (a), the overview spectrum of $CsPbBr_3$ NCs shows the contribution from carbon, lead, cesium and bromide. The core level analysis presented in Figure 3.11 (b,c), which consists of Cs 4d, Br 3d and Pb 4f. The contribution from Cs 4d is very low due to the combined effect of its low cross section at the photon energy of 360 eV and low x-ray flux (1×10^{9}~1×10^{10} photons/sec) at PM4 beamline. The peak of Cs 4d is found at a binding energy of 74. 91 eV and Br 3d at 67.85 eV which are assigned to Cs^{+} and $Br^{-}$of $CsPbBr_3$.[56]

Similarly, the Pb 4f shows a single component at a binding energy of 138.04 eV assigned to the Pb^{2+} of $CsPbBr_3$.[56] When these $CsPbBr_3$ NCs are exposed to infrared (IR) laser of 1.2 eV below the bandgap of NCs (2.30 ± 0.03 eV) with the laser fluence of 12.5 mW/cm^2 for 30 minutes, shift in binding energy of perovskite core levels is observed. However, for the second cycle of 60 minutes more exposure not only shift in the binding energy increases further but a new chemical specie in Pb 4f core level at the binding energy of 136.45 eV appears.

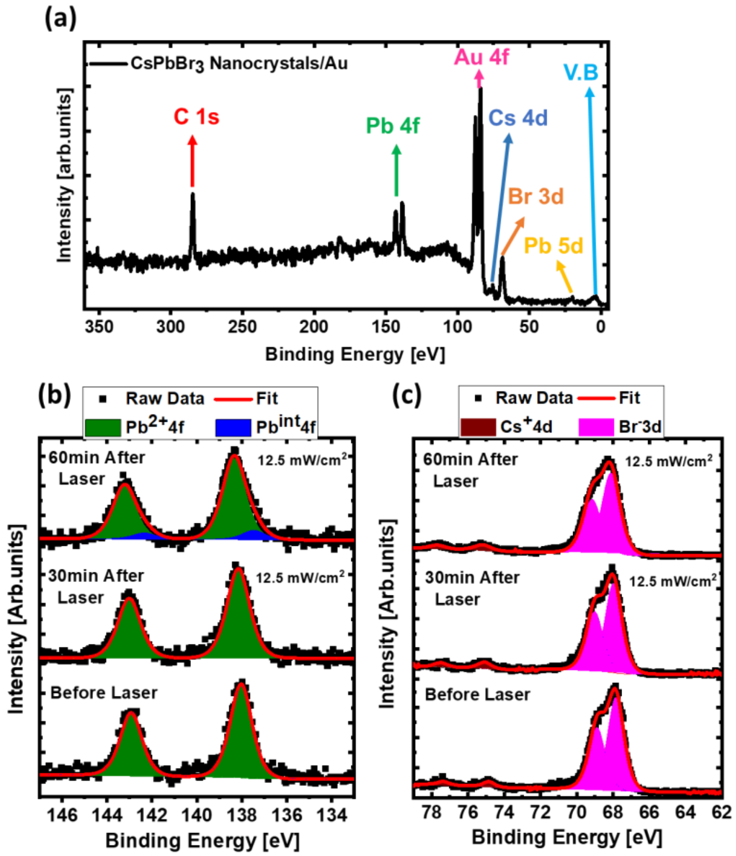

Figure 3.11. (a) Overview spectrum of $CsPbBr_3$ perovskite nanocrystals spin-coated on Au at the photon energy of 360 eV, (b) Cs 4d and Br 3d core levels, and (c) Pb 4f core level measured at photon energy of 360 eV before and after 30 and 60 minutes of infrared (IR) laser of 1.2 eV energy exposure.

Table 3.1 Shows the binding energies (eV) of core levels Cs 4d , Br 3d and Pb 4f extracted from the least squares fit of the corresponding core level of $CsPbBr_3$ NCs on Au before,30 minutes and 60 minutes after IR laser.

	Cs^+ (eV)	**Br^- (eV)**	**Pb^{2+} (eV)**
	Cs $4d_{5/2}$	Br $4d_{5/2}$	Pb $4f_{7/2}$
Before Laser	74.91±0.07	67.85±0.015	138.03±0.03
After 30min IR Laser	75.03±0.07	67.97±0.015	138.15±0.03
After 60min IR Laser	75.21±0.07	68.12±0.015	138.35±0.03
ΔB.E (30min After)	0.12±0.10	0.12±0.025	0.12±0.04
ΔB.E (60min After)	0.30±0.10	0.27±0.025	0.32±0.04

This chemical specie is of unknown origin and assigned it here as Pb^{int} and will be explained later. Also, a clear change in the shape of Br 3d is also evident as the full width at half maximum (FWHM) increases from 1.07 eV to 1.20 eV. The binding energies extracted from least square fits of core levels before and 30 minutes and 60 minutes after IR laser are shown in Table 1. The intensities of Cs 4d, Br 3d and Pb 4f relative to the respective intensities before the laser are plotted as a function of time and shown in Figure 3.12 (a). As it can be seen that there was no change in intensities of Pb 4f core level occurred during and 30 minutes after of IR laser exposure. However, for the second cycle of 60 minutes exposure, at the half time of turning the laser on, a new component in Pb 4f core level appears, assigned as Pb^{int}, with an intensity of 0.07, which increased slightly to 0.11 at the end of the laser. Meanwhile, intensity of Pb^{2+} decreases slightly almost at the same ratio of as increase in Pb^{int}. Interestingly, although a slight broadening in Br 3d core level is observed, which is also evidenced from the shape of Br 3d, no drop in intensity has happened. Similarly, Figure 3.12 (b) shows the relative binding energies as a function of time, calculated as (binding energy of Cs 4d, Br 3d and Pb 4f subtracted from the corresponding core levels binding energies before the laser). Immediately after exposure to laser, Pb^{2+} shifted slightly towards higher binding energy, which increased further with increasing exposure time and ended at the 0.12 eV after 30 minutes laser. Likewise, for Cs^{+} and Br^{-}, shifted with the same magnitude of the shift (0.12 eV) towards higher binding after the laser.

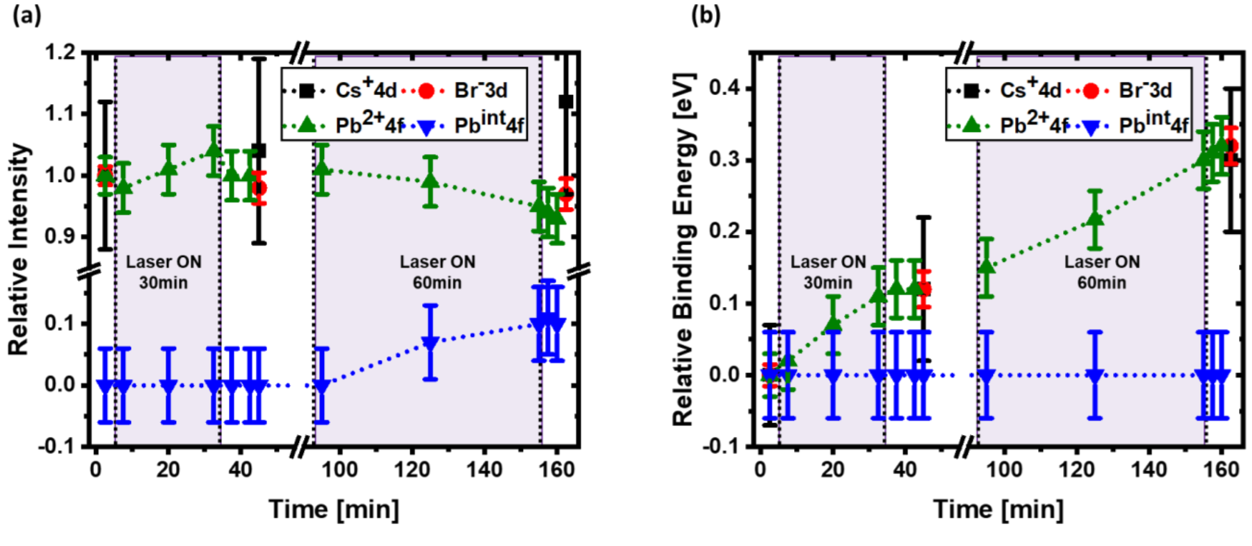

Figure 3.12. (a) relative intensities of Cs 4d, Br 3d and Pb 4f spectra calculated (intensity of Cs 4d, Br 3d and Pb 4f core levels divided by intensity of the corresponding core levels before laser), (b) relative binding energies of Cs 4d, Br 3d and Pb 4f spectra calculated (binding energy of Cs 4d, Br 3d and Pb 4f core levels subtracted from the binding energy of the corresponding core level before laser) of CsPbBr$_3$ NCs on Au with laser fluence of 12.5 mW/cm^2 and laser energy of 1.2 eV. The shaded area in the figure represents 30 minutes and 60 minutes exposure.

For the second cycle of laser, 60 minutes more exposure, the shift in binding energy of Pb^{2+} increases even further and ends up at the total shift of 0.32 eV after the laser. The same shift in the binding energy of about 0.30 eV in Cs^{+} and $Br^{-}$is noticed. These rigid shifts in binding energies of all the core levels after 30 and 60 minutes of IR laser can be inferred, as laser energy of 1.2 eV, below the NCs' bandgap of 2.30 eV,[57,58] can excite the sub-bandgap defects contribution associated with halide interstitial and/or vacancies,[59-62] causing photo-induced charge separation between perovskite nanocrystals and Au substrate. Upon switching off the laser, shift in binding energies should be reversible which would have been consistent with a decay of photovoltage; however, this is not the case here as permanent shift in the binding energies of all the core levels is observed. The explanation for this irreversible shift in binding energy might be related to the damage to the perovskite structure, as indicated by the emergence of a new chemical specie, Pb^{int}, after 60 minutes of further exposure and/or Fermi level pinning.

3.3.2 Effects of ultraviolet (UV) (343 nm or 3.6 eV) illumination

To investigate the stability under ultraviolet radiation, the steady state photoemission spectra of NCs were measured using the installed laser at the PM4 beamline at its third harmonic, which gives the wavelength of 343 nm or an energy of 3.6 eV with a pulse length of about 350 fs, and a repetition frequency of 207.46 kHz. Two fluence of the laser were used with estimated power densities of 3.5 mW/cm^2 and 12.5 mW/cm^2. Two distinct laser exposure times were employed in succession, 30 minutes and 60 minutes. Time evolution measurements of different core levels were performed in the following order: Cs 4d and Br 3d and Pb 4f, 5 minutes each before the laser was switched on, Pb 4f 30 minutes during the laser, Pb 4f, Cs 4d and Br 3d, 10 minutes each after the laser. Then, the same spot was exposed to UV laser for 60 additional minutes and Pb 4f core level is recorded. After switching the laser off, Pb 4f, Cs 4d and Br 3d were measured each for 10 minutes. To differentiate the effect of UV laser on the surface and bulk of NCs, two different photon energies were used of 360 eV and 650 eV, which gives the probing depth of 2.70 nm and 4.60 nm respectively. For the binding energy calibration, Au 4f (7/2) at 84.00 eV was used.

Before discussing the effects of UV laser, it is important to mention here that this experiment is also done at the PM4 beamline which has very low flux of x-ray. Hence the changes that occurred under laser are exclusively attributed to UV radiation. Figure 3.13 (a) shows the Cs 4d and Br 3d core levels of $CsPbBr_3$ NCs deposited on Au substrate before and after exposure to 3.6 eV UV laser illumination which is above the bandgap of NCs (2.30 eV), for 30 minutes. After laser exposure, both the core levels Cs 4d and Br 3d were shifted to higher binding energy of approximately 0.66 eV. Similarly, Pb 4f spectra before and after the laser is shown in Figure 3.13 (b). Before the laser illumination as shown in Figure 3.13 (c), only a single spin-orbit doublet is observed which is assigned to Pb^{2+} of $CsPbBr_3$.[63] After the 30 minutes laser exposure Pb^{2+} shifts to higher binding energy by approximately 0.66 eV and two new components in Pb 4f core-level appeared as shown in Figure 3.13 (d).

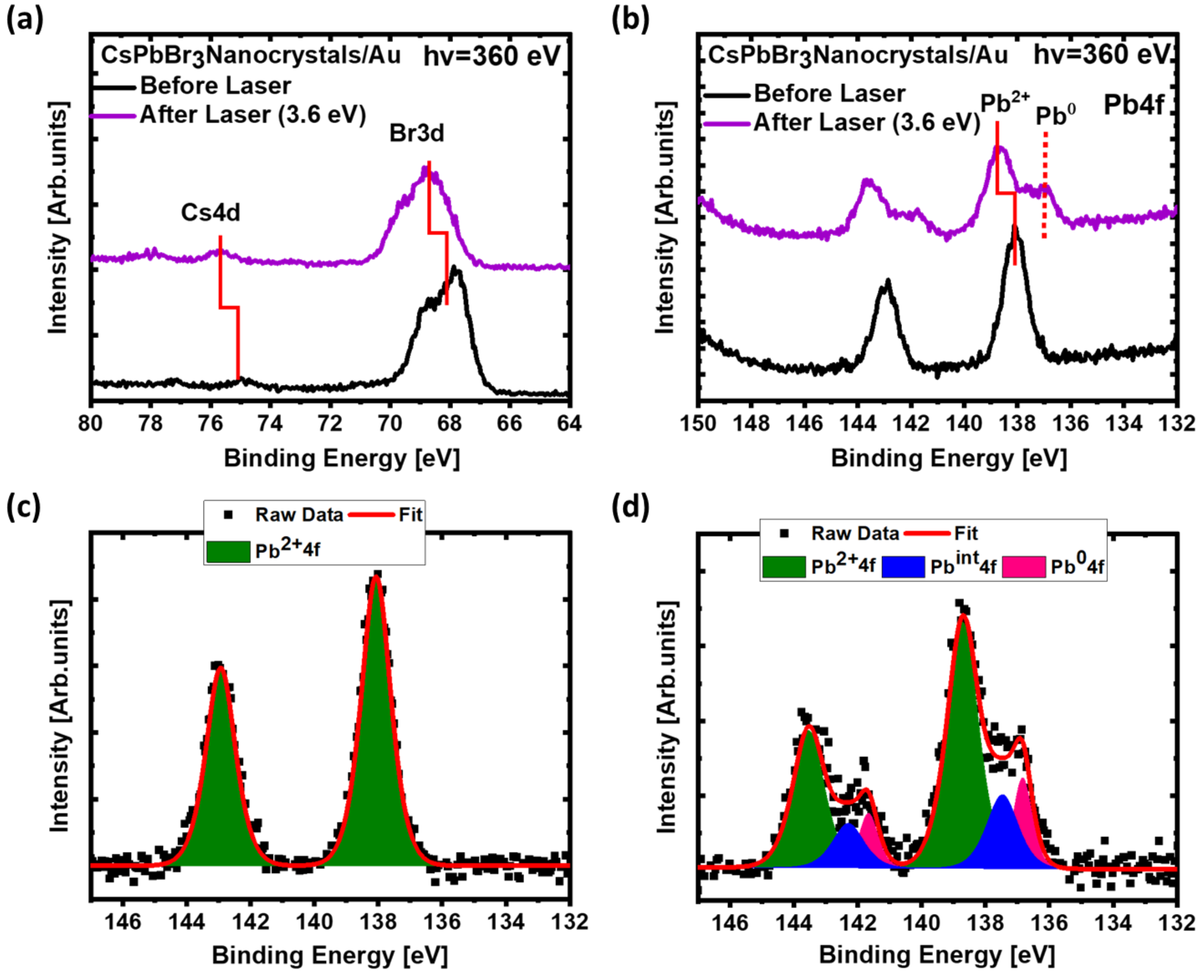

Figure 3.13. (a) Cs 4d and Br 3d, (b) Pb 4f spectra measured with a photon energy of 360 eV before and 30 minutes after laser illumination at 343 nm and a fluence of 3.5 mW/cm^2, and (c) and (d) are the deconvolution spectra of corresponding Pb 4f before and 30 minutes after the laser respectively.

The component at low binding energy of 136.84 eV is assigned to the formation of metallic lead, Pb^0, a common sign of damage to the perovskite structure.[64,65] The second new component, in-between the Pb^{2+} and the Pb^0 at the binding energy of 137.45 eV is of unknown origin and will be referred to as the intermediate component (Pb^{int}), and will be discussed later in this chapter. The core level of the Au substrate is shown in Figure 3.14 (a), where a shift of 0.06 eV is observed after the 30 minutes of UV laser at high fluence.

As discussed before, ligands exist to stabilize the $CsPbBr_3$ NCs and to prevent their aggregation in the solution. Figure 3.14 (a) and (b) show C 1s spectra taken before, 30 minutes after, and 60 minutes after UV laser at low and high fluence to examine the influence of UV light on ligands. Since the number of carbon contributions involved both from the adventitious carbon and acetate ligands, it is complicated to deconvolute the C 1s peak. Apparently, shift in the binding energy of C 1s is seen as well as change in intensity of the peak after the UV laser. At low fluence, no change in intensity of the peak observed, however the peak becomes broader, suggesting no loss of the ligands occur despite their dissociation from the NCs, Figure 3.14 (a). With high fluence, not only did the peak become broader, but a slight decrease in intensity of C 1s was observed. However, it is complicated to describes whether decrease in intensity of C 1s observed due to loss of ligands or from the adventitious carbon.

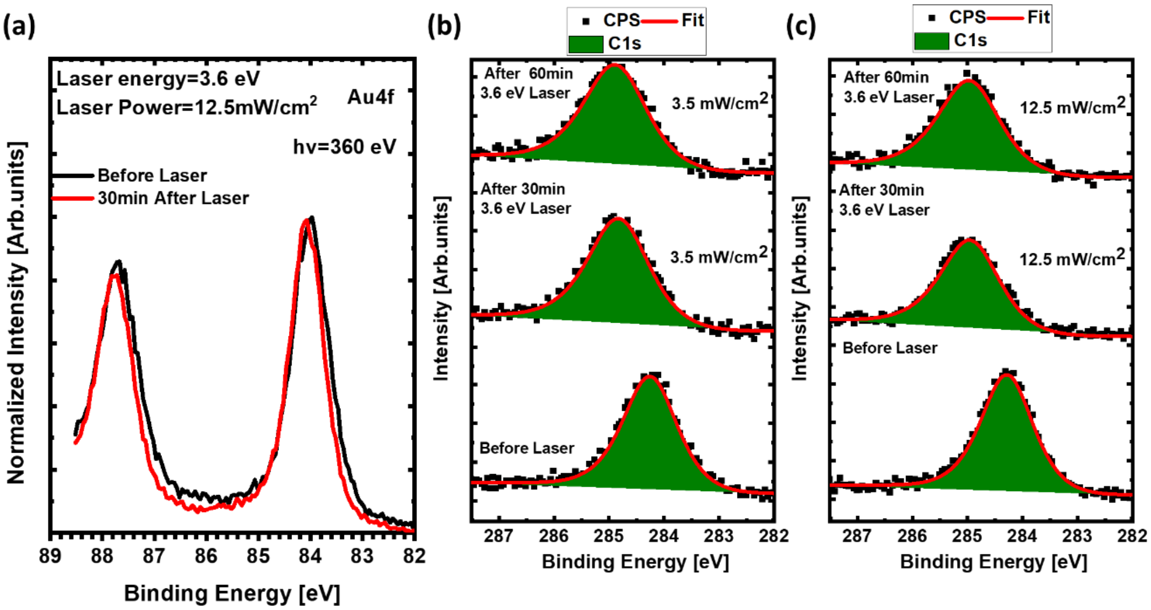

Figure 3.14. (a) Au 4f spectra before and after UV laser for 30 minutes, C 1s spectra before after 30- and 60-minutes UV laser (b) 3.5 mW/cm^2 and (c) 12.5 mW/cm^2.

Time evolution data of Pb 4f were recorded to quantify variations in intensity and binding energies of Pb 4f core level spectra under different laser fluence and exposure time. In Figure 3.15, the intensity ratio of each of the Pb 4f components relative to the Pb^{2+} before laser exposure is plotted as a function of time. The evolution of the three different components of the Pb 4f spectra are shown for a time series with two periods of laser exposure, 30 and 60 minutes, with periods without laser before and after each laser exposure, panel (a) shows the results with laser fluence of 3.5 mW/cm^2 and panel (b) 12.5 mW/cm^2. It can be seen in Figure 3.15 (a), initial laser exposure with low fluence leads to a decrease in relative intensity of Pb^{2+} though no additional component appears, neither Pb^{int} nor Pb^0. At the 15 minutes of laser exposure, Pb^0 and Pb^{int} components appear and show increasing intensity over time. When the laser is turned off, the Pb^{2+} shows a sharp decrease whereas Pb^0 and Pb^{int} show a constant ratio (with a small increase in both Pb^0 and Pb^{int}). Upon switching the laser on again, for 60 additional minutes, the ratio of the three components remains relatively constant. With the high laser fluence, the degradation is stronger as can be seen in Figure 3.15 (b), as soon as laser is switched on, the Pb^0 and Pb^{int} components appears while the intensity of the Pb^{2+} component decreases.

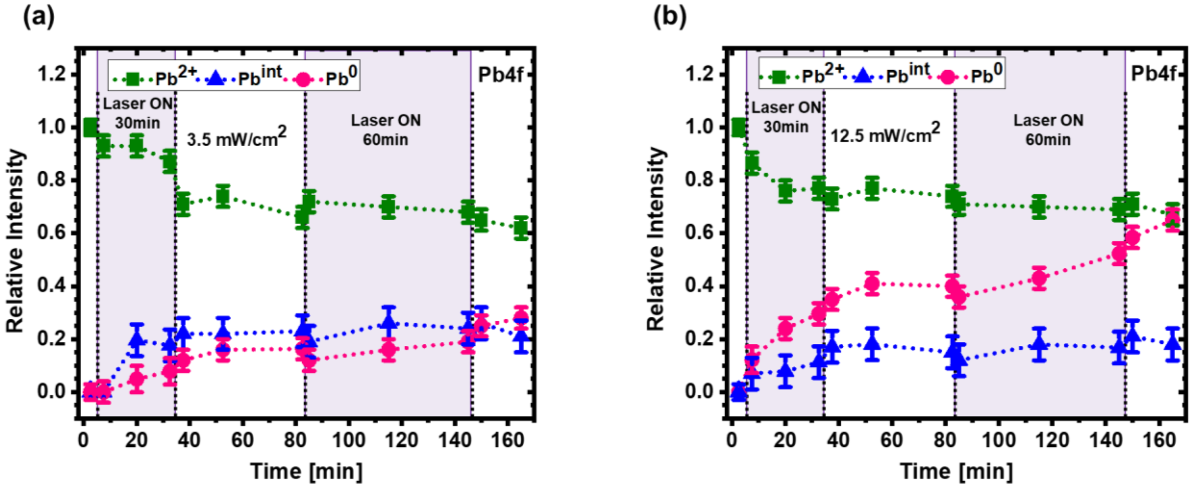

Figure 3.15. Relative intensity of different components of Pb4f spectra calculated (intensity of Pb4f component divided by intensity of Pb 4f before laser) of $CsPbBr_3$ PNCs on Au measured with the photon energy of 360 eV (a) with the laser fluence of 3.5 mW/cm^2 and laser energy of 3.6 eV, (b) with the laser fluence of 12.5 mW/cm^2 and laser energy of 3.6 eV. The shaded area in the figure represents 30min exposure under laser for small rectangle and 60min exposure for large rectangle.

Upon further laser exposure, Pb^0 increases rapidly, the Pb^{int} also increases but at a lower rate while Pb^{2+} decreases. When switching the laser off a gradual decrease in intensity Pb^{2+} and increase in Pb^0 and Pb^{int} was observed. Turning the laser on again, a decrease in intensity of Pb^{2+} and an increase in Pb^0 was observed while only a small change was observed for Pb^{int}. Comparing the low and high fluency exposure, the behavior is relatively similar for both series with some difference in how fast the intensity ratios change. The Pb^{2+} shows a strong decrease during the first laser exposure which then remains more stable and for low and high fluency series ends at approximately 0.6 and 0.7 of the starting intensity. The Pb^{int} exhibits and increase up to a ratio of

0.2 that then remains relatively stable over time for both series. The main difference comes in the Pb^0 which in both series shows and increase over time but that is much larger in the high fluency series. Overall, the largest changes were observed during the first 30 minutes of laser exposure suggesting that the pristine structure of $CsPbBr_3$ NCs is more easily damaged than a structure with more defects, which could be attributed to the transformation from cubic to orthrombhic phase transition upon the light.[66] This orthorhombic phase is much more robust and potentially more stable against light that could explain the less changes observed with 60 additional minutes.[67] Also, Pb^{int} remains almost stable for the both power of laser once its reached to certain threshold.

Similarly, as the data presented for different components of Pb 4f in Figure 3.15, the intensities of Cs 4d, Br 4d and ΣPb 4f (Pb^{2+}, Pb^{int}, Pb^0) core levels relative to respective intensities before the laser are calculated and shown in Figure 3.16 (a) and (b) as a function of laser exposure time with different laser fluences. After the 30 minutes laser exposure with low fluence, intensities of both Cs 4d and ΣPb 4f increases slightly within error margin while intensity of Br 3d decreases. However, for the second cycle of 60 minutes more exposure, no further changes in intensities of the core levels were observed. The same trend but a little more change in intestines is observed with higher fluence of laser except ΣPb 4f, which increased after 60 minutes more exposure due to more Pb^0 formed under high power.

To calculate the shift in the binding energy, the binding energy of perovskite core levels relative to their binding energy position before the laser is plotted as function of time and shown in Figure 3.16 (a) and (b). There is no change in binding energy of Pb^{int} and Pb^0 is found with any laser fluence and any exposure time. For the Pb^{2+}, under the both laser fluences, a large shift of about 0.40 eV towards higher binding energy was observed, followed by a shift that progressed to even higher binding energy up to 0.70 eV when the laser is turned off. Upon exposure to 60 more minutes, for both the fluences, the photo induced shift of Pb^{2+} decrease approximately from 0.70 eV to 0.40 eV. Looking at the shift of Br^-3d rather, the shift is larger than for the Pb^{2+} with the high fluence series shows a shift of ~ 0.90 eV directly after the first exposure which remains same after the second exposure. For the low fluence series, the amount of shift in Br^-3d after second exposure is similar to as of high fluence series but after the first exposure the shift is similar to Pb^{2+} of about 0.70 eV. Likewise, the peak position of Cs^+4d shifted in a comparable way towards higher binding energy after the 30 minutes laser exposure and remains almost unchanged with further 60 minutes exposure. For the C 1s, with high fluence series, a similar shift in the binding energy as for Pb^{2+} observed, however, this shift is little lower than for Pb^{2+} at low fluence series.

From this it can be concluded that UV light damages the NCs structure directly, evidenced as the formation of Pb^0 and Pb^{int}. Despite the formation of two new chemical specie occurring at different rates for two fluences, the binding energy shift of Pb^{2+} is same for both. The damage to the structure is also reflected by the shift in Br^-3d peak, where the full shift occurs immediately for the high fluence and during/after the second exposure for low fluence. And the Pb^{2+} binding energy shift getting closer to Br^-3d shift with prolong exposure.

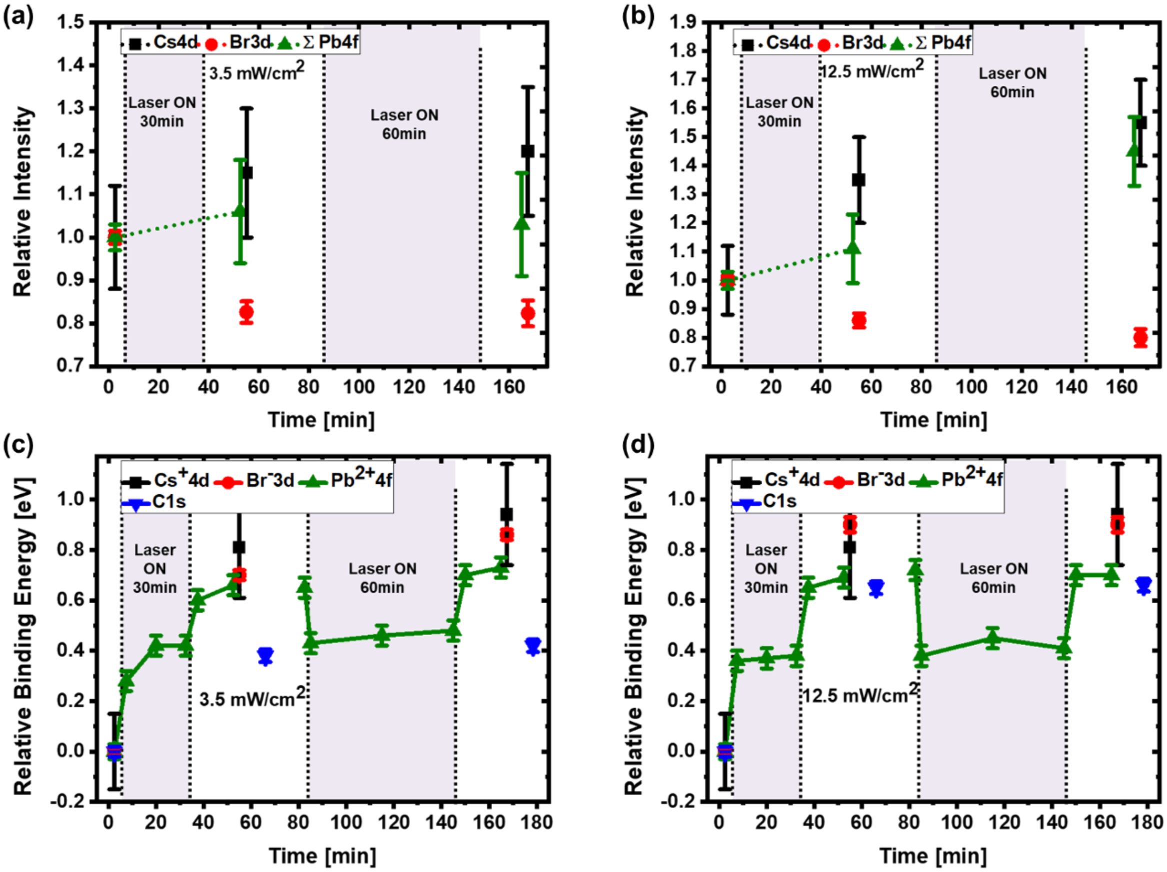

Figure 3.16. Relative intensity of different core levels such as, Cs 4d, Br 3d and Pb 4f spectra calculated (intensity of cesium, bromide and lead core levels divided by intensity of the corresponding core levels before laser) of $CsPbBr_3$ PNCs on Au measured with the photon energy of 360 eV (a) with the laser fluence of 3.5 mW/cm^2 and laser energy of 3.6 eV, (b) with the laser fluence of 12.5 mW/cm^2 and laser energy of 3.6 eV. Relative binding energy of Cs 4d, Br 3d, Pb 4f and C 1s core level calculated (binding energy of cesium, bromide and lead core level subtracted from the binding energy of the corresponding core level before laser) (c) with 3.5 mW/cm^2, (d) 12.5 mW/cm^2.

Considering the shift in Br^-3d occurs quickly with UV light exposure, then the shift occurs for the Pb^{2+} during the laser illumination can be divided into two parts, first, the large shift towards higher binding energy (similar to Br^-3d) a chemical shift and the second, the surface photovoltage towards the lower binding energy from the bandgap excitation of CsPbBr$_3$ NCs. This surface photovoltage is then reversible, even with the damaged structure, as seen by a similar effect during and after the second exposure of the laser, as well as large shift towards lower binding energy (surface photovoltage) with high fluence.

To observe the effect of UV laser illumination in the bulk of NCs, the same experiment was conducted on a different sample of CsPbBr$_3$ NCs spin-coated on Au substrate with the photon energy of 650 eV. The Pb 4f spectra measured at 360 eV and 650 eV photon energy after UV laser exposure at two different laser fluences are compared and shown in Figure 3.17 (a) and (b). At low fluence, although Pb^{int} exist at 650 eV, the relative peak intensity of Pb^{int} is smaller than in the 360 eV. Meanwhile, the Pb^{0}4f specie is found only at higher fluence with the photon energy 650 eV. Also, it is important to mention here that the width of Pb 4f component is large at photon energy of 650 eV than the 360 eV, due to higher resolution at 360 eV because of PM4 beamline settings.[69]

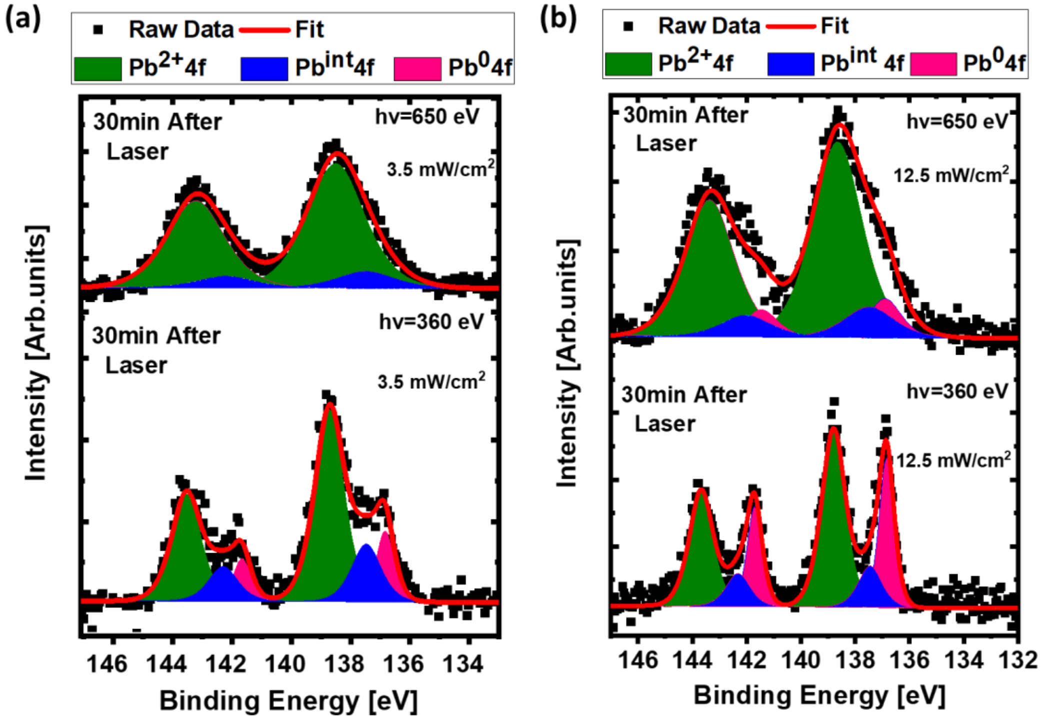

Figure 3.17. Comparison of Pb 4f spectra measured with a photon energy of 360 and 650 eV before and 30 minutes after UV laser illumination of energy 3.6 eV (a) with the fluence of 3.5 mW/cm^2 (b) with the fluence of 12.5 mW/cm^2.

3.3.3 Stability under x-rays

To investigate the effects of x-ray radiation on $CsPbBr_3$ nanocrystals (NCs) deposited on Au substrate, the TEMPO beamline of SOLEIL synchrotron was used. The x-ray flux at TEMPO was 4×10^{13} photons/sec [68] compared to 1×10^{9}~1×10^{10} photons/sec at PM4,[69] which means flux at TEMPO was at least three orders of magnitude higher than at PM4 beamline (used for the stability of NCs under IR and UV laser in previous sections). All the core levels were recorded at photon energy of 360 eV. The core levels were recorded in the following sequence: Cs 4d and Br 3d in one window then Pb 4f for 30 minutes under continuous x-ray exposure followed by Cs 4d and Br 3d. The measured core levels were fitted with Voigt function by using Shirley background, and intensities and corresponding binding energies of the core levels were obtained. As stated previously, analysis of C 1s and valence band will not be discussed due to complexity of fitting different components for carbon and existence of Fermi-step of gold (Au) in the valence band.

The steady state PES spectra of different core levels of $CsPbBr_3$ nanocrystals deposited on gold (Au) substrate, were measured with photon energy of 360 eV. Figure 3.18 (a) shows the Cs 4d and Br 3d spectra measured at fresh spot and after 30 minutes exposure to x-rays. There appears to be negligible change in intensity or binding energy after increasing x-ray exposure time.

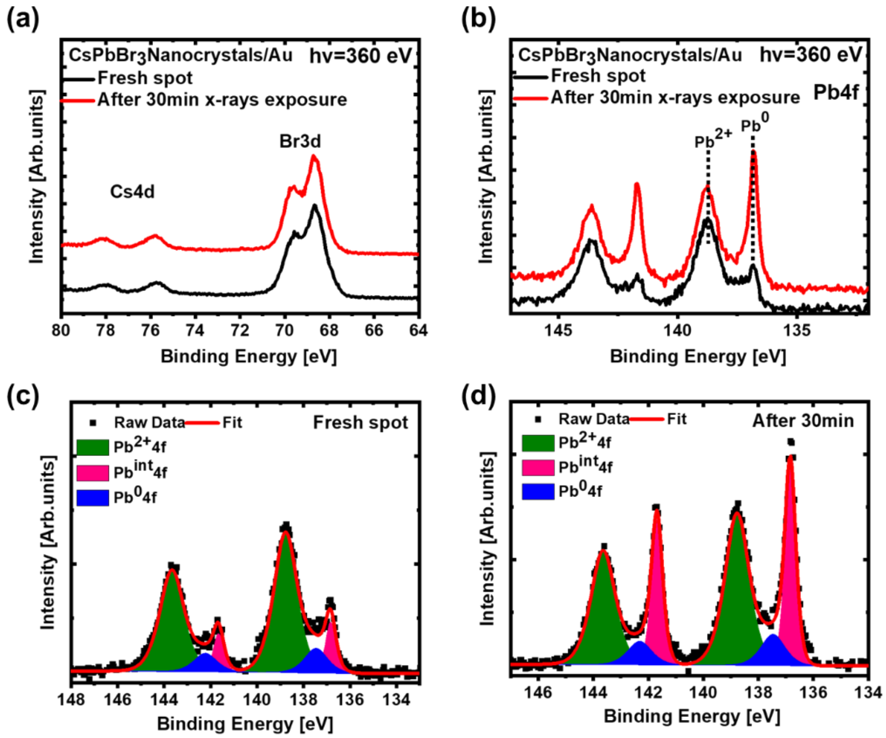

Figure 3.18. shows (a) Pb 4f spectra of fresh spot and after 30 minutes of continuous exposure to x-rays measured with a photon energy of 360 eV, while (b) and (c) are the deconvolution spectra of corresponding Pb 4f fresh spot and 30 minutes after the continuous exposure to x-rays respectively.

Figure 3.18 (b) shows the Pb 4f spectrum measured at fresh spot and after 30 minutes exposure to x-rays with the corresponding fitting spectra in Figure 3.18 (b) and (c). Three contributions are visible in the Pb 4f core level at the binding energies of 138.77 eV, 137.45 eV and 136.84 eV. The main component at the binding energy of 138.77 eV is assigned to the Pb^{2+} of $CsPbBr_3$, while the component at 136.84 eV is assigned to the formation of metallic lead, Pb^0, evidence of damage to the perovskite structure under x-rays.[70] The intermediate component between Pb^{2+} and Pb^0 at the binding energy of 137.45 eV is associated with Pb^{int}, as observed in the NCs following UV laser illumination, and its explanation will be provided later.

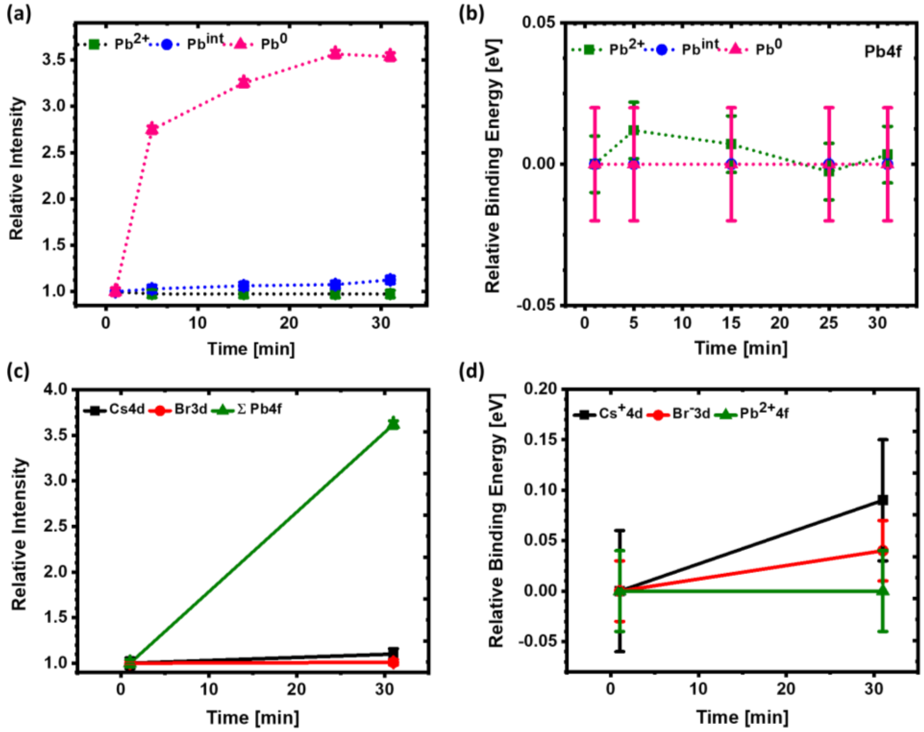

Figure 3.19**.** (a) Relative intensity of different components of Pb4f spectra calculated (intensity of Pb 4f component divided by intensity of Pb 4f (fresh spot)), (b) relative binding energy (binding energy of Pb 4f component subtracted from the binding energy of Pb 4f (fresh spot)) of $CsPbBr_3$ NCs on Au measured with the photon energy of 360 eV. (c) Relative intensity of different core levels such as, Cs 4d, Br 3d and ΣPb 4f spectra calculated (intensity of cesium, bromide and lead core levels divided by intensity of the corresponding core levels (fresh spot)), and (d) Relative binding energy of Cs^+ 4d, Br^- 3d and Pb^{2+} 4f core level calculated (binding energy of cesium, bromide and lead core level subtracted from the binding energy of the corresponding core level (fresh spot)) of $CsPbBr_3$ NCs on Au.

Time evolution data of Pb 4f were collected to investigate the changes in intensity and binding energy of these components over x-ray exposure time. As it can be seen in Figure 3.19 (a), the intensity of Pb^0 increased fast initially and then slowly increased with increasing exposure time, whereas the intensity of Pb^{2+} and Pb^{int} remained relatively constant. However, as shown in Figure

3.19 (b) prolonging the duration of x-ray exposure had no effect on the binding energy of either component. Similarly, when the intensity and binding energy of Cs 4d and Br 3d are examined, no change in intensity of Cs 4d and Br 3d is detected, despite the fact that the intensity of ΣPb 4f (Pb^{2+}, Pb^{int} and Pb^0) increased due to the increase in intensity of Pb^0, Figure 3.19 (c). Meanwhile the binding energy of all the core levels remains unchanged, Figure 3.19 (d).

To sum up, high x-ray flux damages the $CsPbBr_3$ NCs instantaneously as the fresh spot, Pb 4f core level showed two new components, Pb^0 and Pb^{int} in addition to Pb^{2+} (main component) of perovskite. Time taken for the acquisition for the spectrum was less than a minute, meaning that high x-ray flux damages the NCs immediately (faster than acquisition time). However, no further changes observed with increasing further exposure to x-rays.

UV laser and x-rays with high flux cause similar damage in terms of changes in Pb 4f spectra, with the appearance of two new components without any additional component in the Cs 4d and Br 3d core levels. The following section will compare the stability of NCs under UV light and high x-ray flux.

3.3.4 Comparison of $CsPbBr_3$ NCs stability under UV laser & x-rays

The stability of NCs under UV laser and x-rays are compared and shown in Figure 3.20. The Pb 4f spectra of the pristine NCs recorded with a low flux x-ray shown in Figure 3.20 (a) (the bottommost spectrum). The low flux of x-ray exposure ensures that the NCs remains pristine and hence considered undamaged as Pb 4f spectrum shows a single spin-orbit doublet related to Pb^{2+} of $CsPbBr_3$.[63] The corresponding Cs 4d and Br 3d spectra depicted in Figure 3.20 (b) also show the single component associated to Cs^+ and Br^- of $CsPbBr_3$. The binding energy extracted from the least squares fits of the spectra in Figure 3.20 can be found in Table 3.2. After 30 minutes laser exposure at both fluences, not only the shift in Pb^{2+} occurred but also two new chemical specie, Pb^{int} and Pb^0 is also seen, Figure 3.20 (a), with also shift in the other core levels, Cs 4d and Br 3d, Figure 3.20 (b). The Pb 4f spectrum in Figure 3.20 (a) (top spectrum) recorded using high x-ray flux is noticeably similar to the Pb 4f spectrum after laser exposure rather than like the spectrum recorded with low x-ray flux, both in the shape (with the contribution of both Pb^{int} and Pb^0 including Pb^{2+}) and binding energy position. Likewise, the Cs4d and Br 3d spectrum was also at the same binding energy position as to the Cs 4d and Br 3d spectrum after the laser exposure. This leads to the conclusion that first exposure of high x-ray flux damages the structure of perovskite NCs in the same way as UV laser exposure does after 30 minutes.

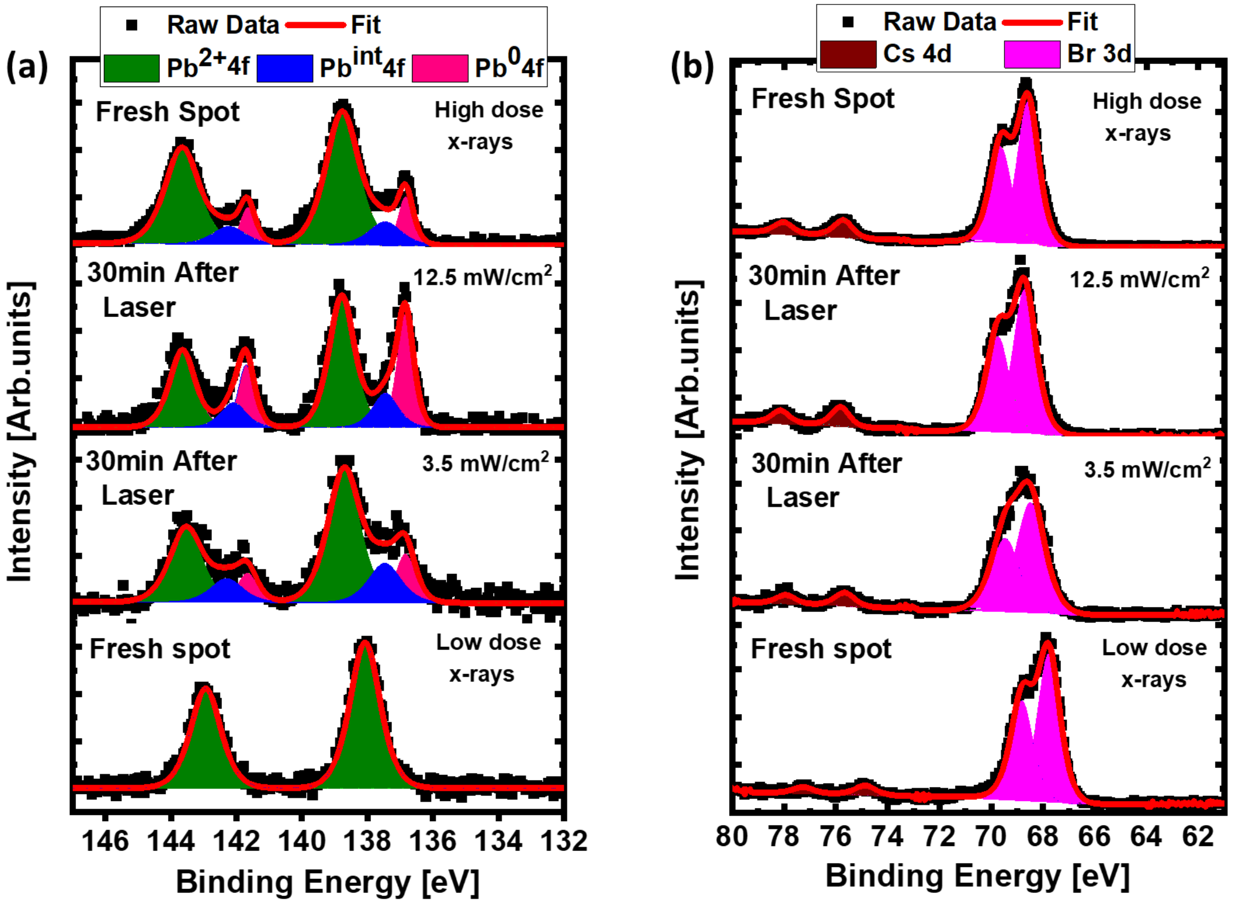

Figure 3.20: (a) Cs 4d and Br 3d, (b) Pb 4f, spectra of CsPbBr$_3$ NCs on gold measured with low x-rays flux with a photon energy of 360 eV, fresh spot before laser, after laser exposure for 30min with laser fluence of 3.5 mW/cm^2 and 12.5 mW/cm^2 and energy of 3.6 eV, and Cs 4d, Br 3d and Pb 4f spectra of CsPbBr$_3$ NCs measured with high x-rays flux with a photon energy of 360 eV.

Table 3.2: Shows the binding energies (eV) extracted from the least square fit of Cs 4d (3/2), Br 3d (3/2), Pb 4f (5/2) spectra of CsPbBr$_3$ NCs on Au in Figure 1. The standard deviation in binding energy position for Br 3d and Pb 4f core levels was within the range of 0.05 eV whereas for Cs 4d in the range of 0.10 eV

	Cs 4d	**Br 3d**	**Pb 4f**		
	Cs^+ (eV)	Br^- (eV)	Pb^{2+} (eV)	Pb^0 (eV)	Pb^{int} (eV)
	Cs $4d_{5/2}$	Br $3d_{5/2}$	Pb $4f_{7/2}$	Pb $4f_{7/2}$	Pb $4f_{7/2}$
Low x-ray flux (undamaged)	74.85	67.78	138.06	-	-
Low laser fluence(damaged)	75.66	68.48	138.66	136.84	137.45
High laser fluence (damaged)	75.82	68.71	138.75	136.84	137.45
High x-ray flux (damaged)	75.70	68.58	138.77	136.84	137.45

3.3.5 Discussion

The chemical changes observed under UV laser illumination are solely attributed to the UV light itself, as the experiment performed using low x-ray flux to prevent any damage from x-rays. This approach enabled the investigation of the effects exclusively caused by UV light since x-rays are usually known to degrade the perovskites NCs as reduction of Pb^{2+} to metallic lead (Pb^0) occurs.[64] In our work, no Pb^0 forms even under IR laser illumination for 30 minutes due to low x-ray flux at the PM4 beamline, as detailed in the experimental section, suggesting that the observed changes are uncorrelated with x-ray illumination. As discussed before, 3.6 eV UV laser excitation of $CsPbBr_3$ perovskite NCs leads to not only the surface photovoltage but also to the significant chemical changes. These observed chemical changes are indicated by the appearance of two new components, metallic lead (Pb^0) and an intermediate component (Pb^{int}) in addition to Pb^{2+}, in the Pb 4f core level. The UV laser induces the photoinduced electron-transfer reaction, in which electron density transferred from halides dominated valence bands to the lead dominated conduction bands, resulting in the formation of $Pb^0(s)$ and $Br_2(g)$. This $Br_2(g)$ leaves the surface as a gas and Pb^0 remains on the surface of perovskite as reported previously.[71] This mechanism is consistent with the decrease of $Br^-$and Pb^{2+} while increase in intensity of Cs^+, can be explained as follows. Usually, the ligands are attached to the PNCs via the surface termination of $CsPbBr_3$ with either $PbBr_2$ or CsBr, but CsBr being favored more.[66] Under the illumination, excitons are generated which subsequently dissociate and diffuse towards the surface of NCs where they are captured by surface ligands, resulting in desorption of ligands from the surface due to their low binding energy with which ligands are attached to NCs. However, since the ligands are detached chemically but not physically (tentatively with high fluence), it cannot explain the increase in intensity of Cs 4d. The potential explanation for the increase in intensity of cesium could be that the loss of bromide causes the inorganic core of NCs to consist predominantly of cesium and lead (albeit not entirely). Since the signal coming from the inorganic core (NCs) is now largely constituted of cesium and lead with little contribution from bromide, the intensity of both cesium and total lead (Pb) increases. This argument is further supported by the increase of cesium and ΣPb in the same ratio.

However, as previously stated, the emergence of Pb^{int} between Pb^{+2} and Pb^0 is of unidentified origin, and we assign it as Pb^{int} due its binding energy position between Pb^{+2} and Pb^0, as well as the lack of obvious and clear indication of which oxidation state of Pb it is. The intermediate Pb state could potentially be explained as small initial formed particles of Pb^0, which are still epitaxially attached to $CsPbBr_3$ crystal lattice as described by Dang et al.[72] Upon continued electrons irradiation, Dang et al. showed that these particles detached from parent crystal lattice and accumulate at the surface of $CsPbBr_3$. However, this is not the case here, though the intensity of Pb^0 increased continuously with illumination, Pb^{int} remains constant once it is formed and to follow the Dang model it would need to decrease at least once the laser is tuned-off. Nonetheless, it explains the increase in intensity of Pb^0 even after turning off the laser due to the increase in temperature caused by the laser irradiation, and also in the case of high x-ray flux, where intensity of Pb^0 increased with continuous exposure to x-rays. As it is described that diffusion of Pb^0 at the surface from the bulk is facilitated by high temperature. Furthermore, it is evidenced that Pb^{int} is a feature that dominates at the surface of NCs but not in the bulk of the crystal. The UV laser illumination at 650 eV photon energy, where the calculated probing depth (3λ) was 4.60 nm compared to 2.70 nm at 360 eV [73] due to larger inelastic mean free path for photoelectrons at 650 eV, shows that Pb^{int} exists under both fluences of the laser, 3.5 mW/cm^2 and 12.5 mW/cm^2. However, compared to 360 eV, at 650 eV the relative intensity of Pb^{int} is small, indicating Pb^{int} is a surface contribution. This gives indication that presence of Pb^{int} is exclusively at the surface and/or at the interface between the NCs and Au, suggesting Au might play a role in the formation of Pb^{int}. Moreover, at 650 eV, Pb^0 appears only at high fluence of the laser, indicating UV induced damage to the perovskite NCs extends deeper into the crystals.

The interaction between Au and perovskite thin-films has previously been studied and reported. For instance, Cha et al.[54(b)] showed that $MAPbI_{3-x}Cl_x$ thin-films deposited on Au revealed the formation of Pb^0 which has been attributed to the interfacial interaction between Au and perovskite. Similarly, Zhao et al.[54(a)] investigated the interaction between $MAPbI_3$ perovskite and thermally deposited Au on the top, observing a shoulder in Pb 4f core level spectra, in-between the Pb^{2+} and Pb^0 but without the formation of Pb^0 at the binding energy of 137.45 eV (exactly the same peak position as we have for Pb^{int}), which has been attributed to the partial charge transfer between Au and perovskite. These reports suggest that Au deposition on-top of perovskite does not result in the formation of Pb^0. However, perovskite on-top of the Au leads to the formation of both Pb^0 and Pb^{int} (speculative in the case of $MAPbI_{3-x}Cl_x$). Thus, it can be concluded that Pb^0 can be formed at the surface under the radiation, whereas Pb^{int} formed only when Au interacts with the perovskite.

Therefore, a possible explanation for Pb^{int} is that it might come from the incorporation of Au in the perovskite such as $Cs_2Au_2Br_6$. [74,75] This is partially supported by the oxidation of Au where a small 0.06 eV shift in the Au 4f binding energy after laser exposure observed. However, this small shift could also be from the drift in photon energy. Also, the formation of noble metal containing perovskite products occur rather at extreme conditions [76] and they should start from the interface of Au substrate and perovskite NCs, however depth profiling shows that Pb^{int} is a specie that dominates at the surface of the perovskite material.

Similarly, under the x-rays of high flux severe dismantling of $CsPbBr_3$ NCs lattice occur through the detachment of surface ligands due to their weak affinity to the surface atoms of NCs, resulting in the collapse of NCs surface.[70] This happens as a result of the excitation of electron density from halide dominated valence band to lead dominated conduction band, leading to the desorption of bromide as a gas and conversion of Pb^{2+} to Pb^0 as explained by Swanstrom et al., for $CsPbBr_3$ thin-film and its degradation under hard x-rays.[29] The redox chemistry at the surface of $CsPbBr_3$ thin-film was described in the following reaction:

$$CsPbBr_3 \rightarrow Pb^0(s) + CsBr(s) + Br_2(g)$$

Where CsBr(s) appears as a new specie derived from the formation of new component in both Cs 4d and Br 3d core level, in addition to their main component. However, no evidence of new components in Cs 4d and Br 3d occur in our case, although a new component in Pb 4f appears, Pb^{int}. Thus, it can be envisioned that charge transfer between NCs and Au may have caused the formation of Pb^{int} as predicted by Zhao et al.[54]; however, no conclusive evidence exist to substantiate this assumption either.

Kerner et al.[55] investigates the degradation of $CH_3NH_3PbI_3$ perovskite thin-film with deposition of Au on-top. Using XPS (Al Kα as x-rays source), even after evaporation of 50 nm Au, they observed a Pb 4f signal which then ascribed to the diffusion during the deposition of Au. Under continuous x-rays illumination, they identify a chemical specie in Pb 4f core level in-between Pb^{2+} and Pb^0 at the binding energy of 137.5 eV, which they assigned to underpotential deposition of Pb (denoted as Pb_{UPD}) on Au surface. The peak position of this intermediate chemical specie (Pb^{int} in our case) is consistent with reported binding energy position for Pb_{UPD}.[77,78] Underpotential deposition is a spontaneous surface adsorption reaction where an ion changes oxidation state upon adsorption at a voltage lower than the bulk reaction potential.[77] The degradation mechanism at $CH_3NH_3PbI_3$/Au interface is proposed as, under x-rays illumination, a strong and spontaneous reaction between iodide/Au separated the Pb^{2+} ions by a layer of adsorbed neutral iodide (I^0_{UPD}). Electrons are released upon the adsorption of I^0_{UPD} onto Au, which decomposes the $CH_3NH_3PbI_3$ into PbI_2 and methylammonium $(CH_3NH_3)^+$. These electrons are captured by a proton from $CH_3NH_3^+$, resulting in the formation of $CH_3NH_2^+$ and H^0_{UPD}. The adsorbed H^0_{UPD} and I^0_{UPD} reacts and are released as volatile HI, I_2 and/or H_2 gases, whereas the remaining PbI_2 and $CH_3NH_2^+$ reacts via proton transfer reaction to form more HI, volatile organic specie and Pb^0_{UPD}. In contrast to $CH_3NH_3PbI_3$/Au, at the interface of PbI_2/Au, similarly the electrons are released due to iodide UPD reaction (I^0_{UPD}). Since the absence of organic species (CH_3NH_3) in PbI_2, there is no availability of protons for capturing these electrons. The only possible destination for these excess electrons is Pb^{2+} cations in the underpotential deposition reaction, resulting in the formation of underpotential deposition of Pb (Pb_{UPD}) on the Au surface rather than Pb^0_{UPD} with the accumulation of oxidized iodide species.

Thus, a more judicious explanation for the formation of Pb^{int} that has the binding energy position of 137.45 eV is attributed to the underpotential deposition of Pb (Pb_{UPD}) at the Au surface. As both with UV laser and high x-rays flux damage the perovskite structure resulting in the release of electrons which are consumed by Pb^{2+} to adsorb at the surface of Au as Pb_{UPD} (Figure 3.21), and the binding energy of Pb^{2+} shifts to slightly lower binding energy. This underpotential deposition reaction is likely to stop once the surface of the Au is covered with Pb_{UPD} (submonolayer or monolayer of Pb on Au),[55] as evidenced by a constant intensity of Pb^{int} once a certain threshold is reached, shown in Figure 3.15. The correlation between the assignment of Pb^{int} to Pb_{UPD} is further strengthened by the observation that Pb^{int} formation exclusively took place when the perovskite structure breaks and Pb^{2+} is freed, as demonstrated by the absence of Pb^{int} formation under low x-ray flux and IR laser for 30 minutes. Moreover, it is worth noting that desorption of bromide is not necessary for the occurrence of Pb_{UPD}, but release of Pb^{2+} is required upon the damage to the perovskite structure. The formation of Pb^{int} is noticed under IR illumination for prolong exposure of 90 minutes where no desorption of bromide occurs, evidenced as unchanged intensity of Br 3d after the laser. However, the broadening of Br 3d core level suggests the apparent release of electrons by bromide to free the Pb^{2+} to form the Pb_{UPD}. The apparent breaking of perovskite under IR laser that frees Pb^{2+} happens as a result of heating of the NCs through reflected IR light by the Au substrate.[79] These results also suggest that for the formation of Pb^0, desorption of bromide should occur but not for the formation of Pb_{UPD}. To sum up, not only the UV excitation and x-rays of high flux, but also the IR illumination for prolonged exposure, can lead to the under potential deposition of Pb on the exposed Au surface. This Pb_{UPD} happens only when perovskite structure breaks and Pb^{2+} is released, which requires excitation above the bandgap or ionization to be activated by x-rays or heating (induced by the IR laser here). Finally, ligands do not play a significant role in the formation or prevention of Pb_{UPD}.

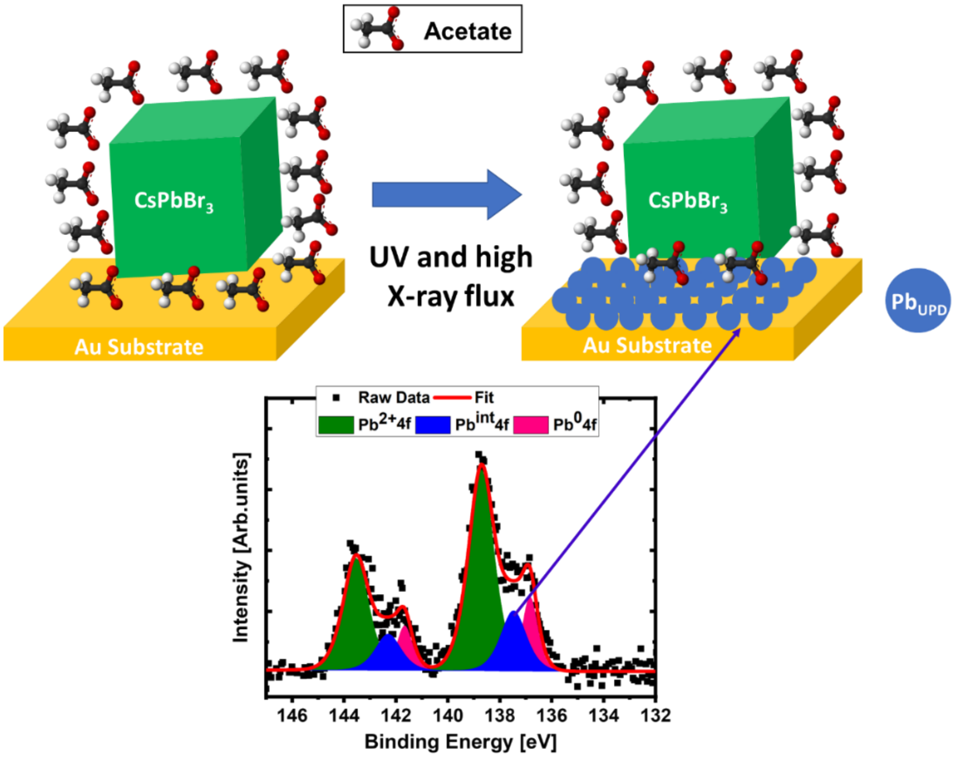

Figure 3.21: shows the schematic illustration of underpotential deposition of Pb on Au surface which occurs when the electrons upon the desorption of bromide as a gas consumed by the Pb^{2+}. This adsorption of Pb is highlighted as Pb^{int} in Pb 4f spectrum.

To summarize, both UV light and x-rays with high flux can cause similar and irreversible damage to the $CsPbBr_3$ NCs deposited on the Au substrate. The degradation mechanism is proposed as the formation of metallic Pb (Pb^0) and halogen gas (Br_2) as a result of charge transfer from halide dominated valence band to lead dominated conduction band. Of greater importance, the interaction between Au and perovskite leads to the adsorption of the Pb via the underpotential deposition of lead (Pb_{UPD}), which was evidenced as an intermediate component (Pb^{int}) between Pb^{2+} and Pb^0 in Pb 4f core level. Moreover, sublimation of bromide is necessary for the formation of Pb^0 but not for the formation of Pb_{UPD}. These insights suggest that the interface of $CsPbBr_3$ NCs with Au is chemically unstable, and irreversible changes can occur when exposed to IR (prolong exposure), UV and intense x-rays radiation.

3.4 Conclusion

In this study we investigate the influence of infrared (IR) laser, ultraviolet laser (UV) light and soft x-rays stability of $CsPbBr_3$ perovskite nanocrystals (NCs) (having the cubic structure and bandgap of 2.30 eV) on gold (Au) substrate using photoelectron spectroscopy. To isolate the effect of IR and UV laser from x-ray induced changes, a Low-Dose PES setup at BESSY II was chosen, where due to low x-ray flux coupled with high transmission ArTOF spectrometer, the effects of laser exposure are isolated from any x-ray induced damage. IR illumination for 30 minutes apparently does not lead to any structural changes of perovskite NCs, however a rigid and irreversible shift in the binding energy of the core levels observed from the excitation of bromide interstitial and/or bromide vacancies located at the midgap position. For the second cycle of the laser, 60 minutes more exposure, not only does the shift in binding energy of the core levels increases, but also a new chemical specie in the Pb 4f assigned as Pb^{int} appears. This emergence of Pb^{int} suggests the chemical changes at the interface of Au and perovskite. The UV (343 nm or 3.6 eV) laser illumination greater than the bandgap of $CsPbBr_3$ NCs (2.30 eV) causes the irreversible damage to the NCs characterized by the formation of two new chemical species, reduced lead (Pb^0) and an intermediate component (Pb^{int}), a component between the Pb^{2+} and Pb^0, in Pb 4f spectra. The induced damage increased with increasing the fluence of the UV light and exposure time. However, after a certain exposure time no further changes observed, implying pristine structure of NCs is more easily damaged than a structure with more defects. Similarly, under the x-ray of high flux, the decomposition of NCs occur in an identical way with the appearance of two new chemical specie, Pb^{int} and Pb^0, in the Pb 4f spectra. It is worth mentioning here that high x-ray flux instantly damages the NCs when exposed. The formation of Pb^0 is related to the transfer of charge from halide dominated valence band to the lead dominated conduction band in $CsPbBr_3$ NCs. The dominance of Pb^{int} on the surface and/or at the interface lends credence to the hypothesis of possible interaction between the Pb and Au. Hence, the damage to the perovskite structure causes the release of Pb^{2+} ions, which are subsequently deposited on the exposed Au surface through the underpotential deposition of lead (Pb_{UPD}) and attributed to the Pb^{int}. Moreover, Pb_{UPD} occurs only when Pb^{2+} is freed, which requires the excitation above the bandgap, or the activation through ionization, achievable either through high x-rays flux or IR laser-induced heating. Additionally, it is revealed that Pb^0 forms when desorption of the bromide occurs but Pb_{UPD} forms only when Pb^{2+} freed during the activation of pristine perovskite. Such an interaction at the contact can influence not only equilibrium concentration of the defects in the bulk of perovskite but also the interfacial energetics at the interface. Thus, these insights highlights that perovskite/Au interface is chemically unstable under IR, UV and intense x-rays illumination, revealing the potential limitations of using Au metal as an electrode for highly stable perovskite-based devices. Furthermore, shown that changes occur only at the surface but not in the bulk, which are frequently overlooked when characterizing the perovskite using pump laser based optical transient spectroscopy techniques such as time-resolved photoluminescence (TRPL), as TRPL assesses bulk properties and disregards any surface modifications, leading to the erroneous characterization of the perovskite materials.

References

1. Akkerman, Quinten A., et al. "Genesis, challenges and opportunities for colloidal lead halide perovskite nanocrystals." Nature materials 17.5 (2018): 394-405.
2. Dey, Amrita, et al. "State of the art and prospects for halide perovskite nanocrystals." ACS nano 15.7 (2021): 10775-10981.
3. Ling, Xufeng, Jianyu Yuan, and Wanli Ma. "The Rise of Colloidal Lead Halide Perovskite Quantum Dot Solar Cells." Accounts of Materials Research 3.8 (2022): 866-878.
4. Dias, Jeferson A., et al. "Perovskite Quantum Dot Solar Cells: An Overview of the Current Advances and Future Perspectives." Solar RRL 5.8 (2021): 2100205.
5. Protesescu, Loredana, et al. "Nanocrystals of cesium lead halide perovskites (CsPbX3, X= Cl, Br, and I): novel optoelectronic materials showing bright emission with wide color gamut." Nano letters 15.6 (2015): 3692-3696.
6. Hao, Mengmeng, et al. "Ligand-assisted cation-exchange engineering for high-efficiency colloidal Cs1− x FA x PbI3 quantum dot solar cells with reduced phase segregation." Nature Energy 5.1 (2020): 79-88.
7. Jeong, Jaeki, et al. "Pseudo-halide anion engineering for α-FAPbI3 perovskite solar cells." Nature 592.7854 (2021): 381-385.
8. Møller, Chr Kn. "A phase transition in cæsium plumbochloride." Nature 180.4593 (1957): 981-982.
9. Mizusaki, Junichiro, Kimiyasu Arai, and Kazuo Fueki. "Ionic conduction of the perovskite-type halides." Solid State Ionics 11.3 (1983): 203-211.
10. Mitzi, David B., et al. "Conducting tin halides with a layered organic-based perovskite structure." Nature 369.6480 (1994): 467-469.
11. Mitzi, David B., Konstantinos Chondroudis, and Cherie R. Kagan. "Organic-inorganic electronics." IBM journal of research and development 45.1 (2001): 29-45.
12. Kojima, Akihiro, et al. "Organometal halide perovskites as visible-light sensitizers for photovoltaic cells." Journal of the american chemical society 131.17 (2009): 6050-6051.
13. Kim, Hui-Seon, et al. "Lead iodide perovskite sensitized all-solid-state submicron thin film mesoscopic solar cell with efficiency exceeding 9%." Scientific reports 2.1 (2012): 591.
14. Rakovich, Yury P., and John F. Donegan. Anti-Stokes photoluminescence in semiconductor nanocrystal quantum dots. Springer Vienna, 2008.
15. Liu, Lu, et al. "Perovskite quantum dots in solar cells." Advanced Science 9.7 (2022): 2104577.

16. Akkerman, Quinten A., and Liberato Manna. "What defines a halide perovskite?" ACS energy letters 5.2 (2020): 604-610.
17. Travis, W., et al. "On the application of the tolerance factor to inorganic and hybrid halide perovskites: a revised system." Chemical Science 7.7 (2016): 4548-4556.
18. Stoumpos, Constantinos C., and Mercouri G. Kanatzidis. "The renaissance of halide perovskites and their evolution as emerging semiconductors." Accounts of chemical research 48.10 (2015): 2791-2802.
19. Kieslich, Gregor, Shijing Sun, and Anthony K. Cheetham. "Solid-state principles applied to organic–inorganic perovskites: new tricks for an old dog." Chemical Science 5.12 (2014): 4712-4715.
20. Frost, Jarvist M., et al. "Atomistic origins of high-performance in hybrid halide perovskite solar cells." Nano letters 14.5 (2014): 2584-2590.
21. Li, Zhen, et al. "Stabilizing perovskite structures by tuning tolerance factor: formation of formamidinium and cesium lead iodide solid-state alloys." Chemistry of Materials 28.1 (2016): 284-292.
22. Masi, Sofia, Andrés F. Gualdrón-Reyes, and Ivan Mora-Sero. "Stabilization of black perovskite phase in FAPbI3 and CsPbI3." ACS Energy Letters 5.6 (2020): 1974-1985.
23. Steele, Julian A., et al. "Phase transitions and anion exchange in all-inorganic halide perovskites." Accounts of Materials Research 1.1 (2020): 3-15.
24. Wang, Qi, et al. "Stabilizing the α-phase of CsPbI3 perovskite by sulfobetaine zwitterions in one-step spin-coating films." Joule 1.2 (2017): 371-382.
25. Masi, Sofia, Andrés F. Gualdrón-Reyes, and Ivan Mora-Sero. "Stabilization of black perovskite phase in FAPbI3 and CsPbI3." ACS Energy Letters 5.6 (2020): 1974-1985.
26. Swarnkar, Abhishek, et al. "Quantum dot–induced phase stabilization of α-CsPbI3 perovskite for high-efficiency photovoltaics." Science 354.6308 (2016): 92-95.
27. Hoye, Robert LZ, et al. "Perovskite-inspired photovoltaic materials: toward best practices in materials characterization and calculations." Chemistry of Materials 29.5 (2017): 1964-1988.
28. Steirer, K. Xerxes, et al. "Defect tolerance in methylammonium lead triiodide perovskite." ACS Energy Letters 1.2 (2016): 360-366.
29. Svanström, Sebastian, et al. "X-ray stability and degradation mechanism of lead halide perovskites and lead halides." Physical Chemistry Chemical Physics 23.21 (2021): 12479-12489.
30. Zhang, Teng, et al. "Pinning down the anomalous light soaking effect toward high-performance and fast-response perovskite solar cells: the ion-migration-induced charge accumulation." The journal of physical chemistry letters 8.20 (2017): 5069-5076.

31. Zu, Feng-Shuo, et al. "Impact of white light illumination on the electronic and chemical structures of mixed halide and single crystal perovskites." Advanced Optical Materials 5.9 (2017): 1700139.
32. Zu, Fengshuo, et al. "Surface state density determines the energy level alignment at hybrid perovskite/electron acceptors interfaces." ACS applied materials & interfaces 9.47 (2017): 41546-41552.
33. Tian, Jingjing, et al. "Inorganic halide perovskite solar cells: progress and challenges." Advanced energy materials 10.23 (2020): 2000183.
34. Miyata, Atsuhiko, et al. "Direct measurement of the exciton binding energy and effective masses for charge carriers in organic–inorganic tri-halide perovskites." Nature Physics 11.7 (2015): 582-587.
35. Herz, Laura M. "Charge-carrier mobilities in metal halide perovskites: fundamental mechanisms and limits." ACS Energy Letters 2.7 (2017): 1539-1548.
36. Stranks, S. D. et al. Electron-hole diffusion lengths exceeding 1 micrometer in an organometal trihalide perovskite absorber. Science 342, 341–344 (2013).
37. Fu, Jianhui, et al. "Hot carrier cooling mechanisms in halide perovskites." Nature communications 8.1 (2017): 1300.
38. Liu, Chongming, et al. "Metal halide perovskite nanocrystal solar cells: progress and challenges." Small Methods 4.10 (2020): 2000419.
39. Zhu, Haiming, et al. "Screening in crystalline liquids protects energetic carriers in hybrid perovskites." Science 353.6306 (2016): 1409-1413.
40. Goodwin, Heather, et al. "Multiple exciton generation in quantum dot-based solar cells." Nanophotonics 7.1 (2018): 111-126.
41. Cong, Muyu, et al. "Carrier multiplication and hot-carrier cooling dynamics in quantum-confined CsPbI3 perovskite nanocrystals." The journal of physical chemistry letters 11.5 (2020): 1921-1926.
42. Semonin, Octavi E., et al. "Peak external photocurrent quantum efficiency exceeding 100% via MEG in a quantum dot solar cell." Science 334.6062 (2011): 1530-1533.
43. Kulbak, Michael, David Cahen, and Gary Hodes. "How important is the organic part of lead halide perovskite photovoltaic cells? Efficient CsPbBr3 cells." The journal of physical chemistry letters 6.13 (2015): 2452-2456.
44. Ullah, Saad, et al. "All-inorganic CsPbBr 3 perovskite: a promising choice for photovoltaics." Materials Advances 2.2 (2021): 646-683.
45. Evarestov, R. A., et al. "First-principles comparative study of perfect and defective CsPbX 3 (X= Br, I) crystals." Physical Chemistry Chemical Physics 22.7 (2020): 3914-3920.

46. Zhao, Minglin, et al. "Ellipsometric study of the complex optical constants of a CsPbBr 3 perovskite thin film." Journal of Materials Chemistry C 6.39 (2018): 10450-10455.
47. Amelot, Dylan, et al. "Revealing the band structure of FAPI quantum dot film and its interfaces with electron and hole transport layer using time resolved photoemission." The Journal of Physical Chemistry C 124.6 (2020): 3873-3880. Zheng, B., et al. "Diffusion as a function of guest molecule length and functionalization in flexible metal–organic frameworks." Materials Horizons 3.4 (2016): 355-361.
48. Talapin, Dmitri V., et al. "Prospects of colloidal nanocrystals for electronic and optoelectronic applications." Chemical reviews 110.1 (2010): 389-458.
49. Nag, Angshuman, et al. "Metal-free inorganic ligands for colloidal nanocrystals: S2–, HS–, Se2–, HSe–, Te2–, HTe–, TeS32–, OH–, and NH2–as surface ligands." Journal of the American Chemical Society 133.27 (2011): 10612-10620.
50. Mir, Wasim J., et al. "Strategy to overcome recombination limited photocurrent generation in CsPbX3 nanocrystal arrays." Applied Physics Letters 112.11 (2018): 113503.
51. Phillips, P. Radiation; International Agency for Research on Cancer, 2012.
52. Grancini, Giulia, et al. "One-Year stable perovskite solar cells by 2D/3D interface engineering." Nature communications 8.1 (2017): 15684.
53. He, Yihui, et al. "High spectral resolution of gamma-rays at room temperature by perovskite CsPbBr3 single crystals." Nature communications 9.1 (2018): 1609.
54. (a) Zhao, Lianfeng, et al. "Redox chemistry dominates the degradation and decomposition of metal halide perovskite optoelectronic devices." ACS Energy Letters 1.3 (2016): 595-602. (b) Cha, Myung Joo, et al. "Depth-dependent electronic band structure at the Au/CH 3 NH 3 PbI 3− x Cl x junction." Physical Chemistry Chemical Physics 21.27 (2019): 14541-14545.
55. Kerner, Ross A., et al. "Reactions at noble metal contacts with methylammonium lead triiodide perovskites: Role of underpotential deposition and electrochemistry." Apl Materials 7.4 (2019): 041103.
56. Xie, Yujun, et al. "Highly efficient blue-emitting CsPbBr3 perovskite nanocrystals through neodymium doping." Advanced science 7.20 (2020): 2001698.
57. Eames, Christopher, et al. "Ionic transport in hybrid lead iodide perovskite solar cells." Nature communications 6.1 (2015): 7497.
58. Cappel, Ute B., et al. "Partially reversible photoinduced chemical changes in a mixed-ion perovskite material for solar cells." ACS applied materials & interfaces 9.40 (2017): 34970-34978.
59. Datta, Kunal, et al. "Effect of light-induced halide segregation on the performance of mixed-halide perovskite solar cells." ACS Applied Energy Materials 4.7 (2021): 6650-6658.

60. Cohen, Ayala V., et al. "Breakdown of the static picture of defect energetics in halide perovskites: the case of the Br vacancy in CsPbBr3." The Journal of Physical Chemistry Letters 10.16 (2019): 4490-4498.
61. Levine, Igal, et al. "Deep defect states in wide-band-gap ABX3 halide perovskites." ACS Energy Letters 4.5 (2019): 1150-1157.
62. Gao, Lei, et al. "γ-ray Radiation Hardness of CsPbBr3 Single Crystals and Single-Carrier Devices." ACS Applied Materials & Interfaces 14.33 (2022): 37904-37915.
63. Xie, Yujun, et al. "Highly efficient blue-emitting CsPbBr3 perovskite nanocrystals through neodymium doping." Advanced science 7.20 (2020): 2001698.
64. Amelot, Dylan, et al. "Revealing the band structure of FAPI quantum dot film and its interfaces with electron and hole transport layer using time resolved photoemission." The Journal of Physical Chemistry C 124.6 (2020): 3873-3880.
65. Cappel, Ute B., et al. "Partially reversible photoinduced chemical changes in a mixed-ion perovskite material for solar cells." ACS applied materials & interfaces 9.40 (2017): 34970-34978.
66. Liu, Jiakai, et al. "Light-induced self-assembly of cubic CsPbBr3 perovskite nanocrystals into nanowires." Chemistry of Materials 31.17 (2019): 6642-6649.
67. Zhang, Baowei, et al. "Stable CsPbBr3 Nanoclusters Feature a Disk-like Shape and a Distorted Orthorhombic Structure." Journal of the American Chemical Society 144.11 (2022): 5059-5066.
68. Bergeard, N., et al. "Time-resolved photoelectron spectroscopy using synchrotron radiation time structure." Journal of synchrotron radiation 18.2 (2011): 245-250.
69. Giangrisostomi, Erika, et al. "Low Dose Photoelectron Spectroscopy at BESSY II: Electronic structure of matter in its native state." Journal of Electron Spectroscopy and Related Phenomena 224 (2018): 68-78.
70. Svanström, Sebastian, et al. "X-ray stability and degradation mechanism of lead halide perovskites and lead halides." Physical Chemistry Chemical Physics 23.21 (2021): 12479-12489.
71. Kim, Gee Yeong, et al. "Large tunable photoeffect on ion conduction in halide perovskites and implications for photodecomposition." Nature materials 17.5 (2018): 445-449.
72. Dang, Zhiya, et al. "In situ transmission electron microscopy study of electron beam-induced transformations in colloidal cesium lead halide perovskite nanocrystals." Acs Nano 11.2 (2017): 2124-2132.
73. Shinotsuka, H., et al. "Calculations of electron inelastic mean free paths. X. Data for 41 elemental solids over the 50 eV to 200 keV range with the relativistic full Penn algorithm." Surface and Interface Analysis 47.9 (2015): 871-888.

74. Kitagawa, Hiroshi, Norimichi Kojima, and Tsuyoshi Nakajima. "Studies of mixed-valence states in three-dimensional halogen-bridged gold compounds, Cs2AuIAuIIIX6,(X= Cl, Br or I). Part 2. X-Ray photoelectron spectroscopic study." Journal of the Chemical Society, Dalton Transactions 11 (1991): 3121-3125.
75. Roman, Benjamin J., et al. "Au exchange or Au deposition : dual reaction pathways in Au–CsPbBr3 heterostructure nanoparticles." Nano letters 17.9 (2017): 5561-5566.
76. Shlenskaya, Natalia N., et al. "Light-induced reactivity of gold and hybrid perovskite as a new possible degradation mechanism in perovskite solar cells." Journal of Materials Chemistry A 6.4 (2018): 1780-1786.
77. Hale, Penny, Stephen Thurgate, and Peter Wilkie. "Lead underpotential deposition on Au (110)." Surface and Interface Analysis: An International Journal devoted to the development and application of techniques for the analysis of surfaces, interfaces and thin films 35.10 (2003): 842-851.
78. Zeng, Xiangqun, and Stanley Bruckenstein. "Underpotential deposition and adsorption of lead on gold polycrystalline electrodes: II. EQCM investigation in acidic 0.1 m NaClO4 and 0.1 m NaCl electrolytes." Journal of the Electrochemical Society 146.7 (1999): 2555.
79. Al-Kuhaili, M. F. "Enhancement of plasmonic transmittance of porous gold thin films via gold/metal oxide bi-layers for solar energy-saving applications." Solar Energy 181 (2019): 456-463.

CHAPTER 4: Radiation Stability of $CsPbBr_3$ Perovskite Nanocrystals at Semiconductor Interface and Oxides

This chapter is about the radiation stability (Infrared and Ultraviolet) of $CsPbBr_3$ perovskite nanocrystals (NCs) at the semiconductor and oxides interface, which includes molybdenum disulfide (MoS_2) single crystal, Molybdenum oxide (MoO_x), and indium tin-doped oxide (ITO).

4.1 Introduction

The Stability of $CsPbBr_3$ NCs at semiconductor interfaces under radiation in particular under ultraviolet is critical given that the solar spectrum contains about 5% of UV region as mentioned in previous chapter.[1] Semiconductors, metal oxides, are used as a buffer layer between metal electrodes and charge transport layers to provide a better energy level alignment to enhance the charge extraction and collection in opto-electronic devices. High transparency, excellent charge carriers mobility and high work function of metal oxides make them desirable for solar cells applications. However, metal oxides, are known for their photocatalytic activity (light greater than the bandgap of metal oxide drives chemical reactions), which can lead to the decomposition of perovskite absorption layer via the release of volatile specie, CH_3NH_2 and HI in $MAPbI_3$ perovskite composition and thus reduce the stability of perovskite solar cells.[2] Furthermore, it has been observed that when a metal oxide is exposed to UV light, the photogenerated holes react with the oxygen adsorbed at surface oxygen vacancies, resulting in the desorption of oxygen, which then become deep trap state leading to charge recombination.[1,2] Despite being concerted efforts to comprehend the UV stability in perovskite devices, the degradation mechanism right at the interface has limited understanding. As a result, it is critical to identify and build a complete knowledge of the UV radiation impacts on perovskite at the metal oxides interfaces.

Recently, 2-D transition metal dichalcogenides have shown great promise in application in solar cells owing to their fascinating properties such as high charge carrier mobilities, tunable bandgap (by changing the number of layers, for instance, from 1.2 eV for the bulk to monolayer of 1.9 eV for the case of MoS_2), and even more so, their excellent chemical stability and inertness.[3] Among transition metal dichalcogenide, an extensive literature exist on the integration of MoS_2 as a charge transport layer in perovskite devices, where improved stability of perovskite has been reported, however the mechanism that dictates stability remains elusive.[4] Furthermore, improved UV stability of perovskite devices with Titanium disulfide (TiS_2) charge transport layer has been described and attributed to the low photocatalytic properties of TiS_2 without defining a comprehensive dictated mechanism.[5]

Molybdenum oxide (MoO_x) is another ubiquitously used metal oxide in photovoltaics, both in organic and perovskite solar cells. Owing to high work function and high transparency of MoO_x, it acts as a buffer layer at the electrode contact to extract and transport holes in the devices. However, being inorganic, MoO_x is highly reactive,[6] and an interfacial oxidation/reduction reaction can occur at its interface with perovskite, altering the stoichiometry, electronic structure, and work function of the MoO_x buffer layer.[6] All of these can influence energy-level alignment and MoO_x role to function as an efficient buffer at the charge selective contact. Furthermore, under UV illumination, stoichiometry of MoO_x is greatly affected and hence the intrinsic properties associated with it, thereby its ability to function as an effective charge transport layer can be compromised.[7] Indium tin-doped oxide (ITO) is another transparent conductive metal oxide which is commonly used as bottom electrode in opto-electronic devices. The low work function of ITO, which is in the close proximity to the conduction band minimum of perovskite, makes it an appropriate cathode for injecting/extraction electrons. A buffer layer is frequently inserted between perovskite and ITO to improve charge collection efficiency.[8] Furthermore, ITO is regarded as a stable electrode; yet UV irradiation might compromise its inherent stability due to its bandgap in the UV region.[9] In contemplating this, we investigated infrared radiation effects on the stability of $CsPbBr_3$ nanocrystals (NCs) at the interface with MoS_2 and MoO_x, as well as effects of UV radiations on these interfaces including the interface of $CsPbBr_3$ with ITO. The findings of these studies will be presented in the following.

4.2 Experimental Section

4.2.1 Sample preparation

The samples of CsPbBr3 perovskite NCs on MoO_x, MoS_2 and ITO substrates were prepared as described in Chapter 3. For the case of MoO_x substrate, the MoO_x films of 30 nm on ITO have been prepared by reactive DC-sputtering from a pure (99.95%) Mo target. They were sputtered with a power of 250 W in 50% oxygen and 50% Argon (pressure of 2.8×10^{-3} mbar).

They were then annealed at 350 °C in UHV. For the MoS_2 single crystal (SC) and ITO substrates, they were purchased from Sigma Aldrich.

4.3 Stability of $CsPbBr_3$ Perovskite NCs under Infrared (IR) Laser

The experiment to study the stability of $CsPbBr_3$ nanocrystals at interface with molybdenum disulfide (MoS_2) single crystal (SC) and molybdenum oxide (MoO_x) is performed at low x-ray flux beamline (PM4) at the synchrotron BESSY II. The steady state photoemission spectra of ligand exchanged nanocrystals spin-coated on MoS_2 single crystal (SC) and MoO_x substrates were measured using an infrared (IR) femtoseconds laser, which have the wavelength 1030 nm or 1.2 eV, a pulse length of about 350 fs, and a repetition frequency of 207.46 kHz. The fluence of the laser was estimated to be about 12.5 mW/cm^2. Time evolution measurements of core level were carried out in the following sequence: Cs 4d Br 3d, Pb 4f, S 2p and Mo 3d, 5 minutes each before the laser was switched on, Pb 4f 30 minutes during the laser exposure, Pb 4f, Cs 4d, Br 3d, S 2p and Mo 3d, 5 minutes each after the laser was switched off. For the NCs on MoO_x, core levels were measured in the same sequence, where Mo 3d core level is measured for the MoO_x substrate. All the core levels were calibrated to the Au $4f_{7/2}$ set to 84.00 eV.

4.3.1 At the interface with MoS_2

The overview spectrum of $CsPbBr_3$ NCs on MoS_2 single crystal (SC) measured at photon energy 650 eV is shown in Figure 4.1 (a). The core-level peaks related to perovskite, cesium, bromide and lead are evident, along with the contribution from the carbon associated with ligands, as well as core-level peaks from the substrate, molybdenum and Sulfur. To study the effects of IR laser, core levels are measured at the photon energy of 360 eV. Figure 4.1 (b) shows evolution of the Pb 4f spectra under IR illumination. Before laser illumination, only a single spin-orbit doublet is observed at the binding of 138.64 eV for Pb $4f_{7/2}$ assigned to Pb^{2+} of perovskite.[10] Upon switching the laser on, the Pb^{2+} shifts to higher binding energy by approximately 0.4 eV. This shift in binding energy was almost completely reversible when the laser switched off. Figure 4.1 (c) shows the Cs 4d and Br 3d spectra before and after the laser illumination. Before laser illumination, the Cs $4d_{5/2}$ was found at the binding energy of 75.64 eV and Br $3d_{5/2}$ at 68.61 eV assigned to Cs^+ and Br^- of $CsPbBr_3$ respectively. Almost no change in binding energy positions of Cs 4d and Br

3d are observed before and after the laser. Similarly, the core levels from the substrate were also measured before and after the laser and shown in Figure 4.1 (d).

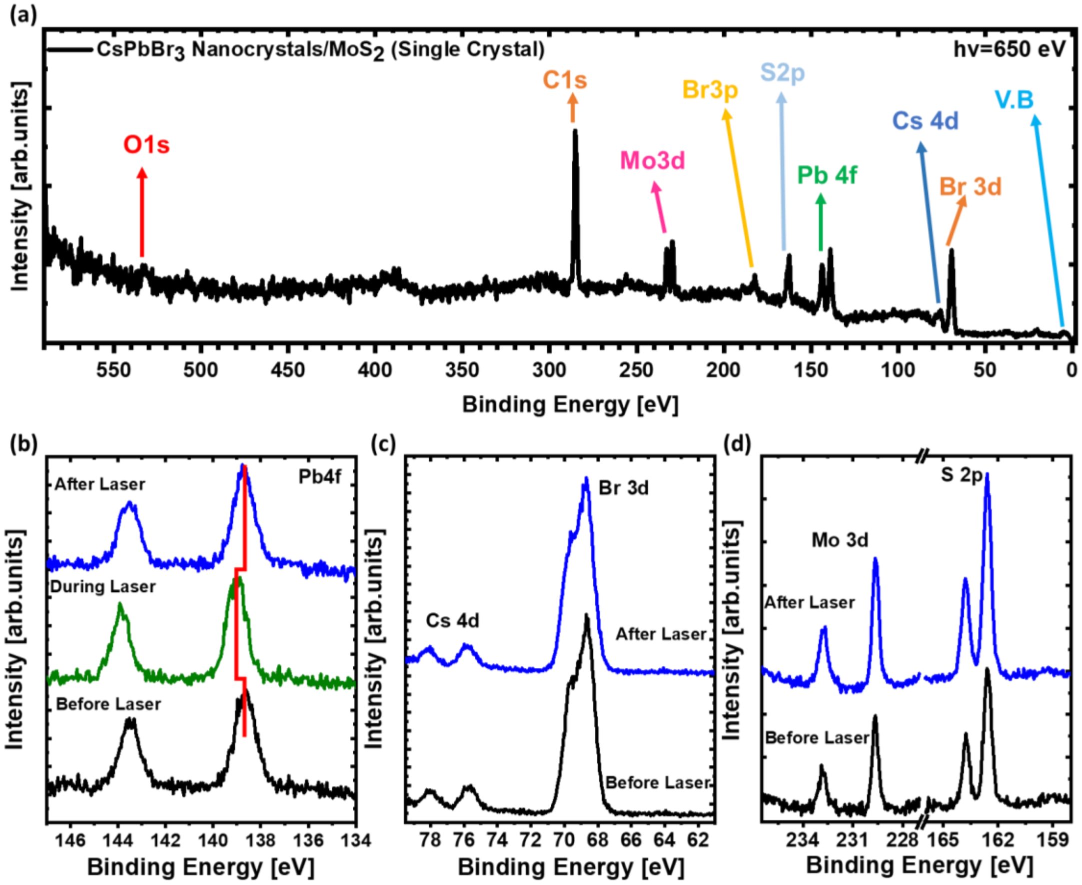

Figure 4.1. (a) Overview spectrum of $CsPbBr_3$ perovskite nanocrystals spin-coated on MoS_2 single crystal at the photon energy of 650 eV. (b) Pb 4f, (c) Cs 4d and Br 3d and (d) Mo 3d and S 2p, core levels measured at photon energy of 360 eV before and after infrared (IR) laser of 1.2 eV energy and laser fluence of 12.5 mW/cm^2.

Table 4.1 Binding energies (eV) of core levels Cs 4d , Br 3d, and Pb 4f, extracted from the least squares fit of the corresponding core levels of $CsPbBr_3$ NCs deposited on MoS_2 single crystal (SC) before and 30 minutes of 1.2 eV laser, together with the core levels S 2p and Mo 3d from the MoS_2 substrate. The standard deviation in binding energy positions for Br 3d, Pb 4f, Mo 3d and S 2p was within the range of 0.05 eV whereas for Cs 4d in the range of 0.08 eV. Δ B.E = $B.E_{\text{After the laser}} - B.E_{\text{Before the laser}}$

	$CsPbBr_3$ perovskite NCs			**MoS_2 (SC) substrate**	
	Cs^+ (eV)	**Br^- (eV)**	**Pb^{2+} (eV)**	**S^{2-} (eV)**	**Mo^{2+} (eV)**
	Cs $4d_{5/2}$	Br $3d_{5/2}$	Pb $4f_{7/2}$	S $2p_{3/2}$	Mo $3d_{5/2}$
Before Laser	75.64	67.61	138.64	162.55	229.65
After 30min Laser	75.75	67.69	138.70	162.56	229.66
ΔB.E	0.11	0.08	0.06	0.01	0.01

Before laser Mo $3d_{5/2}$ shows a single component at the binding energy of 229.65 eV and S $2p_{3/2}$ at the binding energy of 162.55 eV assigned to Mo^{4+} and $S^{2-}$of MoS_2.[11] No change in spectral shape and the binding energy position of Mo 3d and S 2p is observed after laser illumination. The corresponding binding energies of all the core levels are shown in Table 4.1.

4.3.2 At the interface with MoO_x

Figure 4.2 (a) shows the overview spectrum of $CsPbBr_3$ NCs on MoO_x measured with photon energy 650 eV. The contribution of cesium, bromide and lead from the perovskite can be seen and carbon from the ligands, as well as the core-levels from the substrate, molybdenum and oxygen. Evolution of the Pb 4f spectra upon under laser illumination is shown in Figure 4.1 (b). Before laser, only a single component of Pb 4f is observed at the binding of 139.82 eV for Pb $4f_{7/2}$, which is assigned to Pb^{2+} of perovskite. However, the binding energy position of Pb^{2+} of $CsPbBr_3$ on MoO_x is higher compared to its binding energy position on the other substrates in our work including Au and MoS_2, as well as the reported binding energy position of Pb^{2+} for the perovskite on MoO_x in the literature.[8,12] The explanation for this might be that the high work function of MoO_x can cause band bending at the interface, resulting in an upward shift of the Fermi level.[13,14] Since the binding energy in photoemission is measured with reference to the Fermi level, hence Pb^{2+} is observed at higher binding energy. Upon switching the laser on, the Pb^{2+} shifts to lower binding energy by approximately 0.4 eV. This shift in binding energy was almost completely reversible when the laser was switched off, as can be seen in Figure 4.2 (b). Similarly, the core levels of MoO_x were measured before and after the laser to examine the effect of the laser on the MoO_x substrate, as shown in Figure 4.2 (c). Before laser, Mo 3d shows a single component at the binding energy of 232.53 for Mo $3d_{5/2}$ assigned to Mo^{6+} of MoO_x.[15] No reduction of molybdenum oxide is observed which is known to happen under x-rays.[16] This is due to low x-ray flux at the PM4 beamline, as mentioned in experimental chapter, which prevents any x-rays induced damage. Following laser illumination, neither shift in binding energy position nor reduction of Mo 3d is observed. The absence in reduction of MoO_x suggests the lack of possible chemical reaction at the perovskite-MoO_x interface. The corresponding binding energy positions before and after the laser illumination are listed in Table 4.2.

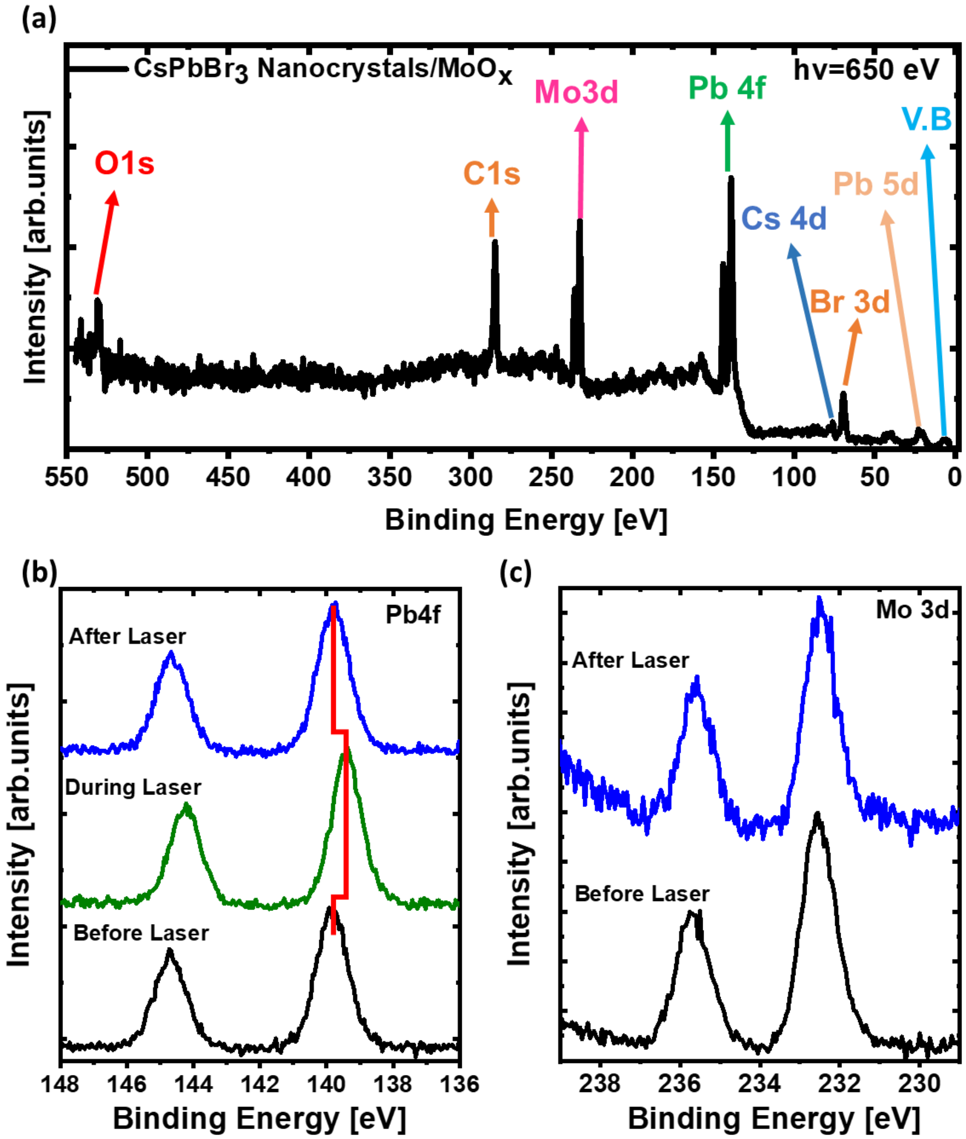

Figure 4.2. (a) Overview spectrum of $CsPbBr_3$ perovskite nanocrystals spin-coated on MoO_x at the photon energy of 650 eV. (b) Pb 4f, (c) Cs 4d and Br 3d and (d) Mo 3d, core levels measured at photon energy of 360 eV before and after infrared (IR) laser of 1.2 eV energy and laser fluence of 12.5 mW/cm^2.

Table 4.2 Binding energies (eV) of Pb 4f core level, extracted from the least squares fit of the corresponding core level of $CsPbBr_3$ NCs deposited on MoO_x before and 30 minutes of 1.2 eV laser, while the core level Mo 3d from the MoS_2 substrate. The standard deviation in binding energy positions for Pb 4f, Mo 3d and was within the range of 0.05 eV. Δ B.E = $B.E_{\text{After the laser}} - B.E_{\text{Before the laser}}$

	$CsPbBr_3$	**MoO_x**
	$Pb^{2+}4f_{7/2}$ (eV)	**$Mo^{2+}3d_{5/2}$ (eV)**
Before Laser	139.82	232.51
After 30min Laser	139.78	232.49
ΔB.E	-0.04	-0.03

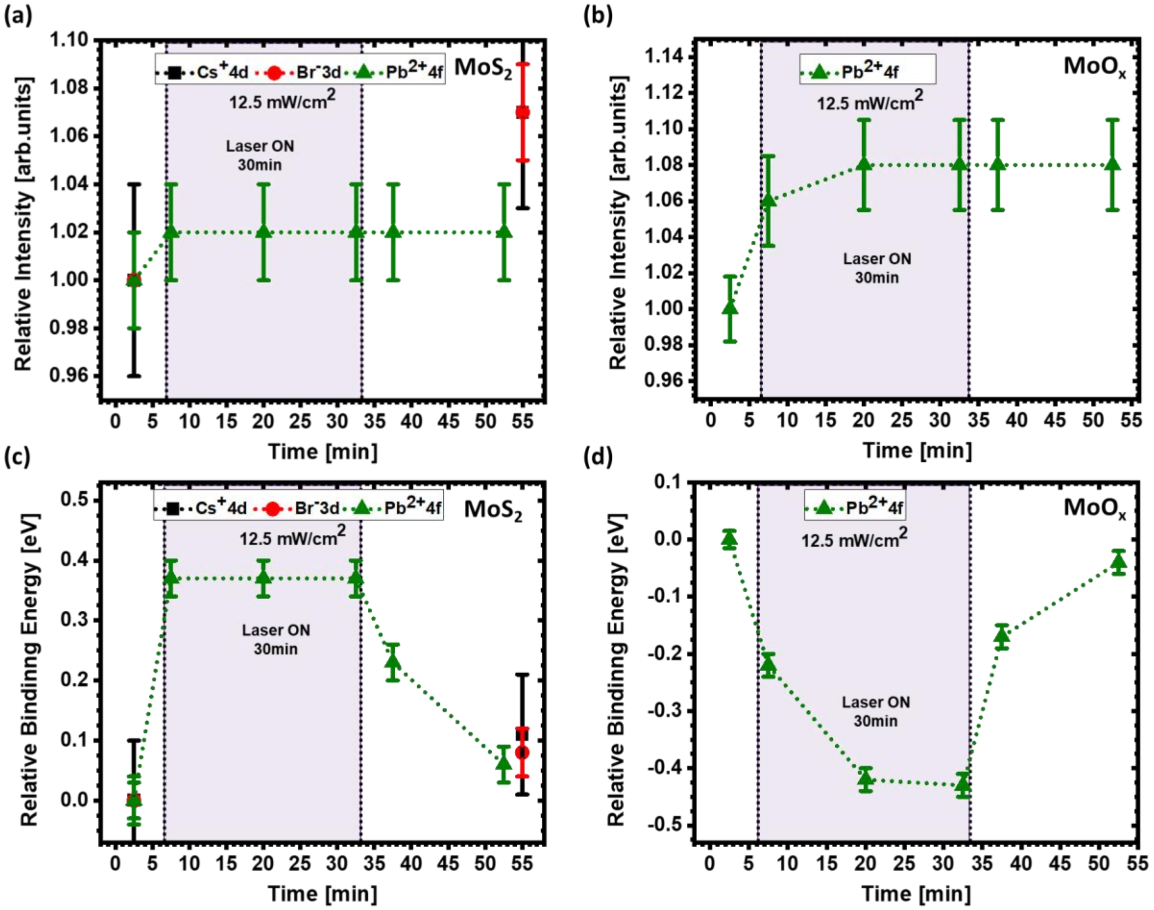

Figure 4.3. (a) and (b) relative intensities of Cs 4d, Br 3d and Pb 4f spectra calculated (intensity of Cs 4d, Br 3d and Pb 4f core levels divided by intensity of the corresponding core levels before laser) of $CsPbBr_3$ NCs on MoS_2 and MoO_x respectively. (c) and (d) relative binding energies of Cs 4d, Br 3d and Pb 4f spectra calculated (binding energy of Cs 4d, Br 3d and Pb 4f core levels subtracted from the binding energy of the corresponding core level before laser exposure) of NCs on MoS_2 and MoO_x respectively. The photon energy used is 360 eV and laser energy is 1.2 eV with a fluency of 12.5 mW/cm^2. The shaded area in the figure represents 30 minutes exposure.

4.3.3 Discussion on IR radiation stability of $CsPbBr_3$ perovskite NCs

Since the shift in the binding energy of Pb 4f core level of $CsPbBr_3$ NCs deposited on MoS_2 and MoO_x are observed in different directions, the intensities and shifts in binding energy are discussed and compared in the following. Figure 4.3 (a) shows the intensities of Cs 4d, Br 3d and Pb 4f relative to their intensities before the laser as a function of laser exposure time for $CsPbBr_3$ NCs on MoS_2. A negligible increase in intensity of Cs 4d and Pb 4f was observed after illumination, whereas the intensity of Br 3d increased slightly up to 1.07. This increase in intensity of Br 3d following illumination could be related to the movement of mobile bromide ions and resulted segregation of bromide at the surface and the origin of it will be explained in the following.[17,18] For the case of MoO_x, a little increase in the intensity of Pb 4f observed as soon as laser is switched on and increase gradually up to 1.07 and remains constant further when the laser is turned off. Increase in intensity of Pb could be assigned to the oxidation of lead and reduction of molybdenum as explained by Schulz et al.,[14] $Pb^{2+} \rightarrow Pb^{4+}$ oxidation from $Mo^{6+} \rightarrow Mo^{4+}$ reduction. However, apparently, no reduction of MoO_x is evidenced, and also the increase in intensity is quite small. Nonetheless, like Pb 4f, tracking of Mo 3d during the laser illumination (below the bandgap of NCs) can conclusively resolve such a notion.

With regard to binding energy shift, for the case of MoS_2, the Pb^{2+} peak position is shifted to higher binding energy by 0.37 eV shortly after the laser is turned on, and then remain constant for the entire period of 30 minutes. However, when the laser is turned off, the Pb^{2+} peak position slowly changes, gradually moving back toward lower binding energy until it nearly returns to its original position of before laser. Since Pb^{2+}4f core level shift is reversible after the laser, it can be interpreted that other core levels such as Cs^+ 4d and Br^-3d, undergo a similar shift during the laser. Therefore, peak position of both Cs^+ 4d and Br^-3d, which are measured after the laser, like Pb^{2+}4f, is found at the same position as it was before the laser. Conversely, for the case of MoO_x, initially, the Pb^{2+} peak shifted to lower binding energy by 0.22 eV under the laser which then increase up to 0.43 eV. Upon turning off the laser, the Pb^{2+} peak position slowly changes, gradually moving back toward higher binding energy until it nearly returns to its original position of before laser.

The instant change for the core levels peak position under the laser is consistent with the generation of surface photovoltage between the MoS_2 or MoO_x substrate and $CsPbBr_3$ perovskite NCs. Illumination, although below the bandgap of NCs (2.30 eV), can excite the defects (interstitial bromide and/or bromide vacancies) inherent to perovskite, which are located in the bandgap of $CsPbBr_3$ at around 1.2 eV.[19,20] Since the energy level of these defects states is at the midgap position (as the bandgap of $CsPbBr_3$ is 2.30 eV), under illumination, there is equal probability of either transition of electron from valence band to the defect state or transition of electron from defect state to conduction band. For the case of MoS_2 substrate, it can be assumed that the photoexcitation results in the excitation of an electrons from the defect states to the conduction band of perovskite, which can then be injected into the MoS_2 substrate, leading to the splitting of Fermi levels between MoS_2 and $CsPbBr_3$ NCs. On the contrary, for MoO_x, optical excitation promotes electrons from valence band to the defect states, resulting in holes in the perovskite that are then injected into MoO_x, resulting in the splitting of the Fermi level. For any injection of electron in MoS_2 leaves a hole behind, leading to the positive charging of $CsPbBr_3$ NCs, and any injection of holes in MoO_x leaves an electron behind, leading to the negative charging of $CsPbBr_3$ NCs. This positive and negative charging of $CsPbBr_3$ NCs causes the core levels to shift towards higher and lower binding energy respectively, shown here for Pb 4f level, i.e., to the generation of surface photovoltage.

The shifting of the peak position of core levels back to their original position after the laser indicates Fermi level splitting is followed by a slower chemical change. The slow chemical changes during and after the laser illumination are likely to be related to the changing in the surface chemistry of the perovskite. Under the illumination, vacancies-mediated diffusion of bromide ions occurs,[21] resulting in Br-rich phase at the surface evidenced as increase in intensity of bromide after the laser is turned off. This bromide segregation might explain the reason for not completely reversible shift in binding energy after the laser is observed, and support the notion that the surface photovoltage is induced by the bromide vacancies. However, shift might be completely reversible once the equilibrium is reached when the laser is off.

To summarize, under IR illumination, a surface photovoltage is evidenced stemming from the intraband photoexcitation of deep-trap states of $CsPbBr_3$ perovskite NCs. Since the trap states are right in the middle of perovskite bandgap, the polarity of surface photovoltage is contingent on the semiconductor type, i,e., positive for P-type substrate, and negative for N-type substrate. However, in terms of structural degradation of perovskite, negligible changes occur under the IR laser illumination, meaning $CsPbBr_3$ NCs on both MoS_2 and MoO_x substrates remain stable.

4.4 Stability of $CsPbBr_3$ Perovskite NCs under Ultraviolet (UV) Laser

The same experimental procedure has been adopted to investigate the effects of (ultraviolet) UV laser on $CsPbBr_3$ NCs at the interface of MoS_2, as it was for IR laser except laser is used at its third harmonic which gives the wavelength of 343 nm (3.6 eV). Also, two different laser fluences were used, 3.5 mW/cm^2 and 12.5 mW/cm^2. It is important to mention here that core levels intensities were normalized to the mirror current for the core levels measured under high laser fluence due to beam dump that occurred after the low laser fluence measurements. Furthermore, as stated in Chapter 3, due to a small probing depth at 360 eV, buried interface of $CsPbBr_3$ NCs with the substrate (MoS_2, MoO_x and ITO) onto which NCs are deposited is inaccessible, albeit the interface at the corner and edges of the NCs with the substrate is accessible.

4.4.1 At the interface with MoS_2

Figures 4.4 (a) and (b) show the core levels of perovskite NCs, Pb 4f, Cs 4d, and Br 3d, respectively, while Figure 4.4 (c) shows the core levels of the MoS_2 substrate, Mo 3d and S 2p, measured before and after 30 minutes of UV laser of energy 3.6 eV with fluence of 3.5 mW/cm^2 and 12.5 mW/cm^2. The Pb 4f core level shows only single components at the binding of 138.64 eV for Pb $4f_{7/2}$ assigned to Pb^{2+} of perovskite.[10] After exposure to 30 minutes laser with both 3.5 mW/cm^2 and 12.5 mW/cm^2 fluence, a new specie at the low binding energy of 136.90 eV for Pb $4f_{7/2}$ appears, assigned to the metallic lead (Pb^0). The origin of Pb^0 and variations in the intensities of Pb^{2+} and Pb^0 will be explained later.

For Cs 4d and Br 3d core levels, before and after the laser, no new components appears albeit the changes in intensities. For the C 1s core level, the fitting and analysis of carbon peak remains complex due to number of carbon contributions involving, adventitious carbon, and two carbon peaks from acetate ligands. Hence, the C 1s is fitted with a single peak by using Gaussian function to identify the appearance of a new chemical species, as shown in Figure 4.7 (d) and (e). No change in intensity is observed before and after laser with two laser fluences except a small increase in the width of the peak. Similarly, the core levels S 2p and Mo 3d from the MoS_2 substrate shown only a single component before and after the laser at the binding energy of 229.65 eV for Mo $3d_{5/2}$ and 162.55 eV for S $2p_{3/2}$ assigned to Mo^{4+} and $S^{2-}$of MoS_2.[11] The absence of change in peak shape and width of Mo 3d and S 2p implies that no new species formed following the UV laser. The changes observed in the binding energy position of perovskite core levels and their intensities during and after laser illumination will be discussed in the following.

The intensities of different component, Pb^{2+}, Pb^0 of the Pb 4f spectrum relative to their intensities before the laser have been calculated and plotted as a function of time for two different laser fluences, 3.5 mW/cm^2 and 12.5 mW/cm^2, and shown in Figure 4.5 (a) and (b) respectively. Initial exposure with low fluence causes a decrease in the intensity of Pb^{2+} without the appearance of an additional specie. At the half time of laser exposure, Pb^0 appears with a further decrease in Pb^{2+} followed by increasing intensity of Pb^0 and decreasing intensity of Pb^{2+}.

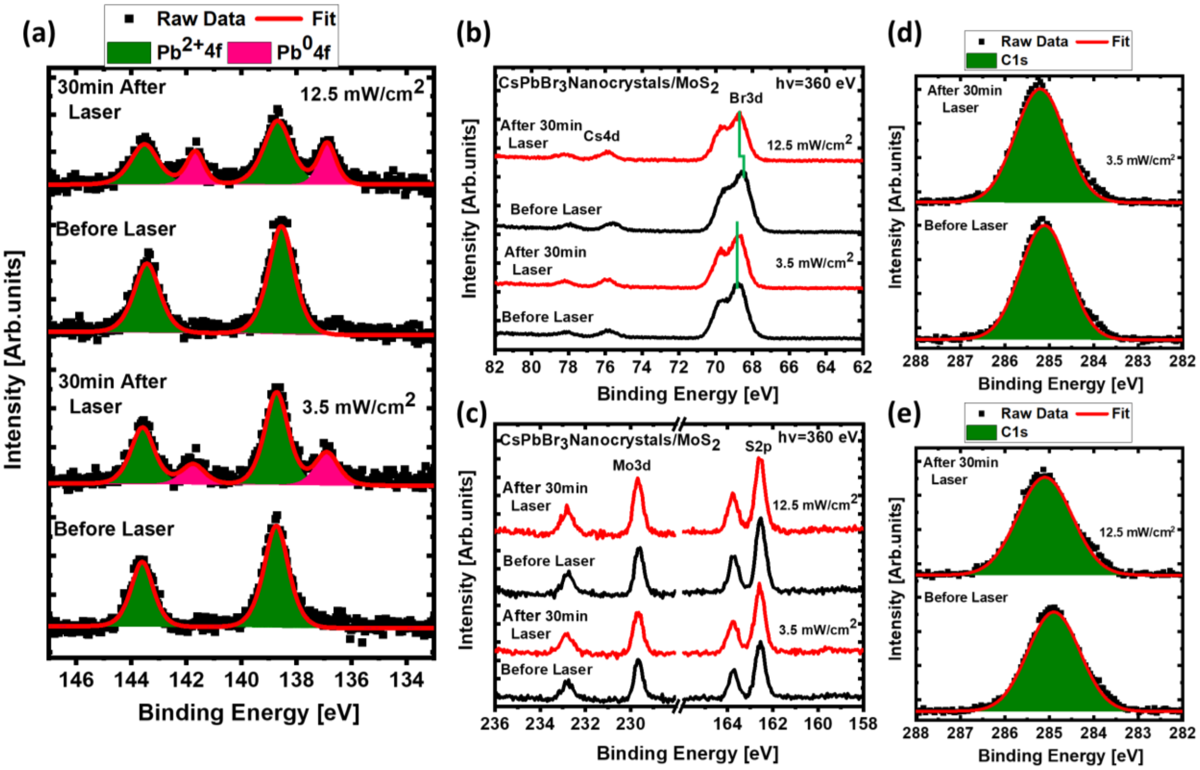

Figure 4.4. Core levels (a) Cs 4d and Br 3d, (b) Pb 4f, (c), (d) C 1s, and (e) Mo 3d and S 2p from the $CsPbBr_3$ perovskite nanocrystals deposited on MoS_2 substrate, measured with the photon energy of 360 eV, before and 30 minutes after ultraviolet (UV) laser of 3.6 eV energy, with two laser fluences, 3.5 mW/cm^2 and 12.5 mW/cm^2.

When the laser is switched off, Pb^{2+} remains unchanged while Pb^0 increases slightly. Under the high laser fluence, during the first 5 minutes, Pb^0 appeared and intensity of Pb^{2+} decreased. Further exposure decreases and increases the intensity of Pb^{2+} and Pb^0 to 0.8 and 0.4 of the starting intensity, respectively. Upon switching the laser off, intensity of Pb^{2+}4f and $Pb^0$4f remains unchanged. Comparing the two fluences of laser, the same trend in the change in intensities of Pb^{2+} and Pb^0 was observed, however the decrease in Pb^{2+} and increase in Pb^0 was faster with high fluence. Similarly, the relative intensities of Cs 4d, Br 3d, ΣPb4f (Pb^{2+}4f and $Pb^0$4f) and S 2p core levels are shown in Figure 4.5 (c) and (d) under low and high fluence laser. After 30 minutes laser exposure with low fluence, relative intensities of Cs 4d and ΣPb4f remains relatively constant, whereas both the intensities increased under high fluence laser. The intensity of Br 3d decreases slightly with low fluence but it decrease sharply with high fluence up to 0.7 relative to the initial value. The intensity of the S 2p remains constant for both laser fluences, as well as intensity of C 1s remains relatively unchanged. Overall, the intensity of Cs 4d and ΣPb 4f remains constant at low fluence of the laser, while both the intensities increased with high fluence. The intensity of Br 3d decreased for both laser fluences, however, decrease was sharper and greater with high fluence.

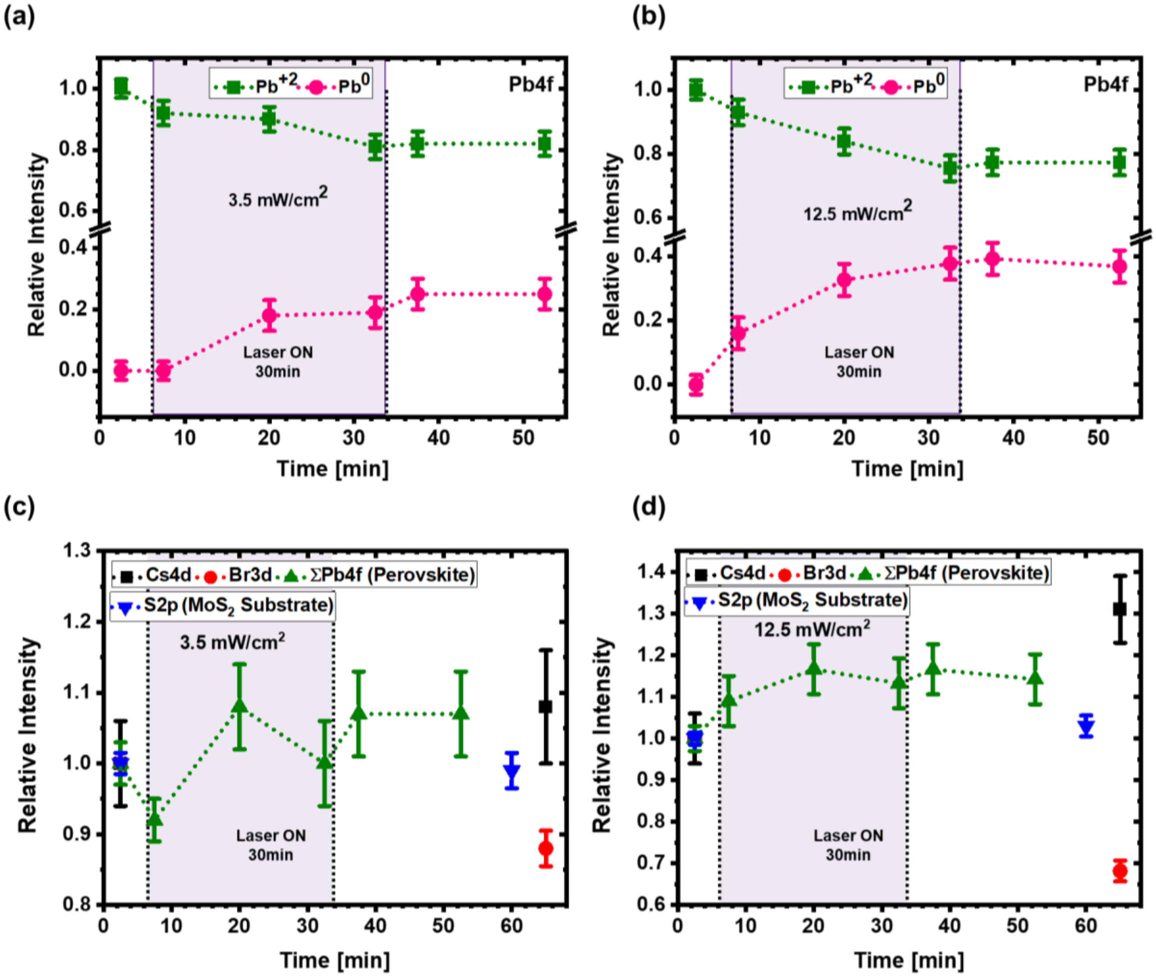

Figure 4.5. Relative intensities of different species of Pb 4f, Pb^{2+}4f and Pb^{0}4f calculated (intensity of Pb 4f component divided by intensity of Pb 4f core level before laser) of $CsPbBr_3$ NCs on MoS_2 measured with photon energy 360 eV (a) with laser fluence 3.5 mW/cm^2 (b) 12.5 mW/cm^2. (c) and (d) relative intensities of Cs 4d, Br 3d and Pb 4f spectra calculated (intensity of Cs 4d, Br 3d and Pb 4f core levels divided by intensities of the corresponding core levels before laser) with laser fluence of 3.5 mW/cm^2 and 12.5 mW/cm^2, respectively.

Likewise, the relative binding energy of all the core levels were calculated and shown in Figure 4.6 (a) and (b) for low and high fluence respectively. At low fluence, initially, Pb^{2+} shifted by 0.05 eV towards higher binding energy and then shifted back, ending at the same Pb^{2+} peak position as it was before the laser. Shift for Cs$^+$4d remains within the error range but no shift is observed for Br^-3d after the laser. With high fluence, Pb^{2+} shifted by around 0.2 eV (almost four times of the low fluence), a consistency in the magnitude of the shift and fluence of the laser. This shift then reversed slightly and finished at around 0.15 eV. Other core level, Cs^+4d and Br^- 3d shifted by same magnitude as Pb^{2+}. The C 1s shifted towards higher binding energy by 0.10 eV and 0.30 eV under low and high laser fluence, respectively. Similarly, a negligible shift within the error margin for the core levels, S 2p and Mo 3d of MoS_2 substrate are observed.

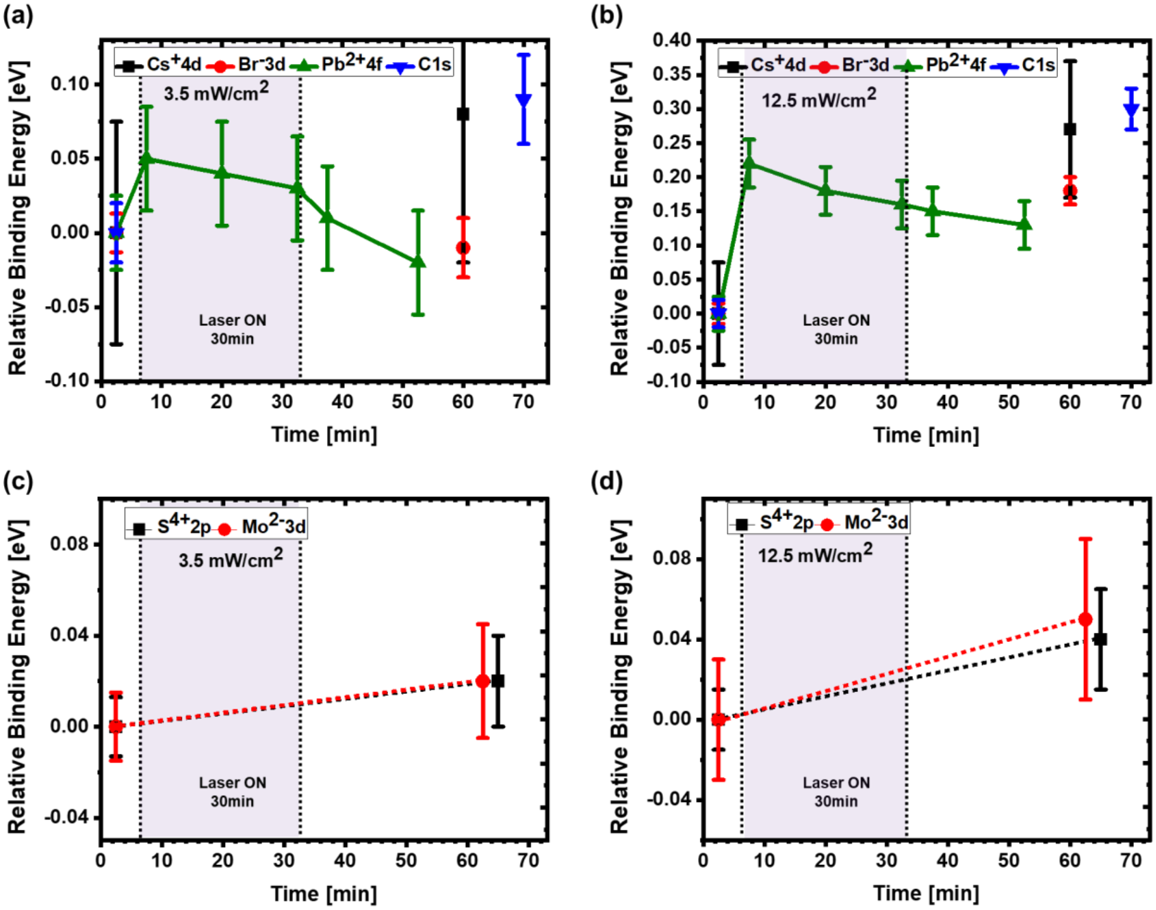

Figure 4.6. Relative binding energies of Cs 4d, Br 3d and Pb 4f spectra calculated (binding energy of Cs 4d, Br 3d and Pb 4f core levels subtracted from the binding energy of the corresponding core level before laser) of NCs on MoS_2 (a) with laser fluence of 3.5 mW/cm^2, (b) with laser fluence of 12.5 mW/cm^2. (c) and (d) relative binding energies of substrate core levels, S 2p and Mo 3d calculated (binding energy of S 2p and Mo 3d core levels subtracted from the binding energy of the corresponding core level before laser) with low and high fluence respectively. The shaded area in the Figure represents 30 minutes laser exposure time.

To sum up, almost no shift in the core levels of perovskite was observed with low fluence, however, a rigid shift towards higher binding energy of the core levels was noticed with high laser fluence. No shift in binding energy of the substrate's core levels were evidenced with both laser fluences. The decrease in intensity of bromide and reduction of Pb^{2+} into Pb^0, as well as binding energy shift of perovskite core levels indicates the substantial surface modifications of $CsPbBr_3$ NCs occurred under UV laser irradiation, which will be discussed later in details.

4.4.2 At the interface with MoO_x

Figure 4.7 (a) and (b) depicts the Pb 4f and Cs 4d, Br 3d core levels of $CsPbBr_3$ perovskite NCs after 30 minutes of UV laser irradiation at fluences of 3.5 mW/cm^2 and 12.5 mW/cm^2 . Before the laser illumination Pb 4f shows a single component at the binding energy of 138.91 eV for Pb $4f_{7/2}$ assigned to Pb^{2+} of the perovskite, however after the laser exposure with both low and high fluence, a new chemical specie at the binding energy of 136.95 eV for Pb $4f_{7/2}$ associated with the formation of metallic lead (Pb^0) appears.[22] Similarly, Cs 4d appears at the binding energy of 75.90 eV for Cs $4d_{5/2}$, and Br $3d_{5/2}$ at 68.91 eV associated with Cs^+ and Br^- of the perovskite.[13] Likewise, core level from the substrate, Mo 3d shows a single component at the binding energy of 232.50 eV for Mo $3d_{5/2}$ assigned to Mo^{6+} state of molybdenum oxide.[15] After the laser exposure for 30 minutes with low fluence, a new chemical specie at the binding energy of 231.68 eV for Mo $3d_{5/2}$ assigned to the Mo^{5+} state of MoO_x emerges, a signature of the reduction of molybdenum oxide, which can have multiple origins,[6,14] and will be discussed later. The high fluence of the laser enhanced the reduction of the MoO_x, as evidenced by increase in intensity Mo^{5+}3d and concurrent decrease in intensity of Mo^{6+}3d. To investigate the changes in intensity of perovskite core levels and their binding energy positions under the laser, time evolution data is measured and presented in the following.

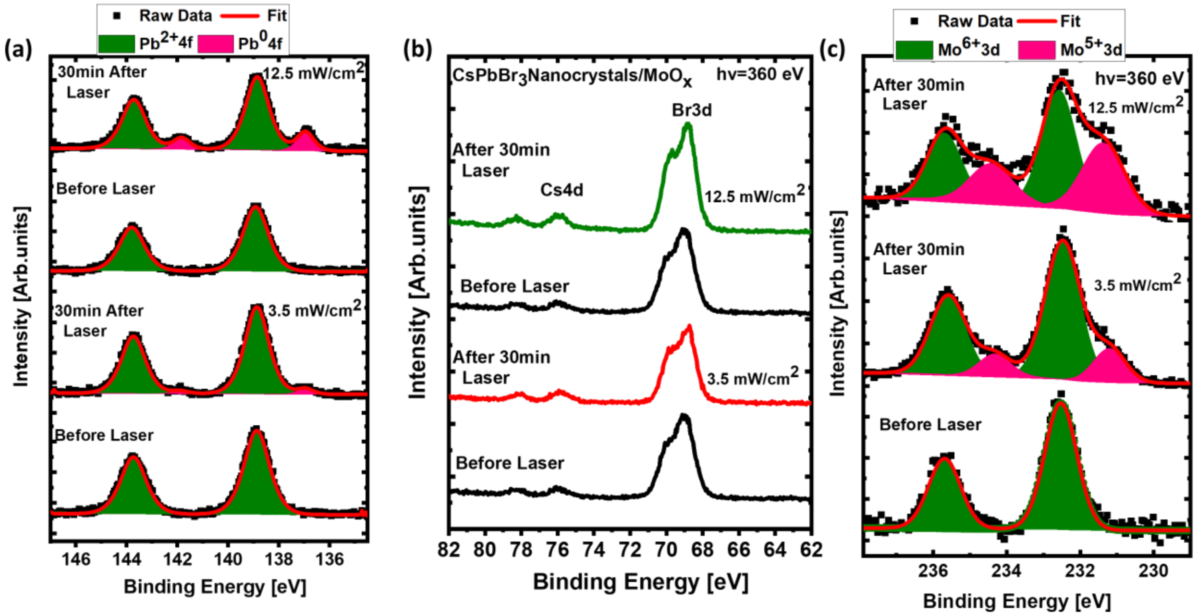

Figure 4.7. Core levels (a) Pb 4f, (b) Cs 4d and Br 3d of $CsPbBr_3$ perovskite nanocrystals on MoO_x, (c) Mo 3d core level of the substrate (MoO_x), measured with the photon energy of 360 eV, before and 30 minutes after (UV) laser of 3.6 eV energy with two laser fluences, 3.5 mW/cm^2 and 12.5 mW/cm^2.

As shown in Figure 4.8 (a) and (b), the relative intensity of Pb^{2+} increases as soon as the laser is turned on with both laser fluences, then decreases slightly until reaching an equilibrium upon turning the laser off. Further exposure to the laser does not show an increase in intensity of Pb^{2+}. Increasing intensity under the laser suggesting the oxidation of Pb^{2+}, conversely, formation of Pb^0 is also occurred, which has intensity of 0.2 under high fluence of the laser. Overall, this suggest many processes might be going on following the laser illumination, which will be explained later. Similar to Pb^{2+}, the intensity of ΣPb 4f (Pb^{2+}4f and $Pb^0$4f) increased when the laser is on and then decreased until an equilibrium is established, and further laser exposure for 60 more minutes does not induce any changes, Figure 4.8 (c) and (d).

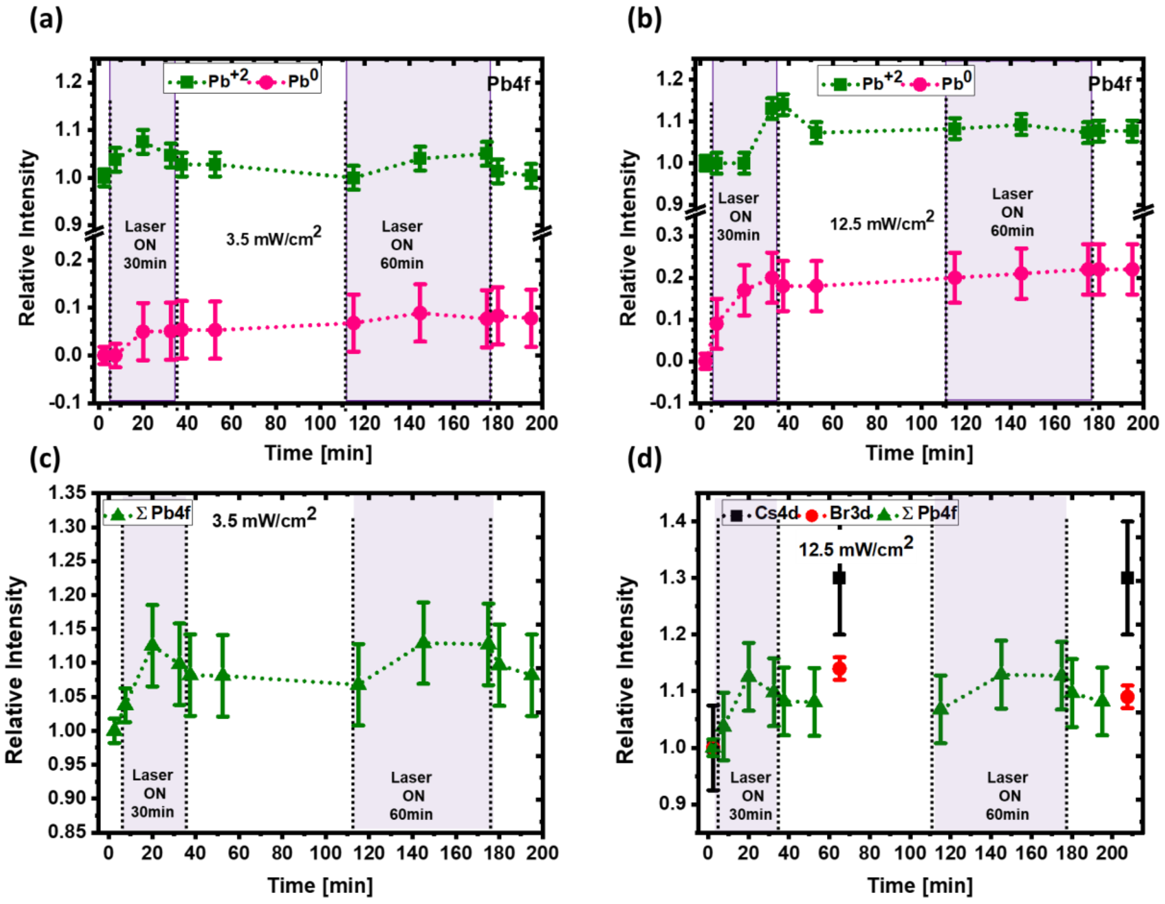

Figure 4.8. Relative intensities of different species of Pb 4f spectra calculated (intensity of Pb 4f component divided by intensity of Pb 4f core level before laser) of $CsPbBr_3$ NCs on MoO_x measured with photon energy 360 eV (a) with laser fluence 3.5 mW/cm^2 (b) 12.5 mW/cm^2 and laser energy 3.6 eV. (c) and (d) relative intensities of Cs 4d, Br 3d and Pb 4f spectra calculated (intensity of Cs 4d, Br 3d and Pb 4f core levels divided by intensities of the corresponding core levels before laser) under the fluence of 3.5 mW/cm^2 and 12.5 mW/cm^2 respectively.

Likewise, intensities of Cs 4d increased after 30 minutes of high laser fluence and remains almost constant with further 60 minutes exposure, and intensity of Br 3d core levels increased to 1.15 of initial intensity after 30 minutes of high fluence laser exposure, with a very slight reduction in intensity after 60 minutes of more exposure.

To summarize, UV exposure to $CsPbBr_3$ perovskite NCs at the interface of MoO_x resulted in an increase in intensity of Pb^{2+}, Cs 4d and Br 3d, as well as the formation of Pb^0. Meanwhile reduction of MoO_x is also observed under the UV laser illumination.

The binding energy position of Pb^{2+}4f increased slightly within the error range under low fluence laser, which then shifted back and ended up at the same binding energy of the one before the laser. However, under high laser's fluence, Pb^{2+} shifted towards low binding energy by

0.07 eV after 30 minutes exposure, along with Br^-3d in the same direction of about same magnitude. The origin of the shift in binding energy positions of $CsPbBr_3$ perovskite NCs core levels will be discussed later, together with changes observed in the core levels of the substrate.

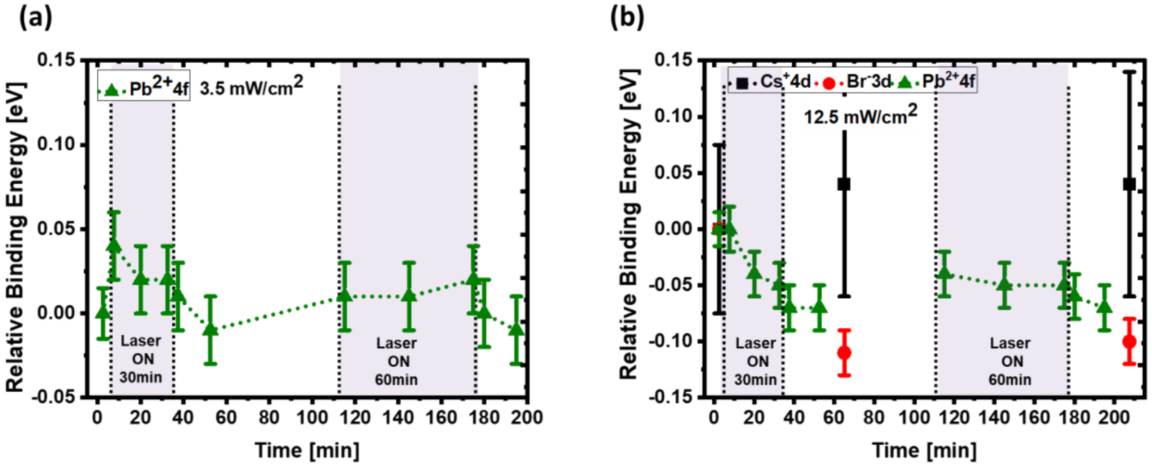

Figure 4.9. Relative binding energies of Cs 4d, Br 3d and Pb 4f spectra calculated (binding energy of Cs 4d, Br 3d and Pb 4f core levels subtracted from the binding energy of the corresponding core level before laser) of NCs on MoO_x substrate (a) with laser fluence of 3.5 mW/cm^2, (b) with laser fluence of 12.5 mW/cm^2

4.4.3 At the interface with ITO

Figure 4.10 (a) shows the overview spectrum of $CsPbBr_3$ NCs spin-coated on ITO substrate, measured with a photon energy of 650 eV. Perovskite core levels: Cs 4d, Br 3d and Pb 4f can be seen, along with the indium (In 3d) and oxygen (O 1s) from the ITO substrate. Figure 4.10 (b), before the laser illumination, the Pb 4f spectra shows single component at the biding energy position at 139.17 eV for Pb $4f_{7/2}$ assigned to Pb^{2+} of perovskite,[8] whereas after the laser with both low and high fluence, an additional component at the binding energy of 137.07 eV for Pb $4f_{7/2}$ appeared, assigned to the formation of metallic lead (Pb^0).[22] Moreover, the width of Pb^{2+} peak increases slightly within error range for low fluence; however, a significant increase in width of the Pb^{2+} peak from 1.20 eV to around 1.40 eV is observed with high laser fluence. The increasing width/broadening of core-level peak indicates a change in the number of chemical bonds contributing to the peak shape and will be discussed later in detail. Similarly, Cs 4d and Br 3d shows single components before and after the laser at the binding energy of 76.15 eV and 69.05, for Cs $4d_{5/2}$ and Br $3d_{5/2}$ respectively, assigned to Cs^+ and Br^- of perovskite.[13] The changes in intensities and binding energies during and after UV laser illumination with different laser fluences will be discussed in the following. Figure 4.10 (d) and (e) shows the C 1s spectra before and after the 30 minutes laser with low and high laser fluence respectively. The relative intensity of C 1s decreased slightly to 0.91 and 0.95 for low and high fluence respectively, but more importantly core-level peak get narrower, meaning that the full width half maximum (FWHM) of C 1s decreased from 1.52 eV to 1.20 eV at laser fluence of 3.5 mW/cm^2 and 1.32 eV to 1.16 eV for 12.5 mW/cm^2. This decrease in peak width suggests variation in the number of chemical bonds that are contributing to the peak shape. This decrease in the intensity of carbon, as well as decrease in the width of C 1s, will be discussed later.

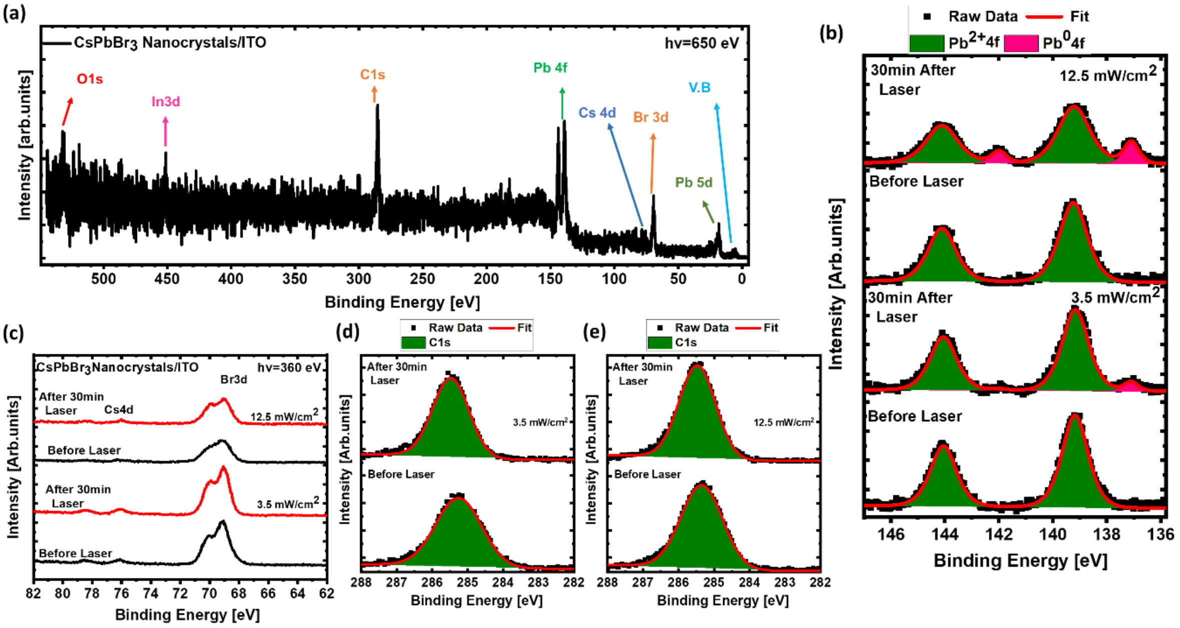

Figure 4.10. (a) Overview spectrum of $CsPbBr_3$ perovskite nanocrystals spin-coated on ITO, measured with the photon energy of 650 eV. (b) Pb 4f, (c) Cs 4d and Br 3d core levels measured with the photon energy of 360 eV before and after 30 minutes of ultraviolet (UV) laser (3.6 eV) exposure for two fluence of the laser 3.5 mW/cm^2 and 12.5 mW/cm^2.

As shown in Figure 4.11 (a) (b), upon switching the laser on, the relative intensity of Pb^{2+} decreases to 0.84 of the same magnitude for both laser fluences, and then remains unchanged upon switching the laser off. However, the intensity of Pb^0 is different for two fluences, increasing to 0.06 and 0.15 for 3.5 mW/cm^2 and 12.5 mW/cm^2, respectively. Similarly, relative intensity of Br 3d increased by 0.06 and 0.10 of their initial values for two laser series, while intensity of ΣPb4f (Pb^{2+} and Pb^0) remains the same. To summarize, UV exposure to $CsPbBr_3$ perovskite NCs at the interface of ITO led to the decrease in intensity of Pb^{2+}, a slight increase in the intensity of Br 3d and Cs 4d, and the formation of Pb^0. With respect to relative binding energies $CsPbBr_3$ perovskite NCs core levels, a slight shift of Pb^{2+}peak towards higher binding energy observed upon turning the laser on, followed by no change in the binding position, Figure 4.12 (a) and (b). Likewise, almost no change in binding energy position of Cs 4d and Br 3d core level is noticed.

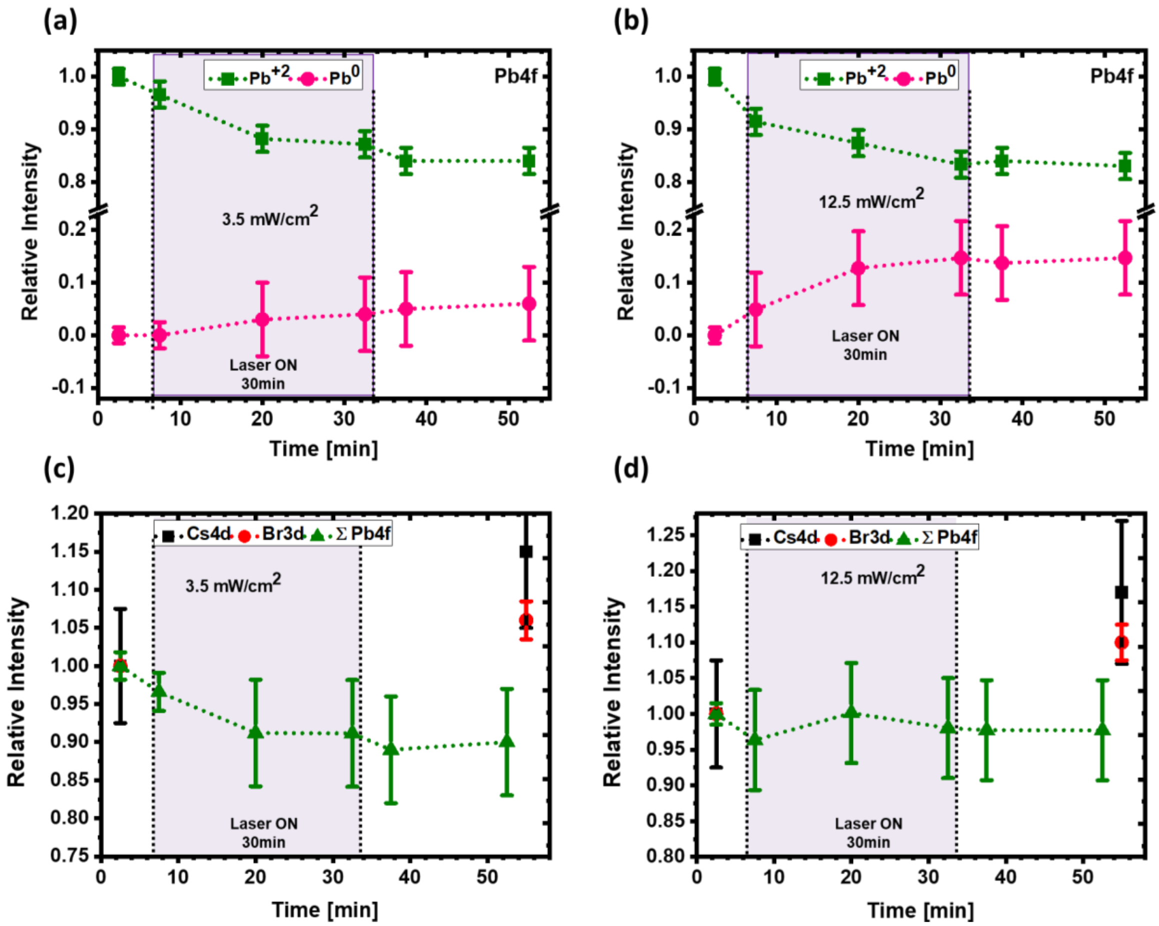

Figure 4.11. Relative intensities of different chemical species of Pb 4f spectra calculated (intensity of Pb 4f component divided by intensity of Pb 4f core level before laser) of $CsPbBr_3$ NCs on ITO substrate, measured with photon energy 360 eV (a) with laser fluence 3.5 mW/cm^2 (b) 12.5 mW/cm^2 and laser energy 3.6 eV. (c) and (d) relative intensities of Cs 4d, Br 3d and Pb 4f spectra calculated (intensity of Cs 4d, Br 3d and Pb 4f core levels divided by intensities of the corresponding core levels before laser).

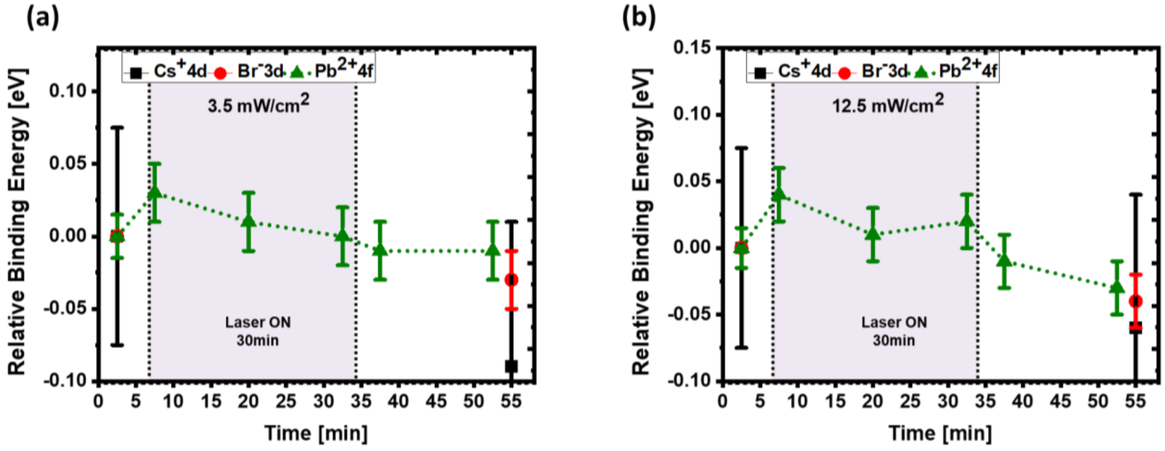

Figure 4.12. Relative binding energies of Cs 4d, Br 3d and Pb 4f spectra of NCs on ITO substrate calculated (binding energy of Cs 4d, Br 3d and Pb 4f core levels subtracted from the binding energy of the corresponding core level before laser) (a) with laser fluence of 3.5 mW/cm^2, (b) with laser fluence of 12.5 mW/cm^2.

4.5 Discussion on UV radiation stability of $CsPbBr_3$ perovskite NCs

At the $CsPbBr_3$ perovskite NCs/MoS_2 interface, under UV laser illumination with low fluence (3.5 mW/cm^2), a small shift of 0.05 eV towards higher binding energy for the peak position of Pb^{2+} was observed upon turning the laser on, which then shifted back when the laser is off and ended up at the same binding energy as it was before laser. With high fluence of the laser (12.5 mW/cm^2), initial shift in the Pb^{2+} was about 0.20 eV, which is roughly four times that of low fluence, indicating some correlation between the magnitude of the shift and the laser power. However, once the laser was turned off, the shift in the binding energy was partly reversible by 0.05 eV. The shift here towards higher binding energy suggests that perovskite has n-type semiconducting property at the MoS_2 interface.[23] Furthermore, the shift might be compatible with the surface photovoltage phenomena, which involves charge separation with electron transfers to the MoS_2 substrate and hole buildup at the perovskite interface. The concept of surface photovoltage is reinforced by the essentially same shift in binding energy of the other core levels of perovskite, such as Br 3d and Cs 4d, as well as carbon C 1s. However, the binding energy shift is not completely reversible due to Fermi level pinning caused by the concurrent formation of donor type states of metallic lead (Pb^0) functioning as traps.[24] Meanwhile, it is important to note that laser exposure damages perovskite structure, as evidenced by the formation of Pb^0 and a decrease in the intensity of Pb^{2+} and Br 3d signals. Consequently, this shift in binding energy may be attributed to the combined effects of surface photovoltage and chemical shift caused by laser-induced structural modifications.

Moreover, a similar shift in the binding energy of C 1s as for the other core levels of perovskite indicates that the ligands attached to the NCs contributed more to the signal of the carbon than the adventitious carbon. Besides, the unchanged relative intensity of C 1s under both laser fluences but broadening of the peak suggests while ligands might be detached from the NCs, they remains on the surface and desorption of ligands does not occur. Nonetheless, the complexity of carbon peaks fitting due to the number of carbon contribution from ligands and adventitious carbon, establishing an appropriate assumption remains intricate, and therefore it should be investigated in future studies where measuring C 1s on the pristine substrate and NCs on top of it will reveal a more unambiguous picture.

The increase in relative intensity of Cs 4d following high fluence laser illumination might be due to desorption of ligands and/or loss of bromide. Since the intensity of carbon remains the same, the increase in relative intensity of Cs 4d is not due to desorption of the ligands. On the other hand, following bromide sublimation as Br_2(g) into the vacuum, as evidenced by the decrease in bromide intensity after the laser, the signal coming from the NC's core is now consisting of cesium and lead with relatively less contribution of bromide, resulting in an increase in intensity of Cs 4d. Yet the weak peak intensity of Cs 4d due to its small cross section at 360 eV, the assumption regarding the variations in Cs 4d intensity may not be entirely correct.

With regards to MoS_2 substrate, core levels of the substrate, S 2p and Mo 3d remains unchanged both in intensity and binding energy position following laser illumination. It has been reported that the presence of sulfur vacancies results in deep defects states 0.5 eV below MoS_2's conduction band.[25] While oxygen can be adsorbed either physically and/or chemically on these sulfur vacancies,[26] which can play the role in the stability of perovskite. Upon the UV illumination, the adsorbed oxygen can be desorbed due to transition of electrons from oxygen to molybdenum in MoS_2. However, no change in spectral shape of Mo 3d and S 2p was observed under the UV laser, implying that such process can be neglected or, even if it occurs, it is not observed in this study and/or does not contribute to the interfacial chemistry of perovskite and MoS_2.

Of even greater importance, the unaffected Mo 3d and S 2p core levels in terms of shape, intensity and binding energy position under the UV laser illumination signifies an apparent lack of chemical interaction at the interface of $CsPbBr_3$ perovskite and MoS_2 interface, as the reaction of perovskite with the substrate is considered one of the leading causes of the instability in perovskite. The chemical intactness and non-existence of chemical reaction at the interface can be attributed to the low photocatalytic activity, non-diffusivity and high robustness of 2D-transiation metal dichalcogenide materials.[27,28] Nonetheless, tracking the changes other than Pb 4f of perovskite core levels such as, Cs 4d and Br 3d, and/or substrate core levels, S 2p and Mo 3d under the UV laser illumination can prove the stated assumption and provide a clearer picture of the interfacial chemistry of perovskite/MoS_2 interface.

At the $CsPbBr_3$ perovskite NCs/MoO_x interface, under UV laser illumination, though intensity of Pb^{2+} increases, at the same time formation of Pb^0 occurs; both increases for the first 30 minutes of laser exposure then remains constant for another 60 minutes. Also, with increasing laser fluence, the intensity of Pb^{2+} and Pb^0 increased. The increase in intensity of bromide also occurred after the laser. Conversely, reduction of molybdenum oxide (MoO_x) becomes evident after 30 minutes laser exposure, which increases with increasing laser fluence. However, interestingly, reduction of MoO_x increased further after 60 minutes of exposure, while the intensity of Pb^{2+} and Pb^0 remains unchanged after first 30 minutes of laser exposure.

Reduction of MoO_x can have multiple origins here, including UV laser illumination induced reduction, heat induced reduction caused by the laser, and perhaps most significant, perovskite induced reduction as a result of chemical reaction between perovskite and MoO_x. For instance, Jorge et al.[29] formulated the accelerated ageing mechanism of MoO_3 reduction under UV light and elevated temperature, and a common mechanism of oxygen vacancies creation is held responsible for driving the degradation of MoO_3. In another report by Fleisch et al.[30] where the UV illumination at 253.7 nm caused the reduction of MoO_3, which was assigned to the transfer of electrons from oxide to molybdenum or in other words, formation of oxygen vacancies. Generally, it has been agreed that oxygen vacancies created by external stimuli, light and/ heat prompted the reduction of molybdenum oxide. Likewise, direct contact of perovskite (where cation is organic) and MoO_3 also drives reduction of molybdenum oxide. Several studies have described the strong redox or Lewis acid base reaction of perovskite with MoO_3, in which decomposition of organic molecules such as Formamidinium (FA) and Methylammonium (MA), a loss of halide, leads to the severe degradation of perovskite at the very interface.[8,31-33]

In a more convincing study, Apergi et al.[34] investigated the interaction of perovskite precursors such as MAI and FAI with the MoO_3, to disentangle whether instability is inherent to MoO_3, the organic cation or halide species. The presence of oxygen vacancies in MoO_3 are identified as reaction centers for the redox reaction at the interface that leads to not only the decomposition of perovskite precursors but also reduction of oxide. In addition to that, the reaction products of precursor decomposition created additional oxygen vacancies thereby reducing MoO_3 even further.

Hence, reduction of MoO_x in our case, can be attributed to the creation of oxygen vacancies due to the UV illumination of oxide and/or the potential reaction between $CsPbBr_3$ and MoO_x upon the creation of oxygen vacancies by illumination. However, due to the absence of sufficient data on the effects of UV exposure solely on the MoO_x substrate, it is not possible to distinguish whether the reduction of MoO_x occurs solely due to the formation of oxygen vacancies caused by UV laser illumination or if there is a potential chemical reaction occurring at the interface of the oxide and perovskite causes reduction of MoO_x, as explained by Apergi et al.[34] Nevertheless, the increase in the intensity of Pb^{2+}4f for first cycle of the laser and then no change for the second laser cycle suggests the possible chemical reaction at perovskite and MoO_x interface, which can be interpreted as oxidation of Pb^{2+} accompanied by reduction of MoO_x.[14] This assumption is further supported by the shift of Pb^{2+} towards higher binding energy with low fluence after five minutes of turning on the laser with tentative reduction of MoO_x. And even more, despite the formation of Pb^0, the intensity of Pb^{2+} does not decrease, suggesting formation of Pb^0 might be compensated by the oxidation of lead caused by reduction of MoO_x. Albeit the exact origin of MoO_x reduction here remains intricated and needs to be investigated further in future studies where tracking the Mo 3d core level together with Pb 4f during the laser illumination can provide a more definitive reason for the reduction of MoO_x.

Counterintuitively, the intensity of Br 3d is increased after the laser illumination which was expected to decrease. As it is assumed that electron stimulated desorption $Br_2(g)$ supposed to occur that leads to reduction of Pb^{2+} to Pb^0 as described previously in Chapter 3 and reported in earlier studies.[35,36] However, the increase in intensity of bromide can be inferred as, following illumination exciton can be generated which subsequently dissociate and diffuse to the surface of NCs and captured by surface ligands leading to dissociation of ligands due to their low binding energy.[37,38] And the presence of Br vacancies on ligands free surface create traps states resulting in reduction of Pb^{2+} to Pb^0 without desorption of bromide.[39] Even though it explains the reduction of Pb^{2+} to Pb^0, not the increase in intensity of bromide. Alternatively, segregation of bromide [40] or desorption of ligands from the surface can lead to increase in intensity of bromide. Since, due to lack of carbon core level and the tracking of bromide core level during the laser illumination, the pinpoint origin of bromide intensity increase under illumination remains unclear and should be the target of future research. The binding energy shift of core levels under high laser fluence towards lower binding energy can be considered as either a chemical shift or a shift due to surface photovoltage.

At the $CsPbBr_3$ perovskite NCs/ITO interface, following UV illumination, the intensity of Pb^{2+} decreases with concurrent formation of Pb^0 at low laser fluence with the same trend with high laser fluence. Moreover, Pb^{2+} peak becomes broader slightly after low laser fluence while broadening increased significantly with high fluency, suggesting formation of potentially additional chemical species apart from Pb^{2+} contributing to the peak shape. Generally, UV radiation from Ultraviolet spectroscopy (UPS) are known to affect the surface properties of ITO.[41,42] Usually, negatively charged species such as $O_2^-$and OH^- are adsorbed at the ITO surface and upon UV illumination photogenerated holes in ITO can recombine with the electron trapped at the adsorbed state, leading to the release of oxygen and increased conductivity of ITO.[43,44,45] This can also lead to the reactivation of surface states on ITO surface.[46,47] Diffusion of indium from ITO is reported in organic light emitting diodes both prior to device operation [48] and under device operation (under applied bias).[49] Similarly, for the case of perovskite on ITO, leaching of indium ion (In^{3+}) into the perovskite at common processing condition (temperature and voltage bias) is reported.[50] Reaction between ITO and organic Brønsted acid salts methylammoniums and formamidinium leads to the etching of ITO, resulting in In^{3+} ions in the form of InI_3 leaching into perovskite. However, in our case, since $CsPbBr_3$ lacking a Brønsted acid salts component, etching of ITO is impractical and so the diffusion of indium ions into perovskite. Zhidkov et al. reported the white light (above 300 nm) soaking for 1000 hours at the intensity of 1 sun leads to the irreversible degradation to the $CH_3NH_3SnI_3$ perovskite deposited on ITO substrate, which was attributed to not only the degradation of perovskite itself under light but also the diffusion of oxygen, tin and indium atoms from the ITO into the perovskite.[51]

Considering this, the intensity of light at high fluence of the laser in our study is about two orders of magnitude higher than the intensity at 1 sun, therefore it is very likely that substrate ions (oxygen, indium and tin) from ITO can diffuse into the perovskite.[52,53] Thus, the broadening of Pb 4f peak could be related to the formation of additional chemical specie. Since the binding energy of O 1s, In 3d and Sn 3d is higher than the photon energy 360 eV used for PES, it remains obscured to distinguish the formation of which kind of chemical specie causes the broadening of Pb 4f peak.

With regard to increase in intensity of Br 3d, as explained in the case of MoO_x, it could be related to the segregation of halide due to movement of Br^-ion towards the surface.[40] However, the formation of Pb^0 and decrease in intensity of Pb^{2+} suggests sublimation of bromide should occur. As explained earlier, without loss of $Br_2(g)$ into the vacuum, reduction of Pb^{2+} to Pb^0 can occur through trapping of photoinduced electrons by bromide vacancies present on the surface when ligands are dissociated from the NCs.[39] Nonetheless, sublimation of Br_2(g) into the vacuum during the illumination cannot be ruled out since the Br 3d core level recorded in our study is only after the illumination. For the C 1s spectra, not only the intensity but also the width of the peak decreased for the carbon with both fluence of the laser. As stated before, due to the number of carbon contribution from the adventitious carbon and carbon from the ligands complicates determining the explanation for narrowing and decreasing intensity of carbon peak.

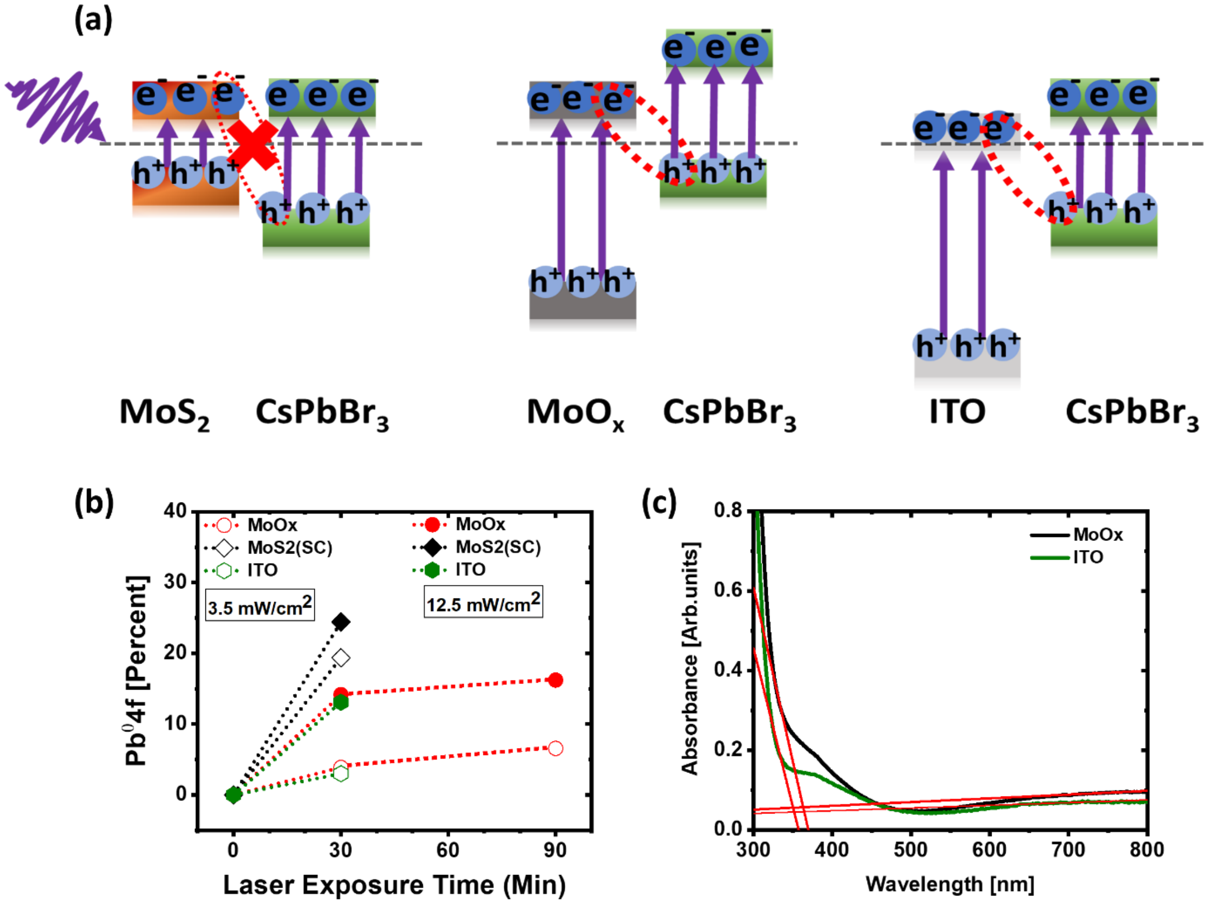

Figure 4.13. (a) schematic illustration of charge recombination at the interface of different substrates (MoS_2, MoO_x and ITO) and $CsPbBr_3$ NCs. The bandgap of 1.20 eV, 3.40 eV, 3.55 eV and 2.30 eV are chosen for MoS_2, MoO_x, ITO and $CsPbBr_3$ NCs respectively. Perovskite is considered as n-type at the interface of MoS_2 and ITO and p-type at the interface of MoO_x on the basis of data obtained from the IR illumination. (b) percentage of Pb^0 4f of $CsPbBr_3$ NCs on different substrates under UV laser illumination for two fluences, 3.5 mW/cm^2 and 12.5 mW/cm^2. (c) Uv-vis absorption spectra of MoOx and ITO substrate.

Intriguingly, a notable rise in bromide intensity is observed, in the case of $CsPbBr_3$ NCs on MoO_x and ITO, while intensity of bromide decreased for the NCs on MoS_2. Besides, significantly less formation of Pb^0 occurred for the NCs on ITO and MoO_x compared to NCs on

MoS_2. The formation of Pb^0 can be comprehended as upon the bandgap excitation of $CsPbBr_3$ NCs, electron transferred into the lead dominated conduction band leaving a hole in bromide dominated valence band.[13] This remaining hole can react with the bromide atoms and form a neutral bromide. This neutral bromide can now easily fit into the interstitial sites due to its smaller radius than bromide ion and leads to creation of a vacancy.[54] Hence, rapid sites change between interstitial and regular site can create large concentration of bromide vacancies which may move independently and might be considered responsible for ionic conductivity in halide perovskite materials.[54] Furthermore, it can be assumed that as long as neutral bromide remains in the lattice no photodecomposition of the perovskite material take place. However, if bromide is removed from the lattice it leads to irreversible formation of Pb^0 along with the decomposition of the material.[55] Meanwhile, the UV illumination can also create electron-hole pairs in the substrates. It is probable that photoexcited electrons in the case of oxide substrates will readily recombine with the remaining holes in perovskite upon its bandgap excitation as illustrated in Figure 4.13 (a). This recombination can limit, if not completely prevent, the formation of neutral bromide interstitial and, thereby the formation of Pb^0. This is partly supported by the increase in bromide concentration at the surface after the laser illumination. On the other hand, in the case of MoS_2, such recombination is very unlikely to happen due to a slightly deeper valence band of perovskite than the valence band of MoS_2 itself. Hence, a higher percentage of Pb^0 formed when the $CsPbBr_3$ NCs are on the MoS_2 than the ITO and MoO_x, Figure 4.13 (b).

A striking revelation from this study, in regard to Pb^0 formation, is that the substrate with larger bandgap (Figure 4.13 (c)) precludes the reduction of Pb^{2+} and thus the Pb^0 formation. Therefore, the charge transport layers with larger bandgap should be investigated in order to circumvent the decomposition of the perovskite structure.

4.6 Conclusion

In this study we investigate the effects of IR (1.2 eV) and UV (3.6 eV) laser illumination on $CsPbBr_3$ NCs deposited on semiconductor substrate, MoS_2 (single crystal), MoO_x and ITO using photoelectron spectroscopy. IR illumination with an energy (1.2 eV) below the bandgap of $CsPbBr_3$ NCs (2.30 eV) leads to the intraband surface photovoltage in the sample without any structural modification of perovskite material. Under illumination, photoexcited electrons and holes in the perovskite transfer towards the MoS_2 and MoO_x, respectively, resulting in the positive and negative charging of NCs on the MoS_2 and MoO_x. This leads to the shift of all the core levels of $CsPbBr_3$ NCs (shown only for Pb 4f) towards higher binding energy for the case of MoS_2 and lower binding energy for the case of MoO_x. The opposite shift in the binding energy of Pb 4f core level is suggesting the n-type and p-type semiconducting properties of perovskite at the MoS_2 and MoO_x interfaces, respectively. Under the dark, recombination of charge carrier reverses the binding energy shift occurred under illumination. Hence, it can be concluded that IR illumination induces sub-bandgap (bromide vacancies and/or bromide interstitial) surface photovoltage, highlighting the presence of deep-trap states in $CsPbBr_3$ perovskite NCs. These deep defects states, which previously predicted,[20] are originating from the surface or grain boundaries of halide perovskite. Since in the case of NCs there are no grain boundaries, the source of these defects is not grain boundaries, and even the presence of ligands on the surface of NCs nullify the assumption of surface being the origin of these defects. Therefore, I believe that these deep trap-states are pertinent to the bulk of $CsPbBr_3$ perovskite material, and are intrinsic to the material itself. Furthermore, since these defects are related to bromide vacancies and/or interstitials, it is likely that under illumination bromide ions which are evident in our result, can diffuse into the top electrode in solar cell devices and lead to the corrosion of metal electrodes, resulting in device degradation. Thus, an ions impermeable layer should be inserted between perovskite and metal electrode to prevent the diffusion of these ions. Also, both in solar cells and light emitting diodes, these deep-trap states can cause the undesired non-radiative recombination, reducing the efficiency of the $CsPbBr_3$ perovskite based optoelectronic devices. With regard to the degradation of perovskite structure, negligible changes are observed under IR illumination for $CsPbBr_3$ NCs deposited on MoS_2 and MoO_x substrate, suggesting that even though sub-bandgap states exist, their concentration is low as IR illumination with an intensity two orders of magnitude higher than the intensity at 1 sun does not lead to the perovskite decomposition.

Under UV illumination, irreversible changes occurred at the interface between MoS_2 and the $CsPbBr_3$ perovskite, as evidenced by electron simulated desorption of bromide atoms, a concurrent reduction of lead (Pb^{2+}) into the metallic lead (Pb^0), and a permanent shift in binding energy of the core levels. Since the decomposition of perovskite structure occurs, shifts in the core-level binding energy are not reversible. With regard to the ligands surrounding the NCs, no significant change in intensity of C 1s core level is observed, indicating a very little loss of the ligands occurs. Although the decomposition of perovskite occurs, no apparent chemical interaction at the interface of perovskite and MoS_2 interface is seen, as no change in the spectral shape, intensity or binding energy of substrate (MoS_2) core levels, S 2p and Mo 3d was observed. This lack of chemical reaction at the interface can be attributed to MoS_2's high chemical stability, low photocatalytic activity, and high robustness. Since MoS_2 appears to prevent any interfacial chemical reaction, it can be a good electron transport layer (on the basis of IR illumination data) to replace SnO_2. Because, even though SnO_2 based perovskite solar cells are efficient, with certified power conversion efficiency of more than 25% ,[56,57] the photocatalytic activity of SnO_2 under UV light,[58] can compromise the stability of these highly efficient perovskite solar cells. Meanwhile, for the case of $CsPbBr_3$ on MoS_2, the existence of reactive and mobile bromide ions (Br^-) in $CsPbBr_3$ can diffuse from the hole transport layer on top to the metal electrode, leading to the corrosion of metal electrode thereby impairs its conductivity.

At the interface of interface of MoO_x and $CsPbBr_3$ perovskite, even though Pb^0 formed under illumination, the intensity of Pb^{2+} increases along with the intensity of bromide. At the same time, reduction of molybdenum oxide is also evidenced as reduction of Mo^{6+}3d to lower oxidation state of Mo^{5+}3d. Reduction of molybdenum oxide could be related to the potential chemical reaction between the perovskite and MoO_x, which should lead to reduction of not only Pb^{2+} to Pb^0 but also a decrease in intensity of Pb^{2+}. The intensity of Pb^{2+}, on the other hand, rose until an equilibrium is reached and then remains constant. However, decrease in intensity of Pb^{2+} might have been compensated by the oxidation of Pb^{2+} by the concurrent reduction of Mo^{6+} to Mo^{5+}, leading to constant intensity of Pb^{2+} after certain threshold is reached. In spite of that, lack of Mo 3d core level spectrum during laser illumination makes it complicated to correlate the exact phenomenon that dictates the observed photochemical changes at $CsPbBr_3$ NCs and MoO_x interface.

$CsPbBr_3$ NCs on ITO, like in the case of NCs on MoS_2, UV laser illumination damages the NCs, revealed by the reduction of Pb^{2+} to Pb^0. However, unlike NCs on MoS_2, the bromide intensity increased instead of decreased. Particularly significant, following the laser illumination, the Pb 4f peak gets broader, suggesting that some new chemical species formed as a result of diffusion of indium, tin, and oxygen from ITO. However, since In 3d, Sn 3d and O 1s core levels are not measured due to their binding energies greater than the photon energy 360 eV used, it is ambiguous which metal ions diffused and resulted in the formation of new chemical species and broadening of Pb 4f core-level. Regarding the ligands that are attached at the surface $CsPbBr_3$ NCs, a slight decrease in intensity of C 1s is observed, which could be attributed to desorption of the ligands, however complexity of peak fitting due to contribution of both adventitious and ligands carbon signals making this assumption less definite.

When comparing the photostability of $CsPbBr_3$ NCs on different substrates in regards to Pb^0 formation, the stability of NCs is in the order of ITO>MoO_x>MoS_2. Photo-induced electron transfer from bromide dominated valence band to lead dominated conduction band leads to the formation of neutral bromide interstitial and bromide vacancies, and resulting formation of bromide gas (Br_2(g)). The subsequent sublimation Br_2(g) resulted in the formation of Pb^0. The formation of neutral bromide interstitial, which eventually led to the formation of Pb^0, is decreased for the NCs on ITO and MoO_x substrate because the photoexcited electrons from the substrate can recombine with holes left behind from the bandgap excitation of perovskite. This recombination will result in fewer holes remaining that can generate neutral bromide interstitial and bromide vacancies, thereby limiting the formation of Br_2(g) and consequent formation of Pb^0. This charge carrier recombination is limited in the NCs/MoS_2 interface due to deeper valence band of the perovskite compared to that of MoS_2. Thus, a crucial insight is that $CsPbBr_3$ NCs deposited on wider bandgap substrates are more stable with regard to Pb^0 formation, signifying the relation of bandgap of underlying substrate and decomposition of perovskite material. In summary, under IR illumination, for $CsPbBr_3$ perovskite NCs on MoS_2 and MoO_x intraband surface photovoltage stemming from deep-trap states has been observed, however negligible changes are observed in terms of decomposition of the perovskite. $CsPbBr_3$ NCs on MoS_2, though degradation occurs which is inherent to halide perovskite, no chemical reaction takes place as substrate remains intact owing to MoS_2 high chemical inertness and high robustness. Therefore, MoS_2 can be an used as an effective buffer layer between charge transport layer and perovskite in the solar cell devices. For the case of NCs on MoO_x, despite the smaller level of decomposition of the perovskite occurring, the reduction of molybdenum oxide occurs that can induce a potential chemical reaction at the interface of perovskite and MoO_x, limiting the stability. Similarly, $CsPbBr_3$ NCs on ITO, even less degradation of the NCs occur but like MoO_x, interfacial chemical reactions are anticipated to occur due to diffusion of metal ions from the ITO substrate into the perovskite.

Therefore, an ion blocking buffer layer should be inserted to avoid direct contact between the perovskite and ITO to mitigate the potential chemical reaction, and thus the instability.

References

1. Chen, Tian, Jiangsheng Xie, and Pingqi Gao. "Ultraviolet Photocatalytic Degradation of Perovskite Solar Cells: Progress, Challenges, and Strategies." *Advanced Energy and Sustainability Research* 3.6 (2022): 2100218.
2. Ji, Jun, et al. "Two-stage ultraviolet degradation of perovskite solar cells induced by the oxygen vacancy-Ti4+ states." Iscience 23.4 (2020): 101013.
3. Elbanna, Ahmed, et al. "Perovskite-transition metal dichalcogenides heterostructures: recent advances and future perspectives." Opto-Electronic Science 1.8 (2022): 220006-1.
4. Qiu, Lei, et al. "Interfacial engineering of halide perovskites and two-dimensional materials." Chemical Society Reviews (2023).
5. Yin, Guannan, et al. "Low-temperature and facile solution-processed two-dimensional TiS 2 as an effective electron transport layer for UV-stable planar perovskite solar cells." Journal of Materials Chemistry A 6.19 (2018): 9132-9138.
6. Greiner, Mark T., and Zheng-Hong Lu. "Thin-film metal oxides in organic semiconductor devices: their electronic structures, work functions and interfaces." NPG Asia Materials 5.7 (2013): e55-e55.
7. Hang, Da-Ren, et al. "Enhanced Photocatalytic Performance of ZnO Nanorods Coupled by Two-Dimensional α-MoO3 Nanoflakes under UV and Visible Light Irradiation." Chemistry–A European Journal 22.36 (2016): 12777-12784.
8. Olthof, Selina, and Klaus Meerholz. "Substrate-dependent electronic structure and film formation of MAPbI3 perovskites." Scientific reports 7.1 (2017): 40267.
9. Legeay, Gérard, et al. "Excimer laser beam/ITO interaction: from laser processing to surface reaction." physica status solidi c 5.10 (2008): 3248-3254.
10. Deshmukh, Akshaya Pisal, et al. "Resistive Switching in CsPbBr3 (0D)/MoS2 (2D) Heterojunction System: Trap-Controlled Space Charge Limited Transport Mechanism." ACS Applied Electronic Materials 5.3 (2023): 1536-1545.
11. Jung, Changki, Hae In Yang, and Woong Choi. "Effect of ultraviolet-ozone treatment on MoS2 monolayers: comparison of chemical-vapor-deposited polycrystalline thin films and mechanically exfoliated single crystal flakes." Nanoscale Research Letters 14.1 (2019): 1-8.
12. Liu, Xiaomin, et al. "Flexible transparent high-efficiency photoelectric perovskite resistive switching memory." Advanced Functional Materials 32.38 (2022): 2202951.
13. Xie, Yujun, et al. "Highly efficient blue-emitting CsPbBr3 perovskite nanocrystals through neodymium doping." Advanced science 7.20 (2020): 2001698.
14. Schulz, Philip, et al. "High-work-function molybdenum oxide hole extraction contacts in hybrid organic–inorganic perovskite solar cells." ACS applied materials & interfaces 8.46 (2016): 31491-31499.
15. F. Cauduro, André L., et al. "Crystalline molybdenum oxide thin-films for application as interfacial layers in optoelectronic devices." ACS Applied Materials & Interfaces 9.8 (2017): 7717-7724.
16. Jorge, Marina, et al. "Accelerated ageing of molybdenum oxide." Materials Research Express 4.11 (2017): 115502.
17. Razera, Ricardo AZ, et al. "Instability of p–i–n perovskite solar cells under reverse bias." Journal of Materials Chemistry A 8.1 (2020): 242-250.
18. Hoke, Eric T., et al. "Reversible photo-induced trap formation in mixed-halide hybrid perovskites for photovoltaics." Chemical Science 6.1 (2015): 613-617.
19. Evarestov, R. A., et al. "First-principles comparative study of perfect and defective CsPbX 3 (X= Br, I) crystals." Physical Chemistry Chemical Physics 22.7 (2020): 3914-3920.
20. Levine, Igal, et al. "Deep defect states in wide-band-gap ABX3 halide perovskites." ACS Energy Letters 4.5 (2019): 1150-1157.

21. Eames, Christopher, et al. "Ionic transport in hybrid lead iodide perovskite solar cells." Nature communications 6.1 (2015): 7497.
22. Amelot, Dylan, et al. "Revealing the band structure of FAPI quantum dot film and its interfaces with electron and hole transport layer using time resolved photoemission." The Journal of Physical Chemistry C 124.6 (2020): 3873-3880.
23. Sloboda, Tamara, et al. "A method for studying pico to microsecond time-resolved core-level spectroscopy used to investigate electron dynamics in quantum dots." Scientific Reports 10.1 (2020): 22438.
24. Zu, Feng-Shuo, et al. "Impact of white light illumination on the electronic and chemical structures of mixed halide and single crystal perovskites." Advanced Optical Materials 5.9 (2017): 1700139.
25. Zhao, Yanfei, et al. "Electrical spectroscopy of defect states and their hybridization in monolayer MoS2." Nature Communications 14.1 (2023): 44.
26. Wang, Yuhang, et al. "UV illumination enhanced desorption of oxygen molecules from monolayer MoS 2 surface." Nano Research 13 (2020): 358-365.
27. Elbanna, Ahmed, et al. "Perovskite-transition metal dichalcogenides heterostructures: recent advances and future perspectives." Opto-Electronic Science 1.8 (2022): 220006-1.
28. Yin, Guannan, et al. "Low-temperature and facile solution-processed two-dimensional TiS 2 as an effective electron transport layer for UV-stable planar perovskite solar cells." Journal of Materials Chemistry A 6.19 (2018): 9132-9138.
29. Jorge, Marina, et al. "Accelerated ageing of molybdenum oxide." Materials Research Express 4.11 (2017): 115502.
30. Fleisch, T. H., and G. J. Mains. "An XPS study of the UV reduction and photochromism of MoO3 and WO3." The Journal of chemical physics 76.2 (1982): 780-786.
31. Liao, Xiaxia, et al. "Chemical Interaction at the MoO3/CH3NH3PbI3–x Cl x Interface." ACS Applied Materials & Interfaces 13.14 (2021): 17085-17092.
32. Liu, Peng, et al. "Interfacial electronic structure at the CH3NH3PbI3/MoOx interface." Applied Physics Letters 106.19 (2015).
33. Li, Lin, et al. "Interfacial electronic structures of MoOx/mixed perovskite photodetector." Organic Electronics 65 (2019): 162-169.
34. Apergi, Sofia, et al. "Decomposition of Organic Perovskite Precursors on MoO3: Role of Halogen and Surface Defects." ACS Applied Materials & Interfaces 14.30 (2022): 34208-34219.
35. Dang, Zhiya, et al. "In situ transmission electron microscopy study of electron beam-induced transformations in colloidal cesium lead halide perovskite nanocrystals." Acs Nano 11.2 (2017): 2124-2132.
36. Svanström, Sebastian, et al. "X-ray stability and degradation mechanism of lead halide perovskites and lead halides." Physical Chemistry Chemical Physics 23.21 (2021): 12479-12489.
37. Chen, Junsheng, et al. "Photo-stability of CsPbBr3 perovskite quantum dots for optoelectronic application." Science China Materials 9.59 (2016): 719-727.
38. Paul, Susmita, and Somobrata Acharya. "Postsynthesis transformation of halide perovskite nanocrystals." ACS Energy Letters 7.6 (2022): 2136-2155.
39. Kirakosyan, Artavazd, et al. "Mechanistic insight into surface defect control in perovskite nanocrystals: ligands terminate the valence transition from Pb2+ to metallic Pb0." The Journal of Physical Chemistry Letters 10.15 (2019): 4222-4228.
40. Knight, Alexander J., et al. "Electronic traps and phase segregation in lead mixed-halide perovskite." ACS Energy Letters 4.1 (2018): 75-84.
41. Schlaf, R., H. Murata, and Z. H. Kafafi. "Work function measurements on indium tin oxide films." Journal of Electron Spectroscopy and Related Phenomena 120.1-3 (2001): 149-154.
42. Kim, J. S., et al. "Kelvin probe and ultraviolet photoemission measurements of indium tin oxide work function: a comparison." Synthetic metals 111 (2000): 311-314.

43. Armstrong, Neal R., et al. "Interface modification of ITO thin films: organic photovoltaic cells." Thin Solid Films 445.2 (2003): 342-352.
44. Zhou, Yinhua, et al. "Direct correlation between work function of indium-tin-oxide electrodes and solar cell performance influenced by ultraviolet irradiation and air exposure." Physical Chemistry Chemical Physics 14.34 (2012): 12014-12021.
45. Furmansky, Yulia, et al. "Photoconductance of ITO/Conductive Polymer Junctions in the UV and Visible Ranges." The Journal of Physical Chemistry C 122.13 (2018): 7288-7295.
46. Gassenbauer, Yvonne, and Andreas Klein. "Electronic and chemical properties of tin-doped indium oxide (ITO) surfaces and ITO/ZnPc interfaces studied in-situ by photoelectron spectroscopy." The Journal of Physical Chemistry B 110.10 (2006): 4793-4801.
47. Legeay, Gérard, et al. "Excimer laser beam/ITO interaction: from laser processing to surface reaction." physica status solidi c 5.10 (2008): 3248-3254.
48. Schlatmann, A. R., et al. "Indium contamination from the indium–tin–oxide electrode in polymer light-emitting diodes." Applied physics letters 69.12 (1996): 1764-1766.
49. Lee, S. T., Z. Q. Gao, and L. S. Hung. "Metal diffusion from electrodes in organic light-emitting diodes." Applied Physics Letters 75.10 (1999): 1404-1406.
50. Kerner, Ross A., and Barry P. Rand. "Electrochemical and thermal etching of indium tin oxide by solid-state hybrid organic–inorganic perovskites." ACS Applied Energy Materials 2.8 (2019): 6097-6101.
51. Zhidkov, Ivan S., et al. "Influence of Ion Migration from ITO and SiO2 Substrates on Photo and Thermal Stability of CH3NH3SnI3 Hybrid Perovskite." The Journal of Physical Chemistry C 124.27 (2020): 14928-14934.
52. Ahmad, Zubair, et al. "Instability in CH3NH3PbI3 perovskite solar cells due to elemental migration and chemical composition changes." Scientific reports 7.1 (2017): 15406.
53. Seo, Hong-Kyu, et al. "Efficient flexible organic/inorganic hybrid perovskite light-emitting diodes based on graphene anode." Advanced Materials 29.12 (2017): 1605587.
54. Kim, Gee Yeong, et al. "Large tunable photoeffect on ion conduction in halide perovskites and implications for photodecomposition." Nature materials 17.5 (2018): 445-449.
55. Senocrate, Alessandro, Eugene Kotomin, and Joachim Maier. "On the way to optoionics." Helvetica Chimica Acta 103.7 (2020): e2000073.
56. Zhao, Yang, et al. "Inactive (PbI2) 2RbCl stabilizes perovskite films for efficient solar cells." Science 377.6605 (2022): 531-534.
57. Min, Hanul, et al. "Perovskite solar cells with atomically coherent interlayers on SnO2 electrodes." Nature 598.7881 (2021): 444-450.
58. Hang, Pengjie, et al. "An interlayer with strong Pb-Cl bond delivers ultraviolet-filter-free, efficient, and photostable perovskite solar cells." Iscience 21 (2019): 217-227.

Conclusions and outlook

During the device operation of a solar cell photogenerated carriers pass through multiple junction or interfaces for their collection at the respective electrodes to generate current, hence these interfaces strongly influence the transport of these carriers and dictates charge collection efficiencies of a solar cell. This thesis focuses on the investigation of dynamical processes that occur at the surface and in the interfaces of lead halide perovskite materials under the infrared (IR) and ultraviolet (UV) light by using photoelectron spectroscopy (PES). The chemical and variable surface sensitivity of synchrotron-based PES allows me to study the chemical changes that occur both at the surfaces and interfaces of the materials.

I have used PES to study the substrate dependent decomposition properties of $CsPbBr_3$ perovskite nanocrystals (NCs). The NCs have an optical bandgap of 2.30 eV, a cubic shape in the form of α-cubic crystalline phase and a size of roughly 13 nm. A Ligand exchange procedure is used to enhance the conductivity of the NCs where long carbon chain native ligands (oleylamine and oleic acid) are exchanged with shorter acetate ligands. Since the charge transport happens through a hopping mechanism between the NCs, an exchange of the ligand reduces the width of tunnelling barrier, allowing efficient transport of the carriers in NCs film.

Halide perovskites are very sensitive and degrades under external stimuli such as high humidity, elevated temperature, oxygen, and more significantly exposure to sunlight. In particular, UV light affects the stability and deteriorates not only the perovskite itself but also the charge transport layers used for charge extraction. The $CsPbBr_3$ perovskite NCs under UV light illumination shows rich chemistry in the interface which is dependent on substrate type. Distinctly different behavior of perovskite NCs on metal substrate, semiconductor and oxide substrates was observed under UV illumination. In addition to that, exposure to infrared (IR) light also affected the NCs differently on metal and semiconductor substrates although without decomposition of the perovskite material in the latter.

I have used PES to study the effects of IR and UV and intense x-rays illumination on $CsPbBr_3$ NCs deposited on gold (Au) metal, which used as a model for the charge collection at the anode to the semiconductor and oxides materials which generate and transport the charge. To isolate the effect of the IR and UV light, the Low-Dose PES end-station at BESSY II was used, where due to the low x-ray flux coupled with the high transmission of ArTOF spectrometer, the effect of IR and UV light can be isolated from x-ray induced damage. Even NCs exposure to IR (1.2 eV) light below the bandgap of $CsPbBr_3$ NCs (2.30 eV) leads to a chemical reaction at the interface between Au and the perovskite. This chemical reaction has been attributed to the underpotential deposition of ionic lead on the exposed Au surface. The reflection of IR light from the Au substrate is assumed as the driving force for such a reaction. Underpotential deposition is surface-limited redox process where ions change oxidation state upon the adsorption and terminates when a monolayer or submonolayer is formed. The $CsPbBr_3$ NCs exposure to the UV (3.6 eV) light above the bandgap of NCs not only catalyzes such a chemical reaction, but also leads to the formation of metallic lead (Pb^0). Furthermore, it is found that underpotential deposition of lead (Pb_{UPD}) is a surface and interface dominated specie and it occurs only when Pb^{2+} ions are freed from the perovskite and when the perovskite is in direct contact with Au. Moreover, ligands does not play a role either in the formation or prevention of Pb_{UPD}. While, on the other hand, Pb^0 is only formed when halide (bromide in our case) escapes from the surface in the form of $Br_2(g)$. Also, it was found that formation of Pb^0 can be extended into the bulk of the NCs from exposure to UV light of high fluence. When the NCs on Au are exposed to high x-ray flux, decomposition of NCs occur, evidenced by the formation of both Pb_{UPD} and Pb^0. With exposure to high x-ray flux, the degradation of the perovskite structure occurs immediately, meaning that the damage occurs on a timescale faster than the spectrum acquisition time. Therefore, $CsPbBr_3$ perovskite NCs on Au substrate are not stable as non-negligible and irreversible changes occur when exposed to IR and UV light, as well as high flux x-rays, and direct contact of perovskite with Au should be considered more cautiously. Additionally, these findings suggest potential limitations of Au being used as a stable electrode in perovskite based optoelectronic devices.

The $CsPbBr_3$ NCs on semiconductor (MoS_2 single crystal)) and metal oxide (MoO_x) substrates, when exposed to IR light, shows the buildup of intraband surface photovoltage in the sample evidenced as shift in the binding energy of Pb 4f core-level, without any decomposition of the perovskite. Such an intraband surface photovoltage stems from deep-trap states (bromide interstitial and/or bromide vacancies) located at the midgap position of $CsPbBr_3$. This leads to the opposite shift in the binding energy of the core levels of perovskite on n-type substrate (MoS_2) versus p-type substrate (MoO_x). It also emphasizes that the substrate upon which $CsPbBr_3$ NCs are deposited dictates the semiconducting property of the perovskite, i.e, perovskite adopts n-type properties on MoS_2 substrate while p-type properties on MoO_x. More importantly, it signifies that substrate dependent semiconducting properties of perovskite is not only at the interface but also in the bulk and at the surface of the perovskite. Furthermore, these sub-bandgap states which acts as undesired non-radiative recombination centers, can lead to poor efficiency of optoelectronic devices based on $CsPbBr_3$ NCs. Also, though sub-bandgap states exist, the concentration of these deep-trap states is low as the intensity of light two orders of higher magnitude than the intensity at 1 sun does not induce the decomposition of perovskite material. Nevertheless, existence of such bandgap states originating from bromide vacancies and/or bromide interstitial underscore the insertion of either a buffer layer between $CsPbBr_3$ perovskite and charge transport layer or a charge transport layer that should prevent the diffusion of Br^-ions. Otherwise, these Br^-ions can diffuse into the metal electrode, leading to oxidation of metal thereby impairing its conductivity.

UV light (3.6 eV) exposure decomposes the $CsPbBr_3$ perovskite NCs on MoS_2 by promoting charge transfer from halide dominated valence bands to the lead dominated conduction bands, resulting in desorption of bromide atoms with concurrent reduction of Pb^{2+} to Pb^0. An increase in the UV laser fluence increases the damage, however the MoS_2 substrate remains chemically intact as evidenced by the unchanged shape, intensity and binding energy of the MoS_2 core level spectra. This means no chemical interaction happens at the interface between the MoS_2 and the perovskite, suggesting MoS_2 might be potentially useful buffer layer, even if not alone it can be used in combination with other materials to enhance the intrinsic stability of perovskite devices. However, band alignment and MoS_2's ability of charge transport needs to be investigated before rationalizing its functionality in a device.

With regards to the perovskites interface with the MoO_x, UV illumination induces decomposition of perovskite, however this is less pronounced than on the MoS_2 substrate. Even more significant, the reduction of MoO_x is observed which could occur as a result of redox reaction at the interface between the perovskite and the metal oxide. This reduction can cause a dramatic change in the interface composition, resulting in the unintended formation of defective layer that hampers the charge extraction and facilitates recombination. Nevertheless, further studies are required to determine whether reduction of MoO_x occurs on its own under UV illumination or if it is caused by a chemical reaction between the perovskite and the MoO_x.

Similarly, at the interface with ITO, the least amount of the damage to perovskite is observed among all the substrates, however a potential chemical reaction at the interface is expected due to a significant increase in peak width of Pb 4f core level of perovskite. This broadening of Pb 4f peak suggests the formation of a new chemical specie, which might come from indium or tin ions diffusion from the ITO. However, this requires a future detailed study of the In 3d and Sn 4d core-level spectra to elucidate. Nevertheless, an ion impermeable layer should be inserted between the ITO and the perovskite to avoid potential interfacial chemical reaction and to preserve ITO's functionality. As stated before, the degradation of the perovskite structure pertaining to the formation of Pb^0 is prevented by using oxide substrate. The prevention of perovskite decomposition on wide bandgap substrates can be rationalized as under UV illumination, bandgap excitation leads to generation of electron-hole pairs in both the substrate and perovskite. Since the bandgap of perovskite is less than the bandgap of the oxides (ITO and MoO_x), it is more probable that photoexcited electron can recombine with the hole left behind upon bandgap excitation of $CsPbBr_3$. This recombination partly reduces the formation of halide interstitial (bromide in our case), which is responsible for the creation of halide vacancies and subsequent migration of halide ions, resulting in a drop in the formation of Br_2(g). Thus, a reduced formation of Pb^0 occurs. However, such a recombination (photoexcited electrons in oxides and holes left behind upon bandgap excitation of perovskite) can reduce the collection of holes at the anode and thus efficiency of a device. Yet this assumption needs to be validated and future research can investigate how this recombination affects device functionality.

Lastly, one can argue that this study explores rather than prevents the process of degradation of $CsPbBr_3$ perovskite NCs occurring at the different interfaces. However, the goal is to comprehend the phenomenon and mechanism that induces and dictates such a degradation, and identify possible ways to inhibit such a decomposition of the perovskite. This study highlights that the interface integrity is an important factor, and developing the atomistic pictures of the interface will assist in the development of highly efficient and stable perovskite NCs based opto-electronic devices. Conceivably, I believe that the findings and understandings acquired from this study can be extended to investigate the other compositions (ubiquitously used hybrid one (mixed organic and inorganic)) and their interfaces with other charge transport layers.

Résumé

Au cours du fonctionnement d'une cellule solaire, les porteurs photogénérés traversent de multiples jonctions ou interfaces pour être collectés aux électrodes respectives afin de générer du courant. Ces interfaces influencent donc fortement le transport de ces porteurs et déterminent l'efficacité de la collecte des charges d'une cellule solaire. Cette thèse porte sur l'étude des processus dynamiques qui se produisent à la surface et dans les interfaces des matériaux pérovskites à base d'halogénure de plomb sous lumière infrarouge (IR) et ultraviolette (UV) en utilisant la spectroscopie de photoélectrons (PES). En utilisant la sensibilité chimique et de surface de la PES réalisée en synchrotron, j'ai étudié les changements chimiques qui se produisent à la fois sur les surfaces et les interfaces des matériaux.

J'ai utilisé la PES pour étudier les propriétés de décomposition des nanocristaux (NCs) de pérovskite $CsPbBr_3$ en fonction du substrat. Les NCs ont une bande interdite optique de 2,30 eV, une forme cubique d’environ 13 nm de côté sous la forme d'une phase cristalline α-cubique. Une procédure d'échange de ligands est utilisée pour améliorer la conductivité des NCs où les ligands natifs à longue chaîne de carbone (olélyamine et acide oléique) sont échangés avec des ligands acétates plus courts. Étant donné que le transport de charges s'effectue par un mécanisme de sauts entre les NCs, l'échange de ligands réduit la largeur de la barrière à traverser, ce qui permet un transport efficace des porteurs dans la pellicule des NCs.

Les pérovskites halogénées sont très sensibles et se dégradent sous l'effet de stimuli externes tels qu'une forte humidité, une température élevée, l'oxygène et, surtout, l'exposition à la lumière du soleil. En particulier, la lumière UV affecte la stabilité et détériore non seulement la pérovskite elle-même, mais aussi les couches de transport de charge utilisées pour l'extraction de charges. Les NCs de pérovskite $CsPbBr_3$ présentent un comportement chimique dynamique dans l'interface sous illumination UV qui dépend du type de substrat. Un comportement différent des NCs de pérovskite a été observé sur des substrats métalliques, semi-conducteurs et d’oxydes de manière distincte sous illumination UV. En outre, l'exposition à la lumière infrarouge (IR) a également affecté différemment les NCs sur les substrats métalliques et semi-conducteurs, bien que sans décomposition du matériau pérovskite sur les substrats semi-conducteurs.

J'ai utilisé la PES pour étudier les effets de l'illumination IR, UV et rayons X intenses sur les NCs CsPbBr3 déposés sur or (Au) qui a été utilisé comme modèle pour la collecte de charge à l'anode vers les matériaux semi-conducteurs et d’oxydes qui génèrent et transportent la charge. Pour isoler l'effet de la lumière IR et UV, l’expérience PES à faible dose de BESSY II a été utilisée, où, en raison du faible flux de rayons X associé à la transmission élevée du spectromètre ArTOF, l'effet de la lumière IR et UV peut être isolé des dommages induits par les rayons X. Même l'exposition des NCs à une lumière IR (1,2 eV) inférieure à la bande interdite des NCs CsPbBr3 (2,30 eV) entraîne une réaction chimique à l'interface entre Au et la pérovskite. Cette réaction chimique a été attribuée au dépôt sous-potentiel de plomb ionique sur la surface Au exposée. La réflexion de la lumière IR sur le substrat Au est supposée être la force motrice de cette réaction. Le dépôt sous-potentiel (*underpotential deposition*) est un processus d'oxydoréduction limité à la surface dans lequel les ions changent d'état d'oxydation lors de l'adsorption et se termine lorsqu'une monocouche ou une sous-monocouche est formée. L'exposition des NCs $CsPbBr_3$ à la lumière UV (3,6 eV) au-dessus de la bande interdite des NCs catalyse non seulement une telle réaction chimique, mais conduit également à la formation de plomb métallique (Pb^0). En outre, il a été constaté que le dépôt sous-potentiel de plomb (Pb_{UPD}) se produit en particulier à la surface et à l'interface et qu'il ne se produit que lorsque les ions Pb^{2+} sont libérés de la pérovskite et lorsque la pérovskite est en contact direct avec l'or. De plus, les ligands ne jouent aucun rôle dans la formation ou la prévention du Pb_{UPD}. En revanche, le Pb^0 n'est formé que lorsque l'halogénure (le bromure dans notre cas) s'échappe de la surface sous la forme de Br_2(g). Il a également été constaté que la formation de Pb^0 peut s'étendre dans le volume NCs à la suite d'une exposition à une lumière UV de forte fluence. Lorsque les NCs sur Au sont exposés à un flux élevé de rayons X, une décomposition des NCs se produit, mise en évidence par la formation de Pb_{UPD} et de Pb^0. Avec l'exposition à un flux élevé de rayons X, la dégradation de la structure pérovskite se produit immédiatement, ce qui signifie que les dommages se produisent à une échelle de temps plus rapide que le temps d'acquisition du spectre. Par conséquent, les NCs de pérovskite $CsPbBr_3$ sur substrat Au ne sont pas stables car des changements non négligeables et irréversibles se produisent lorsqu'ils sont exposés à la lumière IR et UV, ainsi qu'à des rayons X à flux élevé, et le contact direct de la pérovskite avec l'Au devrait être envisagé avec plus de précaution. En outre, ces résultats suggèrent les limites potentielles de l'utilisation de l'Au comme électrode stable dans les dispositifs optoélectroniques à base de pérovskite.

Lorsqu'ils sont exposés à la lumière IR, les NCs de $CsPbBr_3$ sur des substrats semi-conducteurs (monocristal de MoS_2) et d'oxyde métallique (MoO_x), montrent l'accumulation d'une tension photoélectrique de surface intra-bande dans l'échantillon, mise en évidence par le déplacement de l'énergie de liaison du niveau central de Pb 4f, sans aucune décomposition de la pérovskite. Cette tension de surface intra-bande provient d'états de piège profond (défaut interstitiel de bromure et/ou lacunes de bromure) situés à la position de l'intervalle moyen de $CsPbBr_3$. Cela conduit à un décalage opposé de l'énergie de liaison des niveaux centraux de la pérovskite sur un substrat de type n (MoS_2) par rapport à un substrat de type p (MoO_x). Cela souligne également que le substrat sur lequel les NCs de $CsPbBr_3$ sont déposés dicte la propriété semi-conductrice de la pérovskite, c'est-à-dire que la pérovskite adopte des propriétés de type n sur le substrat MoS_2 et des propriétés de type p sur le MoO_x. Plus important encore, cela signifie que les propriétés semi-conductrices de la pérovskite dépendent du substrat non seulement à l'interface, mais aussi dans ce volume et à la surface de la pérovskite. En outre, ces états de sous-bande interdite, qui agissent comme des centres de recombinaison non radiative indésirables, peuvent conduire à une faible efficacité des dispositifs optoélectroniques basés sur les NCs $CsPbBr_3$. En outre, bien qu'il existe des états de sous-bande interdite, la concentration de ces états de piège profond est faible car l'intensité de la lumière, qui est supérieure à l'intensité de 1 soleil (*1 sun*) de deux ordres de grandeur, n'induit pas la décomposition du matériau pérovskite. Néanmoins, l'existence de tels états de bande interdite provenant de lacunes de bromure et/ou de défauts interstitiels de bromure souligne l'insertion d'une couche tampon entre la pérovskite $CsPbBr_3$ et la couche de transport de charge ou d'une couche de transport de charge qui devrait empêcher la diffusion des ions Br^-. Dans le cas contraire, ces ions Br^- peuvent se diffuser dans l'électrode métallique, entraînant l'oxydation du métal et réduisant ainsi sa conductivité.

L'exposition à la lumière UV (3,6 eV) décompose les NCs de pérovskite $CsPbBr_3$ sur MoS_2 en favorisant le transfert de charge des bandes de valence dominées par les halogénures vers les bandes de conduction dominées par le plomb, ce qui entraîne la désorption des atomes de bromure avec une réduction simultanée de Pb^{2+} en Pb^0. Une augmentation de la fluence du laser UV accroît les dommages, mais le substrat MoS_2 reste chimiquement intact, comme le montrent la forme, l'intensité et l'énergie de liaison inchangées des spectres des niveaux centraux du MoS_2. Cela signifie qu'aucune interaction chimique ne se produit à l'interface entre le MoS_2 et la pérovskite, ce qui suggère que le MoS_2 pourrait être une couche tampon potentiellement utile : même s'il n'est pas utilisé seul, il peut être utilisé en combinaison avec d'autres matériaux pour améliorer la stabilité intrinsèque des dispositifs à pérovskite. Cependant, l'alignement des bandes et la capacité de transport de charge du MoS_2 doivent être étudiés avant de rationaliser sa fonctionnalité dans un dispositif.

En ce qui concerne l'interface des pérovskites avec le MoO_x, l'illumination UV induit une décomposition de la pérovskite, qui est cependant moins prononcée que sur le substrat MoS_2. Plus significative encore, la réduction du MoO_x est observée, ce qui pourrait résulter d'une réaction d'oxydoréduction à l'interface entre la pérovskite et l'oxyde métallique. Cette réduction peut provoquer un changement radical de la composition de l'interface, entraînant la formation involontaire d'une couche défectueuse qui entrave l'extraction de la charge et facilite la recombinaison.

De même, à l'interface avec l'ITO, la pérovskite est la moins endommagée de tous les substrats, mais une réaction chimique potentielle à l'interface est attendue en raison d'une augmentation significative de la largeur du pic du niveau central Pb 4f de la pérovskite. Cet élargissement du pic Pb 4f suggère la formation d'une nouvelle espèce chimique qui pourrait provenir de la diffusion d'ions d'indium ou d'étain à partir de l'ITO.

Comme indiqué précédemment, la dégradation de la structure de la pérovskite liée à la formation de Pb^0 est évitée par l'utilisation d'un substrat d'oxyde. La prévention de la décomposition de la pérovskite sur les substrats à large bande interdite peut être justifiée par le fait que, sous illumination UV, l'excitation de la bande interdite conduit à la génération de paires électron-trou à la fois dans le substrat et dans la pérovskite. La bande interdite de la pérovskite étant inférieure à celle des oxydes (ITO et MoO_x), il est plus probable que l'électron photoexcité se recombine avec le trou laissé par l'excitation de la bande interdite du $CsPbBr_3$ (voir figure). Cette recombinaison réduit partiellement la formation d'un défaut interstitiel d'halogénure (bromure dans notre cas) qui est responsable de la création de lacunes d'halogénure et de la migration ultérieure d'ions d'halogénure, ce qui entraîne une baisse de la formation de $Br_2(g)$. La formation de Pb^0 est donc réduite. Cependant, une telle recombinaison (électrons photoexcités dans les oxydes et trous laissés par l'excitation de la bande interdite de la pérovskite) peut réduire la collecte de trous à l'anode et donc l'efficacité d'un dispositif.

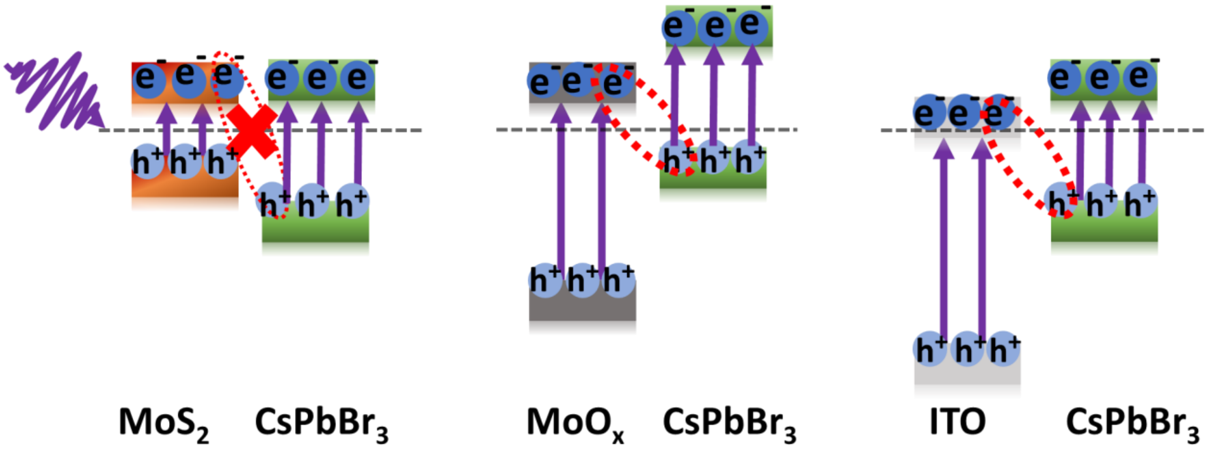

Figure. Représentation schématique de la recombinaison de charge à l’interface entre différents substrats (MoS$_2$, MoO$_x$ and ITO) et les NCs de CsPbBr$_3$.

Enfin, on peut affirmer que cette étude explore plus qu'elle n'empêche le processus de dégradation des NCs de pérovskite CsPbBr$_3$ se produisant aux différentes interfaces. Cependant, l'objectif est de comprendre le phénomène et le mécanisme qui induit et dicte une telle dégradation, et d'identifier les moyens possibles d'inhiber une telle décomposition de la pérovskite. Cette étude souligne que l'intégrité de l'interface est un facteur important, et le développement d'images atomistiques de l'interface contribuera au développement de dispositifs opto-électroniques hautement efficaces et stables à base de NCs de pérovskite.